2013

Thermoacoustic Riemann Solver Finite Volume Method With Application To Turbulent Premixed Gas Turbine Combustion Instability

Perry Johnson
University of Central Florida

Thermoacoustic Riemann Solver Finite Volume Method with Application to Turbulent Premixed Gas Turbine Combustion Instability

by

Perry L. Johnson
B.S. Mechanical Engineering, University of Central Florida, 2011

A thesis submitted in partial fulfillment of the requirements
for the degree of Master of Science
in the Department of Mechanical and Aerospace Engineering
in the College of Engineering and Computer Science
at the University of Central Florida
Orlando, Florida

Spring Term
2013

Major Professor: Jayanta Kapat

ABSTRACT

This thesis describes the development, verification, and validation of a three dimensional time domain thermoacoustic solver. The purpose of the solver is to predict the frequencies, modeshapes, linear growth rates, and limit cycle amplitudes for combustion instability modes in gas turbine combustion chambers. The linearized Euler equations with nonlinear heat release source terms are solved using the finite volume method. The treatment of mean density gradients was found to be vital to the success of frequency and modeshape predictions due to the sharp density gradients that occur across deflagration waves. In order to treat mean density gradients with physical fidelity, a non-conservative finite volume method based on the wave propagation approach to the Riemann problem is applied. For modelling unsteady heat release, user input flexibility is maximized using a virtual class hierarchy within the OpenFOAM C++ library. Unsteady heat release based on time lag models are demonstrated. The solver gives accurate solutions compared with analytical methods for one-dimensional cases involving mean density gradients, cross-sectional area changes, uniform mean flow, arbitrary impedance boundary conditions, and unsteady heat release in a one-dimensional Rijke tube. The solver predicted resonant frequencies within 1% of the analytical solution for these verification cases, with the dominant component of the error coming from the finite time interval over which the simulation is performed. The linear

growth rates predicted by the solver for the Rijke tube verification were within 5% of the theoretical values, provided that numerical dissipation effects were controlled. Finally, the solver is then used to predict the frequencies and limit cycle amplitudes for two lab scale experiments in which detailed acoustics data are available for comparison. For experiments at the University of Melbourne, an empirical flame describing function was provided. The present simulation code predicted a limit cycle of 0.21 times the mean pressure, which was in close agreement with the estimate of 0.25 from the experimental data. The experiments at Purdue University do not yet have an empirical flame model, so a general vortex-shedding model is proposed on physical grounds. It is shown that the coefficients of the model can be tuned to match the limit cycle amplitude of the 2L mode from the experiment with the same accuracy as the Melbourne case. The code did not predict the excitation of the 4L mode, therefore it is concluded that the vortex-shedding model is not sufficient and must be supplemented with additional heat release models to capture the entirety of the physics for this experiment.

ACKNOWLEDGMENTS

Thanks to Dr. Jay Kapat for the years of inspiration and introduction to advanced topics in mechanical and aerospace engineering, as well as his guidance and support in my developing career. Thanks to Dr. Enrique Portillo for his oversight and guidance in my thesis work at Siemens. He took a true interest in the details of my developments and the development of my personal abilities as an engineer. Thanks also to Dr. Rajesh Rajaram, for insightful discussions contributing to the development and presentation of this work. Thanks to Jared Pent, for the teamwork at Siemens that greatly enhanced this thesis. Dr. Aleksander Jemkov and Dr. Hrvoje Jasak of Wikki, Ltd. contributed much of the source code as well as vital insight into OpenFOAM code development. Thanks to Dr. Sen Shivamoggi for two interesting courses in theoretical fluid dynamics as well as many office hours of mathematical correction, career guidance, and philisophical meanderings. Thanks to Drs. Subith Vasu and Marcel Ilie for discussions and lectures in combustion and turbulence, respectively, as well as for sitting on my thesis committee. Thanks to Roberto Claretti, Greg Natsui, Lucky Tran, and others in the CATER group for countless entertaining and wonderful discussions. Thanks to Lance Olimb and Ande Johnson, for their refreshing guidance in my life's journey these past six years at UCF. Thanks to my wife, Cara Johnson, for being my indispensible partner, displaying unyielding humility, grace, and sanity.

TABLE OF CONTENTS

LIST OF FIGURES

LIST OF TABLES

NOMENCLATURE

Symbol	Name	Units
A	area	m^2
a	sound speed	m/s
$\underset{\approx}{A}$	x-oriented flux Jacobian	$-$
AR	cross-sectional area ratio	$-$
$\underset{\approx}{B}$	y-oriented flux Jacobian	$-$
c_p	specific heat at constant pressure	$J/(kgK)$
c_v	specific heat at constant volume	$J/(kgK)$
$\underset{\approx}{C}$	z-oriented flux Jacobian	$-$
Co	Courant number	$-$
E_n^2	orthonormal scaling factor	m^3
e	internal energy per unit mass	J/kg
f	frequency	Hz
$\underset{\sim}{f}$	x-flux function	$-$
f_{face}	flux at finite volume face	$-$
$\mathcal{F}$	momentum source per volume, force	N/m^3
$\underset{\sim}{g}$	y-flux function	$-$

H_{21}	transfer function	$-$
h	enthalpy per unit mass	J/kg
h	source term for spatial averaging	$kg/(ms^4)$
$\underset{\sim}{h}$	z-flux function	$-$
$\mathcal{H}$	enthalpy of reaction per unit mass	m^2/s^2
J_n	nth order first kind Bessel function	$-$
j	electrical current density	A/m^2
$\underset{\approx}{J}$	arbitrarily-oriented flux Jacobian	$-$
k	wave number	$1/m$
$\underset{\approx}{L}$	left eigenvector matrix	$-$
L	length of a duct	m
$\underset{\sim}{l}$	left eigenvector	$-$
$\mathcal{L}_r$	acoustic reference length	m
$\mathcal{L}[]$	Sturm-Liouville operator	$-$
M	Mach number $= u/a$	$-$
$\mathcal{M}$	mass source per volume	$kg/(m^3s)$
n	any integer	$-$
$\hat{n}$	unit normal vector	$-$
p	pressure	Pa
Q	heat release per unit area	W/m^2
q	heat release per unit volume	W/m^3

$\mathcal{Q}$	heat addition per unit volume	W/m^3
R	gas constant	$J/(kgK)$
$R(\omega)$	reflection coefficient	$-$
$\underset{\approx}{R}$	right eigenvector matrix	$-$
$\underset{\sim}{r}$	right eigenvector	$-$
S	cross-sectional area of a duct	m^2
s	entropy per unity mass	$J/(kgK)$
$\underset{\sim}{S}$	hyperbolic system source vector	$-$
$\mathcal{S}$	entropy source per volume	$W/(m^3K)$
T	temperature	K
t	time	s
TR	temperature ratio	$-$
u	x-velocity, velocity in general	m/s
$\underset{\sim}{u}$	velocity vector	m/s
V	volume	m^3
v	y-velocity	m/s
w	z-velocity	m/s
$\underset{\sim}{w}$	characteristic variables	$-$
$\mathcal{W}$	work done per unit volume	W/m^3
$\underset{\sim}{\mathcal{W}}$	wave strength vector	$-$
$\underset{\sim}{x}$	position vector	m

x	x-position	m
Y_n	nth order second kind Bessel function	$-$
y	x-position	m
Z	acoustic impedance	$-$
z	x-position	m
α	linear growth rate	$1/s$
α	wave strength coefficient	$-$
γ	specific heat ratio $= c_p/c_v$	$-$
δ	Dirac delta function	$1/m$
δ_{ij}	Kronecker delta	$-$
ϵ	acoustic smallness parameter	$-$
η	temporal dependence of thermoacoustics	$-$
$\underset{\approx}{\Lambda}$	diagonal eigenvalue matrix	$-$
λ	eigenvalue	$-$
λ	acoustic wavelength	$1/m$
μ	fluid dynamic viscosity	$Pa\ s$
μ	mean flow scaling parameter	$-$
ν	fluid kinematic viscosity	m^2/s
ν	mean gradient scaling parameter	$-$
ρ	fluid mass density	kg/m^3
ρ^{elec}	electrical resistivity	Ωm

σ	orthogonality weight function	$-$
Ψ	total variation diminishing slope limiter	$-$
ψ	normalized modeshape	$-$
ϕ	arbitrary solution variable	$-$
Ω	complex frequency	rad/s
ω	frequency, real part of Ω	rad/s
$\dot{\omega}$	reaction rate	$kg/(m^3 s)$
$\iiint_{\Omega} dV$	control volume integral	m^3
$\iint_{\partial\Omega} dS$	bounding surface integral	m^2

Subscripts	
L	left side of Riemann problem
R	right side of Riemann problem
r	reference value

CHAPTER 1
INTRODUCTION

Gas turbine engines are widely used for both power generation and propulsion. Land-based power generation gas turbines are designed to produce electrical power by converting the chemical energy stored in a fuel into thermal and flow energy through a combustion process. Prior to combustion, a series of compressor stages bring the intake air up to pressure many times the atmospheric pressure. After the combustion, the flow's energy is then converted into work through rows of turbine blades before exhausting back to the ambient surroundings. In modern power plants, a combined cycle can be utilized, in which the hot exhaust from the gas turbine is used to preheat steam for a steam cycle. In this way, combined cycle power plants can achieve impressive efficiencies in the neighborhood of 60% [1]. Thermodynamically, the physics of a power generation gas turbine engine can be described to first order by the ideal Brayton cycle with small deviations accounting for non-isentropic processes [2]. The Brayton cycle is sketched in Fig. 1.1 in therms of an entropy-temperature diagram. From $1 \rightarrow 2$ the compressor adds work to the flow. The flow then enters the combustion chamber, where the exothermic reaction adds heat to the flow from $2 \rightarrow 3$ (nearly isobaric). Then the flow enters the turbine where the rotors extract energy from the flow,

$3 \rightarrow 4$, converting it rotational energy which is transferred to electrical energy via a generator (not shown).

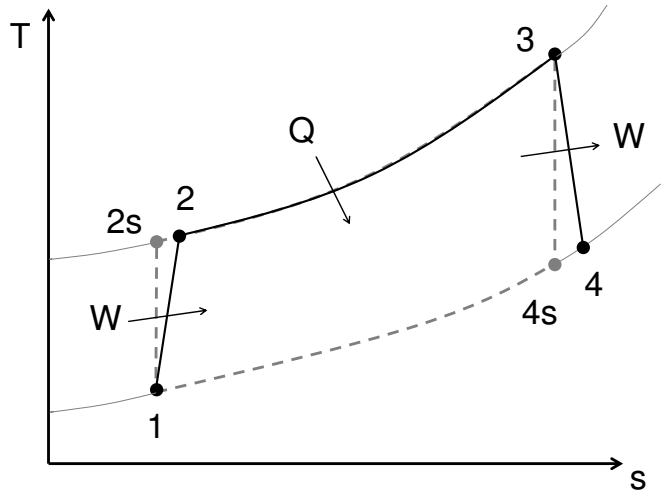

Figure 1.1: Temperature-entropy diagram showing the ideal Brayton cycle along with a cycle accounting for entropy production in the compressor and turbine.

Nitrogen oxides NO_x, primary pollutants formed during the combustion processes of gas turbine engines [3], are heavily-regulated due to environmental concerns [4]. The chemical effects of NO_x in the atmosphere are discussed in [5]. In the past, gas turbine engines used diffusion flames for combustion due to their stability [3]. Recent regulations have pushed gas turbine designs toward use of lean, premixed flames, which produce much less NO_x via the thermal mechanism [6]. Such lean, premixed flames, however, have proven much more sensitive to acoustic disturbances [7]. In this way, the mitigation of combustion instabilities has become a key design task in the development of clean engine technology.

The term "combustion instability" refers to the presence of large amplitude acoustic motions which develop inside combustion chambers, driven by the positive feedback interaction between the unsteady acoustic motions and the unsteady heat release of the flame. Combustion instabilities are not unique to gas turbines, but have also been observed in other scenarios such as liquid rockets, solid rockets, ramjets, and afterburners [8]. Unsteady flames can be viewed as acoustic sources, adding energy to acoustic modes of the enclosed chamber. The unsteady motions of the flames can themselves be driven by acoustic motion, directly or indirectly through acoustically altered hydrodynamic effects. These effects form a closed feedback loop, Fig. 1.2, by which acoustic disturbances can grow. Theoretically, in the linear (small signal) limit, the acoustic modes can grow unbounded. In reality, large amplitude effects and non-linearities quickly intervene to bring the system to a limit cycle.

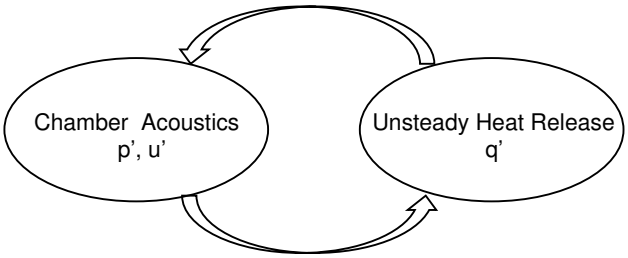

Figure 1.2: Schematic emphasizing the closed loop feedback processes leading to combustion instabilities.

1.1 Linear Behavior

A mathematically concise way to capture the physical behavior in the linear limit is easy to obtain using the method of modal expansion and spatial averaging [8]. Derivation and discussion of this method is reserved for Chapter 2 and Appendix D. The generalized results are shown here for introducing the physical behavior in the linear limit. Using η to describe the temporal evolution of a given mode's amplitude (specifically, the acoustic pressure mode), depending on the nature of the relationship between the acoustic variables and the heat release (feedback mechanism), the temporal evolution can be written as

$$\ddot{\eta} - \alpha\dot{\eta} + (\omega_n - \omega_{sh})\eta = 0. \tag{1.1}$$

To a certain extent, Eq. (1.1) relies on the assumptions of the weighted residual method used to generate it, but in a loose, general sense, conveys the basic physics that lead to combustion instabilities. For example, aside from the details of the weighted residual method, a simple derivation of Eq. (1.1) starts with the temporal evolution for linear acoustics

$$\ddot{\eta} + \omega_n\eta = 0 \tag{1.2}$$

supplied with an arbitrary forcing term, F, coming from the unsteady heat release of combustion

$$\ddot{\eta} + \omega_n\eta = F. \tag{1.3}$$

For a given feedback mechanism, the temporal evolution of forcing term will be a function of the temporal evolution of the acoustic variables and their time derivatives.

$$F = F(\eta, \dot{\eta}, \ddot{\eta}) \tag{1.4}$$

Neglecting, again, non-linear interactions (small signal assumption), the forcing function can be written as a linear combination of the three

$$F = c_1\eta + c_2\dot{\eta} + c_3\ddot{\eta}. \tag{1.5}$$

Substituting Eq. (1.5) into the forced oscillator equation, Eq. (1.3) and organizing all terms to the left hand side

$$(1 - c_3)\ddot{\eta} - c_2\dot{\eta} + (\omega_n - c_1)\eta = 0. \tag{1.6}$$

Thus, the forcing term, depending on its exact form, accomplishes on of three effects. First, the heat release can cause a shift in the frequency (c_1) of the oscillation away from the natural frequency of the linear acoustic mode. Second, the heat release may introduce and (negative) damping term (c_2) into the oscillator equation, which serves to augment or attenuate the acoustic fluctuations in time. Finally, the third term (c_3) works to adjust the inertia of the oscillating system. Normalization of Eq. (1.6) leads to Eq. (1.1) with the following relationships for the growth rate and frequency shift

$$\alpha = \frac{c_2}{1 - c_3} \tag{1.7}$$

$$\omega_{sh} = \omega_n - \frac{\omega_n - c_1}{1 - c_3}. \tag{1.8}$$

The general solution to Eq. (1.1) is

$$\eta(t) = \exp(\alpha t) \begin{bmatrix} cos(\omega_n - \omega_{sh}) \\ sin(\omega_n - \omega_{sh}) \end{bmatrix}. \tag{1.9}$$

Hence, the main two physical effects of unsteady heat release are (1) to shift the frequency, and (2) to cause exponential growth/decay. The nature of the feedback mechanism between the acoustic motions and the unsteady heat release determines the degree to which either of these two effects is manifest.

The conditions for the unsteady heat release to cause an exponential growth or decay in the linear acoustics was first spelled out by Lord Rayleigh [9]: "If heat be periodically communicated to, and abstracted from, a mass of air vibrating in a cylinder bounded by a piston, the effect produced will depend upon the phase of the vibration at which the transfer of heat takes place. If heat be given to the air at the moment of greatest condensation or to be taken from it at the moment of greatest rarefaction, the vibration is encouraged. On the other hand, if heat be given at the moment of greatest rarefaction, or abstracted at the moment of greatest condensation, the vibration is discouraged."

In essence, this quote was the first understanding of what has become known as Rayleigh's Criterion. When the unsteady heat release is in phase with the acoustic pressure oscillations, the maximum mode growth occurs. When the two are 180^o out of phase, the maximum mode damping occurs. At phases greater than -90^o and less than 90^o, the mode will grow exponentially. Modes with phases outside this range will be attenuated. A phase relationship of $\pm 90^o$ between acoustic pressure and unsteady heat release indicates marginal

stability. A concise mathematical statement often used to summarize Rayleigh's Criterion for the growth of acoustic modes is

$$\int_{t_0}^{t_0+T} \iiint_{\Omega} p'q' dV dt > 0 \tag{1.10}$$

where T is the period of oscillation. For this reason, pressure-based mechanisms with no time lag or spatial dependence will lead to maximum growth of the mode. This global measure can be calculated for a domain with known pressure and heat release field histories. Additionally, by leaving out the volume integration, a local value, sometimes referred to as a Rayleigh Index ($R.I.$) can be calculated at all points in the domain. This value is essentially the correlation between the pressure and heat release signals at that point. A positive correlation indicates local contribution to the growth of the mode, while a negative contribution indicates local contribution to the damping of the mode. Such a calculation for a known pressure and heat release field history can reveal regions of the flame which contribute to damping the mode and regions which tend to excite the mode. This can provide insight to underlying feedback mechanisms. A proper understanding of physical feedback mechanisms can aid designers in mitigating combustion instabilities through manipulation of design variables to shift phases in a way so as to discourage positive Rayleigh indices.

As a corollary to Rayleigh's criterion, it can be stated that phase relationships of $\pm 90^o$ lead to maximum frequency shifts. For this reason, acoustic velocity-based mechanisms with no time lag of spatial dependence will lead to no growth rate, but maximum frequency shift. So, the phase relationship between the acoustic pressure and unsteady heat release determines the relative magnitude of the frequency shifts and damping caused by the flame.

The linear growth rate (α) or alternatively the Rayleigh criterion can be used to determine whether a mode will grow or decay in the linear limit. The sign of the linear growth rate predicts the absence or presence of a strong acoustic oscillation at a given mode.

1.2 Finite Amplitude Effects

The previous discussion was encapsulated by the linear acoustic assumption, that is, that the acoustic oscillations remain infinitesimally small. For modes with positive linear growth rates, one can see that linear theory predicts the exponential growth of that mode. Hence, after a finite amount of time, the amplitude of the oscillation will no longer be negligible. The consequences of finite amplitudes are now explored.

1.2.1 Boundary Damping

The perfectly reflecting boundary condition (rigid wall or pressure release) is an ideal approximation of real boundaries. This approximation becomes even worse when the assumptions of linear acoustics break down (finite amplitude signal). For example, walls enclosing the combustion chamber become less rigid in the presence of finite amplitude oscillations. Near wall boundaries, the viscosity and conductivity of the gas will play a larger role (in the boundary layer). The inviscid and non-conducting assumptions of classical acoustics are no longer valid. These viscous and conducting effects will tend to remove acoustic energy

from the system. Additionally, the inlet (for gas turbines, from the compressor exit) and the outlet (to the turbine inlet) or the combustion chamber will be a boundary through which acoustic energy can escape. As the acoustic fluctuations become large, the loss of acoustic energy through the boundaries will also increase, tending to slow the growth of the mode.

1.2.2 Non-Linear Flame Response

A linear flame response indicates that as the acoustic oscillations increase, the heat release oscillations increase proportionally. In reality, this is not the case [10]. The oscillation of the flame will be limited by viscous and heat conduction effects as well as kinematic restoration. Hence, for larger amplitude oscillations, the feedback mechanism driving the instability will not be able to keep up. Therefore, the non-linear nature of the flame response will tend to slow the growth of the mode as acoustic oscillation amplitudes become large.

1.2.3 Non-Linear Acoustics and Loss of Orthogonality

Another physical effect that comes into play at large enough amplitudes is the non-linear interaction of acoustic motions. Linear acoustics assumes small enough motions such that any terms higher than first order in fluctuating variables can be neglected. Such terms can no longer be neglected once a given mode becomes large enough. When the non-linear effects are included, the acoustic modes are no longer orthogonal. The loss of the orthogo-

nality property means that the acoustic modes can now interact with other acoustic modes. For example, modes that are damped can steal acoustic energy from growing modes. In this way, the growth of the mode is also slowed by non-linear mode interactions.

1.2.4 Limit Cycle Amplitudes

Ultimately, these finite amplitude effects which append themselves to linear acoustic theory slow the growth of an excited mode. Eventually, the growth levels off to a steady limit cycle in which the amplitude is large but constant [8]. A visualization of this is shown in Fig. 1.3. The acoustic energy gain from the unsteady flame is initially (for lower amplitude oscillations) greater than the losses from the effects described above. As the amplitude then increases, the non-linear flame response (gain), the increasing losses from other effects becomes dominant. The intersection of these two curves identifies the limit cycle amplitude, that is, where the gains and losses of acoustic energy are in equilibrium.

The amplitude of the limit cycle is often what is sought in engineering analysis of gas turbines, since this is what is of concern to the steady operation of the engine. Figure 1.4 illustrates the progression from the linear regime to the limit cycle as acoustic amplitudes increase. These last two figures are a simplification of the physical behavior in some real cases, since non-linear effects can lead to chaotic behavior of the oscillation amplitude envelope [11], rather than the constant amplitude limit cycle shown in the figure.

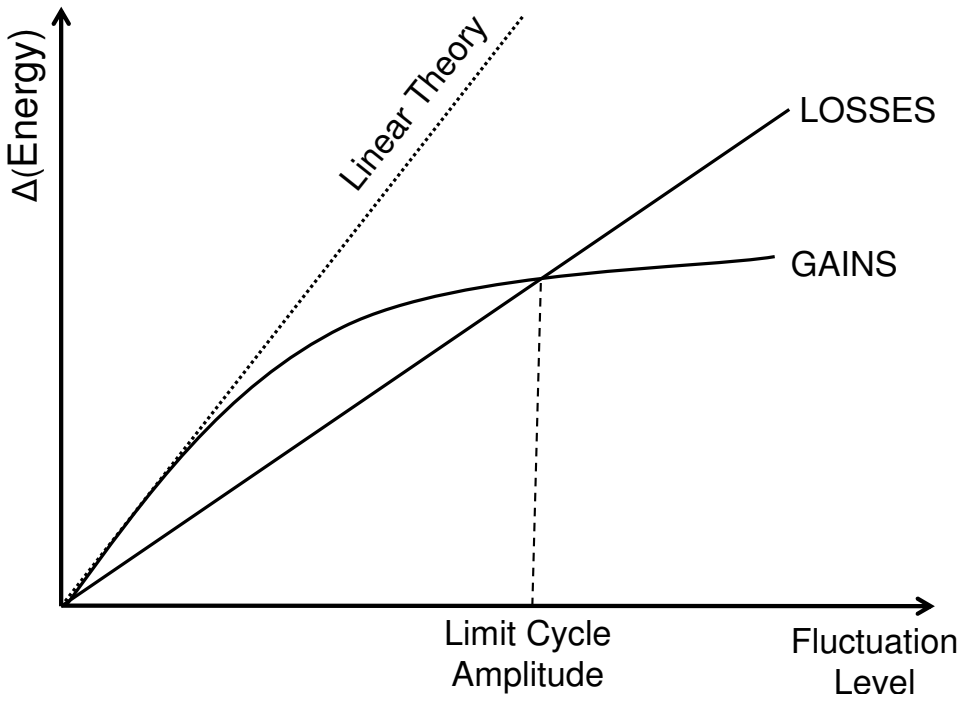

Figure 1.3: Acoustic energy gains and losses as a function of oscillation amplitude.

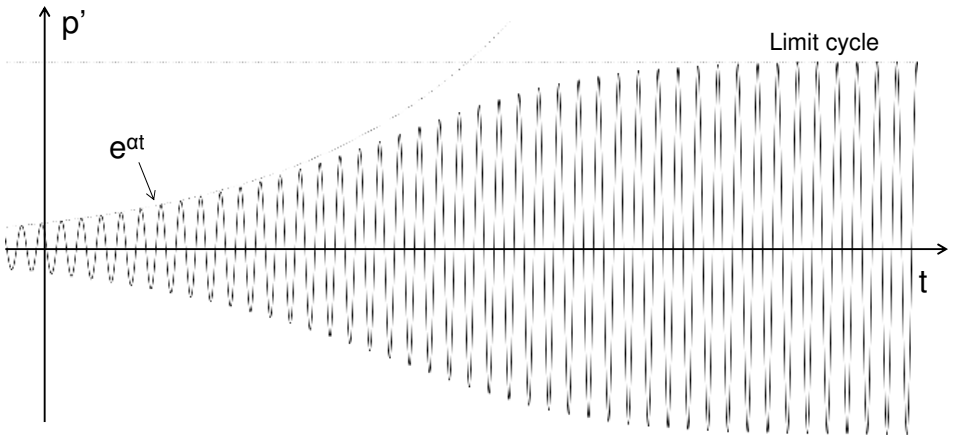

Figure 1.4: Idealization of the evolution of a combustion instability, from exponential growth in the linear regime to limit cycle amplitude in the non-linear regime.

It is somewhat reasonable, yet optimistic, that limit cycle amplitudes would be correlated (proportional) to the relative magnitude of the linear growth rate. For example, by decreasing the linear growth rate of a mode through manipulation of time lags, it is reasonable to think that the limit cycle amplitude would be lowered. In fact, some studies have suggested a rough correspondence [12]. Such a correspondence gives utility to the use of linear theory in analyzing combustion instabilities. It should be stressed, however, that the use of linear theory comes with a number of assumptions that render any such analysis method a first order approximation.

1.3 Some Example Feedback Mechanisms

In the present discussion, the feedback mechanism refers to the physical process (or chain of processes) by which the acoustic fluctuations affect the unsteady heat release in the flame. From the governing equations, as shown in Chapter 2, the influence of the heat release on the acoustics is clear. The unsteady heat release appears as a source term in the linearized energy equation. To close the feedback loop for complete coupling, however, it is necessary to specify the physical mechanism by which the acoustics affect the heat release. In reality, the manner in which the unsteady heat release is influenced by the chamber acoustics is exceedingly complex, given that the such a relationship is governed by the multi-species reacting Navier-Stokes equations. This set of equations is highly non-linear and turbulent for any realistic engine conditions. It is the goal of first order analysis to characterize the

flame behavior simply. With this goal in mind, vast simplifications of the combustion physics are simplified into a flame transfer function (FTF), time lag model [13], or flame describing function (FDF) [14]. Flame describing functions differ from flame transfer functions in that they include non-linear effects in the flame response [1]. For the simulation code developed in this thesis, it is most beneficial to discuss the time lag model.

The time lag model is a method of physical simplification of the feedback mechanism in which the modeller proposes that the essence of the feedback behavior can be captured by modelling the unsteady heat release at time t as a function of acoustic variables at time $t - \tau$. This is a general framework by which many examples of flow physics can by included in the feedback mechanism. Time lag models are sometimes referred to as "$n - \tau$" models, where n is the gain factor and τ is the time lag.

A proposed mechanism could be based on the pressure fluctuations affecting the heat release. Such a mechanism could be stated mathematically as

$$\frac{q'(x, y, z, t)}{\bar{q}(x, y, z)} = n \frac{p'(x - \xi, y - \eta, z - \zeta, t - \tau)}{\bar{p}(x, y, z)} \tag{1.11}$$

where here ξ, η, and ζ refer to spatial shifts between the acoustic event causing a disturbance and the location in the flame at which such disturbance alters the unsteady heat release of the combustion. A physical argument for such a model could be made for flames in which the combustion chemistry is sensitive to the pressure at which the reactions take place [4]. For lean, premixed gas turbine combustion, there can be significant time lag between the pressure fluctuations and the heat release fluctuations caused by them. In other words, the

lean premixed flame chemistry does not necessarily respond instantaneously to the pressure oscillations at frequencies typically seen [10].

Another scenario in which the acoustic pressure can be the primary property in the feedback mechanism occurs when the injection of unburned mixture into the chamber occurs transverse to the direction of acoustic oscillation for a given mode. In this case, the oscillating pressure in the chamber gives oscillating resistance to the injection path. In this way, the oscillating pressure seen by the injection causes an oscillation in the flow rate, leading to pulsing of the injected flow. The pulsing can then be linked to mass conversion rate of the combustion process and coherent structures created from the lip of the injector [15].

Another acoustic variable which can have a significant impact on the unsteady heat release is the acoustic velocity. The mathematical expression relating to this mechanism could be

$$\frac{q'(x,y,z,t)}{\bar{q}(x,y,z)} = n\frac{u'(x-\xi,y-\eta,z-\zeta,t-\tau)}{\bar{u}(x,y,z)}. \tag{1.12}$$

Note that in regions of low Mach number, the mean velocity in the denominator could cause a large predicted growth rate. Instead, the model could be normalized by the local sound speed, which would in effect multiply the gain by the local Mach number. Superposed on the mean and turbulent velocities, the acoustic velocity aerodynamically changes the shape of the flame. Additionally, the flame can be locally wrinkled by the acoustic velocity, causing local increases in the heat release due to surface area enhancement. Aside from direct modification of the flame shape, the acoustic velocity can also trigger vortex shedding

from the lip of a backward facing step. The vortex that is shed then convects at a speed related to the mean velocity and wrinkles the flame. This mechanism is commonly proposed for dump combustors [16].

A final mechanism can for feedback coupling in premixed flames is based on equivalence ratio fluctuations [17]. The pressure and velocity oscillations at the fuel injection site can cause the local equivalence ratio to vary, as well as the level of unmixedness. For lean premixed flames near the blow-off limit, small changes in equivalence ratio can have large effects. This mechanism is not applicable to scenarios in which the premixing takes place in a volume acoustically isolated from the combustion.

1.4 Mitigation of Large Amplitude Limit Cycles

Passive and active control of combustion instabilities is an open and very active topic of research [18]. Aside from modifying designs to adjust time lag relationships and hence diminish instability mechanisms, passive and active components can be added to the combustion system to mitigate large amplitude limit cycles. While effective active controls have been demonstrated [18], they often require too much input energy or increase the level of pollutants such that their implementation in engines is not justified. The most common type of passive control for mitigating combustion acoustics is an acoustically absorbing combustor liner or resonators [19, 20]. When multiple acoustic modes are excited by the unsteady heat release in a combustor, multiple resonators tuned to different frequencies can be used [21].

1.5 Predictive Tools for Combustion Instabilities

1.5.1 Transfer Matrix Approach

On of the most common approaches to predicting linear stability is the use of transfer matrices [22] to represent volume elements, connected at nodes where acoustic variables are specified. The transfer matrix on an element relates the acoustic variables on either of its sides based on solutions to the linearized Euler equations. A given geometry can be broken piecewise into many elements and an overall transfer matrix with boundary conditions can be solved numerically for the complex eigenfrequencies. Flame elements can be used which introduce time lag heat release models as source terms to the linearized Euler equations. The imaginary part of the eigenfrequencies, which is introduced mainly through a flame element, indicates the linear stability of the system. This tools is subject to the assumption of one-dimensional acoustic propagation. It is limited to evaluating the stability of longitudinal modes. Additionally, the flame dynamics must be captured by a one-dimensional flame transfer function.

1.5.2 Modal Expansion with Spatial Averaging

Application of the method of spatial averaging for approximate treatment of combustion instabilities was introduced by Culick in his doctoral thesis [23]. The method was

recently summarized by [8]. In this approach, the acoustic wave equation is solved with source terms on the right hand side accounting for heat release and mean flow effects. An approximate solution is constructed by using the modeshapes (eigenfunctions) from the homogeneous problem as basis functions for an eigenfunction expansion. A weighted residual method is then used, with the homogeneous modeshapes as the weighting functions, to integrate the wave equation spatially and obtain a second-order ODE in time. This ODE resembles a simple harmonic oscillator with source terms stemming from heat release, mean flow, and boundary effects. A numerical ODE solver is used to obtain the temporal development of a given mode. Depending on the type of model, linear or non-linear, a linear growth rate or limit cycle amplitude can be approximated with this method. This predictive methodology is subject to its assumption that the heat release, from the supplied flame response function, is weak relative to the acoustic behavior of the chamber. Appendix D provides further details into the possible shortcomings of this method, as pointed out by [24]. This approximate treatment of combustion instabilities was implemented in the Generalized Instability Model [25], which runs on the MATLAB platform. GIM is a pseudo-3D implementation, but does not allow the accurate treatment of three-dimensional acoustics in complex geometries. It primarily targets longitudinal modes, but can also predict transverse modes in geometries with constant cross-sectional areas. Cross-sections are limited to circular and annular shapes [26].

1.5.3 Large Eddy Simulation

A computationally-intensive approach to combustion instability simulation is the direct solution of the Navier-Stokes equations subject to a spatial filter. With large-eddy simulations (LES), the large turbulent motions are resolved spatially and temporally, and the smaller eddies that are physically present in the real flow are modelled. With a fine enough grid, a large percentage of the turbulent kinetic energy can be resolved, while the prohibitively large computational expense of direct numerical simulation (DNS) is avoided. Large-eddy simulations were first introduced in the context of meteorology by Smagorinsky [27]. With the rapid advance of modern computing power, the large-eddy simulation has become a staple tool in just about all applications of fluid dynamics. Combustion and thermoacoustics is no exception [28].

Two primary means of utilizing LES for insight into thermoacoustic instabilities are the forced response method [29, 30, 1] and the self-excited method [31, 32, 33]. The forced response method provides artificial acoustic forcing of a simulated flame and extracts the resulting heat release fluctuations. From the simulation, a flame transfer or non-linear flame describing function can be constructed [1]. The flame describing function is then useful for lower order methods, such as the transfer matrix approach or spatial averaging procedure in performing quick parametric sweeps of operating conditions and flow variables. Self-excited LES refers to a simulation in which no artificial forcing is introduced. Instead, should the physics be modelled correctly, the acoustic fluctuations develop on their own with in

the simulation. This method targets a physically accurate representation of a combustion instability. Such self-excited simulations are generally costly, as an entirely new simulation must be run for any change in flow or boundary conditions. The LES approach to combustion instabilities, forced response or self-excited, is a promising research field. However, it remains too time-consuming for complete integration into the current engineering design environment.

1.5.4 Other Methods

Now that some of the predominant methods of analysis for combustion instabilities have been discussed, a few others are worth mentioning. A quick, low-fidelity method of predicting combustion instabilties using Green's functions [23, 34] is related to the development of the spatial averaging technique [8]. Dowling [24] showed that this method does not accurately account for the effect of heat release on the oscillation frequency when such effects are not small.

A method based on a conservation equation for acoustic energy was developed recently [35]. The conservation equation for acoustic energy is derived from the governing equations, but much care must be take to accurately model each term. The capacity to model viscous and boundary losses is built into the method. The method provides the ability to approximate acoustic gains and losses at any frequency, regardless of the natural acoustic frequencies of the chamber.

Other numerical approaches include the use of existing commercial software for acoustic predictions, such as Virtual Lab [36]. Such software provides a frequency-domain solution to the acoustics in the combustion chamber with the ability to incorporate inhomogeneous media effects and mean flow. While this is useful for predicting the frequencies at which combustion instabilities are possible, it has no way to predict the stability of any modes.

Finally, most related to this thesis, Jemkov [37] solved the thermoacoustic equations on a Cartesian finite volume mesh for a Rijke tube. To some extent, this thesis is an extension of this method for unstructured grids with an improved flux calculation to correctly account for density gradients.

1.5.5 Motivation for the Present Work

Examining the predictive tools described above, two fundamental approaches can be seen. The first is the approximate and one-dimensional methods, such as the transfer matrix approach and GIM. These approaches offer quick turn-around times and convenient "back-of-the-envelope" approximations. A much greater degree of fidelity is achieved with LES, which resolves the full three-dimensional geometry, as well as the large-scale turbulent dynamics of the fluid flow and flame. The LES approach suffers from long turn-around times which becomes prohibitive for parametric studies required for design. The present work attempts to fill the gap in between the rough, quick methods and the thorough, costly

methods with a predictive tool representative (tacFoam) of a compromise in computational cost and physical fidelity, Fig. 1.5.

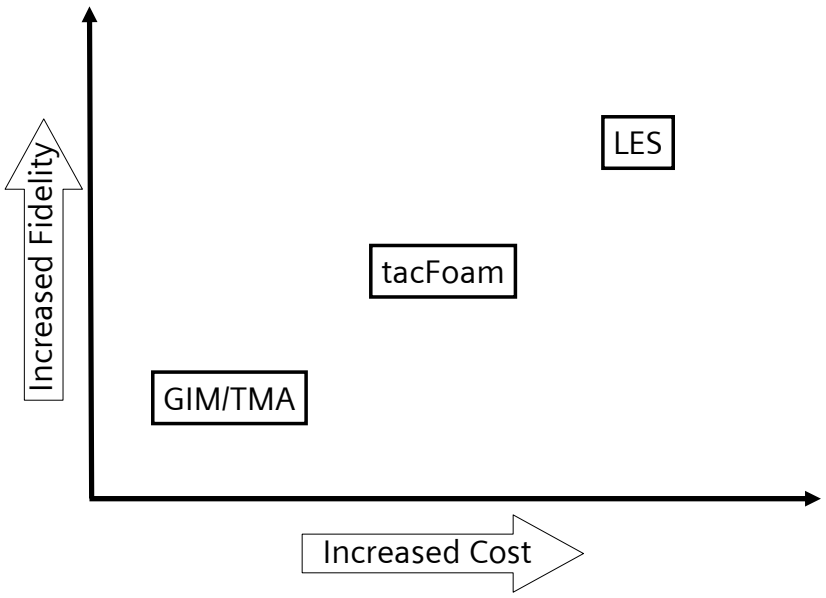

Figure 1.5: Cost vs. fidelity comparison for combustion instability predictive tools.

1.6 Thesis Contributions

The main contributions of this thesis to the state of the art are summarized as follows:

(1) Development, verification, and validation of a novel simulation technique in which pre-computed three-dimensional mean flows are mapped onto an unstructured finite volume mesh, where the linear Euler equations are solved with non-linear heat release models for arbitrary three-dimensional geometries with a broad range of time lag based heat release models. The three-dimensionality of mean field quantities (heat release, density, velocity,

etc...) as well as acoustic quantities are resolved in this method without the computational expense of a full Navier-Stokes solver (LES).

(2) Extension of a high-resolution non-conservative second-order total variation diminishing Godunov flux calculation method based on the wave propagation method of [38] to arbitrarily-oriented faces in an unstructured finite volume mesh suitable for complex engine geometries.

1.7 Thesis Outline

This thesis is organized as follows:

Chapter 2: Derivation the linear thermoacoustic equations from the governing equations of fluid flow.

Chapter 3: Derivation of the wave structure of linear acoustics in inhomogeneous media for an arbitrarily-oriented face. Application of these derivations in the development of a non-conservative flux formulation for unstructured finite volume meshes.

Chapter 4: Verification of the present implementation of the numerical approach in open source software. Comparison with various academic problems with analytical solution demonstrating the ability of the solver to model the basic physics involved in thermoacoustic instabilities.

Chapter 5: Application and validation of the present implementation of the numerical method to laboratory-scale experiments. Demonstration of the code's ability to utilize existing empirically-correlated non-linear heat release functions as well as its ability to implement a physics-based vortex shedding model.

CHAPTER 2
GOVERNING EQUATIONS

2.1 Governing Equations of Fluid Flow

The governing equations of fluid flow are the starting point for arriving at the governing equations for thermoacoustics. Appendix A provides a detailed derivation of these equations. For the purposes of this thesis, thermoacoustics relating to the combustion of premixed gases, the mass source is neglected, $\mathcal{M} = 0$. As viscous forces tend to play a small role in linear acoustics, forces other than the pressure force is neglected, ($\mathcal{F}_i = 0$). Accordingly, the contribution of viscous dissipation to the energy equation. The heat release term on the right hand side of the energy equation is not neglected, $\mathcal{Q} \neq 0$, as it plays a defining role in the development of thermoacoustic instabilities. The resulting equations for fluid flow are summarized below in both conservative and non-conservative form.

2.1.1 Conservative Form Equations

Mass:

$$\frac{\partial \rho}{\partial t} + \frac{\partial (\rho u_j)}{\partial x_j} = 0 \tag{2.1}$$

Momentum:

$$\frac{\partial(\rho u_i)}{\partial t} + \frac{\partial(\rho u_j u_i + p\delta_{ij})}{\partial x_j} = 0 \tag{2.2}$$

Energy:

$$\frac{\partial[\rho(e + \frac{1}{2}u_i u_i)]}{\partial t} + \frac{\partial[\rho u_j(e + \frac{1}{2}u_i u_i + \frac{p}{\rho})]}{\partial x_j} = \mathcal{Q} \tag{2.3}$$

Pressure (energy):

$$\frac{\partial[p + \frac{1}{2}(\gamma - 1)\rho u_i u_i]}{\partial t} + \frac{\partial[\gamma u_j p + \frac{1}{2}(\gamma - 1)\rho u_j u_i u_i]}{\partial x_j} = (\gamma - 1)q \tag{2.4}$$

2.1.2 Non-Conservative Form Equations

Density (Mass):

$$\frac{\partial \rho}{\partial t} + \rho\frac{\partial u_j}{\partial x_j} + u_j\frac{\partial \rho}{\partial x_j} = 0 \tag{2.5}$$

Velocity (Momentum):

$$\rho\frac{\partial u_i}{\partial t} + \rho u_j\frac{\partial u_i}{\partial x_j} + \frac{\partial p}{\partial x_j}\delta_{ij} = 0 \tag{2.6}$$

Temperature (Energy):

$$\rho c_v\frac{\partial T}{\partial t} + \rho c_v u_j\frac{\partial T}{\partial x_j} = -p\frac{\partial u_j}{\partial x_j} + q \tag{2.7}$$

or

$$\rho c_p\frac{\partial T}{\partial t} + \rho c_p u_j\frac{\partial T}{\partial x_j} = \frac{\partial p}{\partial t} + u_j\frac{\partial p}{\partial x_j} + q \tag{2.8}$$

Pressure (Energy):

$$\frac{\partial p}{\partial t} + u_j \frac{\partial p}{\partial x_j} + \gamma p \frac{\partial u_j}{\partial x_j} = (\gamma - 1) q \tag{2.9}$$

2.2 Expansion and Linearization

The equations summarized above represent equations for the instantaneous variables of the flow. For acoustic analysis, the mean flow is not the primary interest, but rather the small signal perturbations on the mean flow. For this reason, the governing equations listed above are decomposed into mean and fluctuating (acoustic) parts and expanded about the mean using a perturbation parameter (ϵ). The equations can then be linearized by keeping only first order terms in ϵ. In the linearization process, other parameters appear in connection with mean flow velocity as well as mean property and flow gradients. In the following, the pressure form of the energy equation will be used, because acoustics is generally expressed primarily in terms of pressure and velocity. Temperature is then expressed through the equation of state.

2.2.1 Decomposition

First, each of the variables are split into mean and fluctuating (acoustic) quantities

$$\begin{aligned} \rho &= \bar{\rho} + \rho' \\ u &= \bar{u} + u' \\ p &= \bar{p} + p' \\ q &= \bar{q} + q' \end{aligned} \tag{2.10}$$

Despite its resemblance to the Reynolds averaging procedure in the analysis of turbulent fluctuations, this decomposition in terms of acoustics is performed here without any regard for turbulent fluctuations. Key distinctions between turbulence and acoustics is the magnitude of the fluctuations for different quantities and the spectral nature of the phenomena. Turbulence is by nature dissipative and broadband, while acoustics (in the linear sense) is conservative and occurs at discrete frequencies. This simplistic view of the physics of turbulent flows with acoustics, namely the lack of interaction between the two fields, is justified primarily by two facts in field of combustion instabilities. First, the turbulent sources of noise are overwhelmingly small compared to the combustion sources. Secondly, in the linearization process, the acoustic disturbances are assumed very small compared to their mean properties, hence the acoustic field is not strong enough to influence the turbulence, except perhaps to trigger the laminar-to-turbulent transition. Substitution of Eq. (2.10) into the governing equations, Eqs. (2.1) - (2.4), and algebraic manipulation yields the expanded forms of these equations.

Mass:

$$\begin{aligned}&\frac{\partial\bar{\rho}}{\partial t}+\frac{\partial\rho'}{\partial t}+\bar{\rho}\frac{\partial\bar{u}_j}{\partial x_j}+\bar{\rho}\frac{\partial u'_j}{\partial x_j}+\rho'\frac{\partial\bar{u}_j}{\partial x_j}+\rho'\frac{\partial u'_j}{\partial x_j}\\&+\bar{u}_j\frac{\partial\bar{\rho}}{\partial x_j}+\bar{u}_j\frac{\partial\rho'}{\partial x_j}+u'_j\frac{\partial\bar{\rho}}{\partial x_j}+u'_j\frac{\partial\rho'}{\partial x_j}=0\end{aligned}\tag{2.11}$$

Momentum:

$$\begin{aligned}&\bar{\rho}\frac{\partial\bar{u}_i}{\partial t}+\bar{\rho}\frac{\partial u'_i}{\partial t}+\rho'\frac{\partial\bar{u}_i}{\partial t}+\rho'\frac{\partial u'_i}{\partial t}\\&+\bar{\rho}\bar{u}_j\frac{\partial\bar{u}_i}{\partial x_j}+\bar{\rho}\bar{u}_j\frac{\partial u'_i}{\partial x_j}+\bar{\rho}u'_j\frac{\partial\bar{u}_i}{\partial x_j}+\rho'\bar{u}_j\frac{\partial\bar{u}_i}{\partial x_j}\\&+\bar{\rho}u'_j\frac{\partial u'_i}{\partial x_j}+\rho'\bar{u}_j\frac{\partial u'_i}{\partial x_j}+\rho'u'_j\frac{\partial\bar{u}_i}{\partial x_j}+\rho'u'_j\frac{\partial u'_i}{\partial x_j}\\&+\frac{\partial\bar{p}}{\partial x_i}+\frac{\partial p'}{\partial x_i}=0\end{aligned}\tag{2.12}$$

Energy (Pressure):

$$\begin{aligned}&\frac{\partial\bar{p}}{\partial t}+\frac{\partial p'}{\partial t}\\&+\bar{u}_j\frac{\partial\bar{p}}{\partial x_j}+\bar{u}_j\frac{\partial p'}{\partial x_j}+u'_j\frac{\partial\bar{p}}{\partial x_j}+u'_j\frac{\partial p'}{\partial x_j}\\&+\gamma\bar{p}\frac{\partial\bar{u}_j}{\partial x_j}+\gamma\bar{p}\frac{\partial u'_j}{\partial x_j}+\gamma p'\frac{\partial\bar{u}_j}{\partial x_j}+\gamma p'\frac{\partial u'_j}{\partial x_j}\\&=(\gamma-1)\bar{\mathcal{Q}}+(\gamma-1)q'\end{aligned}\tag{2.13}$$

2.2.2 Mean Equations

The equations for the mean flow are obtained by taking only the terms that are zeroth order in fluctuating parameters. In the limit $\epsilon\to 0$, all other terms become vanishingly small.

Mass:

$$\frac{\partial\bar{\rho}}{\partial t}+\bar{\rho}\frac{\partial\bar{u}_j}{\partial x_j}+\bar{u}_j\frac{\partial\bar{\rho}}{\partial x_j}=0\tag{2.14}$$

Momentum:

$$\bar{\rho}\frac{\partial \bar{u}_i}{\partial t} + \bar{\rho}\bar{u}_j\frac{\partial \bar{u}_i}{\partial x_j} + \frac{\partial \bar{p}}{\partial x_i} = 0 \tag{2.15}$$

Energy (Pressure):

$$\frac{\partial \bar{p}}{\partial t} + \bar{u}_j\frac{\partial \bar{p}}{\partial x_j} + \gamma\bar{p}\frac{\partial \bar{u}_j}{\partial x_j} = (\gamma - 1)\bar{q} \tag{2.16}$$

2.2.3 Acoustic Equations

The equations for the acoustic fluctuations are obtained by subtracting the mean equations, Eq. (2.14) - (2.16), from the decomposed overall equations, Eq. (2.11) - (2.13). The following equations are obtained for the acoustic variables.

Mass:

$$\frac{\partial \rho'}{\partial t} + \bar{\rho}\frac{\partial u'_j}{\partial x_j} + \rho'\frac{\partial \bar{u}_j}{\partial x_j} + \rho'\frac{\partial u'_j}{\partial x_j} + \bar{u}_j\frac{\partial \rho'}{\partial x_j} + u'_j\frac{\partial \bar{\rho}}{\partial x_j} + u'_j\frac{\partial \rho'}{\partial x_j} = 0 \tag{2.17}$$

Momentum:

$$\begin{aligned}&\bar{\rho}\tfrac{\partial u'_i}{\partial t} + \rho'\tfrac{\partial \bar{u}_i}{\partial t} + \rho'\tfrac{\partial u'_i}{\partial t} + \bar{\rho}\bar{u}_j\tfrac{\partial u'_i}{\partial x_j} + \bar{\rho}u'_j\tfrac{\partial \bar{u}_i}{\partial x_j} + \rho'\bar{u}_j\tfrac{\partial \bar{u}_i}{\partial x_j} \\ &+\bar{\rho}u'_j\tfrac{\partial u'_i}{\partial x_j} + \bar{u}_j\rho'\tfrac{\partial u'_i}{\partial x_j} + \rho'u'_j\tfrac{\partial \bar{u}_i}{\partial x_j} + \rho'u'_j\tfrac{\partial u'_i}{\partial x_j} + \tfrac{\partial p'}{\partial x_i} = 0\end{aligned} \tag{2.18}$$

Energy (Pressure):

$$\begin{aligned}&\tfrac{\partial p'}{\partial t} + \bar{u}_j\tfrac{\partial p'}{\partial x_j} + u'_j\tfrac{\partial \bar{p}}{\partial x_j} + \left(u'_j\tfrac{\partial p'}{\partial x_j} - \overline{u'_j\tfrac{\partial p'}{\partial x_j}}\right) \\ &+\gamma\bar{p}\tfrac{\partial u'_j}{\partial x_j} + \gamma p'\tfrac{\partial \bar{u}_j}{\partial x_j} + \gamma\left(p'\tfrac{\partial u'_j}{\partial x_j} - \overline{p'\tfrac{\partial u'_j}{\partial x_j}}\right) = (\gamma - 1)q'\end{aligned} \tag{2.19}$$

The above equations are large and contain many terms that are, in general, difficult to model. From here, the task at hand is judging the relative importance of the terms in each of the equations. With such judgements in hand, for a given application and desired fidelity, many of the terms in Eqs. (2.17) - (2.19) can be omitted. In the following three section, parameters are defined which allow for the quantitative analysis of the relative magnitude of the terms in the acoustic equations above.

2.2.4 Reference Parameters

In order to proceed with asymptotic analysis of the non-linear acoustic equations stated above, a number of expansion parameters are now defined. These parameters can be given precise definitions, by which they relate the relative importance of the terms in Eq. (2.17) - (2.19). To reduce the number of parameters and simplify the analysis, the practical approach is to group the expansion parameters by orders of magnitude. It is first useful to establish reference values to which the expansion parameters can be compared, given in Table 2.1.

Table 2.1: Reference parameters useful for analysis of acoustic equations.

	Length	Velocity	Time	Density	Pressure	Heat Release
SI Units	m	m/s	sec	kg/m^3	Pa	W/m^3
Reference	$\mathcal{L}_r$	$\bar{a}_r$	$t_r \sim \frac{\mathcal{L}_r}{\bar{a}_r}$	$\bar{\rho}_r$	$\bar{p}_r \sim \bar{\rho}_r \bar{a}_r^2$	$\bar{q}_r$

2.2.5 Perturbation Parameters

The mean quantities from Eq. (2.10) are, by definition, on the same order of magnitude as the reference quantities specified above. The fluctuating quantities defined in Eq. (2.10) are now related to the reference quantities (and, hence, the mean quantities). These are denoted as perturbation parameters, because typical analysis treats them as overwhelmingly small compared to unity. Analysis, then, is often performed in their limit approaching zero. The relevant perturbation quantities are given in Table 2.2.

Table 2.2: Reference parameters useful for analysis of acoustic equations.

Pressure	Velocity	Density	Heat Release
ϵ_p	ϵ_u	ϵ_ρ	ϵ_q
$\frac{p'}{\bar{p}_r}$	$\frac{u'}{\bar{a}_r}$	$\frac{\rho'}{\bar{\rho}_r}$	$\frac{q'}{\bar{q}_r}$

2.2.6 Mean Field Parameters

The mean flow and mean gradients are completely independent of the acoustic variables, and hence must be characterized by a separate group of parameters unrelated to the perturbation parameters. These are differentiated from perturbation parameters in that they are not a specification of acoustic disturbance magnitudes, but rather a specification of the influence of mean flow and mean gradients on the acoustic behavior. Therefore, the main

result of these parameters is the ability to compare the relative importance (or negligibility) of terms arising in the acoustic equations containing these mean flow quantities.

Table 2.3: Definitions of mean field parameters for analysis of acoustic oscillations.

Mean Flow	Mean Flow Gradient	Mean Density Gradient	Mean Pressure Gradient
μ	ν_u	ν_ρ	ν_p
$\frac{\bar{u}}{\bar{a}_r}$	$\frac{\mathcal{L}_r}{\bar{u}}\frac{\partial \bar{u}}{\partial x}$	$\frac{\mathcal{L}_r}{\bar{\rho}}\frac{\partial \bar{\rho}}{\partial x}$	$\frac{\mathcal{L}_r}{\bar{p}}\frac{\partial \bar{p}}{\partial x}$

2.2.7 Estimates of Terms in Acoustic Equations

The reference definitions allow for the temporal and spatial derivatives of acoustic variables to be estimates as

$$\frac{\partial}{\partial t} \sim \frac{1}{t_r} \sim \frac{\bar{a}_r}{\mathcal{L}_r} \tag{2.20}$$

and

$$\frac{\partial}{\partial x} \sim \frac{1}{\mathcal{L}_r}. \tag{2.21}$$

Based on the acoustic equations to first order in these perturbation parameters, Eqs. (2.17) - (2.19), it is possible to collapse the acoustic description into a single perturbation parameter

$$\epsilon \sim \epsilon_p \sim \epsilon_u \sim \epsilon_\rho. \tag{2.22}$$

Culick [8] collapses these into a single parameter μ by arguing their relations through the mean equations. This assumes that each term in the mean equations is equally important, which may not be the case depending on the flow. Instead, it is enough to evaluate an estimate for the mean heat release, starting with

$$\bar{q} \sim \bar{\rho}\bar{u}c_p\Delta T \tag{2.23}$$

and assuming that, for a deflagration wave, the temperature rise across a flame translates into a density drop with negligible change in pressure

$$\bar{q} \sim \mu\nu_\rho\bar{\rho}_r\bar{a}_r^3 \tag{2.24}$$

indicating that a consistent evaluation of thermoacoustics typically should include at least first order terms in μ and ν_ρ. The exception would be situations with strong flame transfer functions, where $\epsilon_q \sim 1 >> \epsilon$. Each term for the mass, momentum, and energy equations are analyzed using the parameters established above in Table 2.4, Table 2.5, and Table 2.6.

2.3 Linear Acoustic Equations

Neglecting all terms which are of order ϵ^2 or higher, the equations become linearized in terms of the acoustic variables. Also, the mean flow is assumed to change very slowly compared to the acoustic fluctuations, so the time derivative of any mean flow variables is negligible as well.

Table 2.4: Estimations for terms in mass equation

Term	Estimation	Order
$\frac{\partial \rho'}{\partial t}$	$\sim \epsilon \frac{\bar{\rho}_r \bar{a}_r}{\mathcal{L}}$	$O(\epsilon)$
$\bar{\rho}\frac{\partial u_j'}{\partial x_j}$	$\sim \epsilon \frac{\bar{\rho}_r \bar{a}_r}{\mathcal{L}}$	$O(\epsilon)$
$\rho' \frac{\partial \bar{u}_j}{\partial x_j}$	$\sim \mu\nu_u \epsilon \frac{\bar{\rho}_r \bar{a}_r}{\mathcal{L}}$	$O(\mu\nu_u\epsilon)$
$\rho' \frac{\partial u_j'}{\partial x_j}$	$\sim \epsilon^2 \frac{\bar{\rho}_r \bar{a}_r}{\mathcal{L}}$	$O(\epsilon^2)$
$\bar{u}_j \frac{\partial \rho'}{\partial x_j}$	$\sim \mu\epsilon \frac{\bar{\rho}_r \bar{a}_r}{\mathcal{L}}$	$O(\mu\epsilon)$
$u_j' \frac{\partial \bar{\rho}}{\partial x_j}$	$\sim \nu_\rho \epsilon \frac{\bar{\rho}_r \bar{a}_r}{\mathcal{L}}$	$O(\nu_\rho\epsilon)$
$u_j' \frac{\partial \rho'}{\partial x_j}$	$\sim \epsilon^2 \frac{\bar{\rho}_r \bar{a}_r}{\mathcal{L}}$	$O(\epsilon^2)$

Mass:

$$\frac{\partial \rho'}{\partial t} + \bar{\rho}\frac{\partial u_j'}{\partial x_j} + \rho' \frac{\partial \bar{u}_j}{\partial x_j} + \bar{u}_j \frac{\partial \rho'}{\partial x_j} + u_j' \frac{\partial \bar{\rho}}{\partial x_j} = 0 \tag{2.25}$$

Momentum:

$$\bar{\rho}\frac{\partial u_i'}{\partial t} + \bar{\rho}\bar{u}_j \frac{\partial u_i'}{\partial x_j} + \bar{\rho} u_j' \frac{\partial \bar{u}_i}{\partial x_j} + \rho' \bar{u}_j \frac{\partial \bar{u}_i}{\partial x_j} + \frac{\partial p'}{\partial x_i} = 0 \tag{2.26}$$

Energy (Pressure):

$$\frac{\partial p'}{\partial t} + \bar{u}_j \frac{\partial p'}{\partial x_j} + u_j' \frac{\partial \bar{p}}{\partial x_j} + \gamma \bar{p} \frac{\partial u_j'}{\partial x_j} + \gamma p' \frac{\partial \bar{u}_j}{\partial x_j} = (\gamma - 1) q' \tag{2.27}$$

Table 2.5: Estimations for terms in momentum equation

Term	Estimation	Order
$\bar{\rho}\frac{\partial u_i'}{\partial t}$	$\sim \epsilon\frac{\bar{\rho}_r\bar{a}_r^2}{\mathcal{L}}$	$O(\epsilon)$
$\rho'\frac{\partial u_i'}{\partial t}$	$\sim \epsilon^2\frac{\bar{\rho}_r\bar{a}_r^2}{\mathcal{L}}$	$O(\epsilon^2)$
$\bar{\rho}\bar{u}_j\frac{\partial u_i'}{\partial x_j}$	$\sim \mu\epsilon\frac{\bar{\rho}_r\bar{a}_r^2}{\mathcal{L}}$	$O(\mu\epsilon)$
$\bar{\rho}u_j'\frac{\partial \bar{u}_i}{\partial x_j}$	$\sim \mu\nu_u\epsilon\frac{\bar{\rho}_r\bar{a}_r^2}{\mathcal{L}}$	$O(\mu\nu_u\epsilon)$
$\rho'\bar{u}_j\frac{\partial \bar{u}_i}{\partial x_j}$	$\sim \mu^2\nu_u\epsilon\frac{\bar{\rho}_r\bar{a}_r^2}{\mathcal{L}}$	$O(\mu^2\nu_u\epsilon)$
$\bar{\rho}u_j'\frac{\partial u_i'}{\partial x_j}$	$\sim \epsilon^2\frac{\bar{\rho}_r\bar{a}_r^2}{\mathcal{L}}$	$O(\epsilon^2)$
$\bar{u}_j\rho'\frac{\partial u_i'}{\partial x_j}$	$\sim \mu\epsilon^2\frac{\bar{\rho}_r\bar{a}_r^2}{\mathcal{L}}$	$O(\mu\epsilon^2)$
$\rho'u_j'\frac{\partial \bar{u}_i}{\partial x_j}$	$\sim \mu\nu_u\epsilon^2\frac{\bar{\rho}_r\bar{a}_r^2}{\mathcal{L}}$	$O(\mu\nu_u\epsilon^2)$
$\rho'u_j'\frac{\partial u_i'}{\partial x_j}$	$\sim \epsilon^3\frac{\bar{\rho}_r\bar{a}_r^2}{\mathcal{L}}$	$O(\epsilon^3)$
$\frac{\partial p'}{\partial x_i}$	$\sim \epsilon\frac{\bar{p}_r}{\mathcal{L}} \sim \epsilon\frac{\bar{\rho}_r\bar{a}_r^2}{\mathcal{L}}$	$O(\epsilon)$

Table 2.6: Estimations for terms in energy (pressure) equation

Term	Estimation	Order
$\frac{\partial p'}{\partial t}$	$\sim \epsilon \frac{\bar{\rho}_r \bar{a}_r}{\mathcal{L}}$	$O(\epsilon)$
$\bar{u}_j \frac{\partial p'}{\partial x_j}$	$\sim \mu\epsilon \frac{\bar{\rho}_r \bar{a}_r}{\mathcal{L}}$	$O(\mu\epsilon)$
$u'_j \frac{\partial \bar{p}}{\partial x_j}$	$\sim \nu_p \epsilon \frac{\bar{\rho}_r \bar{a}_r}{\mathcal{L}}$	$O(\nu_p \epsilon)$
$u'_j \frac{\partial p'}{\partial x_j}$	$\sim \epsilon^2 \frac{\bar{\rho}_r \bar{a}_r}{\mathcal{L}}$	$O(\epsilon^2)$
$\gamma \bar{p} \frac{\partial u'_j}{\partial x_j}$	$\sim \epsilon \frac{\bar{\rho}_r \bar{a}_r}{\mathcal{L}}$	$O(\epsilon)$
$\gamma p' \frac{\partial \bar{u}_j}{\partial x_j}$	$\sim \mu\nu_u \epsilon \frac{\bar{\rho}_r \bar{a}_r}{\mathcal{L}}$	$O(\mu\nu_u \epsilon)$
$\gamma p' \frac{\partial u'_j}{\partial x_j}$	$\sim \epsilon^2 \frac{\bar{\rho}_r \bar{a}_r}{\mathcal{L}}$	$O(\epsilon^2)$
$(\gamma - 1) q'$	$\sim \mu\nu_\rho \epsilon_q \frac{\bar{\rho}_r \bar{a}_r}{\mathcal{L}}$	$O(\mu\nu_\rho \epsilon_q)$

2.4 Isentropic Linear Acoustic Equations

Use of the isentropic signal assumption, that the entropy fluctuation is everywhere zero, a relation between p' and ρ' can be derived.

$$\rho' = \frac{p'}{\bar{a}^2}. \tag{2.28}$$

This relation precludes the necessity of the linearized mass equation, Eq. (2.25). Instead, Eq. (2.28) is substituted into Eqs. (2.26) and (2.27), forming a closed set of four equations which can be solved for the acoustic pressure and acoustic velocity.

Momentum:

$$\frac{\partial u_i'}{\partial t} + \bar{u}_j \frac{\partial u_i'}{\partial x_j} + u_j' \frac{\partial \bar{u}_i}{\partial x_j} + p' \frac{\bar{u}_j}{\gamma \bar{p}} \frac{\partial \bar{u}_i}{\partial x_j} + \frac{1}{\bar{\rho}} \frac{\partial p'}{\partial x_i} = 0 \tag{2.29}$$

Energy (Pressure):

$$\frac{\partial p'}{\partial t} + \bar{u}_j \frac{\partial p'}{\partial x_j} + u_j' \frac{\partial \bar{p}}{\partial x_j} + \gamma \bar{p} \frac{\partial u_j'}{\partial x_j} + \gamma p' \frac{\partial \bar{u}_j}{\partial x_j} = (\gamma - 1) q' \tag{2.30}$$

Equations (2.29) and (2.30) are the governing equations used by the present form of tacFoam. The most serious limitations from the use of these equations is the isentropic assumption of Eq. (2.28). This precludes the solver from capturing physical effects of entropy waves on thermoacoustic behavior. To include entropy wave effects, Eqs. (2.25), (2.26), and (2.27) must be used. This would represent an increase in cost from four to five equations that must be solved numerically.

2.5 Classical Acoustic Equations

Furthermore, neglecting all terms relating to mean flow and mean property gradients, the equations of classical acoustics are obtained, with the obvious exception of retaining the source term in the energy equation.

Mass:

$$\frac{\partial \rho'}{\partial t} + \bar{\rho} \frac{\partial u_j'}{\partial x_j} = 0 \tag{2.31}$$

Momentum:

$$\bar{\rho}\frac{\partial u_i'}{\partial t} + \frac{\partial p'}{\partial x_i} = 0 \tag{2.32}$$

Energy (Pressure):

$$\frac{\partial p'}{\partial t} + \gamma\bar{p}\frac{\partial u_j'}{\partial x_j} = (\gamma - 1)q' \tag{2.33}$$

The wave equation for the acoustic pressure and velocity can be obtained using only the momentum and energy equations, Eq. (2.32) and Eq. (2.19), respectively. The wave equation for the acoustic pressure is built by differentiating Eq. (2.33) in time and differentiating Eq. (2.32) in space and subtracting the results.

$$\frac{\partial^2 p'}{\partial t^2} + \frac{\gamma\bar{p}}{\bar{\rho}}\frac{\partial^2 p}{\partial x_j} = (\gamma - 1)\frac{\partial q'}{\partial t} \tag{2.34}$$

The heat release term has been carried through to illustrate a main idea in combustion acoustics. The unsteady heat release related to fluctuations in the flame from chemical and fluid dynamical effects acts as a forcing term in the acoustic wave equation. While it is true that many of the terms neglected to obtain the wave equation above can play significant roles in the acoustic behavior of combustion chambers, the main point remains. A physical correlation between the heat release fluctuations and the acoustic variables may provide a feedback pathway by which the acoustic field can be excited or damped.

CHAPTER 3
NUMERICAL APPROACH

3.1 Numerical Considerations

The design of a numerical method for a given purpose relies heavily on the goals and challenges for its particular set of predictive uses. In the case of tacFoam, the prediction of thermoacoustic instabilities includes accounting for a number of physics which may drive or damp a particular mode. These physical effects include unsteady heat release, boundary conditions, viscous diffusion, and mean flow interactions. While the governing equations may be adjusted based on the physics one may attempt to capture, the delicate balance between driving and damping forces means that the effects of numerical dissipation are particularly unwanted. Numerical dissipation, common to any stable approach to computational fluid dynamics, can pollute the physical insight of the solution if its magnitude is not managed to be much lower than the operating physical mechanisms. To this end, the present numerical method is designed for low numerical dissipation.

An additional consideration for the numerical method design at hand is the goal of applying the predictive tool to the complex geometries of gas turbine combustion chambers. This application makes the use of structured grids difficult; the construction of a structured

or block-structured grid represents a bottleneck in the user time needed to extract a useful solution from such a scheme. For this reason, many production level codes have resorted to unstructured finite volume methods, including OpenFOAM [39]. Such a method provides the necessary flexibility in domain definition and mesh construction for efficient application of numerical methods to complex geometries.

There are two main approaches in computational fluid dynamics to designing numerical schemes with low dissipation: high-order methods and high-resolution methods. High-order methods, here in reference to spatial discretization of fourth order or higher, can be used to construct low dissipation schemes, but can encounter difficulties at sharp gradients of solution variables or media [40]. Additionally, in the context of unstructured finite volume methods, the application of higher-order methods is particularly difficult. On the other hand, the high-resolution approach is very attractive. High-resolution approaches use the generalized Riemann problem to construct low dissipation schemes with second-order accuracy. This approach is easily applicable to unstructured finite volume methods and is particularly well-suited for wave propagation in discontinuous media, such as the large mean density gradients present across a flame. An introduction to the basics of the Riemann solver approach is given in [41, 40], with the main ideas summarized in Appendix B of this thesis.

3.2 Governing Equations as a Three Dimensional Hyperbolic System

The governing equations are derived in the preceding chapter, Eqs. (2.29) and (2.30). In order to phrase these as a linear hyperbolic system, the terms related to gradients of mean quantities are move to the right hand side to be treated as source terms.

$$\frac{\partial p'}{\partial t} + \bar{u}_j \frac{\partial p'}{\partial x_j} + \gamma \bar{p} \frac{\partial u'_j}{\partial x_j} = (\gamma - 1) q' - u'_j \frac{\partial \bar{p}}{\partial x_j} - \gamma p' \frac{\partial \bar{u}_j}{\partial x_j} \tag{3.1}$$

$$\frac{\partial u'_i}{\partial t} + \bar{u}_j \frac{\partial u'_i}{\partial x_j} + \frac{1}{\bar{\rho}} \frac{\partial p'}{\partial x_i} = -u'_j \frac{\partial \bar{u}_i}{\partial x_j} - p' \frac{\bar{u}_j}{\gamma \bar{p}} \frac{\partial \bar{u}_i}{\partial x_j} \tag{3.2}$$

The system of hyperbolic equations for tacFoam contains four equations.

$$\begin{aligned} &\frac{\partial p'}{\partial t} + \bar{u} \frac{\partial p'}{\partial x} + \bar{v} \frac{\partial p'}{\partial y} + \bar{w} \frac{\partial p'}{\partial z} + \gamma \bar{p} \left(\frac{\partial u'}{\partial x} + \frac{\partial v'}{\partial y} + \frac{\partial w'}{\partial z} \right) = \\ &(\gamma - 1) q' - \left(u' \frac{\partial \bar{p}}{\partial x} + v' \frac{\partial \bar{p}}{\partial y} + w' \frac{\partial \bar{p}}{\partial z} \right) - \gamma p' \left(\frac{\partial \bar{u}}{\partial x} + \frac{\partial \bar{v}}{\partial y} + \frac{\partial \bar{w}}{\partial z} \right) \end{aligned} \tag{3.3}$$

$$\begin{aligned} &\frac{\partial u'}{\partial t} + \bar{u} \frac{\partial u'}{\partial x} + \bar{v} \frac{\partial u'}{\partial y} + \bar{w} \frac{\partial u'}{\partial z} + \frac{1}{\bar{\rho}} \frac{\partial p'}{\partial x} = \\ &- \left(u' \frac{\partial \bar{u}}{\partial x} + v' \frac{\partial \bar{u}}{\partial y} + w' \frac{\partial \bar{u}}{\partial z} \right) - \frac{p'}{\gamma \bar{p}} \left(\bar{u} \frac{\partial \bar{u}}{\partial x} + \bar{v} \frac{\partial \bar{u}}{\partial y} + \bar{w} \frac{\partial \bar{u}}{\partial z} \right) \end{aligned} \tag{3.4}$$

$$\begin{aligned} &\frac{\partial v'}{\partial t} + \bar{u} \frac{\partial v'}{\partial x} + \bar{v} \frac{\partial v'}{\partial y} + \bar{w} \frac{\partial v'}{\partial z} + \frac{1}{\bar{\rho}} \frac{\partial p'}{\partial y} = \\ &- \left(u' \frac{\partial \bar{v}}{\partial x} + v' \frac{\partial \bar{v}}{\partial y} + w' \frac{\partial \bar{v}}{\partial z} \right) - \frac{p'}{\gamma \bar{p}} \left(\bar{u} \frac{\partial \bar{v}}{\partial x} + \bar{v} \frac{\partial \bar{v}}{\partial y} + \bar{w} \frac{\partial \bar{v}}{\partial z} \right) \end{aligned} \tag{3.5}$$

$$\begin{aligned} &\frac{\partial w'}{\partial t} + \bar{u} \frac{\partial w'}{\partial x} + \bar{v} \frac{\partial w'}{\partial y} + \bar{w} \frac{\partial w'}{\partial z} + \frac{1}{\bar{\rho}} \frac{\partial p'}{\partial z} = \\ &- \left(u' \frac{\partial \bar{w}}{\partial x} + v' \frac{\partial \bar{w}}{\partial y} + w' \frac{\partial \bar{w}}{\partial z} \right) - \frac{p'}{\gamma \bar{p}} \left(\bar{u} \frac{\partial \bar{w}}{\partial x} + \bar{v} \frac{\partial \bar{w}}{\partial y} + \bar{w} \frac{\partial \bar{w}}{\partial z} \right) . \end{aligned} \tag{3.6}$$

For three dimensional equations, a system of hyperbolic equations can be written in the form

$$\frac{\partial \underset{\sim}{\phi}}{\partial t} + \frac{\underset{\sim}{f}(\underset{\sim}{\phi})}{\partial x} + \frac{\underset{\sim}{g}(\underset{\sim}{\phi})}{\partial y} + \frac{\underset{\sim}{h}(\underset{\sim}{\phi})}{\partial z} = \underset{\approx}{S}(\underset{\sim}{\phi}) \tag{3.7}$$

where f, g, and h are the flux functions in each of the three Cartesian directions. The Jacobian matrix in each direction can be constructed such that

$$\underset{\approx}{A} = \partial \underset{\sim}{f} / \partial \underset{\sim}{\phi} \tag{3.8}$$

$$\underset{\approx}{B} = \partial \underset{\sim}{g} / \partial \underset{\sim}{\phi} \tag{3.9}$$

$$\underset{\approx}{C} = \partial \underset{\sim}{h} / \partial \underset{\sim}{\phi} \tag{3.10}$$

and the hyperbolic system can be rewritten in non-conservative form as

$$\frac{\partial \underset{\sim}{\phi}}{\partial t} + \underset{\approx}{A}\frac{\partial \underset{\sim}{\phi}}{\partial x} + \underset{\approx}{B}\frac{\partial \underset{\sim}{\phi}}{\partial y} + \underset{\approx}{C}\frac{\partial \underset{\sim}{\phi}}{\partial z} = \underset{\approx}{S}(\underset{\sim}{\phi}). \tag{3.11}$$

The tacFoam equations from Eqs. (3.3) - (3.6) constitute a 4x4 hyperbolic system in the form of Eq. (3.11). The vector of solution variables is

$$\underset{\sim}{\phi} = \begin{pmatrix} p' \\ u' \\ v' \\ w' \end{pmatrix} \tag{3.12}$$

and the Jacobian matrices in each direction are

$$\underset{\approx}{A} = \begin{bmatrix} \bar{u} & \gamma\bar{p} & 0 & 0 \\ \frac{1}{\bar{\rho}} & \bar{u} & 0 & 0 \\ 0 & 0 & \bar{u} & 0 \\ 0 & 0 & 0 & \bar{u} \end{bmatrix} \tag{3.13}$$

$$\underset{\approx}{B} = \begin{bmatrix} \bar{v} & 0 & \gamma\bar{p} & 0 \\ 0 & \bar{v} & 0 & 0 \\ \frac{1}{\bar{\rho}} & 0 & \bar{v} & 0 \\ 0 & 0 & 0 & \bar{v} \end{bmatrix} \tag{3.14}$$

$$\underset{\approx}{C} = \begin{bmatrix} \bar{w} & 0 & 0 & \gamma\bar{p} \\ 0 & \bar{w} & 0 & 0 \\ 0 & 0 & \bar{w} & 0 \\ \frac{1}{\bar{\rho}} & 0 & 0 & \bar{w} \end{bmatrix} \tag{3.15}$$

and the source vector is

$$\underset{\sim}{S}(\underset{\sim}{\phi}) = \begin{pmatrix} (\gamma-1)q' - \left(u'\frac{\partial\bar{p}}{\partial x} + v'\frac{\partial\bar{p}}{\partial y} + w'\frac{\partial\bar{p}}{\partial z}\right) - \gamma p'\left(\frac{\partial\bar{u}}{\partial x} + \frac{\partial\bar{v}}{\partial y} + \frac{\partial\bar{w}}{\partial z}\right) \\ -\left(u'\frac{\partial\bar{u}}{\partial x} + v'\frac{\partial\bar{u}}{\partial y} + w'\frac{\partial\bar{u}}{\partial z}\right) - \frac{p'}{\gamma\bar{p}}\left(\bar{u}\frac{\partial\bar{u}}{\partial x} + \bar{v}\frac{\partial\bar{u}}{\partial y} + \bar{w}\frac{\partial\bar{u}}{\partial z}\right) \\ -\left(u'\frac{\partial\bar{v}}{\partial x} + v'\frac{\partial\bar{v}}{\partial y} + w'\frac{\partial\bar{v}}{\partial z}\right) - \frac{p'}{\gamma\bar{p}}\left(\bar{u}\frac{\partial\bar{v}}{\partial x} + \bar{v}\frac{\partial\bar{v}}{\partial y} + \bar{w}\frac{\partial\bar{v}}{\partial z}\right) \\ -\left(u'\frac{\partial\bar{w}}{\partial x} + v'\frac{\partial\bar{w}}{\partial y} + w'\frac{\partial\bar{w}}{\partial z}\right) - \frac{p'}{\gamma\bar{p}}\left(\bar{u}\frac{\partial\bar{w}}{\partial x} + \bar{v}\frac{\partial\bar{w}}{\partial y} + \bar{w}\frac{\partial\bar{w}}{\partial z}\right) \end{pmatrix}. \tag{3.16}$$

3.3 Finite Volume Formulation for an Unstructured Grid

Most modern CFD codes with heavy use in industry employ unstructured finite volume methods. This method allows great flexibility in terms of mesh topology and domain geometry. The OpenFOAM C++ libraries are written for finite volume methods with unstructured grids. Therefore, it is necessary to write the hyperbolic systems with an unstructured grid in mind. For a finite volume method, the governing equations are integrated over an arbitrary control volume, Ω, to yield

$$\iiint_{\Omega} \frac{\partial \underset{\sim}{\phi}}{\partial t} dV + \iiint_{\Omega} \left(\underset{\approx}{A} \frac{\partial \underset{\sim}{\phi}}{\partial x} + \underset{\approx}{B} \frac{\partial \underset{\sim}{\phi}}{\partial y} + \underset{\approx}{C} \frac{\partial \underset{\sim}{\phi}}{\partial z} \right) dV = \iiint_{\Omega} \underset{\approx}{S}(\underset{\sim}{\phi}) dV. \tag{3.17}$$

For constant coefficient equations, the coefficient matrices (Jacobians) can be taken inside the derivatives

$$\iiint_{\Omega} \frac{\partial \underset{\sim}{\phi}}{\partial t} dV + \iiint_{\Omega} \left(\frac{\partial \underset{\approx}{A} \underset{\sim}{\phi}}{\partial x} + \frac{\partial \underset{\approx}{B} \underset{\sim}{\phi}}{\partial y} + \frac{\partial \underset{\approx}{C} \underset{\sim}{\phi}}{\partial z} \right) dV = \iiint_{\Omega} \underset{\approx}{S}(\underset{\sim}{\phi}) dV. \tag{3.18}$$

The divergence theorem can now be implemented to convert the second volume integral on the left hand side into a surface integral. For an arbitrarily oriented face with unit normal vector given by

$$\hat{n} = (n_x, n_y, n_z)^T \tag{3.19}$$

this term can be written as

$$\frac{\partial \underset{\approx}{A} \underset{\sim}{\phi}}{\partial x} + \frac{\partial \underset{\approx}{B} \underset{\sim}{\phi}}{\partial y} + \frac{\partial \underset{\approx}{C} \underset{\sim}{\phi}}{\partial z} = \frac{(\underset{\approx}{J} \underset{\sim}{\phi})_j}{\partial x_j} \tag{3.20}$$

where the Jacobian is given by

$$\underset{\approx}{J} = \underset{\approx}{A} n_x + \underset{\approx}{B} n_y + \underset{\approx}{C} n_z. \tag{3.21}$$

Using the divergence theorem, the second volume integral of Eq. (3.18) then becomes

$$\iiint_{\Omega} \left(\frac{\partial \underset{\approx}{A} \underset{\sim}{\phi}}{\partial x} + \frac{\partial \underset{\approx}{B} \underset{\sim}{\phi}}{\partial y} + \frac{\partial \underset{\approx}{C} \underset{\sim}{\phi}}{\partial z} \right) dV = \iint_{\partial\Omega} \underset{\approx}{J} \underset{\sim}{\phi} \cdot \hat{n} dS. \tag{3.22}$$

For the arbitrarily-oriented face, this Jacobian matrix is now the equivalent flux matrix as for a one-dimensional case. Analysis to calculate the flux from this matrix proceeds as for the one-dimensional case. For the tacFoam hyperbolic set, the Jacobian is given by

$$\underset{\approx}{J} = \begin{bmatrix} \bar{U} & \gamma \bar{p} n_x & \gamma \bar{p} n_y & \gamma \bar{p} n_z \\ \frac{n_x}{\bar{\rho}} & \bar{U} & 0 & 0 \\ \frac{n_y}{\bar{\rho}} & 0 & \bar{U} & 0 \\ \frac{n_z}{\bar{\rho}} & 0 & 0 & \bar{U} \end{bmatrix} \tag{3.23}$$

where the face-normal mean velocity is given by

$$\bar{U} = \underset{\sim}{\bar{u}} \cdot \hat{n} = \bar{u} n_x + \bar{v} n_y + \bar{w} n_z. \tag{3.24}$$

The flux at a cell face is given by

$$\underset{\sim}{f}_{face} = \left(\underset{\approx}{J} \underset{\sim}{\phi} \right)_{face} \tag{3.25}$$

the total flow through the cell face is given by the integration over the surface

$$\underset{\sim}{E}_{face} = \iint_{face} \underset{\approx}{J} \underset{\sim}{\phi} dS = \underset{\sim}{f}_{face} A_{face} \tag{3.26}$$

using a constant flux approximation for the integration. Likewise, the temporal derivative is approximated by

$$\iiint_{\Omega} \frac{\partial \underset{\sim}{\phi}}{\partial t} dV = \frac{d\underset{\sim}{\phi}_{center}}{dt} V_{cell} \tag{3.27}$$

and the source term is similarly integrated using the cell-centered values

$$\iiint_{\Omega} \underset{\approx}{S}(\underset{\sim}{\phi}) dV = \underset{\approx}{S}(\underset{\sim}{\phi}_{center}) V_{cell}. \tag{3.28}$$

The time advancement at each cell is made by

$$\frac{d\underset{\sim}{\phi}_{center}}{dt} = \underset{\approx}{S}(\underset{\sim}{\phi}_{center}) - \sum_{i}^{N_{faces}} \frac{A_i}{V_{cell}} f_i \tag{3.29}$$

using a four stage explicit Runge-Kutta method. The fluxes f through each face are calculated using a second-order TVD high-resolution upwind method via the Riemann solver approach.

3.3.1 Wave Structure of the Governing Equations

The eigenvalues of the Jacobian are found by solving

$$\det(\underset{\approx}{J} - \lambda \underset{\approx}{I}) = 0 \tag{3.30}$$

where $\underset{\approx}{I}$ is the identity matrix. This yields the characteristic equation

$$(\bar{U} - \lambda)^4 - (n_x^2 + n_y^2 + n_z^2) \frac{\gamma \bar{p}}{\bar{\rho}} (\bar{U} - \lambda)^2 = 0. \tag{3.31}$$

Noting the unit normal has a magnitude of one, $n_x^2 + n_y^2 + n_z^2 = 1$, the solution to this equation yields the eigenvalues, λ, which are the wave speeds for a given cell discontinuity

$$\lambda_1 = \bar{U} - \bar{a} \quad \lambda_2 = \lambda_3 = \bar{U} \quad \lambda_4 = \bar{U} + \bar{a} \tag{3.32}$$

where $\bar{a} = \gamma \bar{p}/\bar{\rho}$ represents the sound speed. These represent a backward travelling acoustic wave, two transverse component convective waves, and a forward travelling acoustic wave, respectively. These waves are shown in a characteristic diagram in Fig. 3.1 under the assumption that the mean face-normal velocity is left to right.

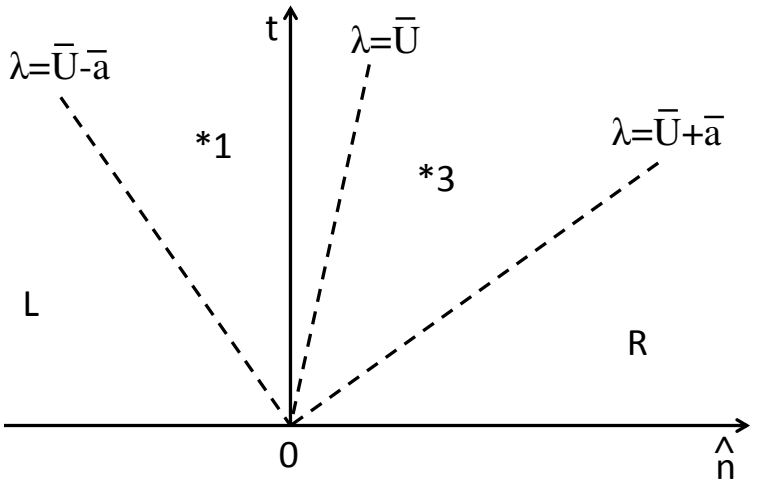

Figure 3.1: Characteristic diagram at a face in the tacFoam hyperbolic system.

The related right eigenvector matrix is

$$\underset{\approx}{R} = \begin{bmatrix} -Z_L & 0 & 0 & Z_R \\ n_x & 1 & 0 & n_x \\ n_y & 0 & 1 & n_y \\ n_z & -\frac{n_x}{n_z} & -\frac{n_y}{n_z} & n_z \end{bmatrix} \tag{3.33}$$

where $Z_L = \bar{\rho}_L \bar{a}_L$ is the acoustic impedance on the left side of the face and $Z_R = \bar{\rho}_R \bar{a}_R$ is the acoustic impedance on the right side. Notice here that variation of the mean density and sound speed across the face is accounted for, whereas such gradients were not allowed in the application of the divergence theorem leading to Eq. (3.20). Inverting this matrix gives the left eigenvector matrix

$$\underset{\approx}{R}^{-1} = \underset{\approx}{L} = \frac{1}{Z_R + Z_L} \begin{bmatrix} -1 & Z_R n_x & Z_R n_y & Z_R n_z \\ 0 & (Z_R + Z_L)(n_y^2 + n_z^2) & -(Z_R + Z_L) n_x n_y & -(Z_R + Z_L) n_x n_z \\ 0 & -(Z_R + Z_L) n_x n_y & (Z_R + Z_L)(n_x^2 + n_z^2) & -(Z_R + Z_L) n_y n_z \\ 1 & Z_L n_x & Z_L n_y & Z_L n_z \end{bmatrix}. \tag{3.34}$$

The characteristic variables are then

$$\underset{\sim}{w} = \underset{\approx}{R}^{-1} \underset{\sim}{\phi} = \begin{pmatrix} \frac{-p' + Z_R U'}{Z_R + Z_L} \\ u' - n_x U' \\ v' - n_y U' \\ \frac{p' + Z_L U'}{Z_R + Z_L} \end{pmatrix} \tag{3.35}$$

where

$$U' = \underset{\sim}{u}' \cdot \hat{n} = u' n_x + v' n_y + w' n_z. \tag{3.36}$$

The wave strengths are then

$$\underset{\sim}{\alpha} = \underset{\sim}{w}_R - \underset{\sim}{w}_L = \begin{pmatrix} \frac{-(p'_R - p'_L) + Z_R(U'_R - U'_L)}{Z_R + Z_L} \\ (u'_R - u'_L) - n_x(U'_R - U'_L) \\ (v'_R - v'_L) - n_y(U'_R - U'_L) \\ \frac{(p'_R - p'_L) + Z_L(U'_R - U'_L)}{Z_R + Z_L} \end{pmatrix}. \tag{3.37}$$

Multiplying the wave strengths by the right eigenvalues results in the wave vectors.

$$\underset{\sim}{\mathcal{W}}^1 = \alpha^1 \underset{\sim}{r}^1 = \begin{pmatrix} p'_{*1} - p'_L \\ u'_{*1} - u'_L \\ v'_{*1} - v'_L \\ w'_{*1} - w'_L \end{pmatrix} = \begin{pmatrix} \frac{Z_L}{Z_R+Z_L}(p'_R - p'_L) - \frac{Z_L Z_R}{Z_R+Z_L}(U'_R - U'_L) \\ -\frac{n_x}{Z_R+Z_L}(p'_R - p'_L) + \frac{n_x Z_R}{Z_R+Z_L}(U'_R - U'_L) \\ -\frac{n_y}{Z_R+Z_L}(p'_R - p'_L) + \frac{n_y Z_R}{Z_R+Z_L}(U'_R - U'_L) \\ -\frac{n_z}{Z_R+Z_L}(p'_R - p'_L) + \frac{n_z Z_R}{Z_R+Z_L}(U'_R - U'_L) \end{pmatrix} \tag{3.38}$$

$$\underset{\sim}{\mathcal{W}}^2 + \underset{\sim}{\mathcal{W}}^3 = \alpha^2 \underset{\sim}{r}^2 + \alpha^3 \underset{\sim}{r}^3 = \begin{pmatrix} p'_{*3} - p'_{*1} \\ u'_{*3} - u'_{*1} \\ v'_{*3} - v'_{*1} \\ w'_{*3} - w'_{*1} \end{pmatrix} = \begin{pmatrix} 0 \\ (u'_R - u'_L) - n_x(U'_R - U'_L) \\ (v'_R - v'_L) - n_y(U'_R - U'_L) \\ (w'_R - w'_L) - n_z(U'_R - U'_L) \end{pmatrix} \tag{3.39}$$

$$\underset{\sim}{\mathcal{W}}^4 = \alpha^4 \underset{\sim}{r}^4 = \begin{pmatrix} p'_{*1} - p'_L \\ u'_{*1} - u'_L \\ v'_{*1} - v'_L \\ w'_{*1} - w'_L \end{pmatrix} = \begin{pmatrix} \frac{Z_R}{Z_R+Z_L}(p'_R - p'_L) + \frac{Z_L Z_R}{Z_R+Z_L}(U'_R - U'_L) \\ \frac{n_x}{Z_R+Z_L}(p'_R - p'_L) + \frac{n_x Z_L}{Z_R+Z_L}(U'_R - U'_L) \\ \frac{n_y}{Z_R+Z_L}(p'_R - p'_L) + \frac{n_y Z_L}{Z_R+Z_L}(U'_R - U'_L) \\ \frac{n_z}{Z_R+Z_L}(p'_R - p'_L) + \frac{n_z Z_L}{Z_R+Z_L}(U'_R - U'_L) \end{pmatrix}. \tag{3.40}$$

3.3.2 Conservative Flux Formulation

To calculate the fluxes for the conservative formulation, the only remaining step is the use of Roe's method

$$\underset{\sim}{f}_{face} = \frac{1}{2}\underset{\approx}{A}(\underset{\sim}{\phi}_L + \underset{\sim}{\phi}_R) - \sum_{p=1}^{m} |\lambda^p| \underset{\sim}{\mathcal{W}}^p \tag{3.41}$$

with the wave speeds and wave vectors of the tacFoam Riemann problem, Eqs. (3.32), (3.38), (3.39), (3.40). If the coefficients of the non-conservative hyperbolic system present in the matrices of Eqs. (3.13), (3.14), and (3.15) are not constant in space, the divergence theorem used in Eq. (3.20) is not applicable because the coefficients cannot be brought inside the spatial derivatives.

3.3.3 Non-conservative Flux Formulation

If the coefficients of the non-conservative hyperbolic system present in the matrices of Eqs. (3.13), (3.14), and (3.15) are not constant in space, the divergence theorem used in Eq. (3.20) is not applicable because the coefficients cannot be brought inside the spatial derivatives. Instead of this approach, a better formulation is inspired by the wave propagation forms put forward by LeVeque, originally in [38] and more completely in [40]. The key step for this non-conservative flux formulation is the assumption of piecewise constant coefficients (mean variables). The coefficients are constant except at each face, where they

undergo an finite jump over an infinitesimal distance. The preceding wave analysis remains valid except at the face, where the discontinuity needs to be taken into account. One minor change is the use of two different mean velocities. The wave speeds given by Eq. (3.32) become

$$\lambda_1 = \bar{U}_L - \bar{a}_L \quad \lambda_2 = \lambda_3 = \bar{U}_+ \quad \lambda_4 = \bar{U}_R + \bar{a}_R \tag{3.42}$$

where $\bar{U}_+$ indicates the left mean velocity $\bar{U}_L$ if the face-normal mean velocity is right to left and $\bar{U}_R$ if the face-normal mean velocity is left to right. The major change in this formulation only concerns the last step of the previous derivation. Instead of using Roe's method to calculate a single flux through the face, it is recognized that two different fluxes are needed, one for either side of the face. Therefore, the left flux is calculated using

$$\underset{\sim}{f}_{face,L} = \underset{\approx}{J}_L \underset{\sim}{\phi}_L + \sum_{p=1}^{m} (\lambda^p)^- \underset{\sim}{\mathcal{W}}^p \tag{3.43}$$

and the right flux is calculated using

$$\underset{\sim}{f}_{face,R} = \underset{\approx}{J}_R \underset{\sim}{\phi}_R - \sum_{p=1}^{m} (\lambda^p)^+ \underset{\sim}{\mathcal{W}}^p. \tag{3.44}$$

The non-conservative finite volume formulation uses the left flux when computing the surface integrals of Eq. (3.22) for the cell on the left of the face and the right flux when computing the surface integrals for the cell on the right side of the face. Second order TVD extrapolation is used to obtain the left and right solution variables at each face from the cell-centered values. It is important to note that, because of the assumption of piecewise constant mean variables, no extrapolation of the mean variables (pressure, velocity, density)

to the faces is performed. The differences between the conservative and non-conservative formulations are depicted in Fig. 3.2. The current version of tacFoam uses this non-conservative formulation, because verification cases that included mean density gradients (shown in the next chapter) failed when the conservative formulation was used.

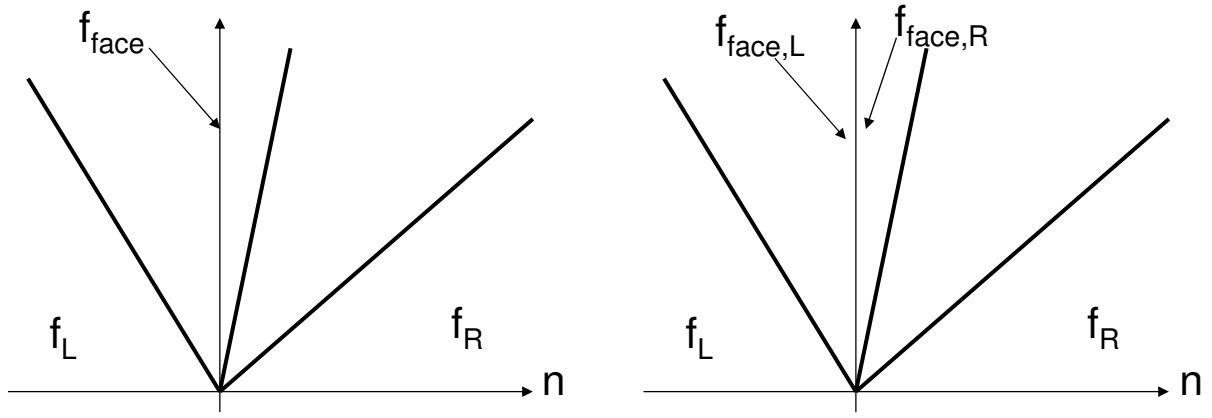

(a) (b)

Figure 3.2: Schematic showing the flux calculation using (a) Roe's method – conservative formulation and (b) non conservative formulation.

3.3.4 Extension to Second-Order Method

Second-order methods can be constructed by evaluating the gradient of each solution variable at each cell center and extrapolating the cell center variables to either side of the face using this gradient. For a given variable

$$\phi_L = \phi_{L,center} + \Psi \left.\frac{\partial \phi}{\partial n}\right|_L (\underline{x}_{face} - \underline{x}_{center}) \tag{3.45}$$

and

$$\phi_R = \phi_{R,center} + \Psi \left. \frac{\partial \phi}{\partial n} \right|_R (\underset{\sim}{x}_{face} - \underset{\sim}{x}_{center}) \tag{3.46}$$

where Ψ is a total variation diminishing (TVD) slope limiter. That is, when the solution varies smoothly, $\Psi = 1$ and the method is second-order. When there is a sharp gradient in the solution near a face, $0 < \Psi < 1$ and the method is reduced to first-order. The limiter of Barth and Jespersen [42] is used for tacFoam.

3.4 Practical Considerations

3.4.1 Initialization

With no forcing, the numerical scheme must initialized with noise in order to provide acoustic energy for modes in the frequency of interest. This can be done either by specifying initial conditions with spatial white noise or by adding a forcing term in a region of the domain for a given startup time. After the startup time is complete, the forcing is turned off and the main part of the simulation can be started.

3.4.2 Calculation of Resonant Frequencies

The solver advances the solution for a satisfactory amount of time with probes placed in locations away from any expected pressure nodes. The probes read pressure data at a

single point in the domain for each time step and write to a file. The probe signals are analyzed in the frequency domain after performing a fast-Fourier transform (FFT) on the data. Since the initial conditions contain wavenumbers (and hence, frequencies) across the entire spectrum, those corresponding to the resonant frequencies of the domain dominate the spectrum from the transformed probe data. Sharp peaks in the spectrum mark the resonant frequencies, which are calculated with a frequency domain resolution inversely proportional to the total time of the simulation.

3.4.3 Calculation of Modeshapes

Modeshapes can be calculated from the tacFoam solver using a discrete Fourier transfer (DFT) calculation which is calculated during the simulation time. The DFT is carried out as a numerical integration (or summation) which is updated at each time step for each cell in the domain. Because a DFT can be very costly when calculated at each cell in a large domain, it is more efficient to calculate the DFT for only a few frequencies rather than the whole spectrum. In general, a second simulation is required to calculate the modeshapes for a given domain, because the user must know the resonant frequencies a-priori in order to specify the frequencies for the DFT calculation. In most cases, the DFT is costly enough such that running two simulations with negligible computational effort spent on the DFT for only a few frequencies on interest (Fig. 3.3a) is much faster than the expense of computing the DFT for a single simulation over the entire frequency domain (Fig. 3.3b). The results

of the DFT give the amplitude and phase of fluctuation for a given resonant frequency as a function of space, which is the acoustic modeshape. As a final note, when the resonant frequencies are known a-priori (e.g. from an analytical solution), the verification may be performed in one simulation if the tacFoam code proves that it can match the analytical frequencies, which are specified by the user prior to the first simulation. If small errors in the tacFoam frequencies exist, an additional simulation may be needed with updated frequencies to extract the modeshapes from the time domain solver (Fig. 3.3c).

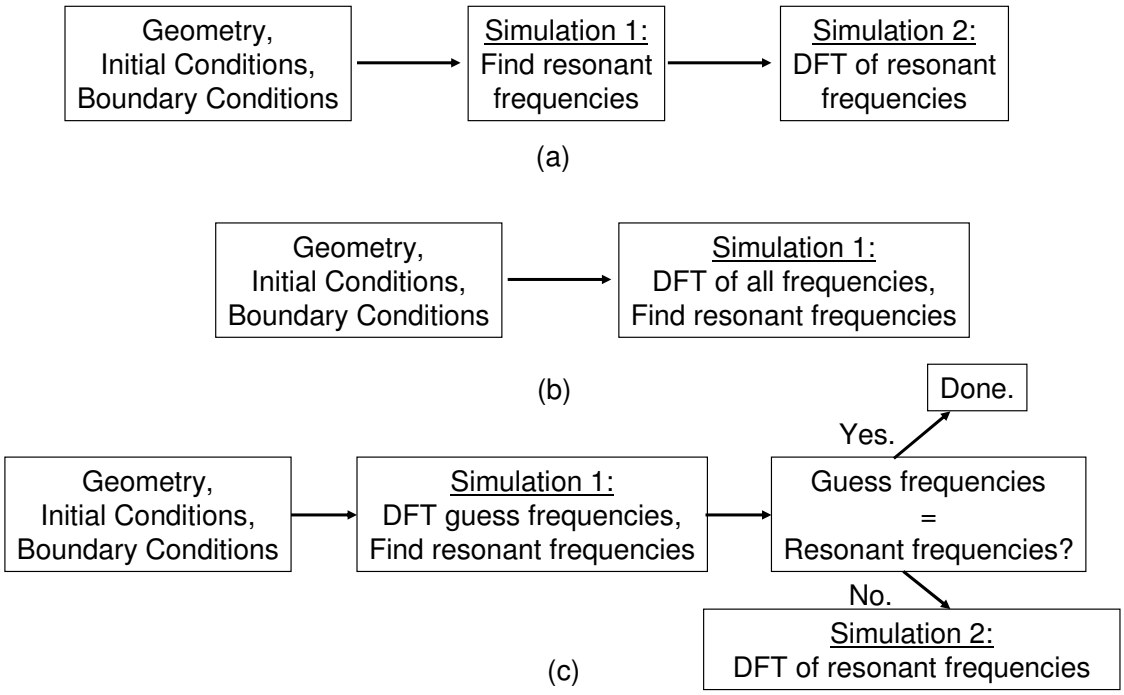

Figure 3.3: Flowchart showing the strategy for obtaining resonant frequencies and modeshapes from tacFoam simulations.

3.4.4 Calculation of Growth Rates

Growth rates for a particular mode can also be calculated from the time domain data. First, the time domain data from a point probe is filtered with a narrow bandpass filter ($\pm 5Hz$) so that only information from the desired mode is retained. Second, the extrema are selected from the data. Finally, an exponential curve fit is performed through the absolute values of the extrema. The exponent from this curve fit provides the growth rate. It is recommended that R^2 values are checked to ensure that the fit is appropriate and a visual inspection of the data is quickly performed if the R^2 value is low.

CHAPTER 4
VERIFICATION

In this chapter, the tacFoam solver is verified for a number of simple problems with analytical solutions. Key phenomena which tacFoam attempts to account for include mean flow, mean flow gradients, density gradients, three-dimensional geometries, acoustic boundary conditions, and unsteady heat release. The verification of the solver includes test cases designed to demonstrate the ability of the solver to accurately capture the physical effects of these phenomena when compared with known analytical solutions. Derivations of the analytical solutions corresponding to each verification case can be found in the appendix.

Aside from verification with respect to physical phenomena, the solver is tested for accuracy in parallel computation. It is important that the numerical solution be independent of parallelization across many processors. Finally, the behavior of numerical damping is quantified with respect to the most influential parameters. The possible pitfalls from uncontrolled numerical damping are illustrated with suggestions for avoiding them.

4.1 Acoustic Verification

The main objective of pure acoustic testing is to verify that the solver produces the correct resonant frequencies, modeshapes, and/or linear growth rates for problems with the various important phenomena. A number of simple cases are presented, ranging from one-dimensional to three-dimensional, in which the solver is tested for its ability to correctly capture the acoustic behavior for a number of physical effects that are important for the present application to gas turbine combustion. The resonant frequencies and modeshapes are used as the metric for the assessment of accuracy.

First, the solver is verified for one-dimensional acoustics in a very simple test. The first one-dimensional test is a duct with uniform properties and zero mean flow. The objective of this test is to verify the ability of the solver to replicate results from classical acoustics. Then the solver is tested in a one-dimensional duct with linearly varying mean temperature and constant mean pressure. This second test has a smooth variation of mean properties inside the domain, which provides a first test of the solvers ability to handle density gradients. Afterwards, the solver is tested with the same one-dimensional duct but with an acoustically-compact temperature rise. This "thin flame simulation" with steady heat release tests the ability of the solver to correctly simulate the effect of sharp density gradients on acoustic modes. The final one-dimensional test returns to a duct with uniform mean properties, but adds a mean flow.

Following the set of one-dimensional tests, a set of two-dimensional cases involving cross-sectional area variation can be compared with one-dimensional analytical solutions, provided that the area changes are not too dramatic. This set includes a horn with an exponentially-varying cross-sectional area followed by two constant area ducts connected by a sudden area change. Finally, the ability of tacFoam to predict three-dimensional modeshapes is tested using circular and annular cylinders. Table 4.1 summarizes the acoustic verification tests.

Table 4.1: Reference conditions for uniform duct verification.

Test	Physics
Uniform Duct	Simple Acoustics
Linear Temperature	Gradual Mean Density Gradient Effects
Temperature Jump	Compact Mean Density Gradient Effects
Uniform Mean Flow	Mean Velocity Effects
Mean Flow + Temp. Jump	Mean Velocity Gradient Effects
Exponential Cross-Sectional Area	Gradual Multidimensional Effects
Cross-Sectional Area Jump	Compact Multidimensional Effects
Circular Cylinder	Multidimensional Modes
Annular Cylinder	Multidimensional Modes

4.1.1 1D Acoustics in a Uniform Duct

A one-dimensional grid was constructed for the domain (Fig. 4.1) with 100 cells. The physical parameters of the simulation are shown in Table 4.2.

Table 4.2: Reference conditions for uniform duct verification.

$R[J/kg-K]$	γ	$\bar{p}[kPa]$	$\bar{\rho}[kg/m^3]$	$\bar{T}[K]$	$\bar{a}[m/s]$	$L[m]$	$f-Range[Hz]$
287	1.40	100	1.17	298	346	1.0	87-865

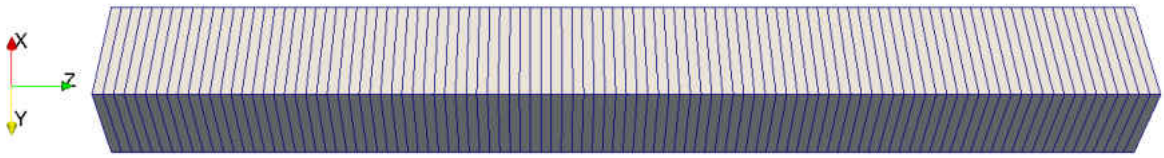

Figure 4.1: The mesh for uniform duct verification.

Linear acoustics in a one-dimensional uniform duct is governed by the wave equation, resulting in sinusoidal modeshapes. Both closed-closed and closed-open boundary conditions were simulated. The pressure modeshapes for closed-closed boundaries are given by [43]

$$\psi(z) = \cos(n\pi z/L) \tag{4.1}$$

with corresponding frequencies (in Hz) of

$$f_n = \frac{n\bar{a}}{2L} \tag{4.2}$$

For closed-open boundaries, the modeshapes become

$$\psi(z) = \cos((n-1/2)\pi z/L) \tag{4.3}$$

with resonant frequencies given (in Hz) by

$$f_n = \frac{(n - \frac{1}{2})\bar{a}}{2L}. \tag{4.4}$$

The resonant frequencies for the first five modes found by the solver are compared in Fig. 4.2 with the analytical values from Eqs. (4.2) and (4.4). As shown in Fig. 4.3, the frequency errors were less than 0.6%, mostly falling within the resolution uncertainty of the FFT. Figure 4.4 shows the comparison of pressure modeshapes for tacFoam DFT solution against the analytical modeshapes from Eqs. (4.1) and (4.3).

Figure 4.2: Resonant frequencies for uniform one-dimensional duct.

The ability of the solver to match frequencies and modeshapes with classical acoustic theory is no surprise, but provides a first check that the numerical algorithm contains no fatal flaws in its development or implementation.

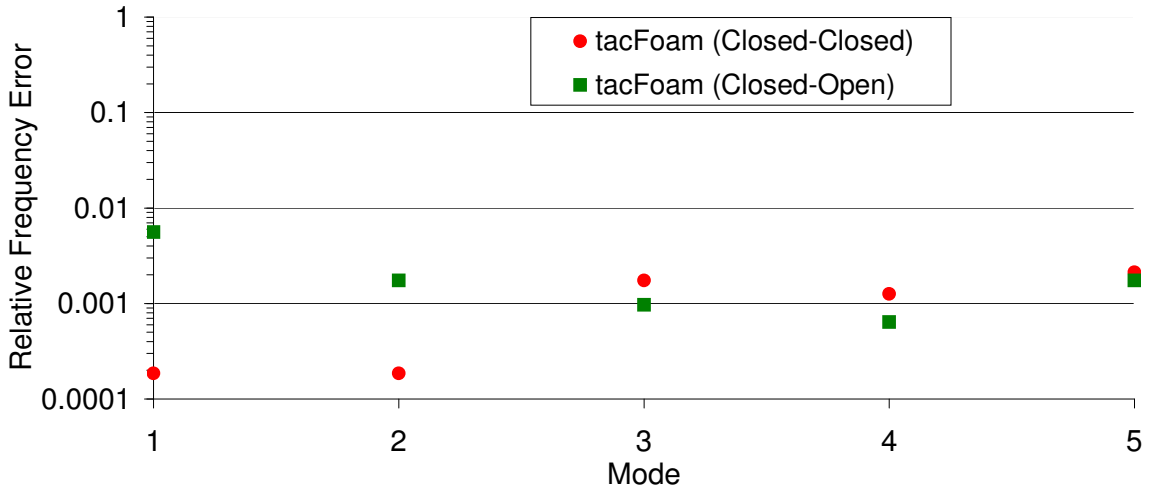

Figure 4.3: Relative frequency errors for uniform one-dimensional duct.

4.1.2 1D Acoustics with a Linear Temperature Distribution

An important physical effect for modelling thermoacoustics in gas turbine combustors is the effect of inhomogeneous media. The first test applied to tacFoam involving mean density gradients is a one-dimensional duct with a linear temperature profile and constant mean pressure. The mean density profile was calculated from the ideal gas equation ($\bar{p} = \bar{\rho} R \bar{T}$) and the sound speed is given by $\bar{a} = \sqrt{\gamma R \bar{T}}$. Mathematically, the temperature profile is given by

$$T(z) = T_{inlet} + mz \tag{4.5}$$

where m is the temperature gradient given by

$$m = \frac{T_{exit} - T_{inlet}}{L}. \tag{4.6}$$

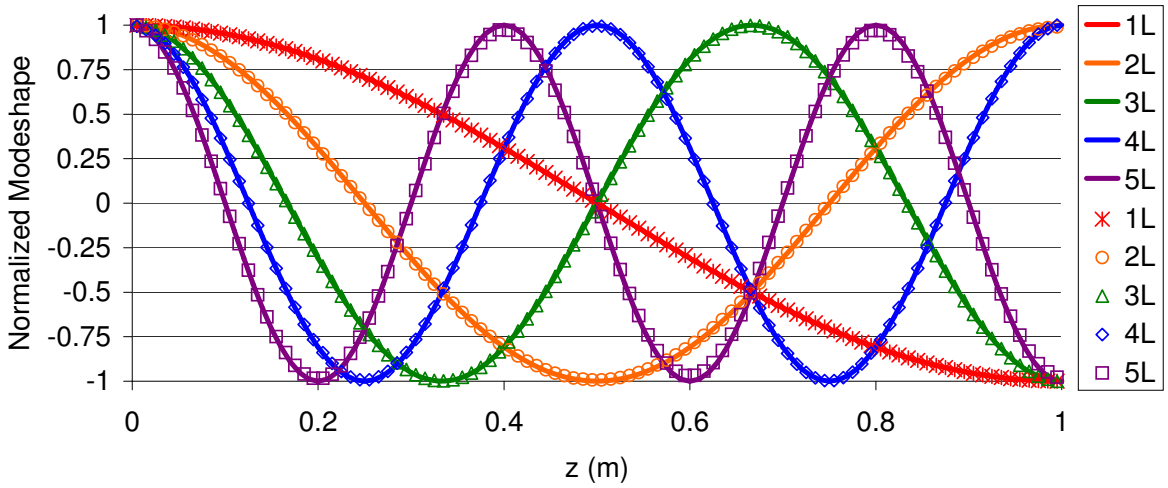

(a)

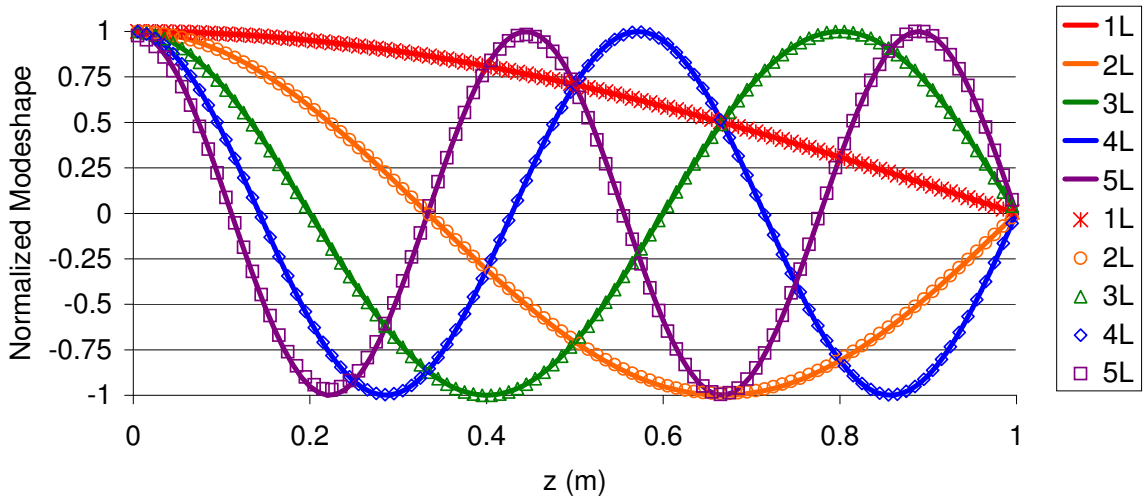

(b)

Figure 4.4: Pressure modeshapes for uniform one-dimensional duct. Solid lines are analytical solutions, symbols are tacFoam solutions.

The boundary conditions are closed at the inlet and open at the exit. The same domain and grid shown in Fig. 4.1 was used for this case. The acoustics were simulated in this problem for a range of temperature gradients. The parameters for the simulations are given in Table 4.3. Example temperature and density profiles for a temperature ratio of 8 are given in Fig. 4.5.

Table 4.3: Reference conditions for linear temperature verification case.

R [J/kg-K]	γ	$\bar{p}$ [kPa]	$\bar{T}_{inlet}$ [K]	$\bar{T}_{exit}$ [K]	$\bar{T}_{exit}/\bar{T}_{inlet}$	L [m]	f-Range [Hz]
287	1.40	100	298	298-2384	1-8	1.0	86.5-1496

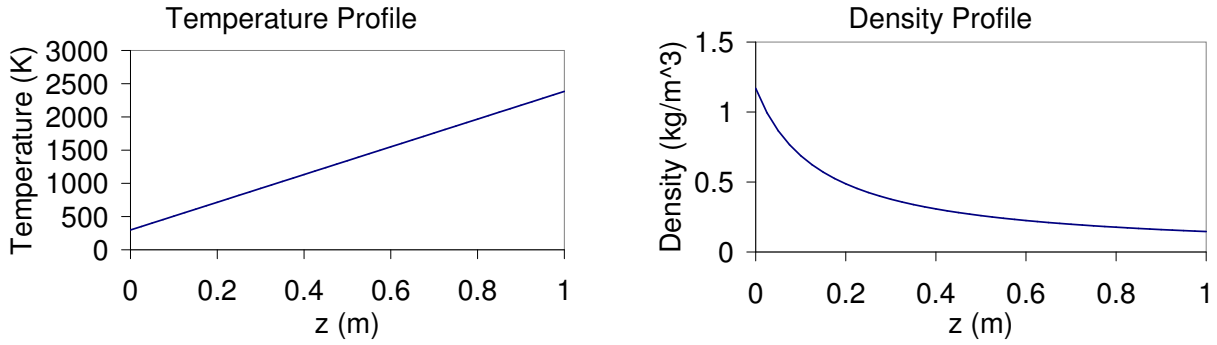

(a) (b)

Figure 4.5: Mean (a) temperature and (b) density profiles for the linear temperature verification case; here a temperature ratio of eight is shown.

With closed-open boundaries, the analytical modeshapes derived in Appendix C are given by

$$\psi(z) = -Y_1\left(\frac{2\omega\sqrt{\bar{T}_{inlet}}}{|m|\sqrt{\gamma R}}\right) J_0\left(\frac{2\omega\sqrt{\bar{T}_{inlet}+mz}}{|m|\sqrt{\gamma R}}\right)$$

$$+ J_1\left(\frac{2\omega\sqrt{\bar{T}_{inlet}}}{|m|\sqrt{\gamma R}}\right) Y_0\left(\frac{2\omega\sqrt{\bar{T}_{inlet}+mz}}{|m|\sqrt{\gamma R}}\right) \tag{4.7}$$

where the frequencies ω satisfy the characteristic equation

$$Y_1\left(\frac{2\omega\sqrt{\bar{T}_{inlet}}}{|m|\sqrt{\gamma R}}\right) J_0\left(\frac{2\omega\sqrt{\bar{T}_{exit}}}{|m|\sqrt{\gamma R}}\right) - J_1\left(\frac{2\omega\sqrt{\bar{T}_{inlet}}}{|m|\sqrt{\gamma R}}\right) Y_0\left(\frac{2\omega\sqrt{\bar{T}_{exit}}}{|m|\sqrt{\gamma R}}\right) = 0. \tag{4.8}$$

This characteristic equation can be solved with an appropriate root-finding numerical scheme for the resonant frequencies of the duct.

The resonant frequencies found by tacFoam are compared with theoretical values from Eq. (4.8) in Fig. 4.6. The relative errors for this test case, plotted in Fig. 4.6b, were less than or equal to the relative error from the first case. The first verification case is the same as the temperature ratio of unity case shown here. The corresponding modeshapes are shown in Fig. 4.7 for a temperature ratio of eight, compared with the analytical modeshapes from Eq. (4.7).

As with the first verification case, the analytically-derived frequencies and modeshapes are matched accurately by the tacFoam solutions. This confirms that mean density gradients are treated properly by the tacFoam solver.

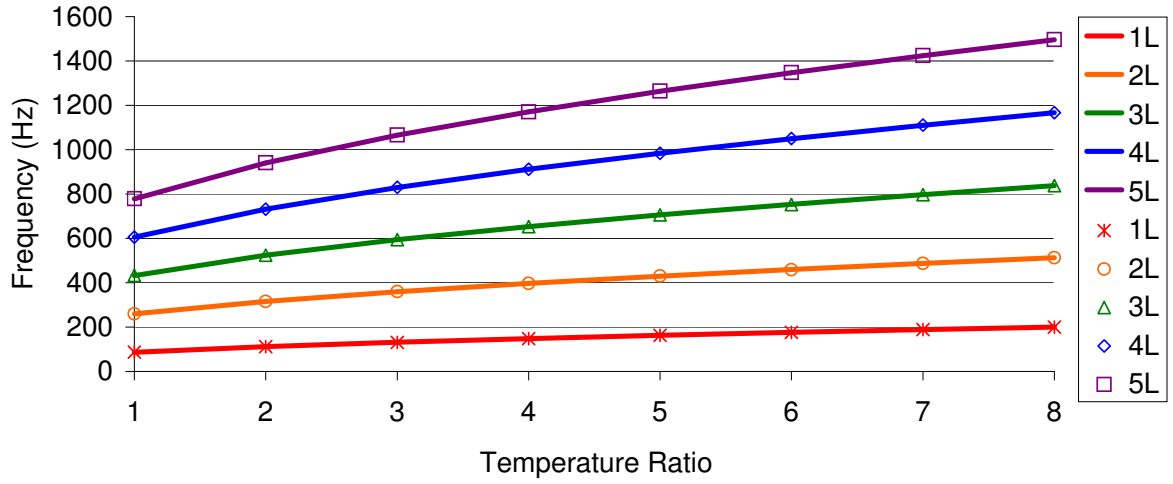

(a)

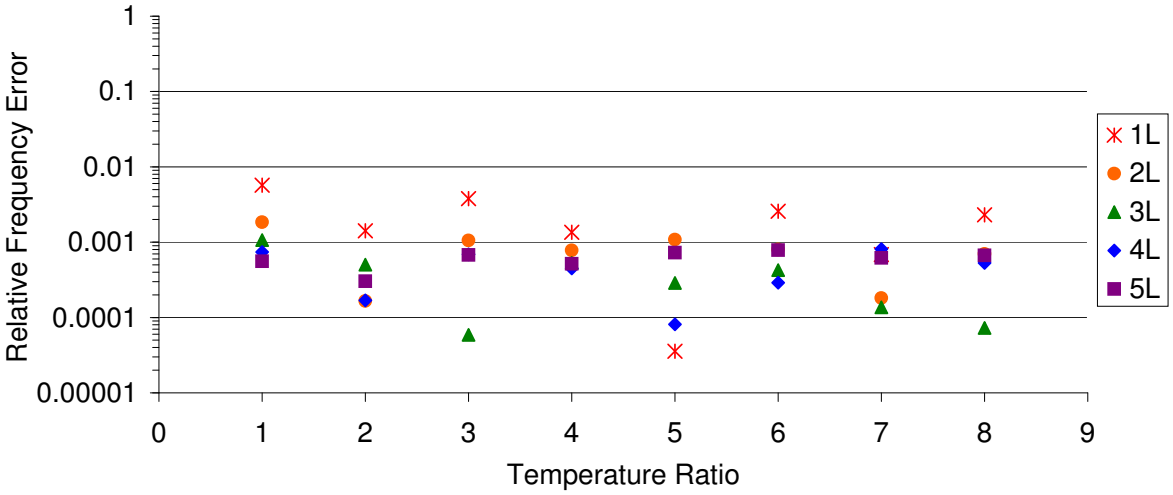

(b)

Figure 4.6: Linear temperature case (a) resonant frequencies and (b) relative frequency errors. Solid lines are analytical solutions, symbols are tacFoam solutions.

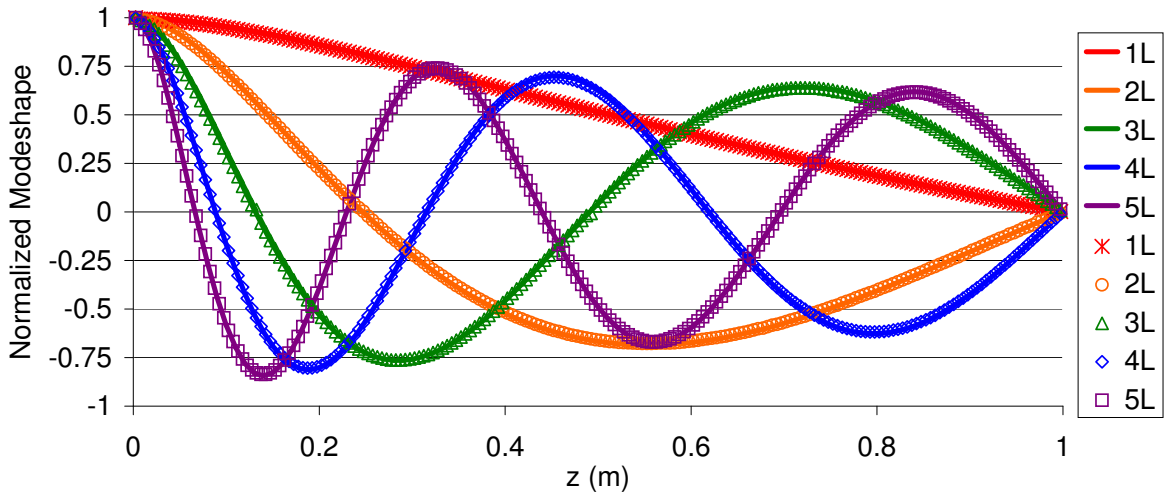

Figure 4.7: Modeshapes for first five longitudinal modes for the linear temperature verification case; a temperature ratio of eight is shown here. Solid lines are analytical solutions, symbols are tacFoam solutions.

4.1.3 1D Acoustics with an Acoustically Compact Temperature Rise

Motivated by the nature of density gradients within typical gas turbine combustion chambers, namely their relatively thin nature, another density gradient test is simulated with tacFoam and compared with analytical solution. For this case the linear temperature distribution is concentrated in an infinitessimal region at the center of the domain ($z = b = 0.5m$), with constant temperature regions on either side of the temperature discontinuity. Acoustically, because the flame thickness is much less than the wavelength of the first few acoustic modes, the density gradient appears as a discontinuity. Mathematically, an equivalent statement for the compactness of the flame is

$$t << L \tag{4.9}$$

where t is the thickness of the flame region and $L = 1.0m$ is the length of the duct, which is the length scale for the acoustic wavelengths. The analytical solution is found by matching two acoustic waves from constant density regions using interface conditions at the flame. In most gas turbine combustors for power generation, the flames are acoustically compact [10]. This verification case is carried out with temperature ratio of eight for various grid resolutions to quantify any effect of resolving the thin density gradient region. With 100 cells ($\Delta = 0.01m$), this mesh represents the case in which the flame is not resolved at all, appearing as a discontinuity to the mesh. Therefore, the effective thickness of the flame is assumed to be $t < 0.01m$. The temperature and density profiles are shown in Fig. 4.8.

Table 4.4: Reference conditions for compact temperature rise verification.

R [J/kg-K]	γ	$\bar{p}$ [kPa]	$\bar{T}_{inlet}$ [K]	$\bar{T}_{exit}$ [K]	t [m]	L [m]	b [m]	f-Range [Hz]
287	1.40	100	298	2384	0.010	1.00	0.50	152-1182

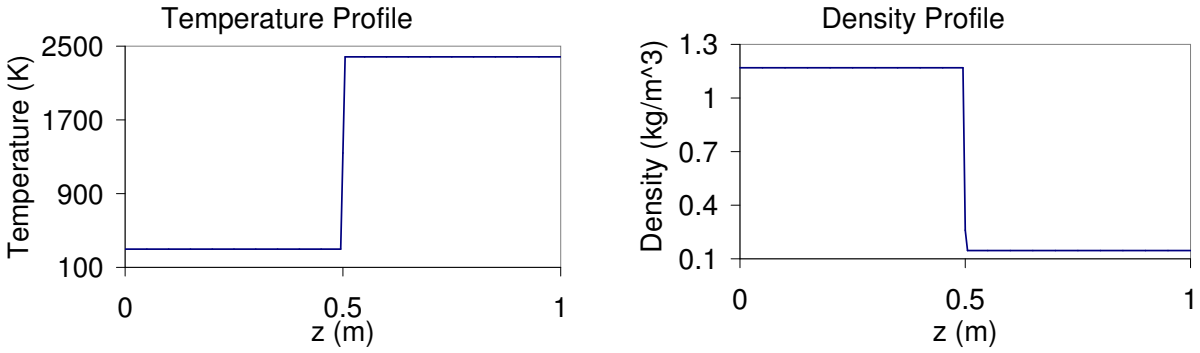

(a) (b)

Figure 4.8: Mean (a) temperature and (b) density profiles for the compact temperature rise verification case.

The analytical modeshapes for closed-open boundaries are given by

$$\psi(z) = \begin{cases} \cos\left(\frac{\omega}{\sqrt{\gamma R\bar{T}_{inlet}}}z\right) & z < b \\ \frac{\cos\left(\frac{\omega}{\sqrt{\gamma R\bar{T}_{inlet}}}b\right)}{\sin\left(\frac{\omega}{\sqrt{\gamma R\bar{T}_{exit}}}(L-b)\right)} \sin\left(\frac{\omega}{\sqrt{\gamma R\bar{T}_{exit}}}(L-z)\right) & z > b \end{cases} \tag{4.10}$$

where the resonant frequencies, ω, satisfy the characteristic equation

$$\tan\left(\frac{\omega}{\sqrt{\gamma R\bar{T}_{exit}}}(L-b)\right) \tan\left(\frac{\omega}{\sqrt{\gamma R\bar{T}_{inlet}}}b\right) - \sqrt{\frac{\bar{T}_{exit}}{\bar{T}_{inlet}}} = 0 \tag{4.11}$$

The resonant frequencies for the first five modes are plotted in Fig. 4.9a as a function of the resolution of the flame.

Not only does tacFoam correctly match the trends, the relative errors in the frequencies remain below one percent for all cases simulated. The modeshapes for the $TR = 8$ case are shown in Fig. 4.10. As before, the modeshapes match their analytical counterparts.

The suitability for tacFoam to handle flame-like thin density gradient regions is supported by this verification case. Such ability is important for the design environment for which it is intended, namely, lean premixed flames in gas turbine engines for power generation.

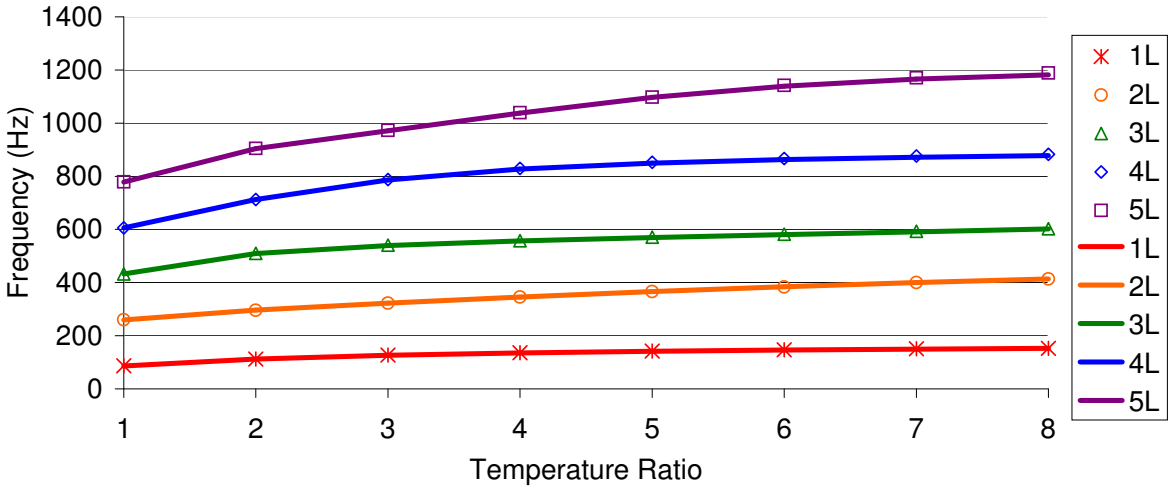

(a)

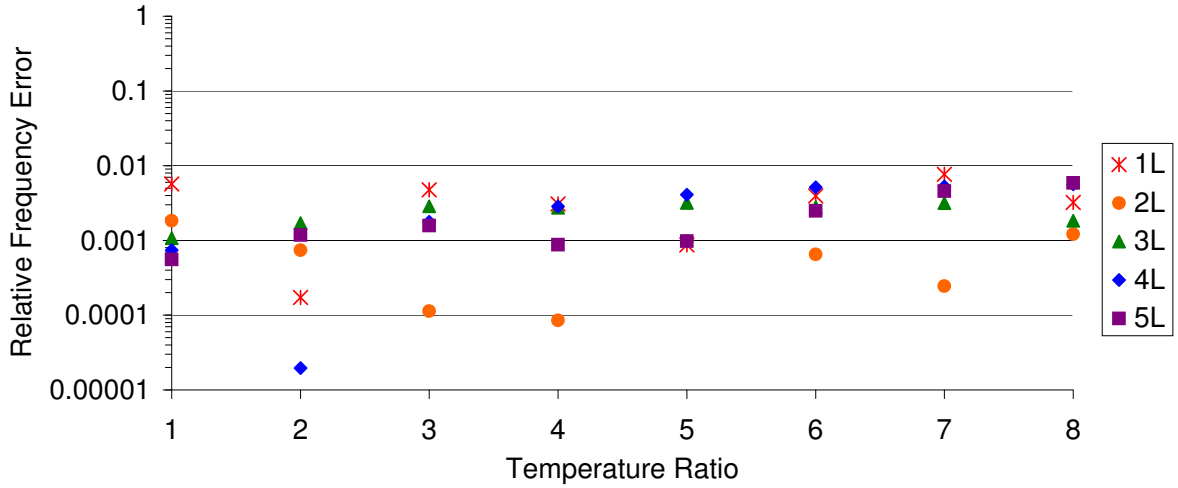

Figure 4.9: Compact temperature rise (a) frequencies and (b) relative errors. Solid lines are analytical solutions, symbols are tacFoam solutions.

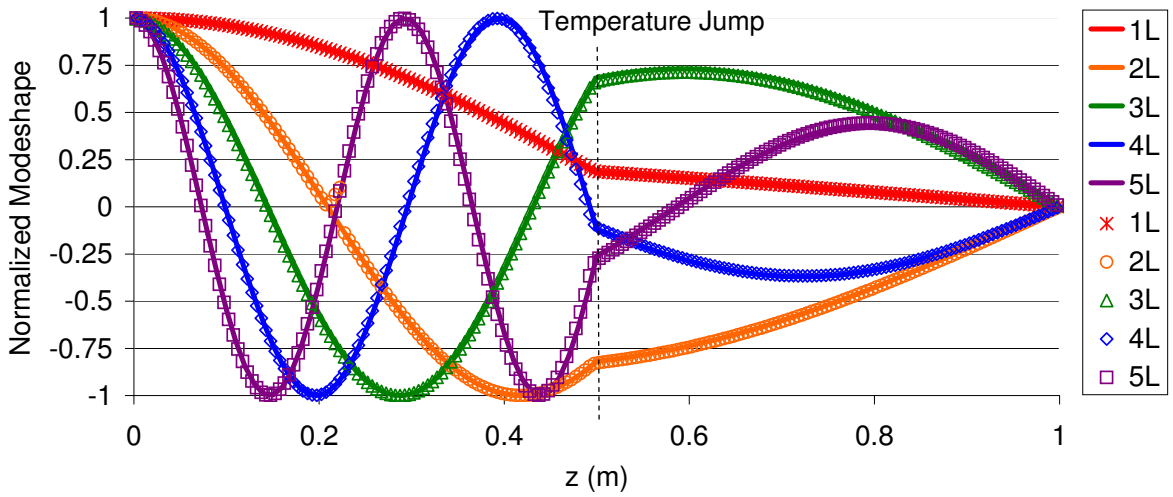

Figure 4.10: Modeshapes for first five modes of the compact temperature rise case. Solid lines are analytical solutions, symbols are tacFoam solutions.

4.1.4 1D Acoustics with a Uniform Mean Flow

Another aspect of combustor acoustics that can present a challenge is the presence of mean flow at a high enough Mach number to alter the behavior of the acoustic modes. Dowling [24] emphasized the important role that mean flow can play in thermoacoustic oscillations for realistic combustors. A simple test case is constructed to verify the ability of tacFoam to handle the effect of mean flow. The same domain and grid from the previous verification cases is used with uniform density throughout the duct. The only complication above the first verification case is the addition of a uniform mean flow into the tacFoam model. The simulations for this verification case are performed over a range of Mach numbers.

The details of the model parameters are recorded in Table 4.5. Note that the $M = 0.0$ case is identical to the verification case from the first section.

Table 4.5: Reference conditions for uniform mean flow verification.

R [J/kg-K]	γ	$\bar{p}$ [kPa]	$\bar{T}$ [K]	$\bar{a}$ [m/s]	$\bar{u}$ [m]	$\bar{M}$	f-Range [Hz]
287	1.40	100	298	346	0-312	0.0-0.9	16-779

For this verification case, closed-open boundaries are used. As shown in Appendix C, the analytical frequencies are

$$f_n = \frac{(n - \frac{1}{2})\bar{a}}{2L}(1 - \bar{M}^2) \tag{4.12}$$

Note that this is the same as the resonant frequencies for the uniform duct in Eq. (4.4), except for the added factor $(1 - \bar{M}^2)$, which reduces the frequency as the Mach number is increased.

The resonant frequencies for the tacFoam simulations with uniform mean flow in the constant property duct are shown in Fig. 4.11a along with the analytical solutions. The relative error in the tacFoam simulations, Fig. 4.11b, remains below 0.6%. This verifies that no significant additional error is added by the presence of a mean flow.

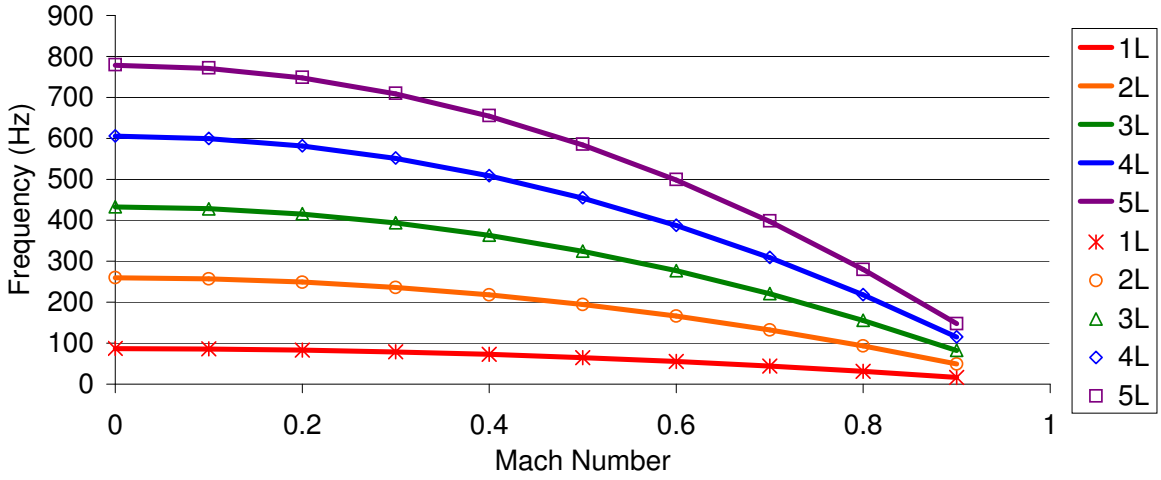

(a)

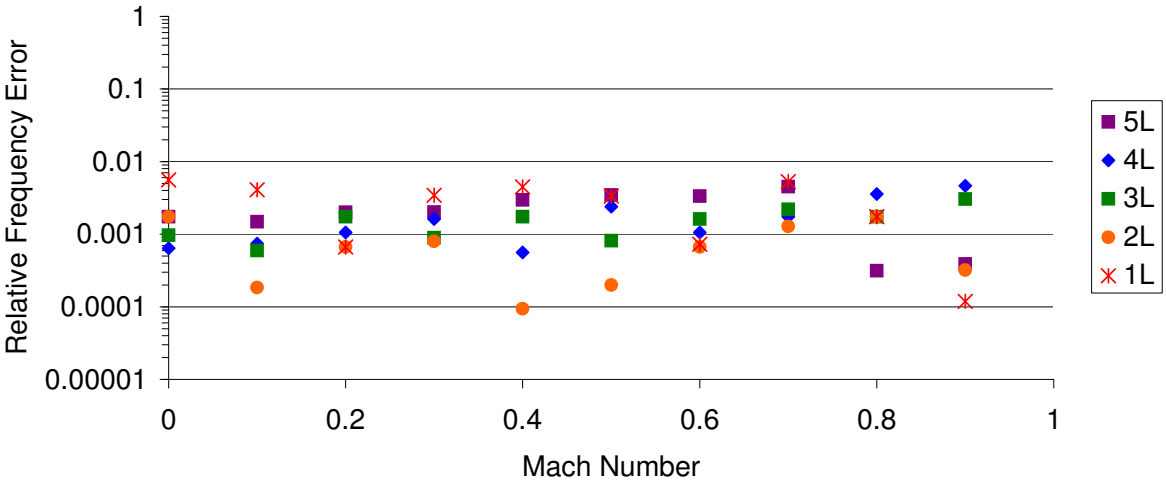

(b)

Figure 4.11: Uniform mean flow (a)frequencies and (b) relative errors. Solid lines are analytical solutions, symbols are tacFoam solutions.

4.1.5 1D Acoustics with Temperature Jump and Mean Flow

A combination of the previous two cases involves a one-dimensional flow with a temperature jump normal to the flow. This roughly simulates the physics present in the combustion chambers of gas turbine engines. From a physical point of view, the key addition for this verification case is the presence of a mean flow gradient, caused by the jump in density and the necessity to conserve mass flow rate. In the interest of brevity, only one temperature ratio was simulated, with a range of Mach numbers. The conditions used are shown in Table 4.6. The same domain and grid are used as in all the previous one-dimensional cases. Acoustic boundary conditions are closed at the inlet and open at the outlet.

Table 4.6: Reference conditions for mean flow temperature jump verification.

R [J/kg-K]	γ	$\bar{p}$ [kPa]	$\bar{T}_{inlet}$ [K]	$\bar{T}_{exit}/\bar{T}_{inlet}$	$\bar{M}_{inlet}$	f-Range (Hz)
287	1.40	100	298	8	0.0-0.25	152-1182

The frequencies and growth rates found are compared with those obtained from the Transfer Matrix Approach (TMA) [44]. First, a simulation is performed in which the source terms on the right hand side of Eqs. (3.1) and (3.2) are neglected. These terms contain the physical effects of mean velocity gradients, therefore neglecting them should be fatal to the accuracy of the simulation. The relative frequency error as a function of inlet Mach number is shown in Fig. 4.12. The relative errors in frequency are small (below one percent) for small inlet Mach numbers (0.05 and below). As the inlet Mach number increases, and

hence the velocity gradient at the flame increases, the relative error increases. By an inlet Mach number of 0.2, the relative error in frequency is as high as 10%. The errors are more dramatic for the growth rate. The zero Mach number case has no growth rate. With finite Mach number, the velocity gradient at the flame works to damp or excite acoustic modes. This effect is completely missing from the tacFoam solution, which only shows the numerical damping (comparatively very small). These results are not surprising given that the terms necessary to capture the physical effects of mean velocity gradients on acoustics are missing from the governing equations used.

In a follow-up simulation, the source terms related to mean flow gradients are added back into the governing equations of the code and the above simulation is repeated. As expected based on the analytical solutions shown in Fig. 4.12, strong damping of the modes becomes evident. The results are shown for two low Mach number cases in Fig. 4.13. The presence of strong damping in the time domain simulation become problematic for post-processing at higher Mach numbers. Because the modes die out quickly, the filtering and curve-fitting technique used to extract growth rates no longer yields quality results. Therefore, the figure shows only the small Mach number, low damping rate cases.

The agreement is excellent for the limited number of cases for which comparison is available. Relative errors remain under 5%, even for Mach = 0.025 when the damping rates become $\sim 40\ rad/s$. This verification case concludes that the mean velocity gradient source terms are effective in modelling the interaction between gradients in the mean velocity field and acoustics.

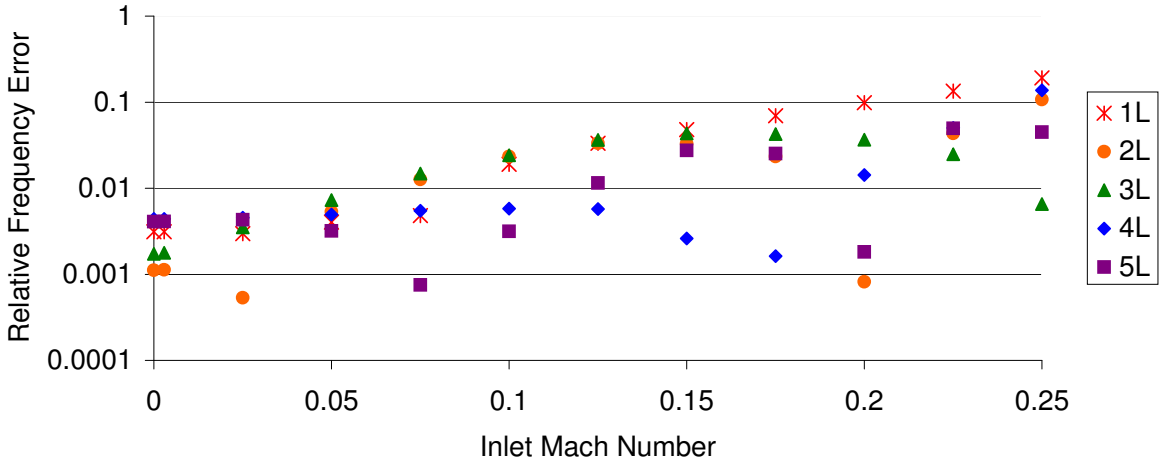

(a)

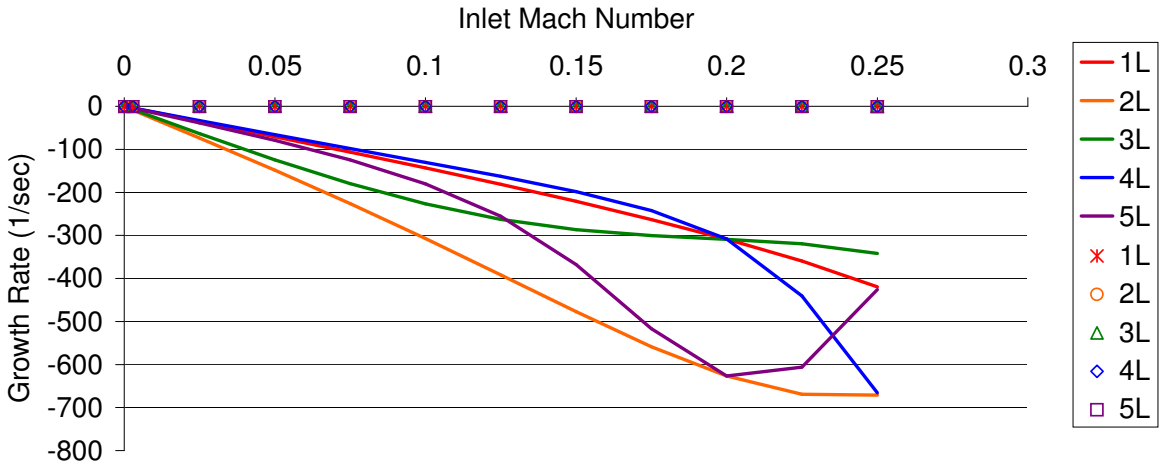

(b)

Figure 4.12: Two temperature with mean flow: (a)relative frequency errors and (b) growth rates. Solid lines are TMA solutions, symbols are tacFoam solutions.

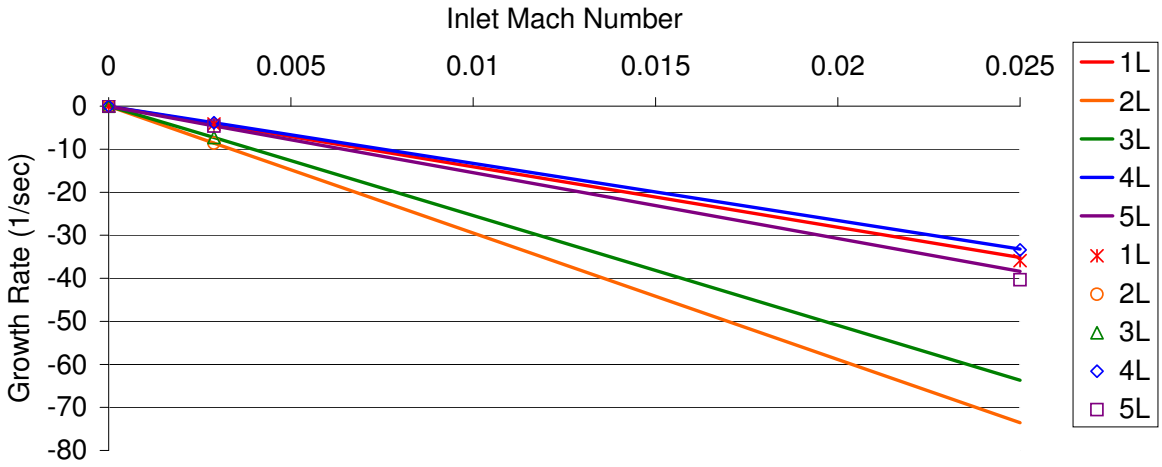

Figure 4.13: Two temperature with mean flow: growth rates from simulation including source terms previously neglected. Solid lines are TMA solutions, symbols are tacFoam solutions.

4.1.6 1D Acoustics with an Exponential Cross-sectional Area Distribution

With the previous verification cases covering important phenomena for modeling gas turbine combustors with regard to the flow variables, the other significant influence on the thermoacoustics in combustors is multi-dimensional effects. In some cases, only longitudinal modes are of interest. Longitudinal modes, in this context, are defined as modes in which the wavenumber vector is approximately aligned with the streamlines of the mean flow. If only longitudinal modes are of concern and the cross-sectional area varies little relative to the length of the duct, a one-dimensional approach may be maintained analytically for approximating the acoustic behavior. The next set of verification cases includes two dimen-

sional geometries in which only longitudinal modes are concerned. The solutions provided by tacFoam are compared with analytical solutions using the one-dimensional approximation.

The first such case is of the exponentially-varying cross-sectional area. Simulations are run in tacFoam for a number of exit-to-inlet area ratios with constant mean properties and no mean flow. The simulation parameters are given in Table 4.7. Note that the cross-sectional areas are given in meters because the simulation is two-dimensional in nature. A unit depth in the third direction could be assumed to make the units m^2. Also note that area ratios up to 64 are simulated. At these higher area ratios, the one-dimensional assumption inherent in the analytical solution becomes inaccurate. Closed-closed boundary conditions are used and the area ratio of unity is equivalent to the first verification case.

Table 4.7: Reference conditions for exponential cross-sectional area verification.

R [J/kg-K]	γ	$\bar{p}$ [kPa]	$\bar{T}$ [K]	S_{inlet} [m/s]	S_{exit} [m]	f-Range [Hz]
287	1.40	100	298	0.01	0.01-0.64	173-873

The domain and mesh for a typical case (AR = 16) is shown in Fig. 4.14. The transverse direction is meshed with 20 cells and the longitudinal direction is meshed with the number of cells necessary for an aspect ratio of unity.

The cross-section area is given by

$$S(z) = S_{inlet} e^{mz} \tag{4.13}$$

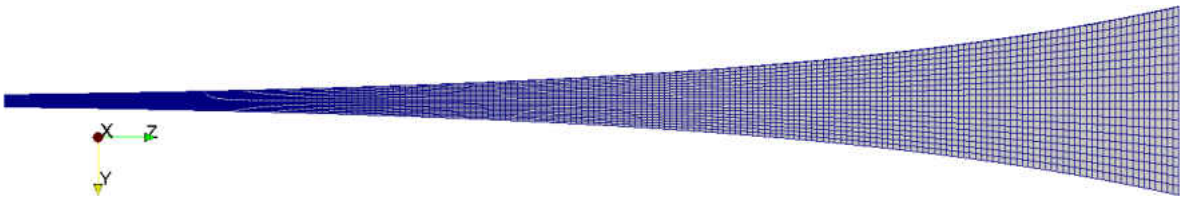

Figure 4.14: The (mesh for the exponentially-varying cross-sectional area verification case.

where the exponential factor m is given by

$$m = \frac{1}{L} \ln \left(\frac{S_{exit}}{S_{inlet}} \right) \tag{4.14}$$

The analytical solution derived in the appendix shows that the modeshape should be

$$\psi(x) = e^{-(m/2)z} \sin(n\pi z/L) \tag{4.15}$$

and the frequencies are

$$f = \sqrt{\left(\frac{n\bar{a}}{2L} \right)^2 + \left(\frac{m\bar{a}}{4\pi} \right)^2} \tag{4.16}$$

Note that the frequency increases as the area ratio increases.

The comparison of frequencies and modeshapes are given in Figs. 4.15 and 4.17, respectively. The frequencies in Fig. 4.15 are non-dimensionalized by the constant cross-section frequency ($m = 0$). The relative errors in the tacFoam frequencies are shown in Fig. 4.16. At lower area ratios, the tacFoam solution matches the analytical solution well, with maximum error around 0.2%. At area ratios of 32 and 64, there begins to develop a discrepancy between the two-dimensional tacFoam results and the one-dimensional theory. This discrepancy is not due to a limitation of the tacFoam code, but rather a limitation

of the one-dimensional theory of describing acoustics in ducts when the cross-sectional area varies dramatically.

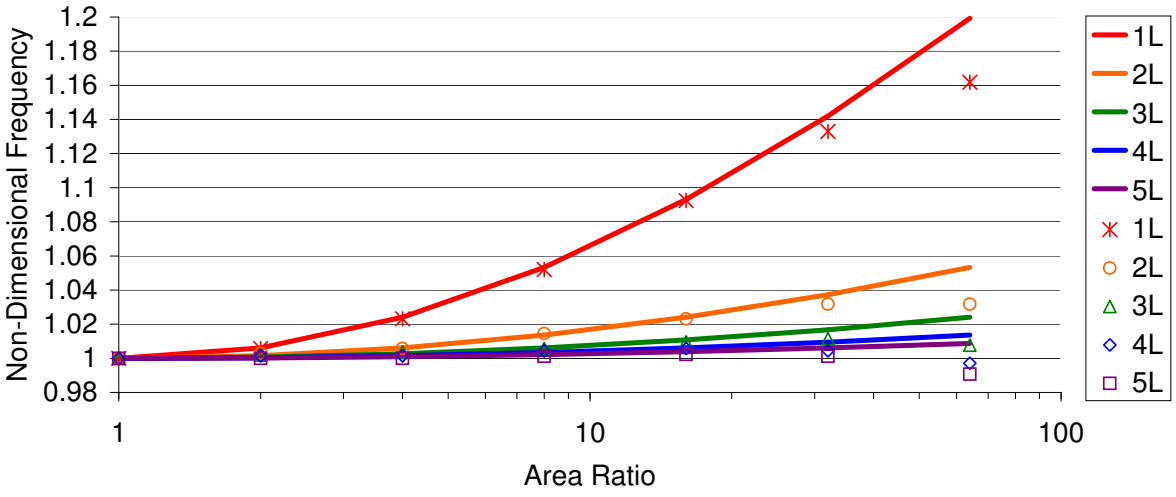

Figure 4.15: Resonant frequencies for first five modes for the exponentially-varying cross–sectional area case. Solid lines are analytical solutions, symbols are tacFoam solutions.

The modeshapes shown in Fig. 4.17 are shown for the example case of area ratio (S_{exit}/S_{inlet}) of 16. This was the highest area ratio at which the simulations matched the frequency of the analytical solution. As a note, the modeshapes were taken from a line probe through the center of the duct. No observations were made of any possible transverse variation in the modeshape because the comparison at hand is made with one-dimensional theory.

The conclusion of this test is that, as far as possible, tacFoam shows agreement with analytical frequencies and modeshapes. When the assumptions of the analytical solution

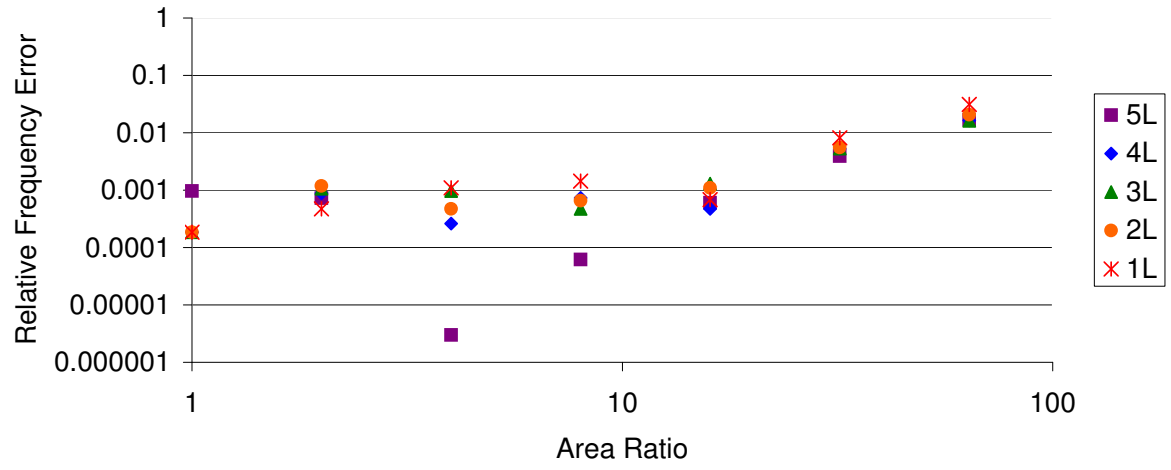

Figure 4.16: Relative frequency error for first five modes for the exponentially-varying cross–sectional area case.

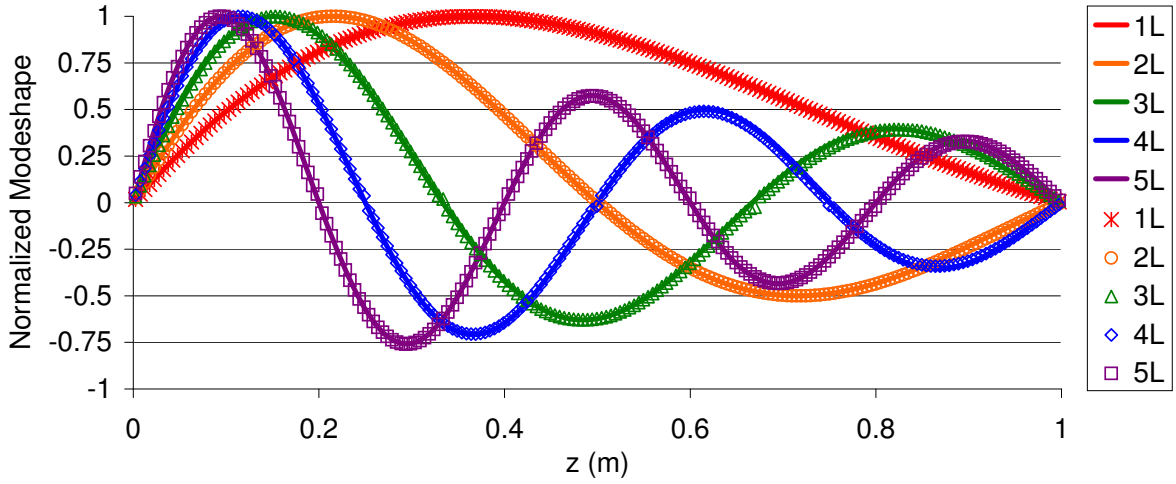

Figure 4.17: Modeshapes for first five modes of the exponential area verification case. Solid lines are analytical solutions, open symbols are tacFoam solutions.

breakdown, tacFoam predictably fails to replicate the limited analytical solutions outside of the their range of applicability.

4.1.7 1D Acoustics with an Acoustically Compact Area Change

While the previous verification case showed that tacFoam could handle smooth changes in cross-sectional area, it is worthwhile to pursue the question of more sudden area changes. In combustor geometries, sudden area changes are often used as part of the scheme to anchor the flame. Therefore, the most relevant verification case is two constant area ducts joined by an area discontinuity. The parameters for this case are given in Table 4.8. Closed-open boundary conditions are used. The area ratios for this test case were not chosen as large as the previous test case, since the limits of the one-dimensional theory had already been tested.

Table 4.8: Reference conditions for sudden area change verification.

R [J/kg-K]	γ	$\bar{p}$ [kPa]	$\bar{T}$ [K]	S_{inlet} [m/s]	S_{exit} [m]	f-Range [Hz]
287	1.40	100	298	0.01	0.01-0.08	87-828

The domain for the area ratio of four case is shown in Fig. 4.18a. The one-dimensional acoustic theory gives a good approximation of this geometry because the total area change is much less than the length of the duct (wavelength). A close-up snapshot of the mesh near the discontinuity is shown in Fig. 4.18b. Upstream, the mesh includes 20 cells in the

transverse direction. Downstream, the cell size remains constant and hence the number of transverse cells scales with the area expansion ratio. The longitudinal resolution was chosen to give aspect ratios near unity.

(a)

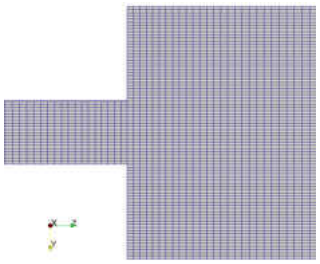

(b)

Figure 4.18: The (a) domain and (b) mesh for area discontinuity verification.

The analytical modeshapes for closed-open boundaries, constructed by matching constant area duct solutions at the interface, are

$$\psi(z) = \begin{cases} \cos(kz) & x < b \\ \frac{\cos(\omega b/\bar{a})}{\sin[\omega(L-b)/\bar{a}]} \sin[\omega(L-z)/\bar{a}] & x > b \end{cases} \tag{4.17}$$

The resonant frequencies can be solved for numerically from the following characteristic equation

$$\tan\left(\frac{\omega}{\bar{a}}(L-b)\right) \tan\left(\frac{\omega}{\bar{a}}b\right) - \frac{S_{exit}}{S_{inlet}} = 0 \tag{4.18}$$

The frequencies found by the tacFoam solver are compared with the analytical frequencies in Fig. 4.19. The trends in frequency are matched. Note that, as the area ratio tends to infinity, the acoustic frequencies become those of half the duct. Figure 4.20 shows that the frequency error is this verification case remains below 1%.

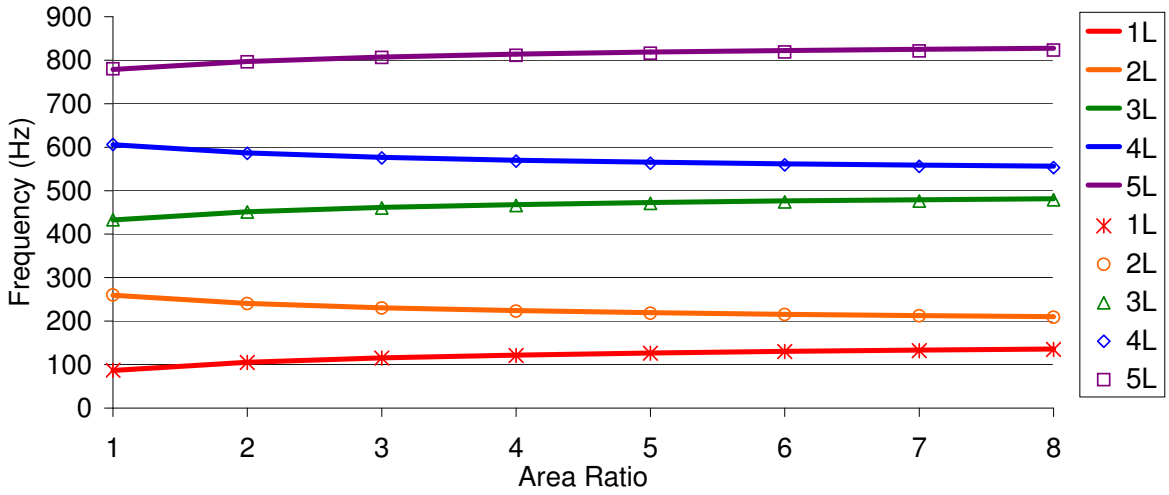

Figure 4.19: Resonant frequencies for first five modes for the area discontinuity case. Solid lines are analytical solutions, symbols are tacFoam solutions.

The comparison between the 1D analytical solution and tacFoam modeshapes is shown in Fig. 4.21. As with the previous case, the modeshapes are taken from a line probe along the centerline of the two-dimensional tacFoam domain. Any transverse variation is not explored.

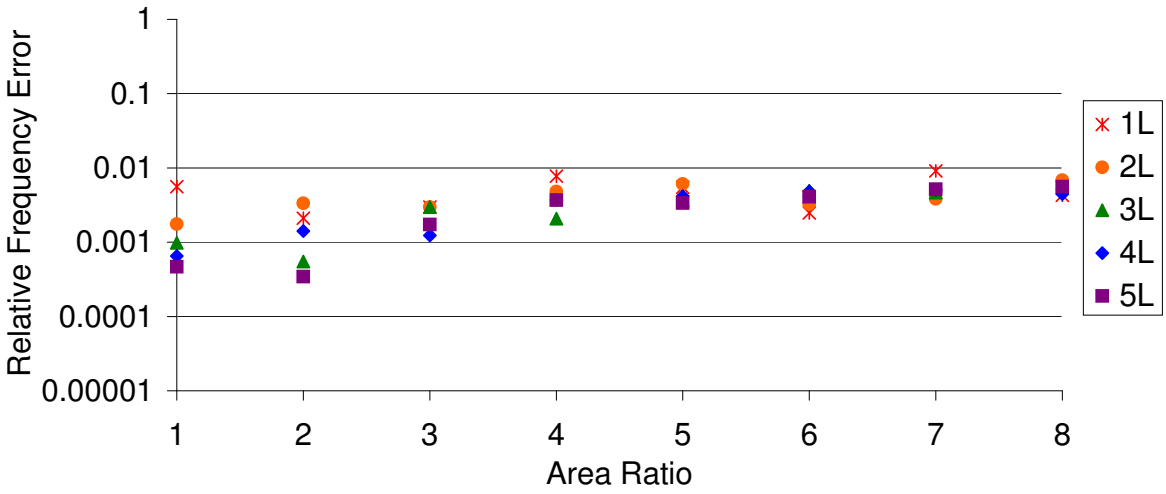

Figure 4.20: Relative frequency errors for first five modes for the area discontinuity case.

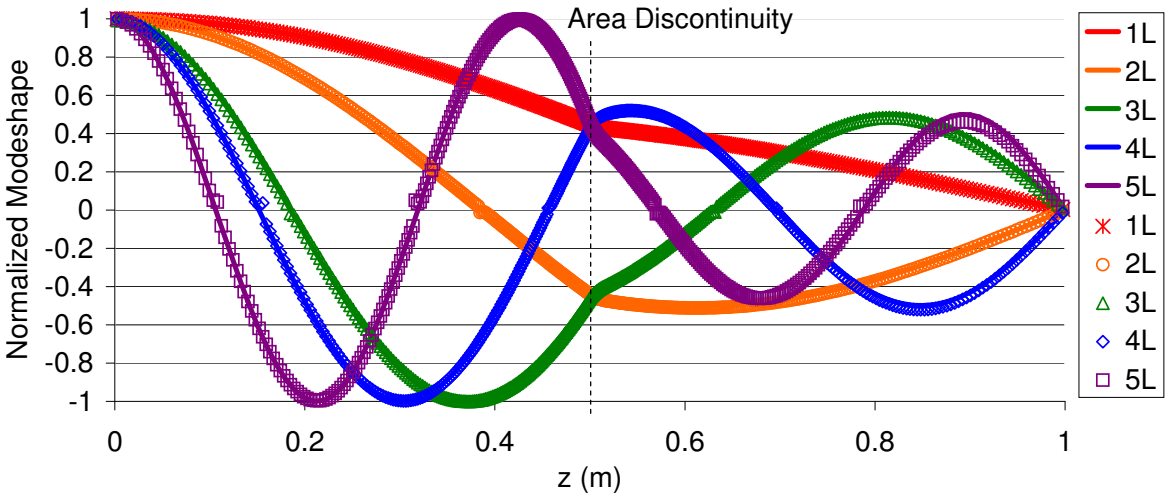

Figure 4.21: Modeshapes for first five modes of the area discontinuity case. Solid lines are analytical solutions, symbols are tacFoam solutions.

4.1.8 Three-Dimensional Acoustics in a Circular Cylinder

All the previous verification cases shown above investigate frequencies and mode-shapes for acoustic propagation in one-dimension. The final two cases show the ability of the solver to reproduce three-dimensional modes. The first example is the circular cylinder, which is solved analytically in Appendix C. The circular cylinder is a good approximation of the shape of a combustion chamber for can-annular engine configurations. The particular circular cylinder chosen for the verification case had a length of one meter, consistent with the previous verification cases. The radius of the circular cross-section was a half meter. The domain and mesh constructed in OpenFOAM using the blockMesh utility is shown in Fig. 4.22. The basic information about the case is tabulated in Table 4.9.

Table 4.9: Reference conditions for circular cylinder verification.

R [J/kg-K]	γ	$\bar{p}$ [kPa]	$\bar{T}$ [K]	Radius [m]	Length [m]	f-Range [Hz]
287	1.40	100	298	0.5	1.0	87-496

The three-dimensional modeshapes are found via separation of variables to be

$$\phi_{mn}(r)\chi_m(\theta)\psi_j(z) \tag{4.19}$$

where the axial component of the modeshape is

$$\psi(z) = A_1 \cos(k_z z) + A_2 \sin(k_z z) \tag{4.20}$$

and the transverse component of the modeshape is

$$\chi_m(\theta)\phi_{m1}(r) = \cos(m\theta)J_m\left(\xi_1^{(m)}\frac{r}{R}\right). \tag{4.21}$$

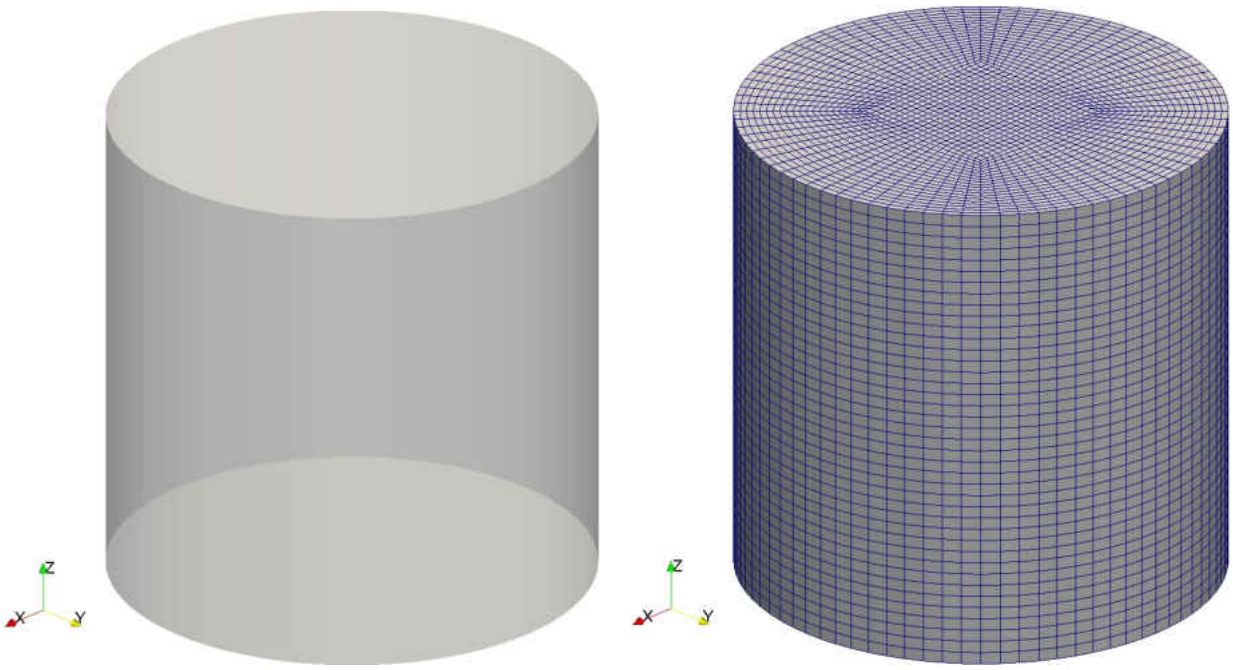

(a) (b)

Figure 4.22: The (a) domain and (b) mesh for circular cylinder verification.

Note, for these modeshapes, the radial boundary has been assumed to be closed, while the axial boundary has been left arbitrary. For more details on this solution, please consult the appropriate section of Appendix C. The resonant frequencies from the analytical solution are

$$\omega_{jmn} = \bar{a}\sqrt{(k_r)_{mn}^2 + (k_z)_j^2} \tag{4.22}$$

where the axial wave number for closed-closed boundary conditions is

$$(k_z)_j = \frac{j\pi}{L} \tag{4.23}$$

or for closed-open boundary conditions is

$$(k_z)_j = \frac{(j-1/2)\pi}{L} \tag{4.24}$$

and the radial wavenumber is

$$(k_r)_{mn} = \frac{\xi_n^{(m)}}{R}. \tag{4.25}$$

Therefore, the frequencies and modeshapes are easily plotted using tabulated roots of the Bessel functions and derivatives. All modes with frequencies under 500 Hz will be evaluated. The resonant frequencies of the tacFoam simulations are given in Fig. 4.23. The solver found all the relevant frequencies for both sets of boundary conditions using white noise initial conditions. It should be noted that some of the amplitudes were larger than others, which led to a large amount of noise in the smaller amplitude modes coming through the signal filtering operations.

The relative error in the simulation frequencies for the closed-closed and closed-open boundary conditions is shown in Fig. 4.24. All frequency errors were below 1% and there is no visible trend with respect to grid resolution. The lack of a trend with resolution highlights the fact that the main source of frequency error was the resolution uncertainty of the FFT. These simulations were run for one second, giving a resolution of 1 Hz, or a resolution uncertainty of 0.5 Hz. This was the dominant source of error in almost all of the verification cases.

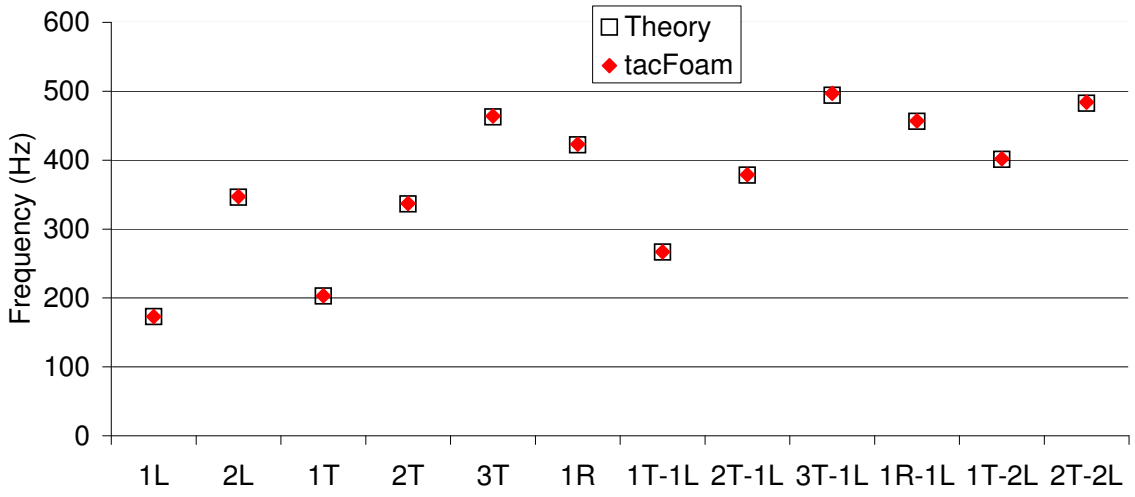

(a)

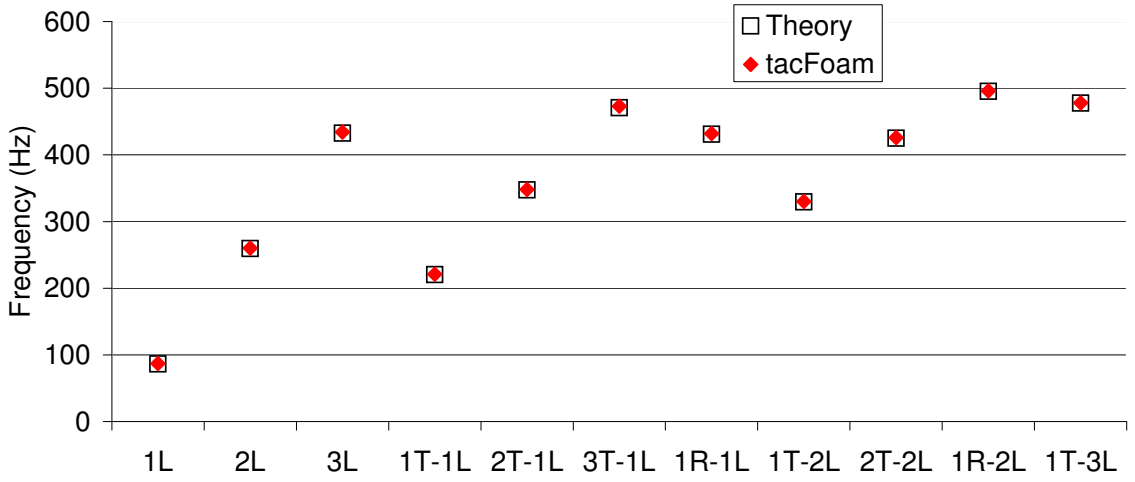

(b)

Figure 4.23: All resonant frequencies under 500 Hz for cylindrical case: (a) closed-closed, (b) closed-open.

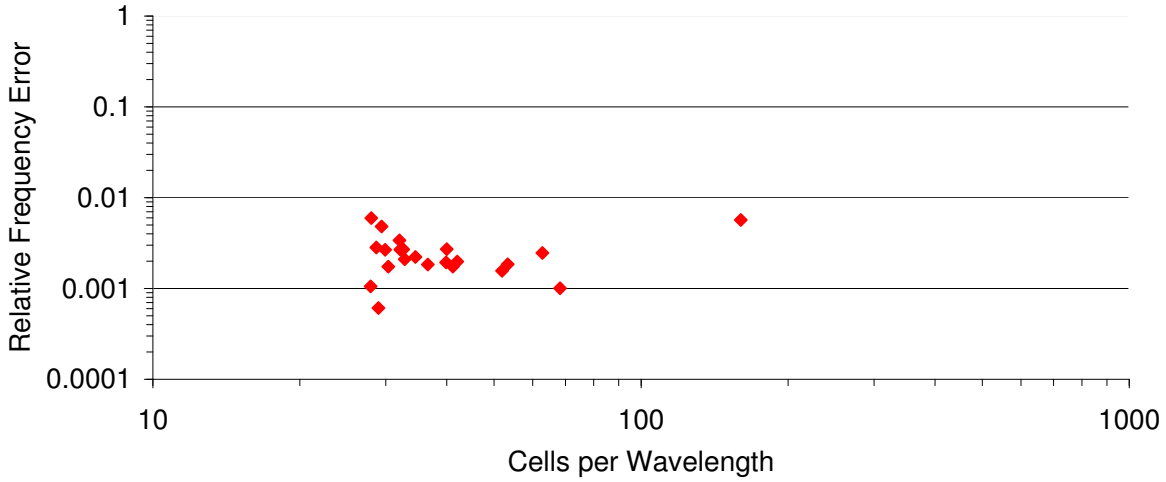

Figure 4.24: Relative error in resonant frequency prediction for the closed-closed and closed-open boundary conditions of the cylindrical verification case.

The next set of figures shows the three-dimensional modeshapes resulting from the cell-by-cell DFT calculation. The first pure axial mode (1L) is shown in Fig. 4.25. The first pure tangential mode is shown in Fig. 4.26. The first pure radial mode (1R) is shown in Fig. 4.27. A combined axial-tangential mode (2L-2T) is shown in Fig. 4.28. A combined axial-radial mode (1L-1R) is shown in Fig. 4.29. These figures are not a comprehensive set of all the modes shown in the Figs. 4.23 and 4.24, but rather a sampling to show the ability of the solver to capture three-dimensional modeshapes. All the other modes, not shown for brevity, were also captured correctly. Due to the randomness of the initial conditions, some modes were not as strong as other modes, hence a higher presence of noise polluted the DFT signal in these weaker mode cases. The DFT magnitudes are not normalized in order that the reader can observe the variation in strength of different modes.

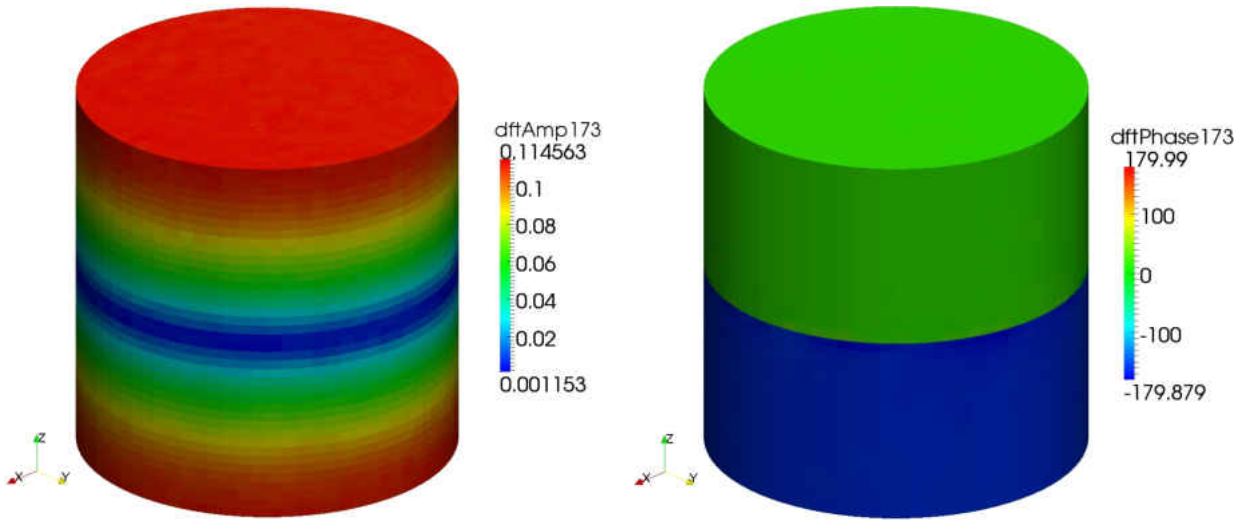

(a) (b)

Figure 4.25: First pure axial mode, 1L, (a) amplitude and (b) phase.

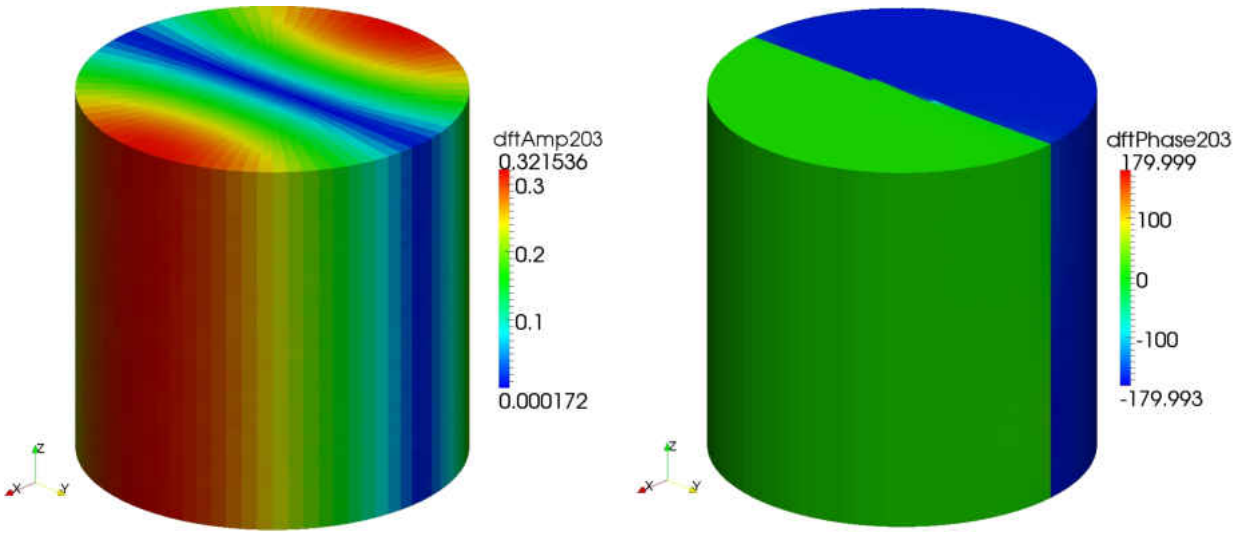

(a) (b)

Figure 4.26: First pure tangential mode, 1T, (a) amplitude and (b) phase.

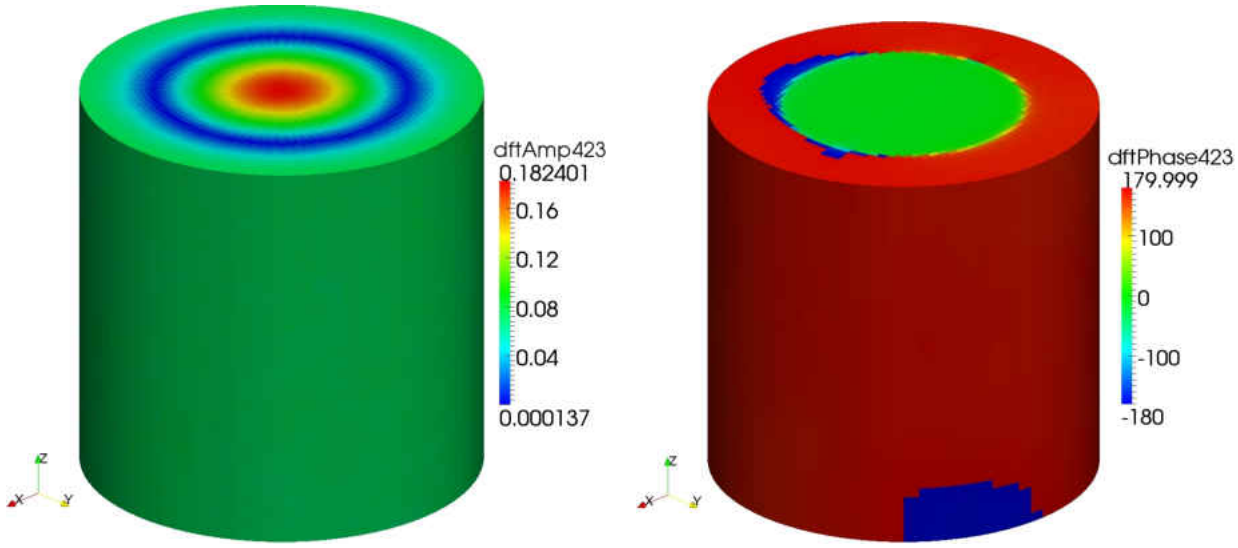

(a) (b)

Figure 4.27: First pure radial mode, 1R, (a) amplitude and (b) phase.

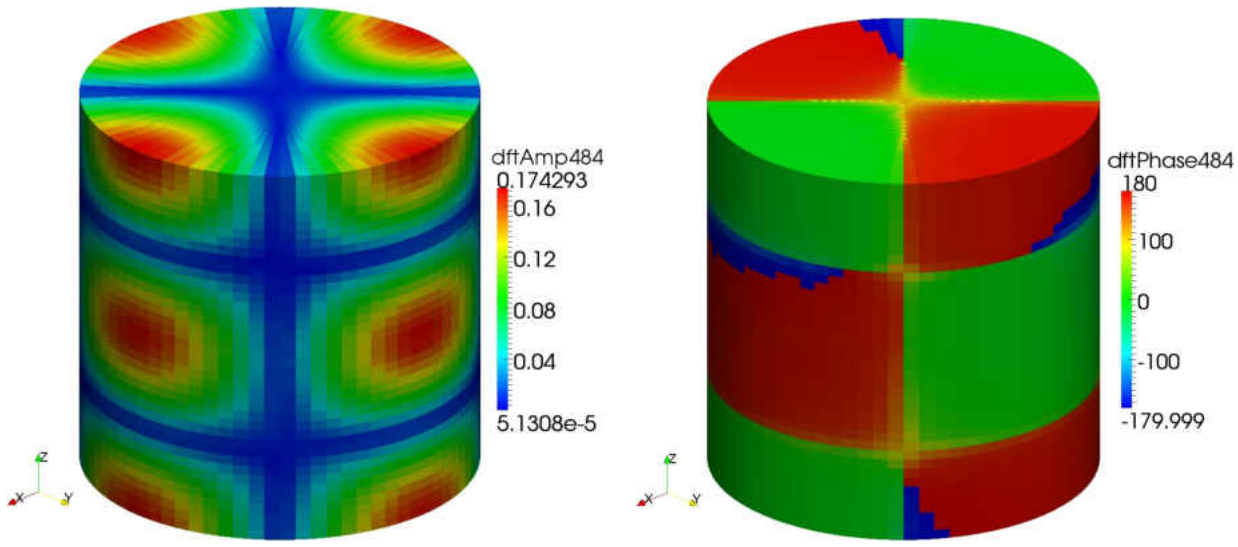

(a) (b)

Figure 4.28: Combined axial-tangential mode, 2L-2T, (a) amplitude and (b) phase.

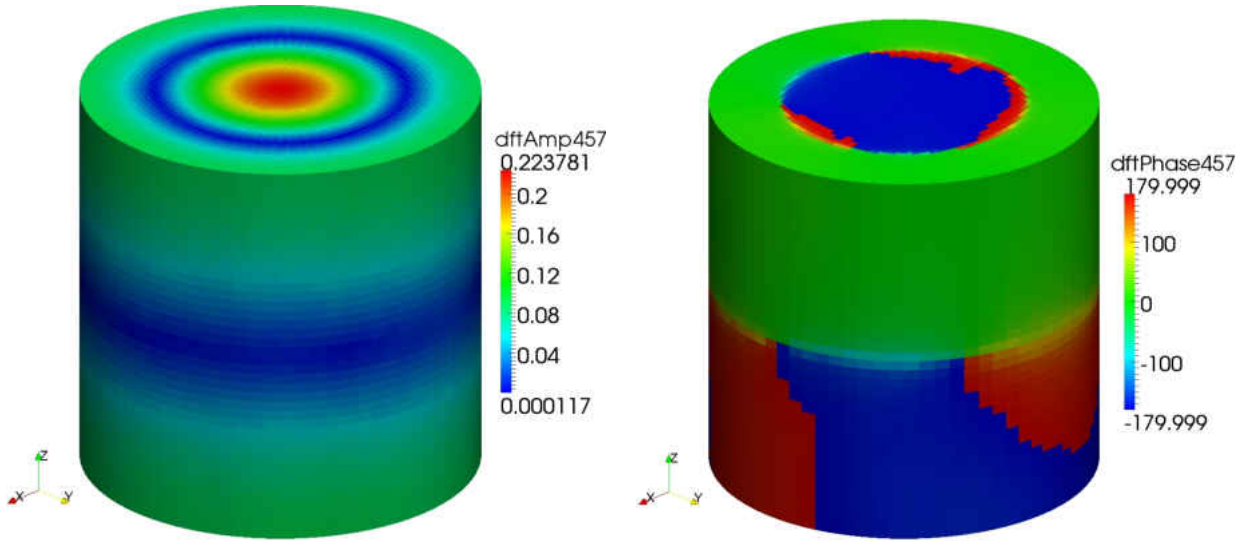

(a) (b)

Figure 4.29: Combined axial-radial mode, 1L-1R, (a) amplitude and (b) phase.

4.1.9 Three Dimensional Acoustics in an Annular Cylinder

Similar to the previous verification case, this case involves three-dimensional mode-shapes in an annular cylinder. This geometry is also very relevant to real engine configurations, as many gas turbine engines use annular combustion configurations. The analytical solution can be found in Appendix C. The particular annular cylinder chosen for the verification case had a length of one meter, consistent with the previous verification cases. The inner radius of the annular cross-section was a quarter meter and the outer radius was three quarters of a meter. The domain and mesh constructed in OpenFOAM using the blockMesh

utility is shown in Fig. 4.30. The basic information about the case is tabulated in Table 4.10.

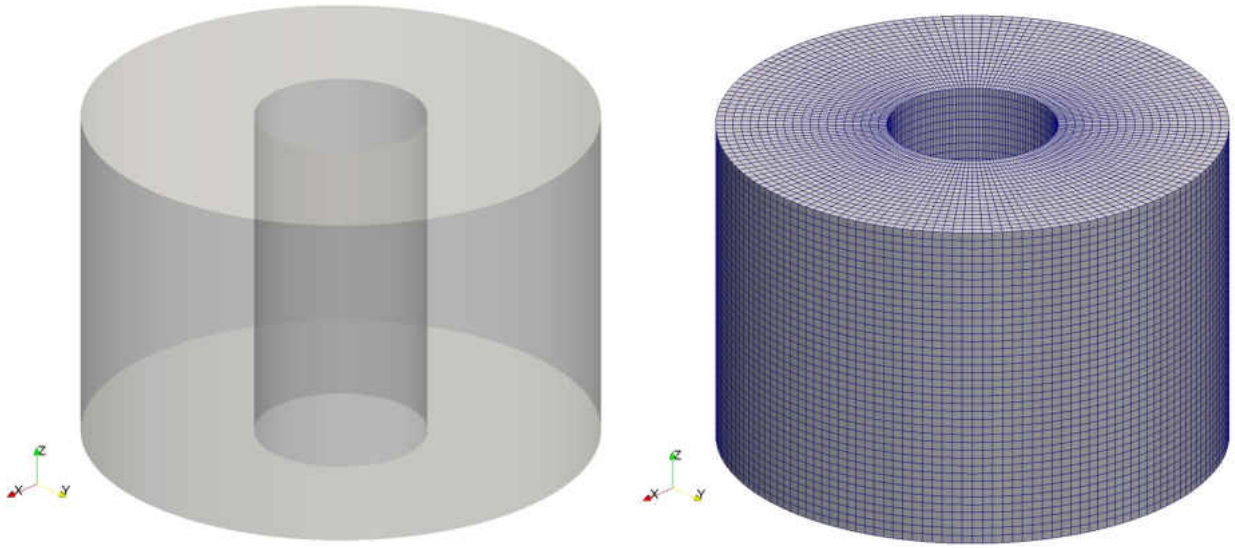

(a) (b)

Figure 4.30: The (a) domain and (b) mesh for annular cylinder verification.

Table 4.10: Reference conditions for annular cylinder verification.

R [J/kg-K]	γ	$\bar{p}$ [kPa]	$\bar{T}$ [K]	Inner/Outer R [m]	Length [m]	f-Range [Hz]
287	1.40	100	298	0.25/0.75	1.0	173-400

The modeshapes are expressed in a similar fashion to the circular cylinder

$$\phi_{mn}(r)\chi_m(\theta)\psi_j(z) \tag{4.26}$$

where the axial component of the modes are unaffected by the change from circular to annular cross-section

$$\psi(z) = A_1 \cos(k_z z) + A_2 \sin(k_z z). \tag{4.27}$$

The circumferential component of the modes is given by

$$\chi_m(\theta) = \cos(m\theta) \tag{4.28}$$

and the radial component is given by

$$\phi_{mn}(r) = Y'_m((k_r)_{mn} R_{inner}) J'_m((k_r)_{mn} r) - J'_m((k_r)_{mn} R_{inner}) Y'_m((k_r)_{mn} r). \tag{4.29}$$

The frequency for any given combination

$$\omega_{jmn} = \bar{a} \sqrt{(k_r)^2_{mn} + (k_z)^2_j} \tag{4.30}$$

where the axial wave number is found the same as before and the radial wave number is found by solving

$$J_1(k_r R_{outer}) Y_1(k_r R_{inner}) - J_1(k_r R_{inner}) Y_1(k_r R_{outer}) = 0. \tag{4.31}$$

As with the circular cylinder, closed boundaries have been assumed at the radial boundaries. Only the closed-closed boundary conditions is used for the annular geometry. All frequencies under 400 Hz are analyzed. The frequencies for all such modes are shown in Fig. 4.31. Once again, the simulation produces peaks in the FFT at all frequencies corresponding to resonant frequencies. The relative error of these frequencies is shown in Fig. 4.32. The errors remain well below 1% and once again are dominated by the resolution of the FFT in

the frequency domain, which is 1 Hz as before. The dominance of the frequency resolution error is manifest in the lack of trends for frequency error versus cells per wavelength.

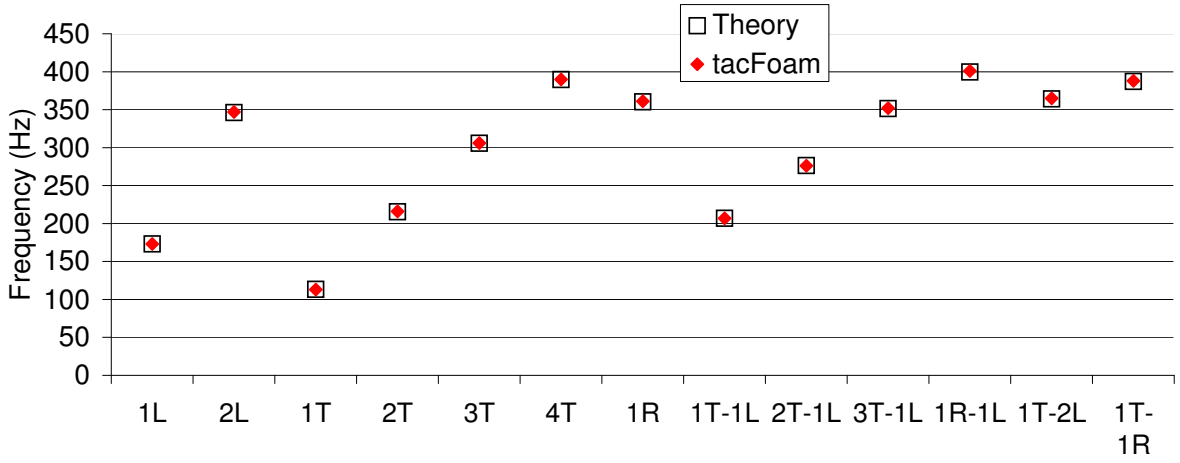

Figure 4.31: Relative error in resonant frequency prediction for the closed-closed and closed-open boundary conditions of the annular verification case.

As with the circular cylinder, a cell-by-cell calculation of the DFT is performed, resulting in three-dimensional modehshapes. The 1L, 1T, and 1R modes are shown in shown in Fig. 4.33, 4.34, and 4.35, respectively. Combined modes are also resolved. The 1L-3T mode is shown in Fig. 4.36 and the 1T-1R is shown in Fig. 4.37. These figures are not comprehensive for all modes shown in the Figs. 4.31 and 4.32, but rather provide a sample of a few modes to demonstrate the ability of the solver to capture three-dimensional modeshapes. As with the circular cylinder, the DFT magnitudes are not normalized in order that the reader can observe the variation in strength of different modes. The various strengths are indicative of the white noise initial conditions used to trigger all modes.

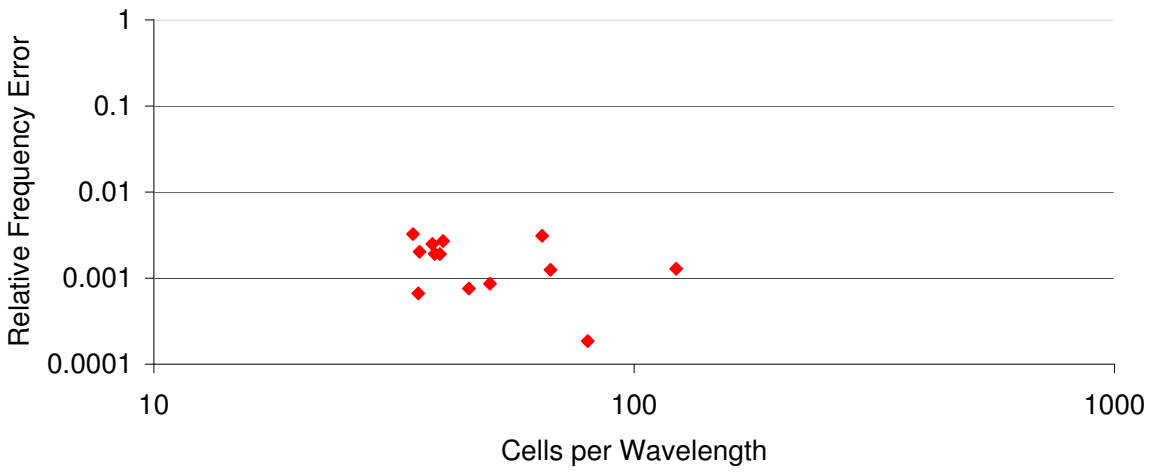

Figure 4.32: Relative error in resonant frequency prediction for the closed-closed and closed-open boundary conditions of the annular verification case.

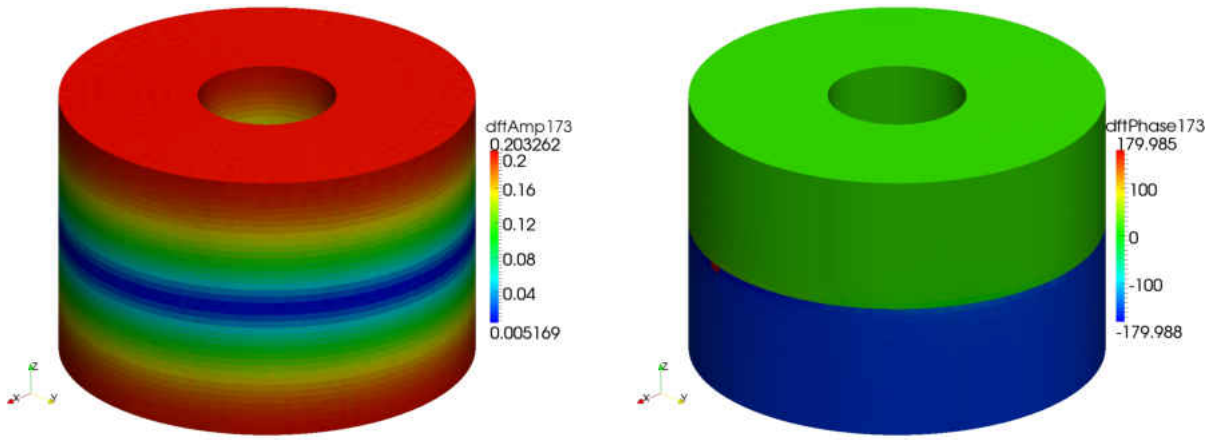

(a) (b)

Figure 4.33: First pure axial mode, 1L, (a) amplitude and (b) phase.

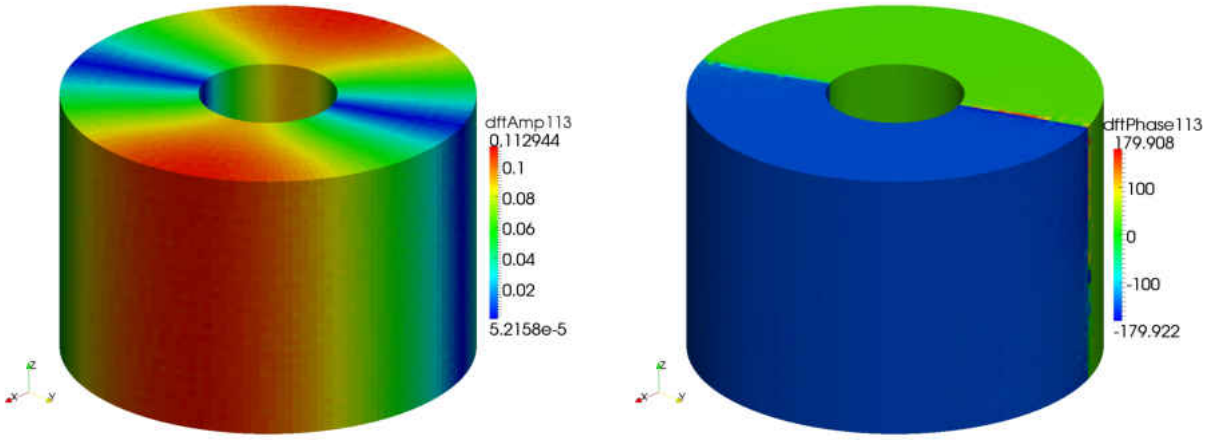

(a) (b)

Figure 4.34: First pure tangential mode, 1T, (a) amplitude and (b) phase.

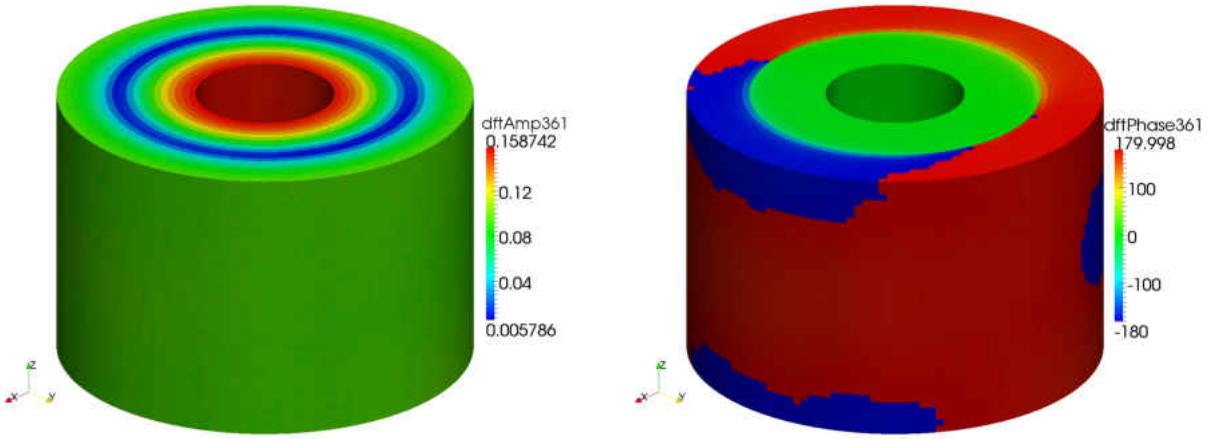

(a) (b)

Figure 4.35: First pure radial mode, 1R, (a) amplitude and (b) phase.

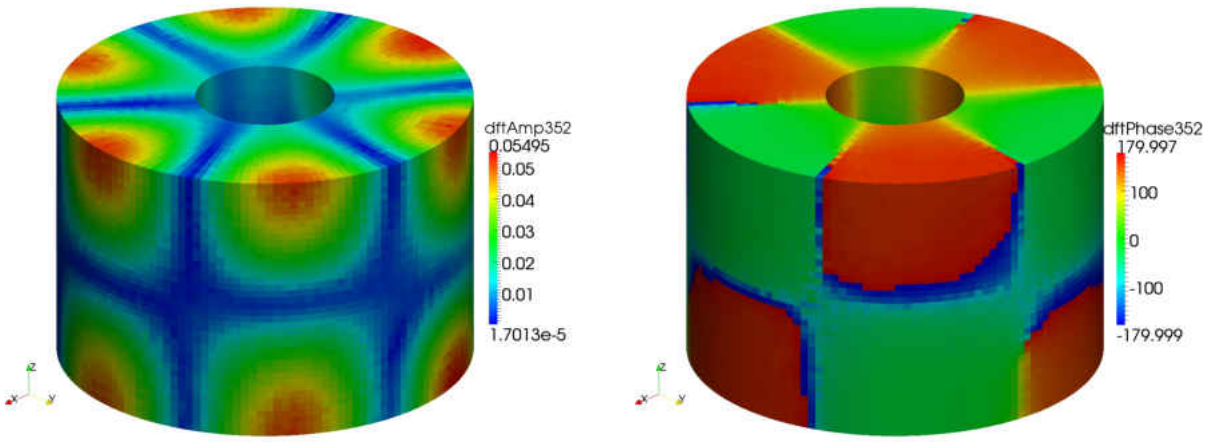

(a) (b)

Figure 4.36: Combined axial-tangential mode, 1L-3T, (a) amplitude and (b) phase.

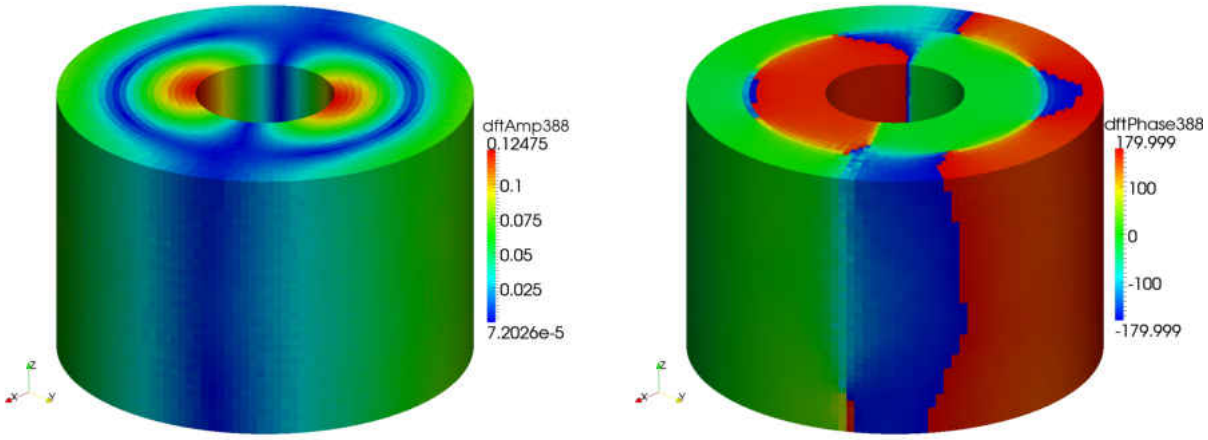

(a) (b)

Figure 4.37: Combined radial-tangential mode, 1T-1R, (a) amplitude and (b) phase.

For the geometry shown, the focus was kept on modes in the hundreds of Hertz. Higher frequency modes can be captured in a similar way to the verification cases above, provided that the proper grid resolution is supplied and the time step provides a low Courant number for stability. This may increase the computational cost for tangential and radial modes in higher aspect ratio geometries due to the difference in time scale between the longitudinal and transverse frequencies.

4.2 Boundary Conditions Verification

Common acoustic boundary conditions include closed, open, and choked. These acoustic boundary conditions can be generalized to specifying the acosutic impedance at the boundary. The acoustic impedance is defined as the ratio of the acoustic pressure to the acoustic velocity normal to the boundary

$$Z(\omega) = \frac{\hat{p}}{\bar{\rho}\bar{a}\hat{u}_n} \tag{4.32}$$

where

$$\hat{p} \sim \exp(i\omega t) \tag{4.33}$$

$$\hat{u} \sim \exp(i\omega t). \tag{4.34}$$

A closed boundary ($\hat{u}_n = 0$) represents the limit as $Z \to \infty$ while an open boundary represents the limit as $Z \to 0$. A choked boundary is in between these limits, the specific value depending on the Mach number of the mean flow in the chamber. These three simple

boundary conditions have real values of impedance that are independent of frequency. In general, the impedance of an arbitrary boundary is a complex quantity, with both magnitude and phase being a function of frequency.

Two different boundary conditions are developed for the tacFoam solver. The first boundary condition, designed for real impedances only, uses the mixed value boundary condition from OpenFOAM with a value fraction tuned to give the appropriate reflection coefficient for a given impedance. The second boundary condition applies a piecewise constant approximation for calculating the convolution integral. The numerical details of the boundary conditions are given in Appendix E.

For this test, rather than follow the procedure used for previous tests, a procedure for determining the reflection coefficient of the boundary is used. One boundary is forced with an overlay of sinusoidal signals with random phase. The other boundary is given the arbitrary real, constant impedance. Two pressure probes at designated locations capture pressure signals. The two-microphone method [45] is used to measure the reflection coefficient of the boundary. The reflection coefficient from the two-microphone method is calculated by

$$R(\omega) = \frac{H_{21} - \exp(-iks)}{\exp(iks) - H_{21}} \exp(i2kL) \tag{4.35}$$

where $k = \omega/\bar{a}$ is the wavenumber, s is the distance between the microphones, L is the distance from the boundary to the midpoint between the two microphones and H_{21} is the transfer function between the two signals given by

$$H_{21} = \frac{p_2}{p_1} \tag{4.36}$$

The subscript $_2$ denotes the microphone closer to the boundary of interest and the subscript $_1$ denotes the microphone further away. The value calculated from Eq. (4.35) is compared with the analytical value of the reflection coefficient, given by

$$R = \frac{Z - 1}{Z + 1} \tag{4.37}$$

4.2.1 Real Constant Impedance

The first test is of the boundary condition written to handle real impedance (no imaginary component) that is constant over all frequencies.

4.2.1.1 1D Acoustic Boundary

A one-dimensional domain, the same as used in previous tests, is initialized to zero. The reference conditions for this verification case are provided in Table 4.11.

Table 4.11: Reference conditions for mean flow temperature jump verification.

R [J/kg-K]	γ	$\bar{p}$ [kPa]	$\bar{T}$ [K]	Z	f-Range (Hz)
287	1.40	100	298	0-∞	10-1000

Over the entire frequency range forced by the opposite boundary condition, the reflection coefficient was found to be constant, as specified. An example is shown in Fig. 4.38 where the impedance of the boundary was set at $Z = 3$, so a reflection coefficient of $R = 0.5$

was expected, per Eq. (4.37). Some minor noise was seen in the data, which is attributed to the signal processing. Also, a minor shift in phase ($< 5^o$) is noticed at high frequencies, which can be attributed to the zeroth order interpolation done by the numerical probes (slight discrepancy in the distance separating the probes from the boundary).

The impedance set at the boundary was adjusted from 0 to ∞. An impedance of zero corresponds to the fully-reflective ($R = -1$) open boundary condition. The other limit, $Z \to \infty$, corresponds to the fully reflective ($R = 1$) closed boundary. These two limits were check and verified with error below 0.1% for the one-dimensional case. Intermediate impedances were also simulated, and the average reflection coefficient over all frequencies for each impedance is plotted against the expected relationship, Eq. (4.37). The reflection coefficient for this plot was calculated from the average magnitude, $|Z|$, and average phase, $\angle Z$, by

$$Z = |Z| \cos(\angle Z) \tag{4.38}$$

The relative error of impedance for this plot was less than 0.6% for all calculations.

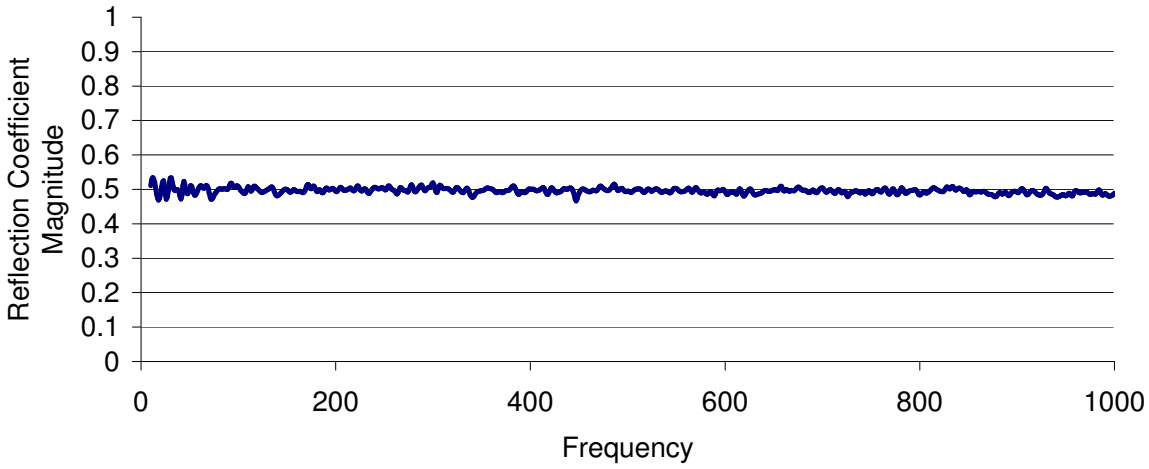

(a)

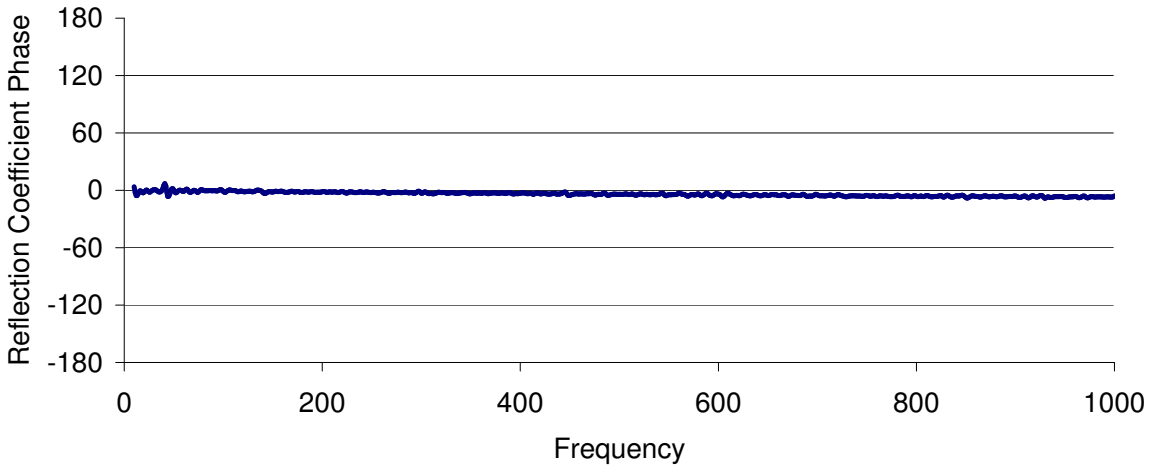

(b)

Figure 4.38: As a function of frequency for $Z = 3$, the reflection coefficient (a) magnitude and (b) phase.

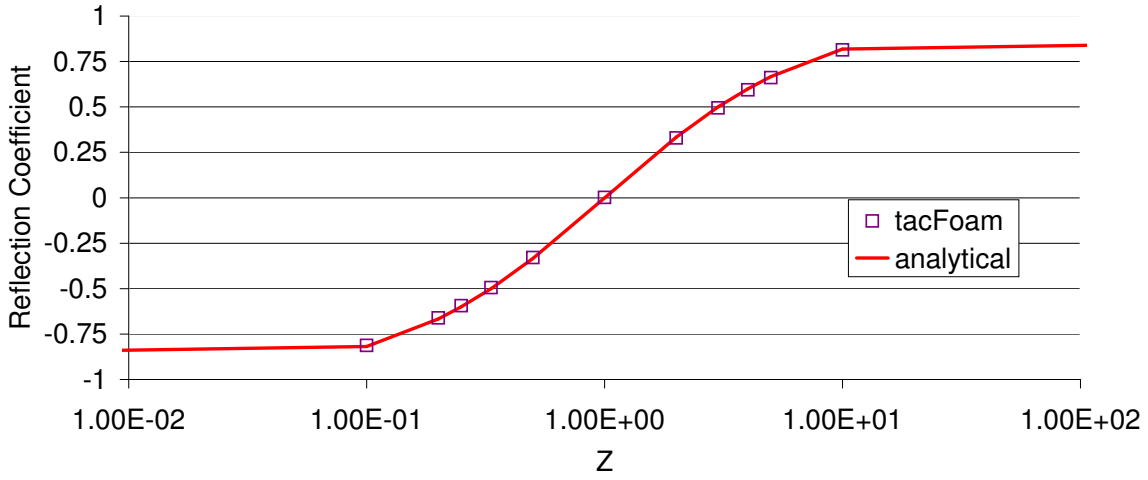

Figure 4.39: Average reflection coefficients as a function of impedance for the 1D case.

4.2.1.2 3D Acoustic Boundary

The one-dimensional real impedance test showed that the implementation gave excellent results. The same test was also preformed in three-dimensions using the three dimensional circular cylinder from section 4.1.8. Additionally, the test was performed on a similar geometry that was square rather than circular in cross-section. Figure 4.40 shows that excellent agreement was again achieved for these tests. There is almost no difference between the circular and square cross-section results, indicating that the application of this boundary condition has low sensitivity to the geometrical shape.

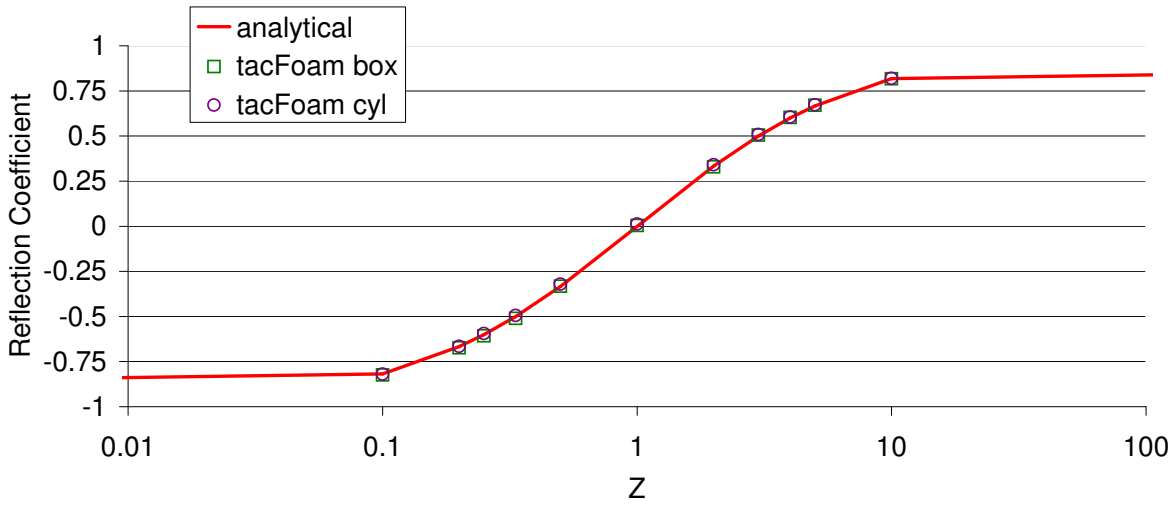

Figure 4.40: Reflection coefficients as a function of impedance for the 3D cylinder and square cases.

4.2.2 Complex Impedance as a Function of Frequency

A curve fitting procedure for the magnitude and phase of complex impedance boundary conditions is shown in Appendix E. Three example curve fits with input values for tacFoam's complex impedance boundary conditions are given. Preliminary results of this boundary condition in terms of complex reflection coefficient are now shown. The reflection coefficient is determined by the two-microphone method using a one-dimensional grid as shown above for the real impedance boundary condition.

4.2.2.1 Real Pole

The reflection coefficient magnitude and phase of a complex impedance boundary with only a single real pole is shown in Fig. 4.41 compared to the analytical value. Magnitude and phase are matched in the low frequency limit, but at relevant frequencies, the changes magnitude and phase with increasing frequency are under-predicted.

4.2.2.2 Complex Conjugate Poles

The reflection coefficient magnitude and phase of a complex impedance boundary with only a single pair of complex conjugate poles is shown in Fig. 4.42 compared to the analytical value. Magnitude and phase are matched in the low frequency limit, but at relevant frequencies, the changes magnitude and phase with increasing frequency are under-predicted.

4.2.2.3 Real Pole and Complex Conjugate Poles

The reflection coefficient magnitude and phase of a complex impedance boundary with both a real pole and a pair of complex conjugate poles is shown in Fig. 4.43 compared to the analytical value. Magnitude and phase are matched in the low frequency limit, but at relevant frequencies, the changes magnitude and phase with increasing frequency are under-predicted.

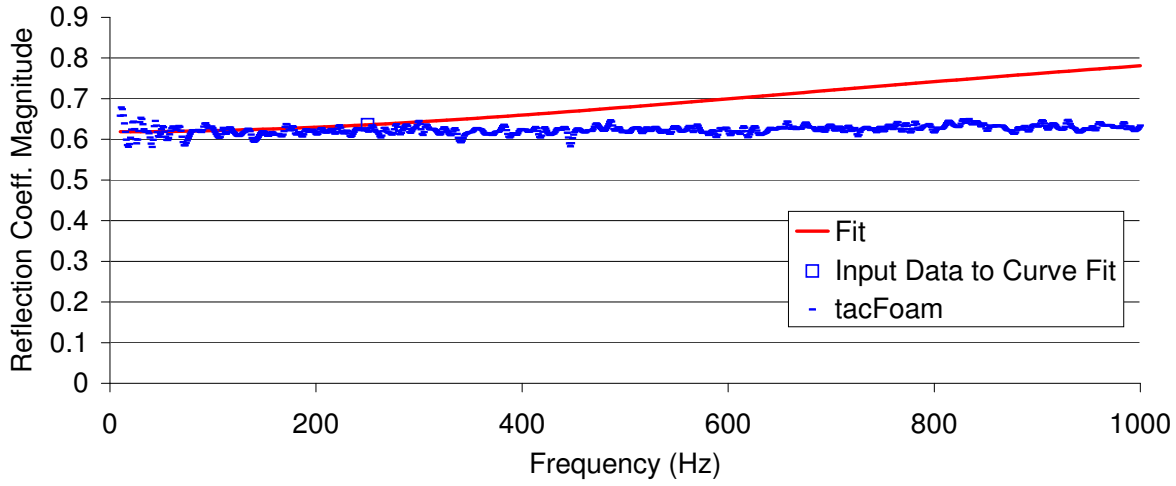

(a)

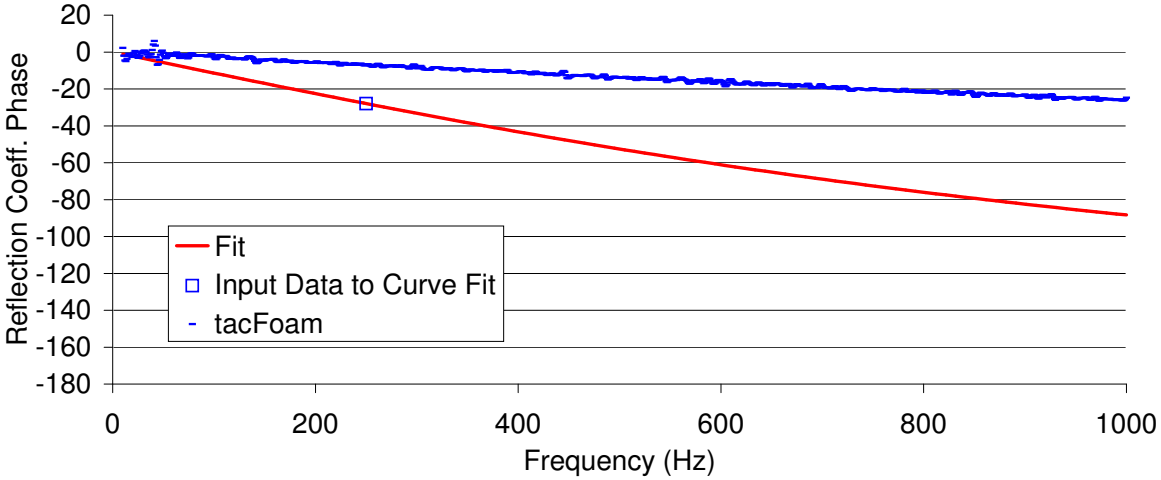

(b)

Figure 4.41: Curve fits for complex impedance example with a single real pole.

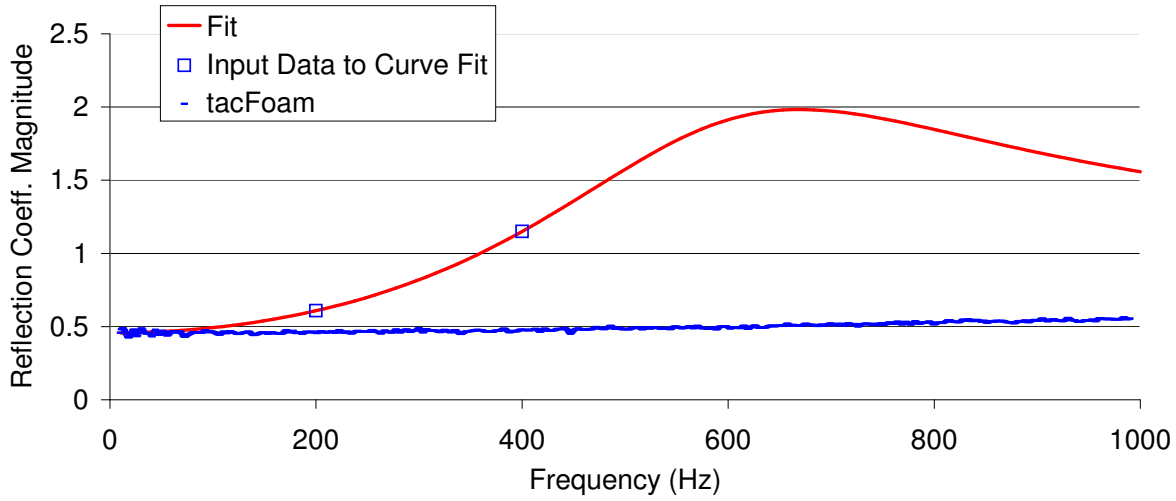

(a)

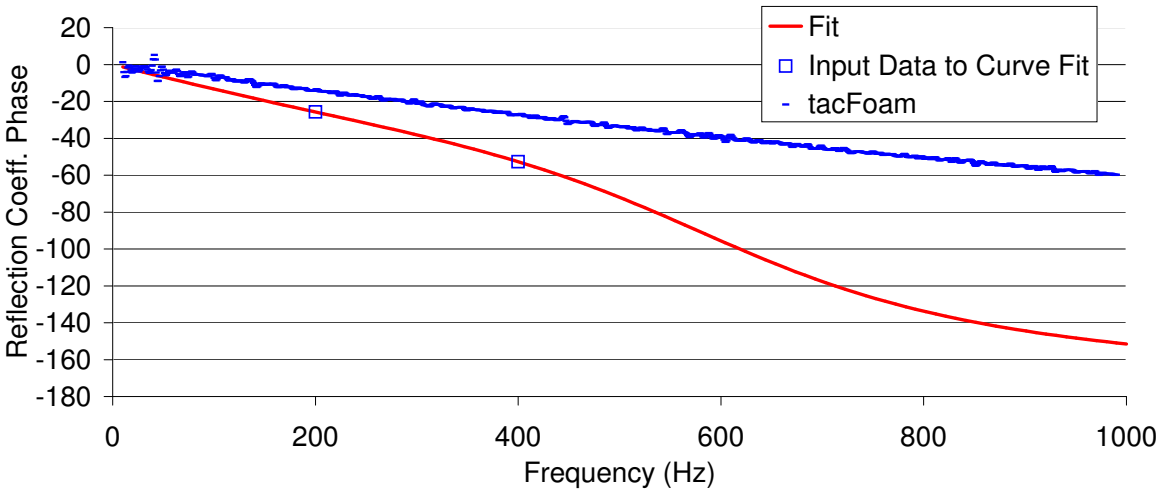

(b)

Figure 4.42: Curve fits for complex impedance example with a single pair of complex conjugate poles.

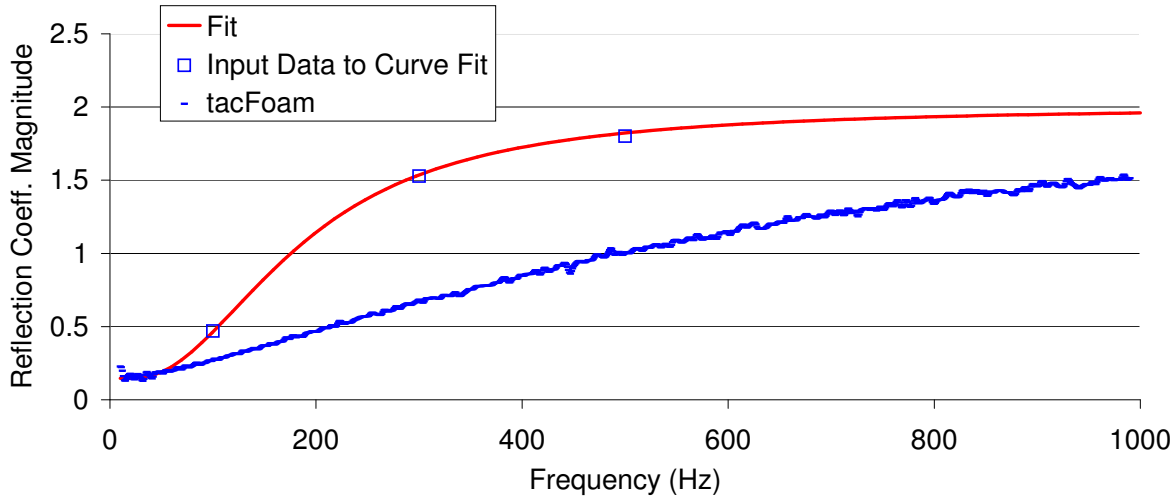

(a)

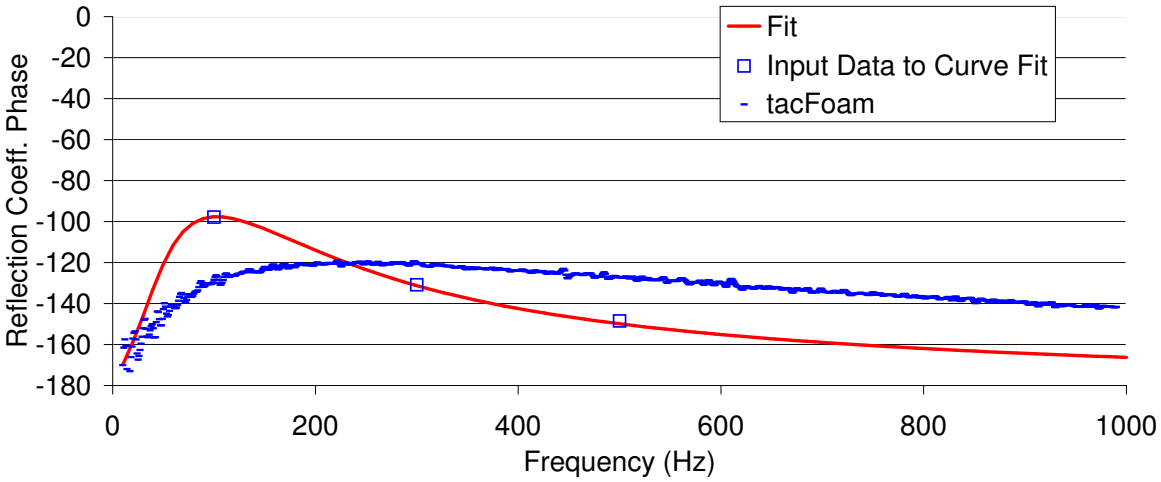

(b)

Figure 4.43: Curve fits for complex impedance example with a real pole and a pair complex conjugate poles.

4.3 Thermoacoustic Verification

The vital verification that needs to be addressed in this work is that of the unsteady heat release models. For these verification cases, the $n - \tau$ family of heat release models are used. This family of models is based on the time lag theory proposed by [46] and used heavily since then in describing combustion instability mechanisms [8]. These cases used the conditions from the $TR = 8$ temperature jump case, which represent an extreme operating condition. The flame is located over two cells ($0.01m$ long), where the mean heat release is placed and the density drops from the reactant density to the product density. Key parameters for these cases are listed in Table 4.12. The solutions by which the solvers results were benchmarked are found using the method described in Appendix C, which is similar to that described by Dowling [24].

Table 4.12: Reference conditions for uniform mean flow verification.

R [J/kg-K]	γ	$\bar{p}$ [kPa]	$\bar{T}$ [K]	TR	$\bar{Q}$ $[W/m^2]$	$\bar{q}$ $[W/m^3]$	f-Range [Hz]
287	1.40	100	298	8.0	2.45e6	2.45e8	152-1183

4.3.1 Rijke Tube: Pressure Mechanism

The first heat release model is based on a relationship between the acoustic pressure oscillations and the heat release oscillations. Mathematically, the pressure mechanism can

be written as

$$q'(x,t) = n(x)\frac{\bar{q}}{\bar{p}}p'_{sender}(t-\tau) \tag{4.39}$$

where p'_{sender} denotes the acoustic pressure at the location where the mechanism is caused and the $n(x)$ is the gain distribution which identifies the region where the mechanism for unsteady heat release takes effect. For this case, the sender region is the flame region itself. The gain is set to unity in the flame region and zero outside the flame region. The frequency shifts caused by this mechanism, given that it is a weak mechanism, are very small and typically on the order of magnitude of the frequency resolution of the FFT ($1Hz$). Therefore, the useful comparisons of tacFoam with theory are in terms of growth rate.

The results from the baseline simulation are shown in Fig. 4.44. At zero time lag, the pressure and heat release fluctuations are in phase, leading to maximum growth rate. For each mode, depending on the frequency of the mode, as the time lag increases, the pressure slowly moves out of phase and the growth rate reaches a minimum with the heat release when the time lag is one half of the period. When the time lag reaches a full period, the heat release and pressure are once again in phase and the growth rate reaches another maximum. Hence, the growth rate for each mode displays a sinusoidal patter with respect to time lag, with the period of the sinusoid equal to the period of the mode.

The modes are plotted in two different graphs to indicate an important dichotomy. Figure 4.44, shows the first three modes. These modes are such that, at the given resolution, the numerical damping coefficient measured by a $q' = 0$ simulation is order of magnitudes

less than the growth rates shown in the figure

$$|\alpha_{numerical}| << |\alpha_{q'}|. \tag{4.40}$$

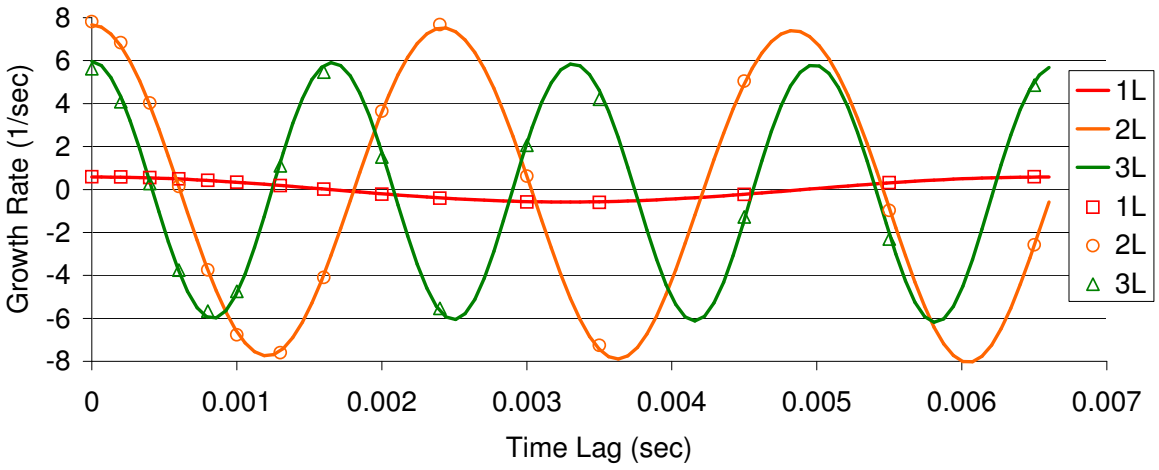

Figure 4.44: Growth rates for the first three modes in the Rijke tube verification case. Solid lines are analytical solution and symbols are the tacFoam solution.

The simulation predicts the stability map very accurately, with growth rate errors less than 5% for these first three modes. The inequality shown in Eq. (4.40) is vital for this accurate prediction, as will be demonstrated in a later section.

4.3.2 Rijke Tube: Velocity Mechanism

The other heat release model tested here is based on a relationship between the acoustic velocity oscillations and the heat release oscillations. Mathematically, the velocity

mechanism can be written as

$$q'(x,t) = n(x)\frac{\bar{q}}{\bar{a}}u'_{sender}(t-\tau) \tag{4.41}$$

where u'_{sender} denotes the acoustic velocity at the location where the mechanism is caused and the $n(x)$ is the gain distribution which identifies the region where the mechanism for unsteady heat release takes effect. For this case, the sender region is set to the region just prior to the flame, to conform as closely as possible to the model in the theoretical development. Across the flame, with non-zero unsteady heat release, there is a jump in acoustic velocity. Therefore, since the pre-flame acoustic velocity is desired for the model, the sender region and flame region must not overlap. The gain is set to unity in the flame region and zero outside the flame region. As for the pressure mechanism, comparisons of tacFoam with theory are in terms of growth rate due to the weak mechanism. The results from the baseline simulation are shown in Fig. 4.45.

At zero time lag, the velocity and heat release fluctuations are in phase. For slightly perturbed acoustic waves, the velocity and pressure are 90^o, which means that the pressure and heat release are 90^o out of phase. This makes the zero time lag case marginally stable, i.e. the growth rate is zero. For each mode, depending on the frequency of the mode, as the time lag increases, the phase between the pressure and heat release slowly changes in the same sinusoidal manner as in the pressure mechanism case above. Hence, the growth rate for each mode also displays a sinusoidal patter with respect to time lag, with the period of the sinusoid equal to the period of the mode. The errors are again small due to the negligibility of numerical damping with respect to the growth rate from the heat release mechanism.

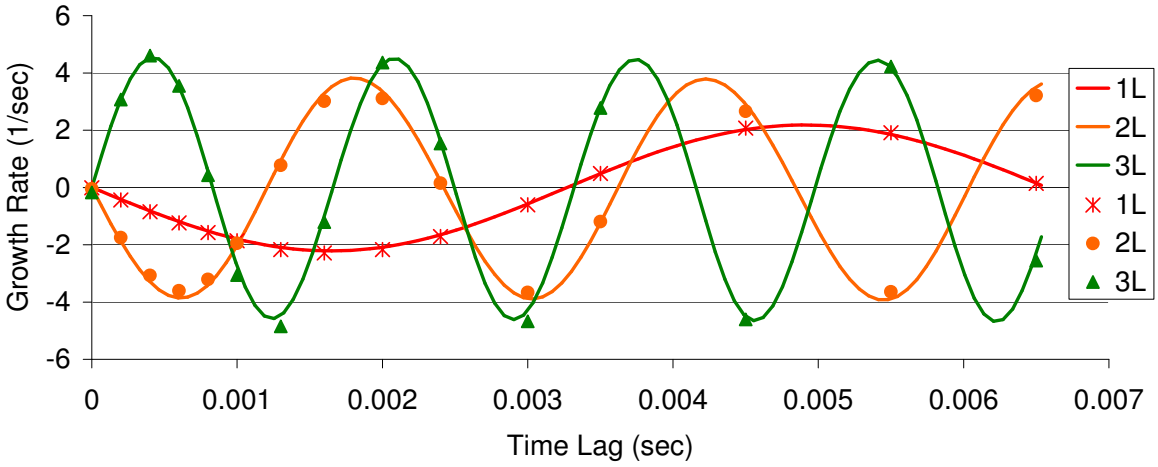

Figure 4.45: Growth rates for the first three modes in the velocity mechanism Rijke tube verification case. Solid lines are analytical solution and symbols are the tacFoam solution.

4.4 Numerical Damping

Since the tacFoam solver applies TVD limiters to the second order flux calculation in which solution variables are extrapolated from cell centers to faces, numerical diffusion is introduced in the effort to maintain solution stability and limit overshoot [41, 40]. Such numerical diffusion damps existing acoustic waves in a tacFoam solution, which can pollute the numerical estimation of growth rates. One of the main target capabilities of tacFoam is the prediction of linear growth rates for combustor geometries. In order to ensure the suitability of tacFoam for that task, it is vital to understand its numerical damping behavior.

Placing a probe in the domain and extracting time series data from the simulation as before, the results gave a damped oscillation. By extracting the extrema and curve fitting with an exponential curve fit, the growth rate α of the oscillations can be found, where

$$p' \sim \exp(\alpha t). \tag{4.42}$$

The numerical damping rate is given by $-\alpha$ and quantifies the amount of numerical damping present in the simulation. The spatial and temporal resolution of the mode is important in determining the numerical damping in a given simulation for a given mode. The spatial resolution of a given mode is best quantified by measuring the number of cells within a wavelength of oscillation. This can be calculated locally as

$$\textit{cells per wavelength} = \frac{\lambda}{\Delta z} = \frac{\bar{a}}{f\Delta z} \tag{4.43}$$

where λ is the wavelength given by $\bar{a}/f$ and Δz is the length of the cell in the direction of the wave vector.

The temporal resolution can likewise be measured quantitatively by the number of time steps in one period of oscillation, or

$$\textit{time steps per period} = \frac{T}{\Delta t} = \frac{1}{f\Delta t} \tag{4.44}$$

where T is the period of oscillation, f is the frequency in Hertz and Δt is the time step of the simulation. The dimensionless number most often associated with numerical simulations of fluids is the Courant number, which is contructed by dividing Eq. (4.43) by Eq. (4.44). This results in

$$Co = \frac{\bar{a}\Delta t}{\Delta z}. \tag{4.45}$$

Note that in the presence of mean flow, a better metric for spatial resolution is given by

$$cells\ per\ wavelength = \frac{\bar{u} + \bar{a}}{f\Delta z} \tag{4.46}$$

which gives a Courant number of

$$Co = \frac{(\bar{u} + \bar{a})\Delta t}{\Delta z}. \tag{4.47}$$

For this thesis, the cells per wavelength and Courant number will be used to report dimensionless spatial and temporal resolution (noting that the actual temporal resolution is best represented by the product of the cells per wavelength and the Courant number).

4.4.1 1D Uniform Duct

To begin the exploration of numerical damping, the uniform duct from section 4.1.1 is excellent. Instead of exciting the simulation with white noise, the initial conditions are carefully prescribed using sine or cosine waves to be one of the modeshapes of the duct. In this case, the second mode was chosen and the velocity was initialized with the corresponding modeshape (derivative of the pressure modeshape). With closed-open boundaries (differentiating Eq. (4.3) and normalizing, with $n = 2$), the velocity initial conditions were

$$w'(z, 0) = w_0 \sin(1.5\pi z/L) \tag{4.48}$$

where the frequency and numerical damping rate of the solver should be insensitive to the wave magnitude w_0. For this case, the length of the duct was $L = 1m$ and the initial

magnitude of the velocity mode was $w_0 = 0.25m/s$, which for the given conditions (Table 4.2) gave a pressure fluctuation magnitude of around $100Pa$.

For the simple duct verification case at hand, the effect of spatial and temporal resolution on damping coefficient is given in Fig. 4.46. First, the temporal resolution has little to no effect on the damping in comparison with the spatial resolution. The exception to this rule is at Courant numbers close to 2, where the numerical damping is elevated.

Notice that a special procedure was used for initialization for the first numerical damping test. Because for a given complex geometry, the modeshapes will not be known a-priori, the numerical damping should be determined from a simulation starting with a more generic initial condition (e.g. white noise) than the precise modeshape. In this way, the numerical damping for all modes can be determined from a single simulation within the strategy outlined in Fig. 3.3. A bandpass filter with bandwidth of 5 Hz was used to filter the pressure signal at the frequencies of each of the first five resonant modes. The same exponential curve fitting procedure was then used to calculate a growth rate for each of the modes. The results are plotted against the previous "2L mode only" simulation in Fig. 4.47.

There are two important consequences stemming from this figure. First, notice that for 133 cells per wavelength, the closed-open 2L modes matches numerical damping coefficient regardless of the initialization method and whether filtering of the signal needs to be applied. This validates the bandpass filtering approach to acquiring numerical damping coefficients. Secondly, the rest of the data is not completely colinear.

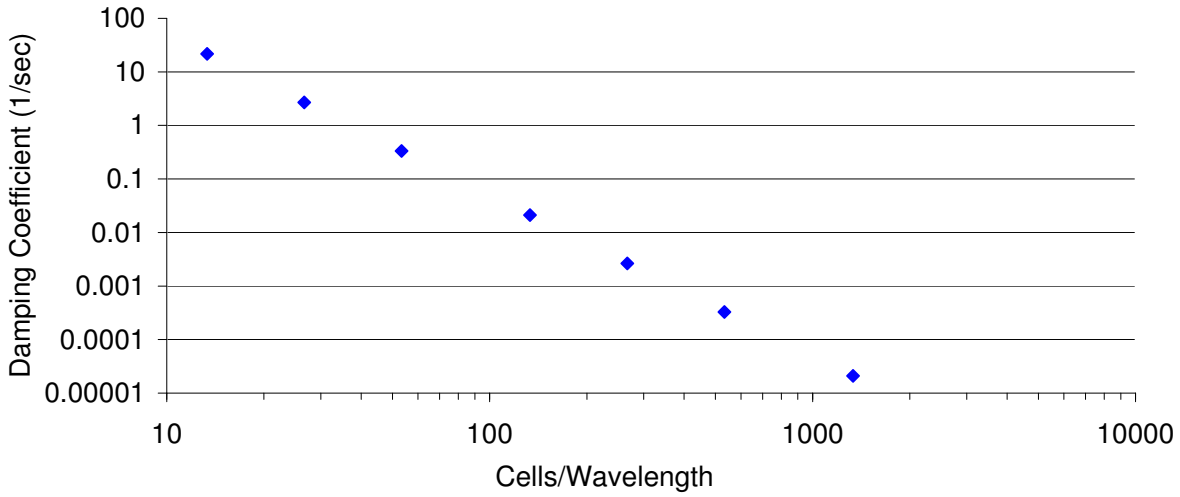

(a)

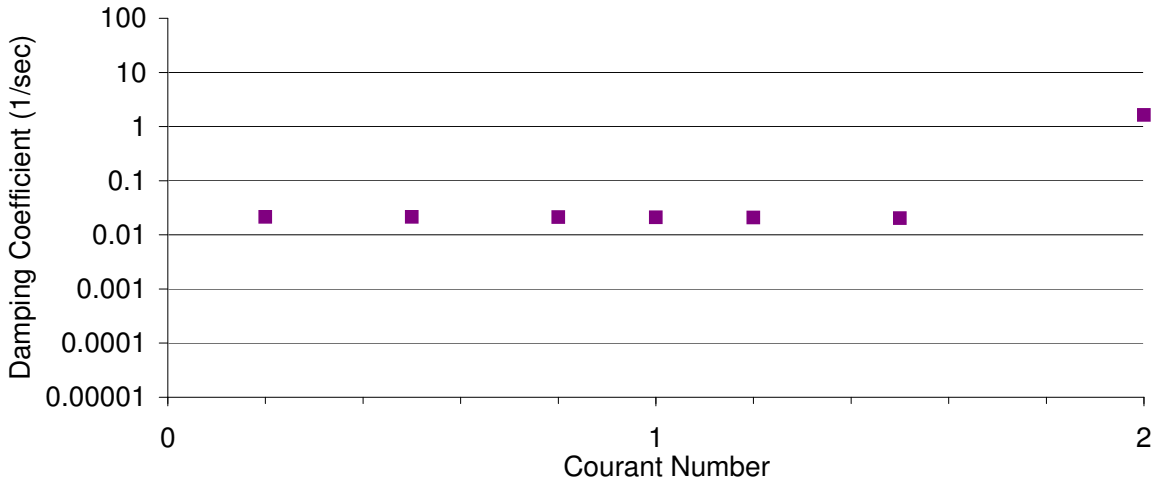

(b)

Figure 4.46: Numerical damping coefficients as a function of (a) cells per wavelength (at unity Courant number) and (b) Courant number at 133 cells per wavelength.

Therefore, the numerical damping is not simply a function of spatial resolution only. Nonetheless, as will be shown more fully later, the general trend of numerical damping vs cells per wavelength holds regardless of whether the wavelength or the number of cells is varied.

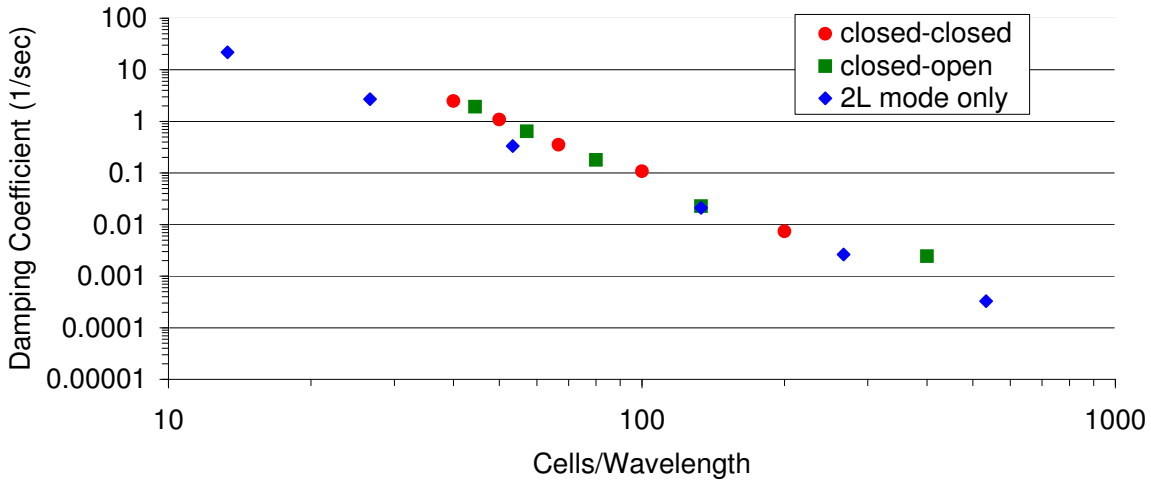

Figure 4.47: Comparison of numerical damping coefficients for the single mode initialization (2L mode) and the white noise initialization for two different boundary configurations.

4.4.2 Area Expansion

This verification case provided an excellent opportunity to study the behavior of numerical damping when effected by geometrical features (in this case, an area expansion). In addition to the cells per wavelength measure introduced in the one-dimensional verification cases, another important parameter for this case is the cells per step height. This parame-

ter measures the relative refinement of the geometrical feature and does not vary with the frequency of the mode. The numerical damping results for the first five modes with various resolution of the area jump is shown in Fig. 4.48. The numerical damping increases significantly when the resolution of the area change is coarse. The conclusion from this test is important: for domains with important geometrical features, the user must design a mesh with both sufficient resolution of the desired modeshapes and sufficient resolution of the geometrical features. The definition of "sufficient resolution" may vary depending on the task and desired accuracy. As a note, the frequency prediction was hardly effected (within previous uncertainty bounds) by changing the resolution of the area change.

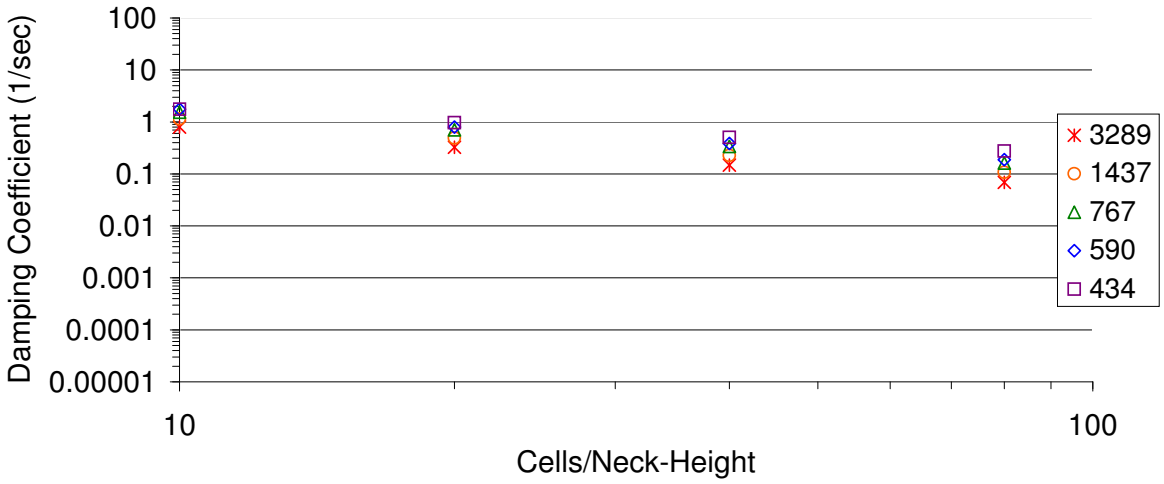

Figure 4.48: Numerical damping coefficients for various resolution of the area jump. Legend denotes the cells per wavelength measure for each symbol.

4.4.3 3D Circular Cylinder

The numerical damping for the modes analyzed above was calculated from probe data for the following simulations: (1) a closed-closed boundary condition set on the baseline grid, (2) a closed-open boundary condition set on the baseline grid, (3) a closed-closed boundary condition set with 2x local hanging node refinement for $0.7 > z > 1.0$, and (4) a closed-open boundary condition set with 4x global refinement. Note that for the 2x local refinement, the cells per wavelength calculation ignored the local refinement. This case tested the effect of local refinement, most importantly its effect on numerical damping. The 4x global refinement case did recalculate the cells per wavelength based on the refined grid size, since this grid size was everywhere applicable. This global refinement case enabled testing of numerical damping at high cells per wavelength. The four grids are summarized in Table 4.13.

Table 4.13: Four grids used for circular cylinder numerical damping study.

Refinement	Boundary Conditions	Title
1x	Closed-Closed	"Closed-Closed Uniform Grid"
1x	Closed-Open	"Closed-Open Uniform Grid"
2x, $0.7 < z < 1.0$	Closed-Closed	"Closed-Closed Non-Uniform Grid"
4x, Global	Closed-Open	"Closed-Open Fine Grid"

The results in Fig. 4.49 show that the local refinement had little effect on the numerical damping when the larger (unrefined) cell size was used to calculate the cells per

wavelength measure. The results for all four cases seem to follow a second order decrease in damping with respect to grid resolution, as would be expected from the numerical method. The amount of scatter amongst this second order descent is due to the difficulty of precisely measuring cells per wavelength in each direction, particularly the radial and tangential directions. In these directions, the grid lines do not follow the wave vector lines, hence the cells per wavelength is an estimate at best. Nonetheless, there is still a noticeable 2nd order trend.

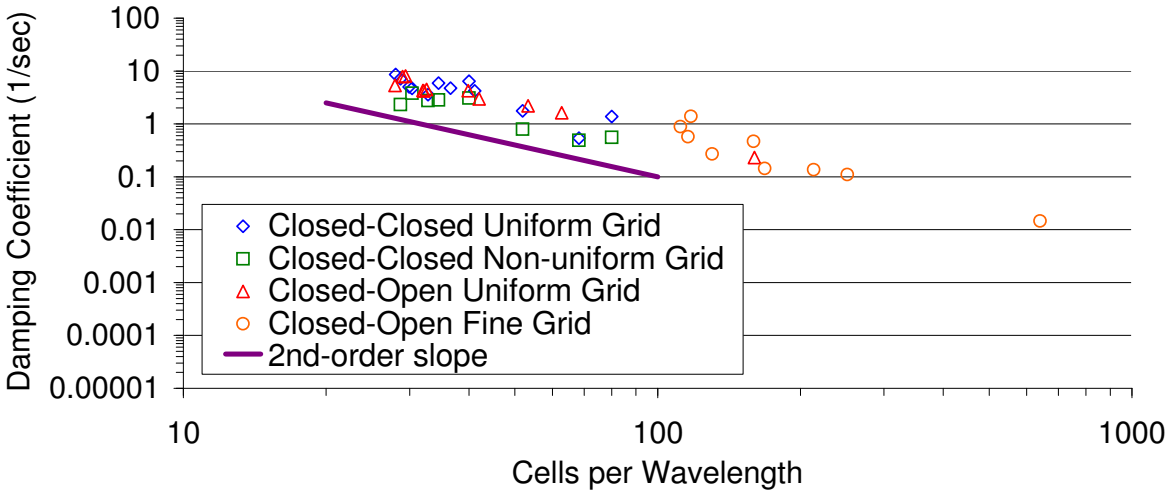

Figure 4.49: Numerical damping as a function of grid resolution for modes less than 500 Hz in the cylindrical verification case.

4.4.4 Rijke Tube

In order to show the reason for such a detailed look into numerical damping, it is instructive to consider again the Rijke tube example from section 4.3. Figure 4.50 shows the fourth and fifth mode, for which the numerical damping is on the same order of magnitude as the theoretical growth rate

$$|\alpha_{numerical}| \sim |\alpha_{q'}|. \tag{4.49}$$

The difference in the quality of prediction between Fig. 4.44 for the first three modes and Fig. 4.50 for the fourth and fifth modes is remarkable. The first three modes exhibit relative errors less than 5%, but the errors in the fourth and fifth modes are on the order of 100%. The cause is simple. When the numerical damping is large enough to compete with the heat release forcing term, large errors in the prediction will occur. When the numerical damping is too small to compete, the solver produces an accurate result for the growth rate. For this reason, careful quantitative characterization and control of the numerical damping in vital for each application.

To further understand the role of numerical damping in polluting the growth rate predictions, the values of numerical damping calculated from the zero heat release case are added to the results of each time-lag simulation. This effectively shifts the growth rate curve to correct for numerical damping. The results of this shift are shown in Fig. 4.51. Indeed the shift improves the simulation results dramatically, but there are still noticeable errors and a few points for which the sign of the growth rate is incorrect. Therefore, while shifting

to correct for the numerical damping is a realistic strategy for users to employ, and it is seen that such a strategy dramatically improves the stability predictions, it is recommended that the numerical damping is mitigated rather than corrected for. Mitigation of numerical damping can be accomplished through an increase in grid refinement. This results in an increase in computational cost.

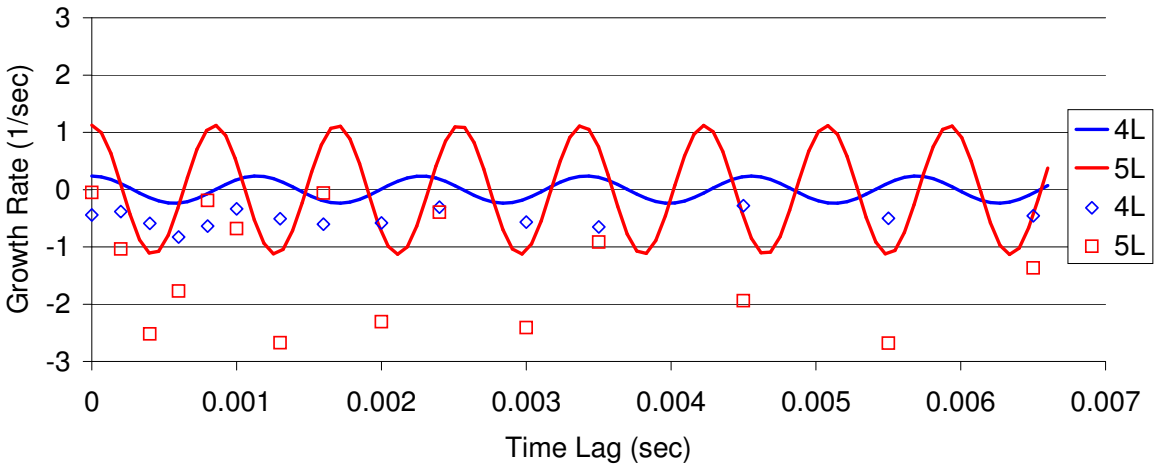

Figure 4.50: Growth rates for modes 4 and 5 in the pressure mechanism Rijke tube verification case. Solid lines are analytical solution and symbols are the tacFoam solution.

To illustrate strategies for reducing the numerical damping, the resolution of the grid was increased by 10x (2000 cells). The numerical damping was dramatically reduced by this ten-fold increase in cells per wavelength, as shown in the previous verification cases dealing with numerical damping. The result is shown in Fig. 4.52. The relative errors are now with 5%, as with the lower frequency modes. This effectively shows that, by reducing numerical

damping such that it is overwhelmed by the growth rate due to heat release, the linear growth rates can be accurately predicted.

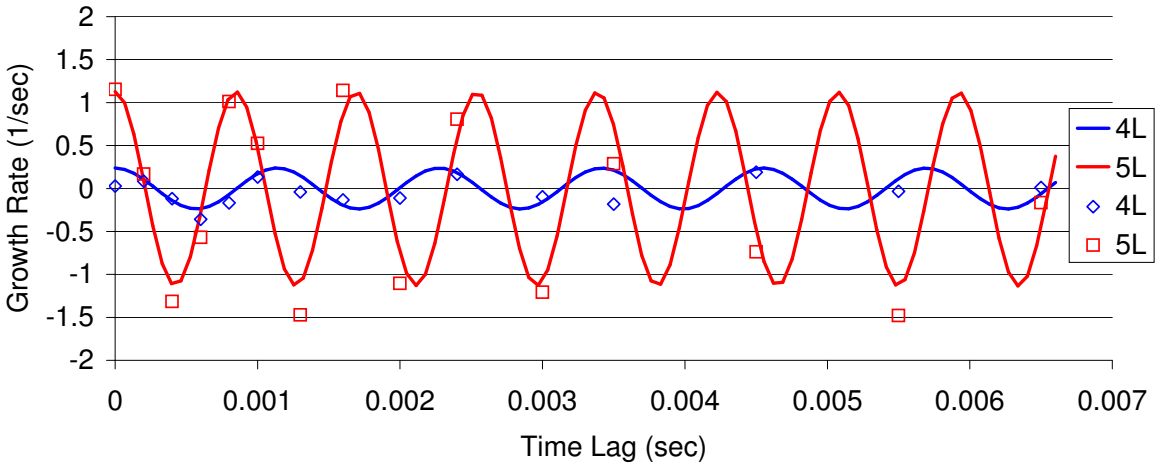

Figure 4.51: Growth rates for modes 4-5 in the pressure mechanism Rijke tube case, corrected for numerical damping. Solid lines are analytical solution and symbols are the tacFoam solution.

The same dichotomy noted in the pressure mechanism case is again observed for the velocity mechanism. The first three modes, shown in Fig. 4.45 give good agreement with the theoretical solution. The errors are within 10%, which is impressively small given that the sender region was offset by a finite length in order to incorporate the same physics and the theoretical model. When the numerical damping becomes large enough to compete with the growth rates for the fourth and fifth modes, the simulation does not produce accurate results, Fig. 4.53. This can be partially overcome by shifting the results to correct for numerical damping, shown in Fig. 4.54, but the results still contain noticeable errors. Such practice

is not recommended. Rather, it is recommended to increase the grid refinement (at more computational cost) to obtain a more accurate solution.

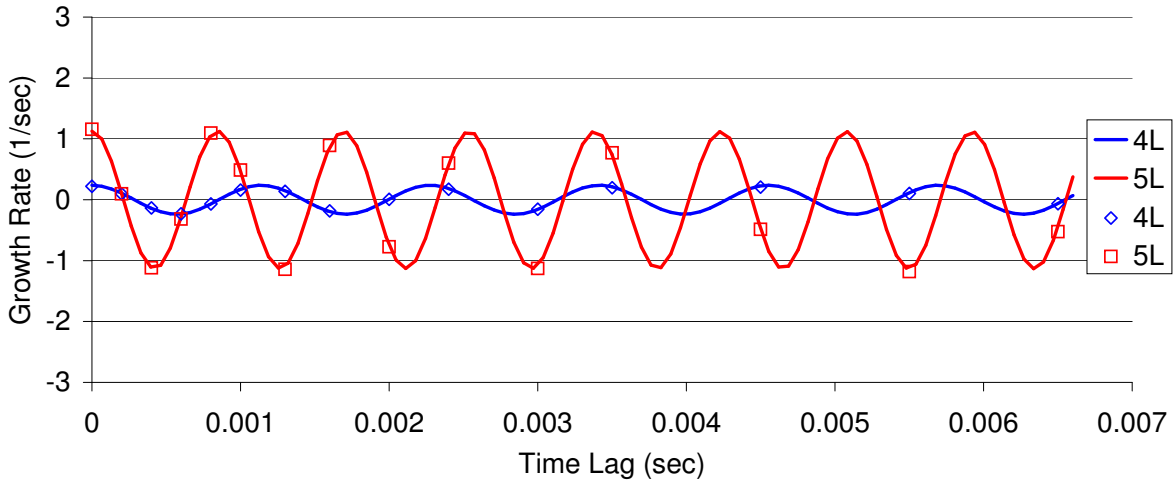

Figure 4.52: Growth rates for modes 4-5 in the pressure mechanism Rijke tube case, using a 10x refined grid. Solid lines are analytical solution and symbols are the tacFoam solution.

There is no easy rule of thumb for determining the grid resolution necessary for a given scenario. The numerical damping for a given resolution can be approximated by calculating the cells per wavelength using Eq. (4.43) and the approximate "cells per step height" (cells per relevant geometric feature length) and using Figs. 4.49 and 4.48 as a guide. In most cases, the numerical damping can be calculated using the bandpass filtering and curve fitting method described at the end of chapter 3 from an initial "no unsteady heat release" simulation. Such a simulation is also useful for determining the resonant frequencies and modeshapes of the geometry. Once the numerical damping for each targeted mode is determined, one must compare that damping coefficient to an expected growth rate, which

will likely be much less than the frequency of the mode in rad/sec. If results show that the apriori estimates for the necessary grid resolution yield a numerical damping coefficient near the same order of magnitude as physical sources of growth or damping, then the grid should be refined and the simulation process iterated.

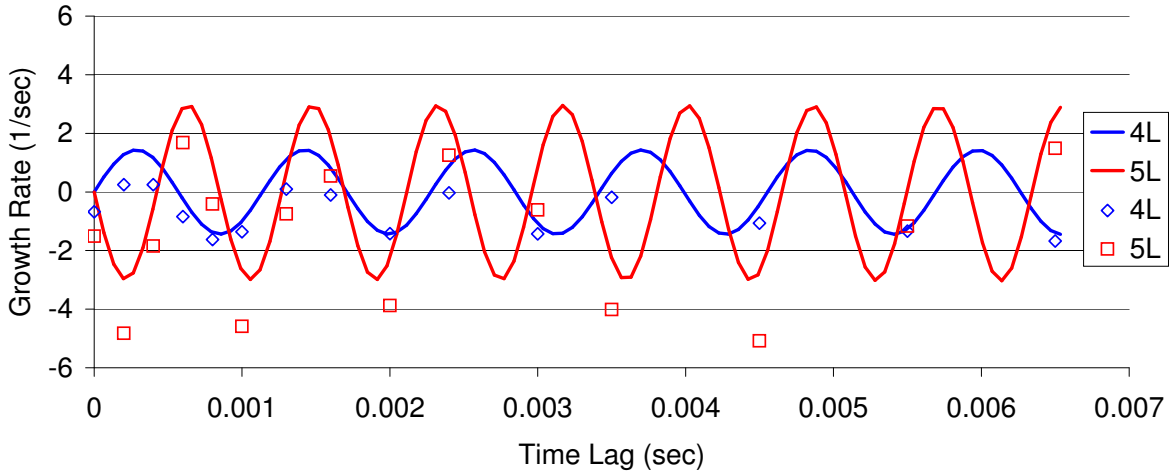

Figure 4.53: Growth rates for the fourth and fifth modes in the velocity mechanism Rijke tube verification case. Solid lines are analytical solution and symbols are the tacFoam solution.

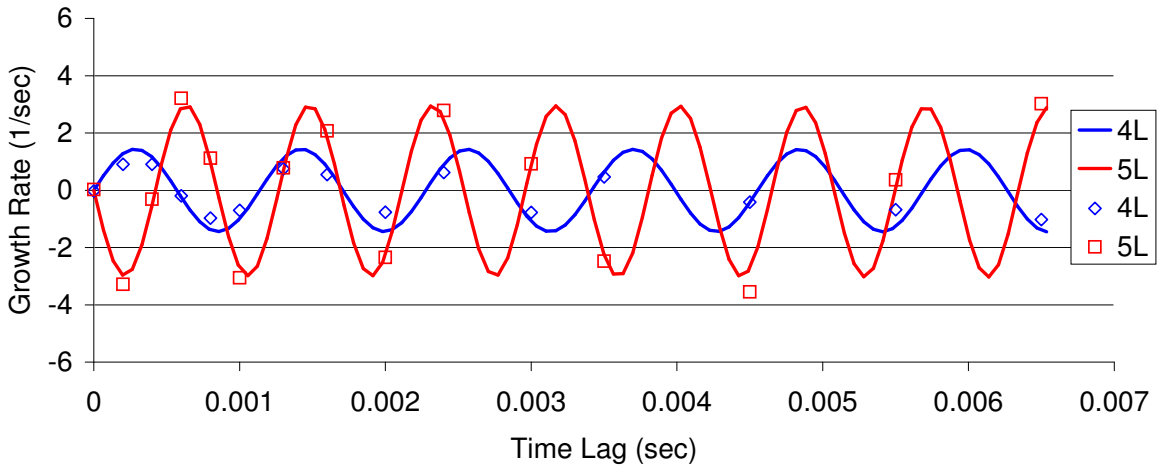

Figure 4.54: Growth rates, corrected for numerical damping, for modes 4-5 in the velocity mechanism Rijke tube case. Solid lines are analytical solution and symbols are the tacFoam solution.

4.5 Parallel Computation Verification

Another important feature of the solver is the ability to calculate spatio-temporal acoustic fields in parallel. In order to compute acoustic fields in larger, more complex geometries, larger numbers of cells with smaller time steps will be necessary. For this tool to be useful for practical engineering design and analysis, the simulation code must be parallelized. The code must give the same answer with the same numerical damping regardless of the number of processors used to compute the simulation.

4.5.1 1D Uniform Duct

The uniform duct case from section 4.1.1, using the procedure described in Fig. 3.3, was run multiple times, varying the number of processors used for the computation. The resulting frequency errors and numerical damping coefficients are shown in Fig. 4.55 as a function of number of processors used. As desired, the simulation did not show any variation with number of processors.

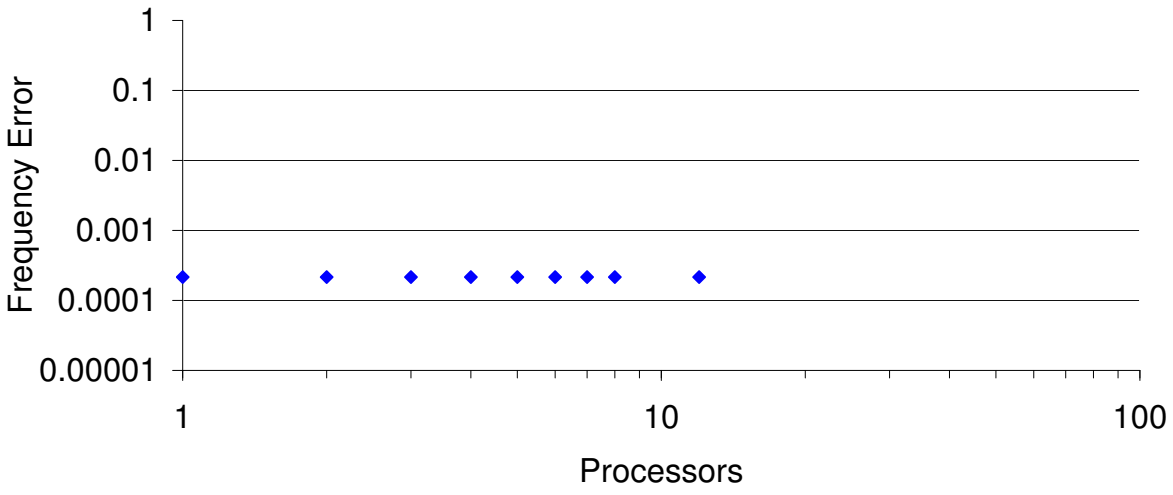

(a)

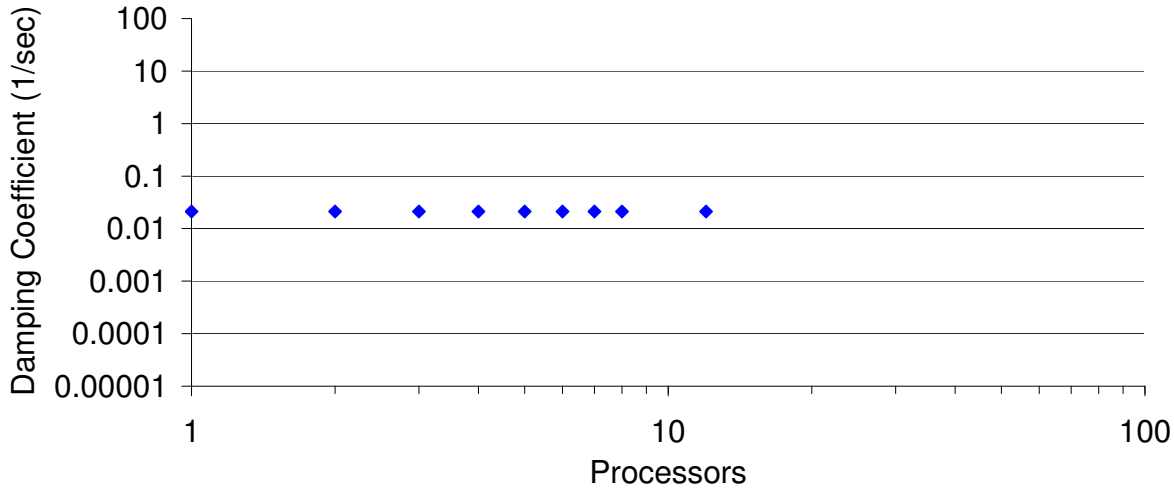

(b)

Figure 4.55: Parallelization accuracy for (a) frequency error and (b) damping coefficient.

4.5.2 Area Jump

While parallel computation was verified for the one-dimensional case with 100 cells, it was also thought wise to check parallelization behavior for a multi-dimesional case with many more cells. The 2D simulation with acoustically-compact area change from section 4.1.7 was chosen to suit this purpose. The grid with 10 cells per neck height (15,000 cells) was chosen and run on various numbers of processors, from 1 to 12. The frequency and numerical damping coefficient was monitored. As shown in Fig. 4.56, no changes in frequency or numerical damping coefficient were observed. These two tests were sufficient for verifying the successful parallelization of the code. Due to constraints in present computing resources, no scaling tests were performed to determine the efficiency of the parallelization.

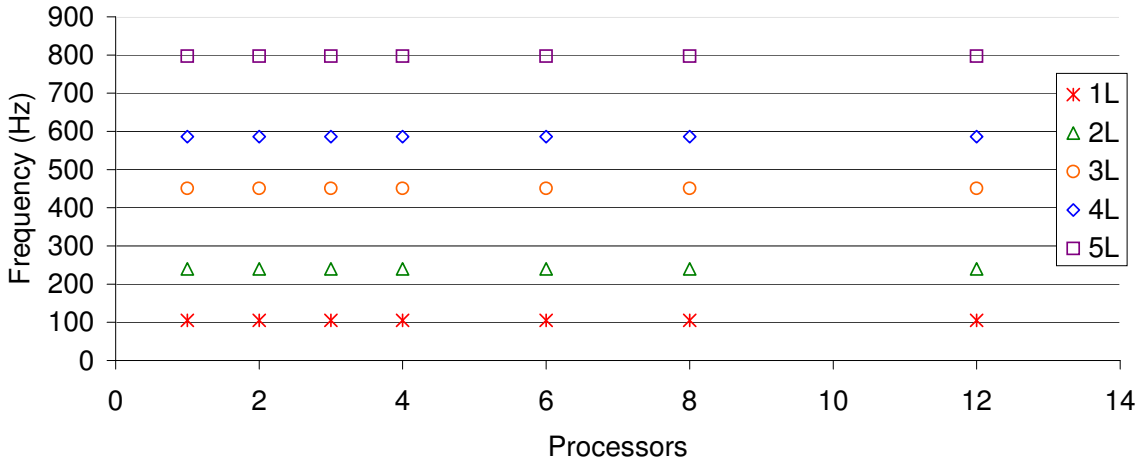

(a)

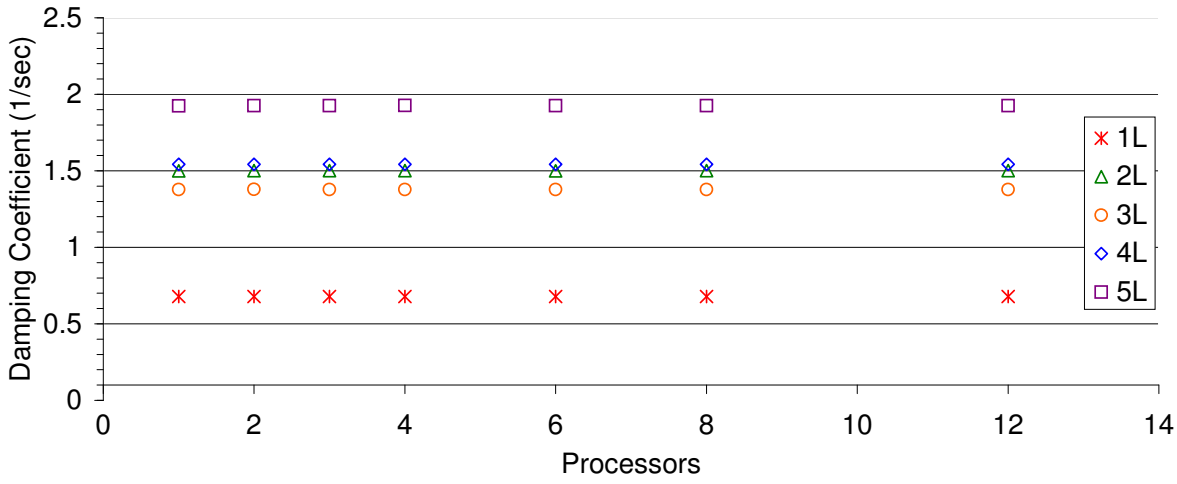

(b)

Figure 4.56: The (a) frequency and (b) numerical damping coefficient of the two area case with various number of processors.

CHAPTER 5
VALIDATION

The previous chapter included numerous verification cases by which the integrity of the solver was established for simple academic cases. This chapter focuses on extending the use of the solver to physically relevant cases. Specifically, this chapter predicts the thermoacoustic instabilities for two lab scale experiments.

5.1 University of Melbourne Bluff Body Combustor

The first validation case is a simulation of a laboratory combustor at the University of Melbourne [47, 48]. A schematic of the combustion chamber from the experimental study is reproduced in Fig. 5.1, whjch is reproduced from [47]. Premixed air and fuel enter the one-meter-long circular cylinder test section through a choke plate. The fuel is liquified petroleum gas with composition of 98% propane. Upstream of the choke plate, the fuel and air is allow to completely mix. The upstream mixing region is acoustically isolated from the combustion region. The flame is anchored by a bluff body located at the approximate center of the meter-long duct. Downstream of the flame, the combustion chamber walls were fused silica to allow optical access for chemiluminescence measurements. The diameter of

the combustion chamber is 0.05 meters and the diameter of the bluff body is 0.025 meters. The length of the bluff body is 0.06 meters, and the length downstream of the bluff body to the open exit is 0.45 meters. The 20:1 aspect ratio of the combustion chamber is designed to investigate longitudinal modes. The limit cycle pressure amplitudes are measured at a probe aligned with the center of the bluff body.

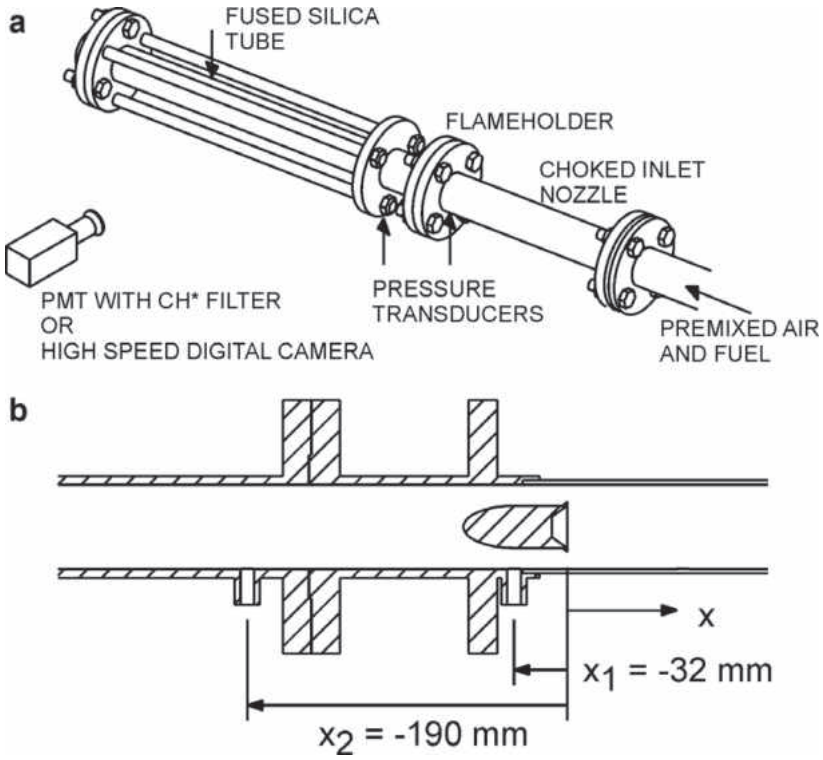

Figure 5.1: University of Melbourne experimental test section: (a) isometric view, (b) slice of internal view.

5.1.1 Validation Case Selection

The experimental test matrix [47, 48] included varying the equivalence ratio, inlet Mach number, and exit boundary condition. The open exit test case, with unity equivalence ratio, provided the best validation case for the present code. The reference conditions of this experiment are given in Table 5.1. Other tests ran had different exit geometries, including a choked boundary. This experiment resulted in a large amplitude mode at the second resonant frequency of the duct (three-quarter wave frequency). This 2L mode was the only dominant frequency observed in the experiment.

Table 5.1: Reference conditions for liquified petroleum gas bluff body combustor at the University of Melbourne.

ϕ	$\bar{T}_{preheat}[K]$	$\bar{p}[kPa]$	$\dot{m}[kg/m^3]$	$f[Hz]$
1.0	345	101	0.029	364

The flow conditions upstream and downstream of the flame are given in Table 5.2. The mean pressure was approximately constant across the flame and equal to the atmospheric pressure imposed at the exit boundary. The temperature shown here is the calculated adiabatic flame temperature, though some heat transfer did occur through the sides of the combustor due to the fused silica walls. The RANS simulation did account for small pressure changes and heat release through the walls. The Mach number remains low, indicating that mean velocity influences on the acoustics may be small.

Table 5.2: Flow conditions for liquified petroleum gas bluff body combustor at the University of Melbourne.

Section	$\bar{T}[K]$	$\bar{p}[kPa]$	$\bar{\rho}[kg/m^3]$	$\bar{V}[m/s]$	$\bar{M}$
Products	345	101	1.0	15	0.04
Reactants	2425	101	0.16	92	0.10

This experiment was also simulated by [47, 48] using the matrix approach of [49] and by [50, 1] using the Generalized Instability Model (GIM) of [25]. These two one-dimensional simulations provide a nice context for the present prediction code.

5.1.2 Summary of Simulation Approach

For this case, a RANS simulation and four tacFoam simulations are run. The purpose of each tacFoam simulation is to build upon the knowledge of the other simulations and reveal a particular behavior of the model. The simulations for this case are summarized in Table 5.3.

Table 5.3: Summary of simulations for Hield bluff body combustor.

Solver	Type	Purpose
RANS		To obtain the mean flow
tacFoam	no q', closed BC	to evaluate numerical damping
tacFoam	no q', choked BC	to evaluate boundary damping
tacfoam	non-linear q', choked BC	to predict limit cycle amplitude

5.1.3 RANS Simulation of Mean Flow

The Reynolds Averaged Navier Stokes (RANS) equations were solved using the finite volume method in OpenFOAM. The k-ω SST model was used for turbulence closure [51]. The combustion was modelled using a single-step reaction tracked by a reaction progress variable b. Chemical closure was obtained through a turbulent flame speed correlation [52] using a laminar flame speed calculated from a network reactor modelling tool in Cantera [53].

The velocity, turbulent quantities, and temperature were specified at the inlet with zero pressure gradient and the pressure was specified at the outlet with zero gradient for all other variables. The wall used the no slip condition with wall functions for the turbulent quantities. While the boundary condition for the wall in terms of the energy equation is not clear from the experiments, the RANS simulation used a constant temperature wall at the pre-heat temperature. This essentially assumes that the walls are steady at the pre-heat

temperature before ignition, and they rise in temperature only negligibly after the flame is ignited.

The domain for the RANS study began at the inlet choke point and ended at the open exit, Fig 5.2. A fully hexahedral mesh was created using the snappyHexMesh utility in OpenFOAM with a STL file of the cylinder and bluff body dimensions given in Hield's thesis [48]. Two different grids were run (125k cells, 275k cells) and the results of the finer resolution mesh were taken for interpolation to the acoustic mesh. The differences between the simulations were judged to be insignificant for the current purposes (extracting a realistic temperature and heat release field). It is emphasized that the purpose of the RANS was not to focus on providing a high-fidelity mean field, but rather to quickly produce realistic mean fields for the acoustic simulation. Thus, the RANS simulation was "quick-and-dirty" as compared to a formal RANS investigation, including a formal grid resolution study. An example of a grid resolution study is shown for the Purdue University validation case.

The simulation was advanced to a steady solution using OpenFOAM's bi-conjugate gradient solver. The simulation converged to a steady-state solution when the residuals dropped by three or more orders of magnitude and simulation variables from point probes showed negligible changes. The flame is anchored by the recirculation region in the wake of the bluff body and propagates toward the outer walls downstream. Three-isosurfaces of reaction progress variable (at b = 0.25, 0.5, 0.75) are shown in Fig. 5.3, outlining the main reaction region. The flame extends about 20 centimeters downstream of the bluff body, close to half of the downstream section of the chamber.

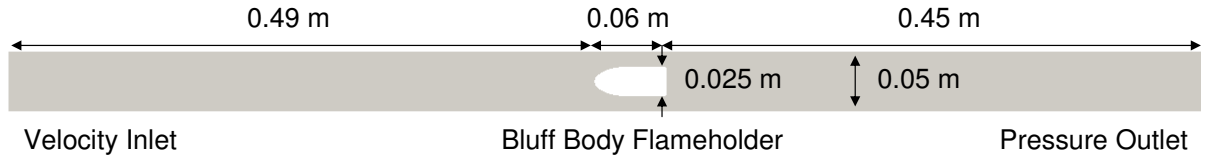

(a)

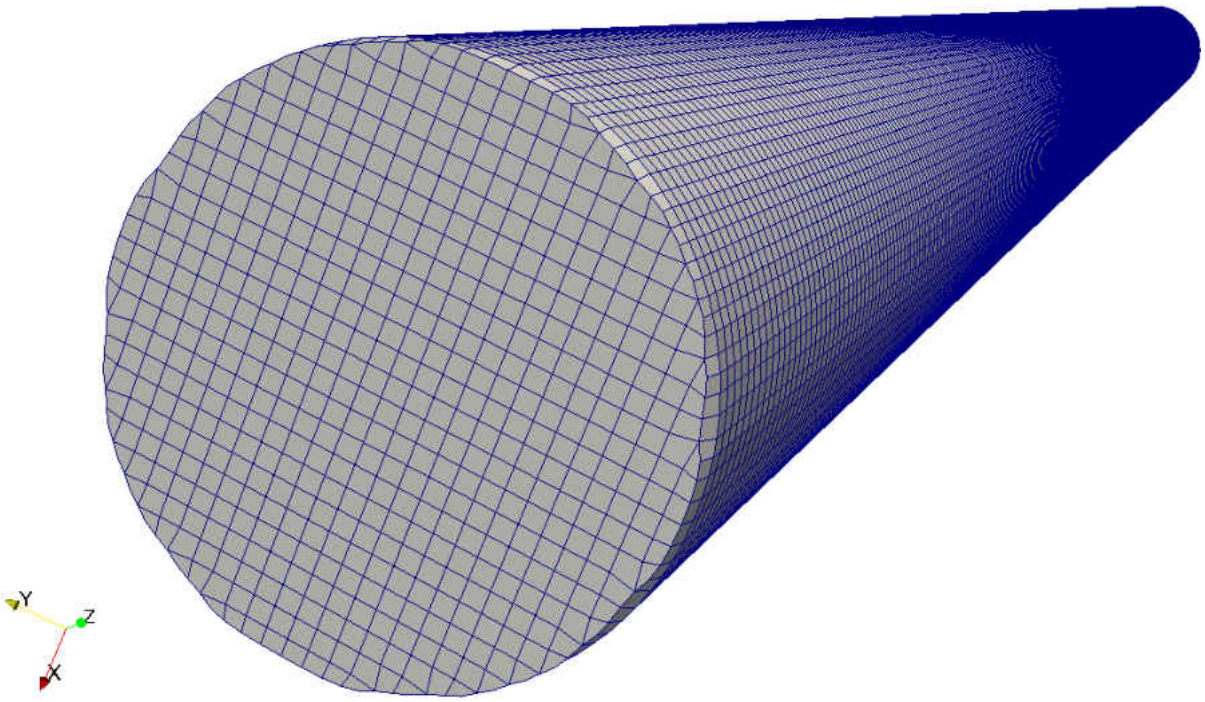

(b)

Figure 5.2: Melbourne bluff body combustor, RANS (a) domain and (b) finite volume mesh.

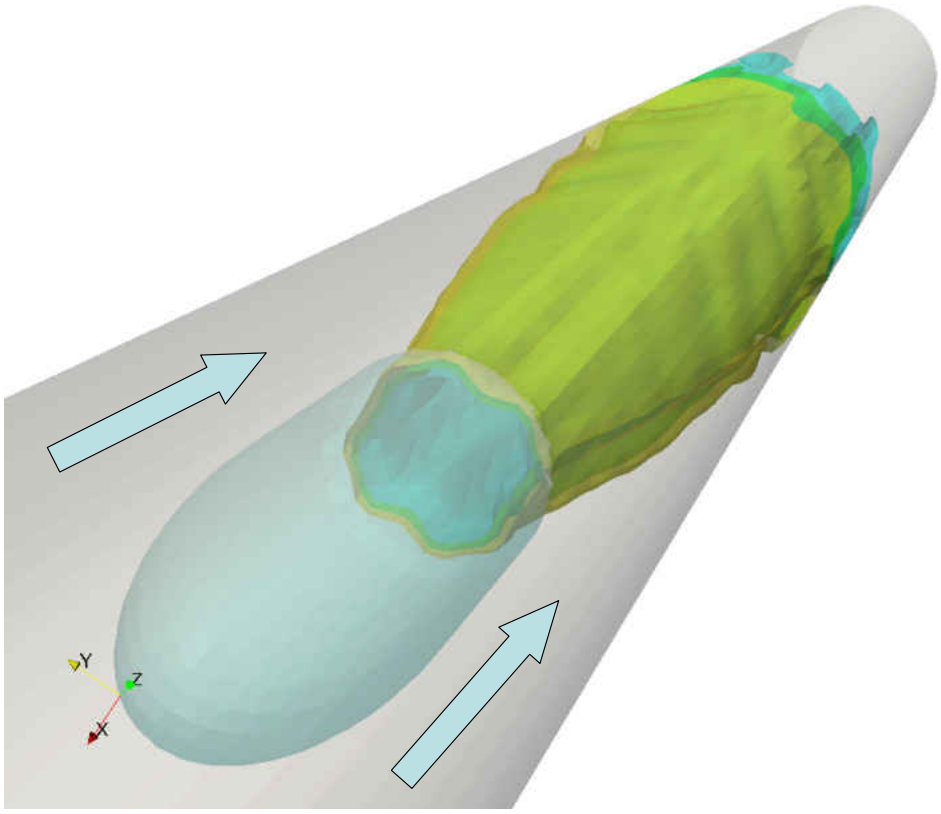

Figure 5.3: Translucent iso-surfaces of reaction progress variable outlining the spatial structure of the flame. Flow is bottom to top as shown by arrows.

The variables relevant to the thermoacoustic simulation are shown in Fig. 5.4 along the center-plane of the duct. The temperature determines the sound speed, while the velocity determines the extent to which the mean flow affects the acoustic behavior of the duct. The temperature increases dramatically across the flame and remains close to the adiabatic flame temperature in the center of the pipe. Near the edges, the cooling at the wall produces lower temperatures. The transfer of heat from the combusted flow plays an important role in determining the acoustic behavior downstream. Closely tied to the temperature and also affecting the propagation of the acoustic waves is the mean velocity, Fig. 5.4b. The flow accelerates after the flame due to the drop in density (increase in temperature). The local Mach number exceeds the mean Mach number due to non-uniformity of temperature and velocity in the cross-section. The Mach number, however, remains modest (< 0.15). The heat release is also an important quantity to be mapped from the RANS solution. It provides a main factor in determining the location and intensity of heat release oscillations.

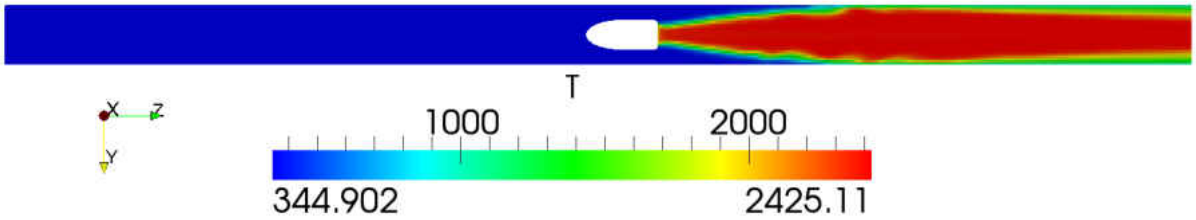

(a)

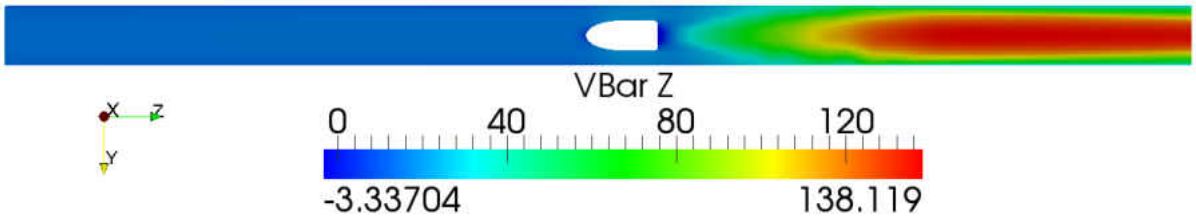

(b)

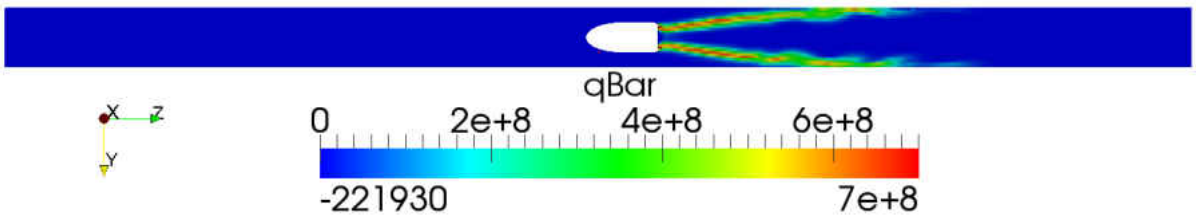

(c)

Figure 5.4: Center-plane of Melbourne case RANS results: (a) temperature $[K]$ and (b) axial velocity $[m/s]$ and (c) heat release $[W/m^3]$.

5.1.4 Comparison of Frequencies and Modeshapes

To elucidate the acoustic behavior of the combustor in question, initial simulations with no mean flow, perfectly-reflecting boundaries, and no unsteady heat release were run. A discrete Fourier transform calculated alongside the simulation provided acoustic pressure and velocity magnitudes at each cell, allowing for the reconstruction of the acoustic modeshape. The acoustic domain and grid are shown in Fig. 5.5. The domain is the same as the RANS domain, except that now boundary conditions must be specified in terms of the acoustic field rather than the mean field. The inlet boundary condition is choked, which for the modeshape calculations can be approximated by a closed boundary. The grid shown here is the finer of the two grids used. The finer grid shown includes refinement around the bluff body and flame region, while the coarser grid included no such refinement. The coarse grid had a resolution of 6 cells across the bluff body diameter, while the fine mesh had twice as much due to local refinement of the grid.

Table 5.4: Grid characteristics for thermoacoustic grids of Melbourne experiment.

	No. Cells	Min. Cells/Wave (2L)	Cells/Step-Height	Max. Aspect Ratio
coarse	16,588	150	3	1.6
fine	50,386	300	6	1.6

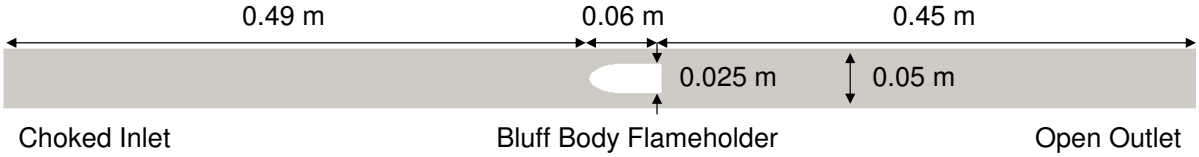

(a)

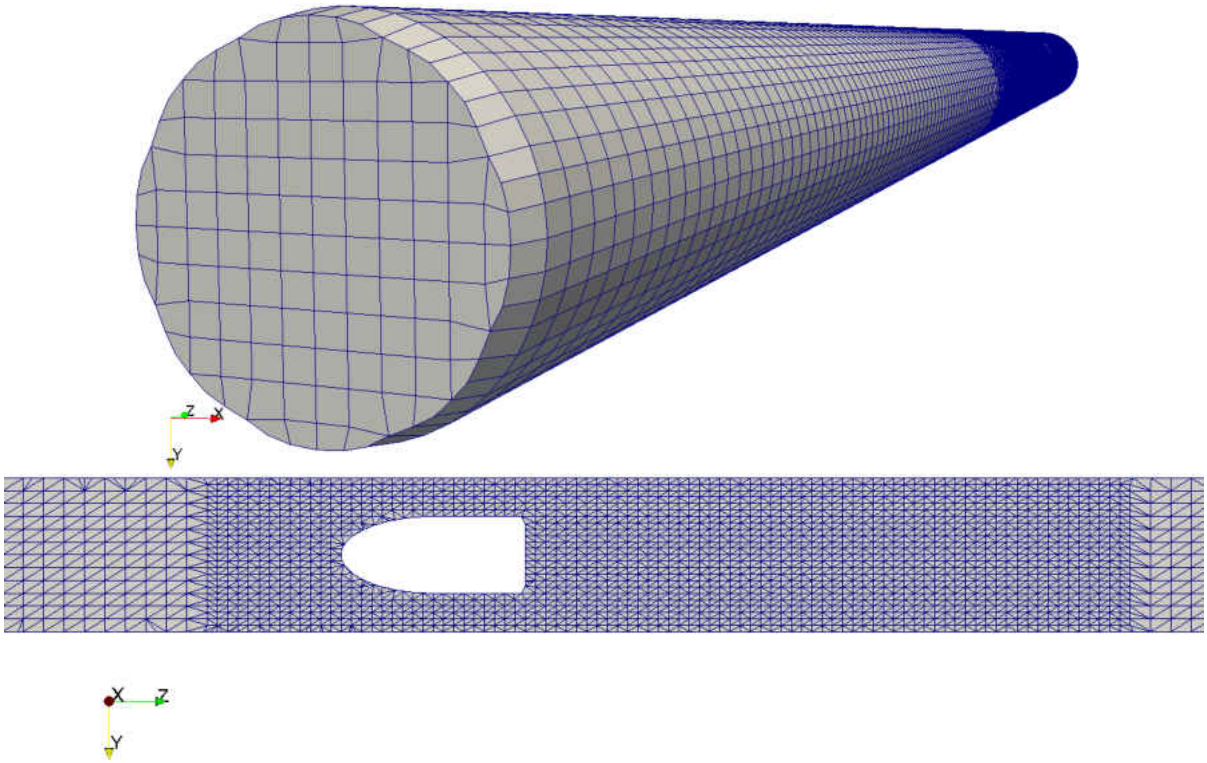

(b)

Figure 5.5: Melbourne bluff body combustor acoustic simulation (a) domain and (b) finite volume mesh.

This initial simulation has no acoustic damping or growth sources except for the grid-dependent damping of the numerical method. Because of this, it provides a convenient quantification of the numerical damping for the two grids. For the present analysis, the first three modes are the only modes of interest, the second mode being the excited mode in the experiments. The first three resonant frequencies for the two acoustic grids based on this initial simulation are shown in Table 5.5. Note that there is significant over-prediction of the frequency (more than 8% error) for the second mode. Similar over-prediction can be seen in previous analytical predictions based on one-dimensional analysis with compact flames, including that of the experimentalist himself [47, 1]. It is postulated here that the over-prediction is a result of the flame dynamics discussed by the experimentalist. A large periodic fluctuation of the flame length occurred over the acoustic period of oscillation. During this cycle, the flame changed from very short to very long, even as long as the entire length of the downstream section. Because of this, the extent of the downstream hot products region may be severely shortened during some phases of the cycle, leading to lower overall sound speeds and a lower frequency. Such unsteady (non-turbulent) fluid mechanical behavior is not captured by the steady RANS calculation nor is there currently a method of including it within the current thermoacoustic simulation methodology. Other possibilities include the under-prediction of heat transfer by the RANS model, as well as a poor prediction of the mean flame position. It is unclear whether the first and third mode frequencies are correctly predicted because these modes were stable in the experiment.

The prediction of the GIM code from [50] shows better agreement than the present code. It is observed, however, that the lower frequency in this prediction is caused by a lower prediction of the adiabatic flame temperature than the RANS procedure used here and a different placement of the bluff body location (evidently in conflict with the location shown by [48]). The simulation from [47] did not give an "unshifted frequency", therefore it is not included here. In this context, "unshifted" refers to the natural frequency of the domain without any frequency shifts caused by the unsteady flame.

Table 5.5: Resonant frequencies (Hz) for first three modes with perfectly-reflecting boundaries. The GIM results are the unshifted frequency, which is the appropriate comparison here.

	1L	2L	3L
(Exp.)	–	364	–
coarse	137	397	578
fine	138	396	578
(GIM [50])	86	382	629

The numerical damping coefficient for the first three modes on each of the two acoustic grids is shown in Table 5.6. These damping coefficients are clearly orders of magnitude less than the frequency, but the more important comparison is with the physical sources of acoustic damping (here, the choked boundary). The damping follows the expect trends,

namely, that the increase in grid resolution decreases the numerical damping and that the increase in frequency (moving to higher modes) results in an increase in numerical damping.

Table 5.6: Numerical damping coefficient (1/sec) for first three modes.

	1L	2L	3L
coarse	8.6	5.9	10.8
fine	4.9	4.3	6.9

The pressure modeshapes are shown in Fig. 5.6 for the first three modes. The images shown are taken from the fine grid with a slice through the mid-plane. No color scale appears on these figures because the modeshapes are typically normalized by the maximum value. The color red represents anti-nodes (maximum fluctuation) while the color blue denotes nodes (zero fluctuation). The first mode is the quarter wave mode, with maximum at the closed inlet and minimum (zero) at the open outlet. As such, the large pressure fluctuations for this mode occur upstream of the combustion. The potential of the coupling of pressure and heat release fluctuations necessary to drive mode growth is severely limited for this mode because its amplitude is relatively small in the combustion region. The second mode is the three-quarter wave mode. The combustion region is more advantageously placed for the growth of this mode. Meanwhile, the third mode contains a pressure maximum in the combustion region, leading to the highest possibility of mode growth from the point of view of the pressure modeshape.

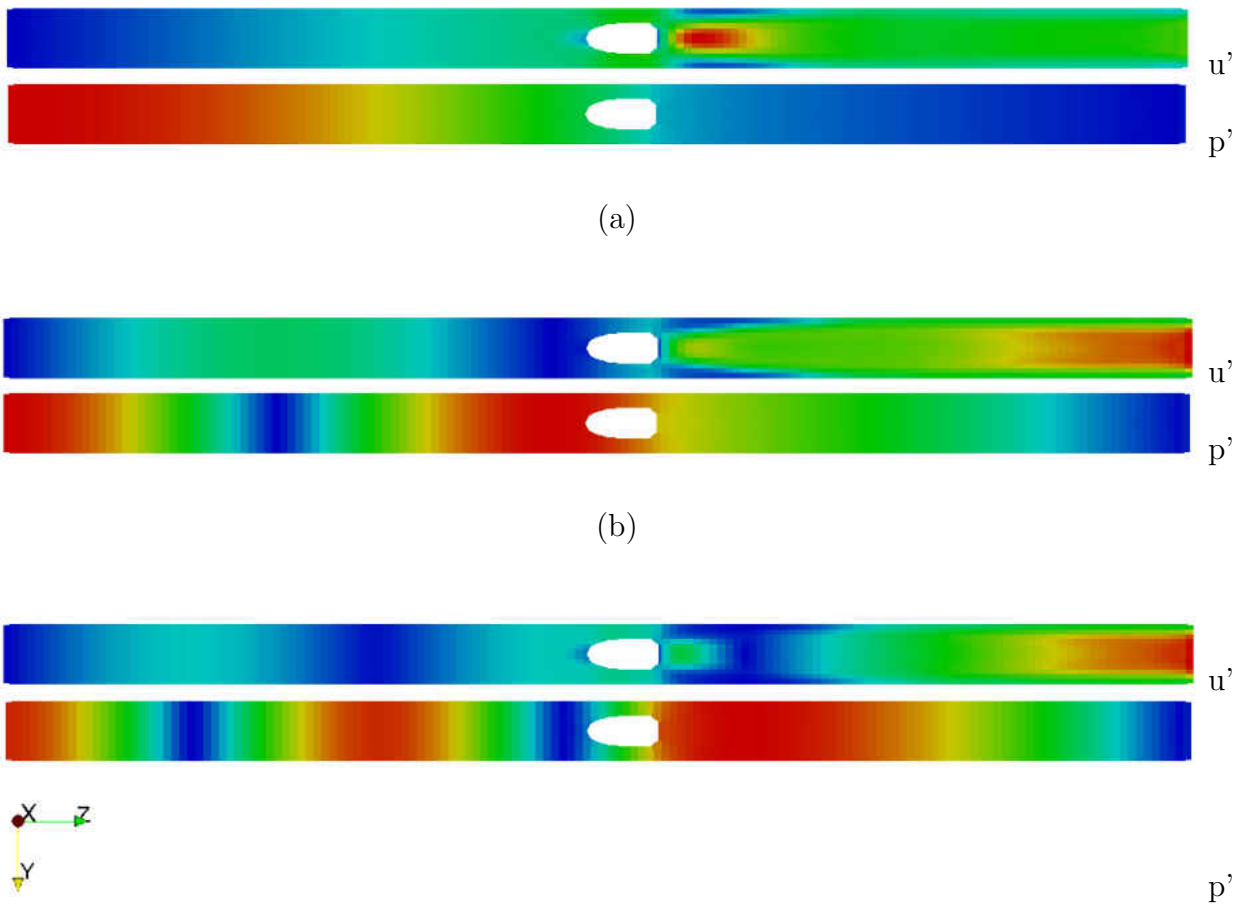

Figure 5.6: Melbourne rig acoustic velocity (u') and pressure (p') mode amplitudes on a color scale of blue (zero amplitude) to red (max amplitude) : (a) 1L, (b) 2L, (c) 3L.

For this validation case, however, the unsteady heat release mechanism is based on velocity fluctuations. Therefore, the velocity modeshape is just as influential in determining the outcome of the stability analysis. Figure 5.6 also shows the axial velocity modeshape for the first three modes. The first mode contains large velocity fluctuations in the flame region, leading to the possibility of a strong mechanism. However, the fact that the heat release is located at a pressure minimum, any unsteady heat release generated by the 1L velocity fluctuations cannot couple with pressure and therefore cannot drive instability. The second mode also shows relatively strong velocity fluctuations in the flame region. The third mode, which contained a pressure anti-node at the flame region, contains a velocity node. Because the unsteady heat release is dependent on the acoustic velocity, which is taken from the flame region, there is little opportunity for the growth of the third mode. Therefore, based on preliminary analysis of the modeshapes, it can be concluded that the most likely mode to exhibit thermoacoustic instability is the second mode.

5.1.5 Boundary Damping

Before simulating the heat release model developed with the experiment [47, 48], it is instructive to assess the damping extent of the choked inlet. The first simulation replaced the choked inlet with a closed inlet so that the impact of numerical damping on baseline acoustic modes could be assessed. For a second simulation, a choked inlet boundary is restored, with the reflection coefficient given by [24]

$$R_{inlet} = \frac{1 - \bar{M}}{1 + \bar{M}} \tag{5.1}$$

For this case, with Mach number of 0.04, the reflection coefficient is 0.923. Note that this reflection coefficient is valid only in the absence of entropy waves [54]. However, because the current simulation ignores entropy waves, this formula is appropriate here.

In the second simulation, the presence of the absorbing boundary condition adds damping to the system. It is important that this damping is not overwhelmed by the numerical damping. The first three frequencies for this second solution did not change by more than a couple Hz, as expected due to the small Mach number. The damping coefficient for the first three modes on each of the two acoustic grids is shown in Table 5.7. The boundary damping for all three modes is indeed greater than the numerical damping, but not quite by an order of magnitude. In fact, the influence of numerical damping on these results is evident in the noticeable drop in damping coefficient from the coarser to finer grid (10%-30%). Therefore, the numerical damping for these two grids is expected to assert some effect on the final heat release simulation.

Table 5.7: Boundary damping coefficient (1/sec) for first three modes ("choked"), compared with numerical damping ("closed").

	1L	2L	3L	BC
coarse	29.3	21.0	23.2	choked
fine	24.9	18.9	18.1	choked
coarse	8.6	5.9	10.8	closed
fine	4.9	4.3	6.9	closed

5.1.6 Nonlinear Heat Release Model

The non-linear heat-release model proposed by Hield et al. was given in the frequency domain [47, 48].

$$q' = nF(\omega)\frac{\bar{q}}{\bar{u}}u'(t-\tau) \tag{5.2}$$

with non-linear n and τ given by [1]

$$n = 1.6\exp(-0.2u'_{RMS}) + 0.225 \tag{5.3}$$

$$\tau = 0.0075\exp(-0.0744u'_{RMS}) + 0.0025 \tag{5.4}$$

[1]Note that the experimentalist's paper [47] contains a typo in the time lag formula. The leading coefficient in the time lag correlation is given as 0.075 by Hield et al., but the Fig. 10c of [47] shows that the time lag should be 0.01 in the zero amplitude limit. Therefore, the leading coefficient should be 0.0075 as shown in Eq .(5.4)

The function $F(\omega)$ in Eq. (5.2) is a second-order low-pass filter given by

$$\frac{\omega_{co}^2}{\omega_{co}^2 + 2i\zeta\omega_{co}\omega - \omega^2} \tag{5.5}$$

where ω_{co} is the cut-off frequency and ζ is the damping coefficient. For this model, Hield et al. suggested $\omega_{co} = 350Hz$ and $\zeta = 0.5$. For the implementation of this model, it was necessary to transform this filter into a state space model so that the filter could be applied in the time domain. The discrete state space model is given by

$$\underset{\sim}{x}^n = \underset{\approx}{A}\underset{\sim}{x}^{n-1} + \underset{\sim}{B}u^{n-1} \tag{5.6}$$

$$y^n = \underset{\sim}{C} \cdot \underset{\sim}{x}^n + Du^n \tag{5.7}$$

Equation (5.6) updates the state variables given by the vector $\underset{\sim}{x}$ based on its previous value and the value of the input. Then, Eq. (5.7) generates the output based on the state variables and the input. For a discretized version of the filter proposed by [47], the coefficients A, B, C, and D are

$$\underset{\approx}{A} = \begin{pmatrix} 1 & \omega_{co}\delta t \\ -\omega_{co}\delta t & 1 - 2\zeta\omega_{co}\delta t \end{pmatrix} \tag{5.8}$$

$$\underset{\sim}{B} = (0 \quad \omega_{co}\delta t)^T \tag{5.9}$$

$$\underset{\sim}{C} = (10)^T \tag{5.10}$$

$$D = 0 \tag{5.11}$$

Of course, this is a crude filter, and more advanced filters (e.g. Chebyshev filters) can be constructed in state space and applied in the same manner. In the interest of matching

the experiment, the above second-order filter is applied. This heat release model is applied to the present case for a third simulation. The velocity fluctuations are taken just behind the bluff body, with the heat release applied to the region downstream of the bluff body. Note also that the RMS velocity fluctuation needed for these non-linear models is estimated using an exponentially weighted averaging technique. Therefore, the influence of past values on the current estimation of the RMS value decays exponentially.

The temporal evolution of a the pressure for the non-linear heat release simulations is shown in Fig. 5.7. The two grids show similar histories, which is expected since the numerical and boundary damping for each was similar. At first, the 3L mode begins to grow rapidly at about 0.2 seconds, but then abruptly disappears. The 1L mode then replaces it and exhibits a transient large amplitude fluctuation from about 0.25 to 0.5 seconds in both simulations. Then, the 1L dies out and the 2L grows to a steady limit cycle amplitude. This switching of modes is due to the non-linear time lag which can bring the modes in and out of phase based on the relationship between the present time lag and the frequency of the mode. Finally, both simulations settle on a limit cycle amplitude about 20% of the mean pressure. The coarse grid limit cycle had a dominant frequency of $410Hz$ and the refined grid had a dominant frequency of $412Hz$. For comparison in terms of limit cycle amplitude, a time history of the experimental data is reproduced from [48] in Fig. 5.8.

Table 5.8 gives the quantitative comparison of limit cycle amplitude for the two simulations with experimental data for these flow conditions. The experimental limit cycle is based on an approximation made by the experimentalists [47], noting that there is not

a clean limit cycle amplitude visible in Fig. 5.8. Even with the approximation of the experimentalists, the calculation is within 20% of the experimental limit cycle. The under-prediction of the limit cycle amplitudes is foreseeable given the impact of the numerical damping noted in Table 5.7.

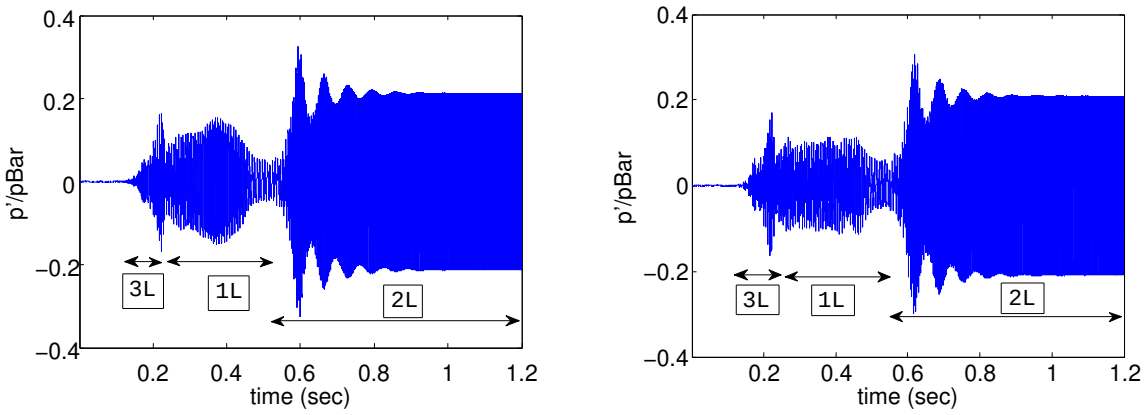

Figure 5.7: Pressure time histories for a simulation probe near the bluff body : (a) coarse grid, (b) fine grid

It is interesting to compare the results of the present simulations to previous 1D simulations in the open literature for this case. The simulations of [47] also under-predict the limit cycle amplitude and over-predict the frequency. In fact, for this simulation, the agreement is worse on both counts. The GIM simulations performed by [50] also over-predict the frequency, but to a lesser extent than the present simulations. The explanations for this have already been discussed in terms of the "unshifted" frequency in Table 5.5. The limit cycle amplitude is over-predicted by the GIM model, with about the same percent error as

the present simulation. It is worth noting that the non-linear heat release model used in the GIM simulation only included the non-linearity in gain factor. A constant time lag was used, perhaps contributing to the over-prediction of limit cycle amplitude.

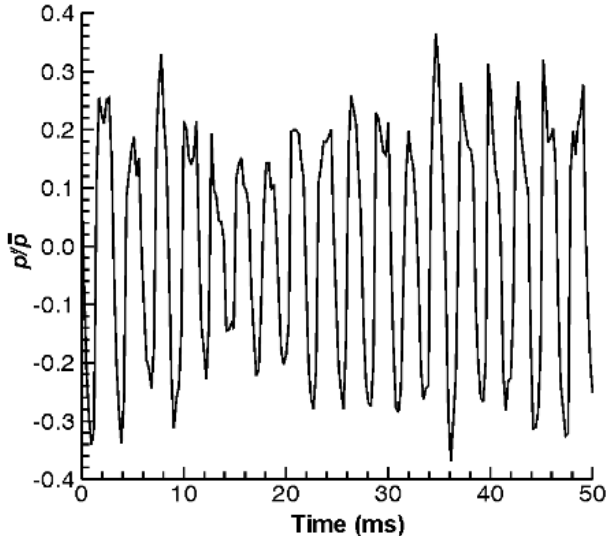

Figure 5.8: Pressure time histories for the experimental probe near the bluff body, from Hield et al.

Overall, the agreement with experiment for the present simulation is acceptable for the scope of the predictive tool. The thermoacoustic simulation correctly predicted the existence of the 2L mode limit cycle and the absence of the other modes. The predicted limit cycle amplitude was within 20% error of the experimental limit cycle amplitude approximation. Other simulations verified that the low-pass filter operated correctly by lowering the cut-off frequency to 100 Hz (from 350 Hz). This lead to the existence of only a 1L mode at a limit cycle amplitude of 4.3 millibars, much smaller than the 200+ millibar limit cycles seen for the 2L mode in Table 5.8.

Table 5.8: Frequency (Hz) and limit cycle amplitude ($p'/\bar{p}$) for 2L mode, compared with experiment as well as the simulation of and Hield et al.

2L	Unshifted Freq	Shifted Freq	Amplitude
(Exp.)	–	364	0.25
coarse	396	410	0.21
fine	397	412	0.21
(GIM)	424	399	0.06
(Sim. [47])	–	450	0.18

5.2 Purdue University Dump Combustor

The second validation case is a simulation of a lab-scale dump combustor experiment preformed at Purdue University [55]. A schematic of the test section is shown in Fig. 5.9 with dimensions shown in millimeters. Premixed air and natural gas (92% methane) enter the test section through a choke plate. The choke plate is an orifice plate with multiple holes through which the incoming flow enters. By choking the flow at the inlet ($M = 1$), the upstream duct is isolated from the acoustics within the combustion chamber, eliminating the possibility of equivalence ratio driven mechanisms. The dump plane is located approximately 1.4 meters downstream of the choke plate. The duct connecting the choke plate to the dump plane has a square cross-section with sides approximately 3.8 centimeters in length. The dump plane is a square-square expansion with an area ratio of four. The flame is ignited at the dump

plane and is anchored by the recirculation region in the outer part of the downstream duct. The combustion chamber duct downstream of the dump plane has sides of 7.6 centimeters and extends about 2.1 meters in length. At the end of the combustion chamber, a nozzle chokes the flow again, providing well-defined acoustic boundary conditions at the exit. Thus, the rig is designed to investigate longitudinal modes with choked inlet and outlet boundary conditions. More detailed information regarding the experimental rig is given by [55].

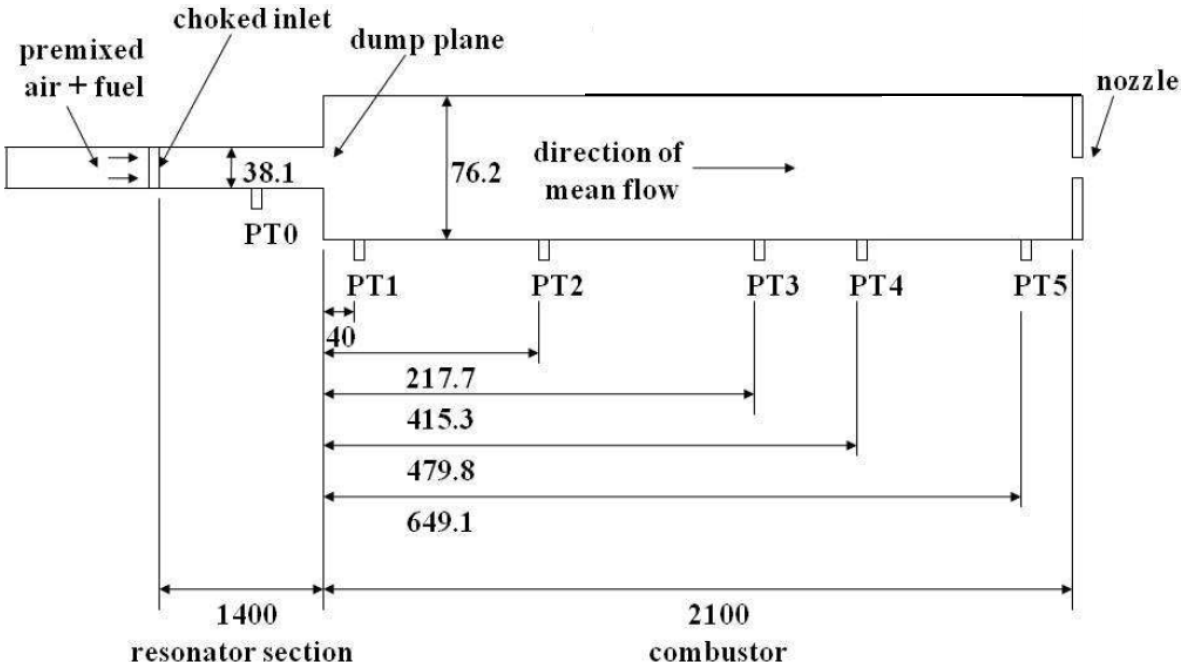

Figure 5.9: Purdue University experimental test section.

5.2.1 Validation Case Selection

Of the test cases performed on this rig, one operating condition is selected for validation of the present numerical code. Table 5.9 gives the operating conditions for the test. The design of the rig was such that the even numbered longitudinal modes contained pressure anti-nodes (velocity nodes) at the dump plane while the odd numbered modes contained pressure nodes (velocity anti-nodes) at the dump plane. In this way, the flame was located in a low pressure oscillation region for the odd modes and a high pressure oscillation regions for the even modes. Therefore, the even modes showed the strongest tendency for high limit cycle amplitudes. In particular, this test show limit cycle amplitudes at 189 and 382 Hz, which are the second and fourth modes, respectively.

Table 5.9: Reference conditions for natural gas dump combustor at Purdue University.

ϕ	$\bar{T}_{preheat}[^oC]$	$\bar{p}[bar]$	$\dot{m}[kg/s]$	$f[Hz]$
0.64	399	7.83	0.40	189, 382

The flow conditions upstream and downstream of the flame are given in Table 5.10. For this table, the mean pressure is assumed constant across the flame and the adiabatic flame temperature calculated from an equilibrium chemistry code is reported for the mean temperature downstream of the flame. In reality, there was some pressure drop due and friction and significant heat transfer through the combustion chamber walls, as shown in the RANS results to be shown later.

Table 5.10: Flow conditions for natural gas dump combustor at Purdue University.

Section	$\bar{T}[^oC]$	$\bar{p}[bar]$	$\bar{\rho}[kg/m^3]$	$\bar{V}[m/s]$	$\bar{M}$
Products	399	7.83	4.1	68	0.13
Reactants	1767	7.83	1.5	46	0.056

5.2.2 Summary of Simulation Approach

For this case, a RANS simulation and four tacFoam simulations are run. The purpose of each tacFoam simulation is to build upon the knowledge of the other simulations and reveal a particular behavior of the model. The simulations for this case are summarized in Table 5.11.

Table 5.11: Summary of simulations for Purdue dump combustor.

Solver	Type	Purpose
RANS		To obtain the mean flow
tacFoam	no q', no mean flow, closed BC	to evaluate numerical damping
tacFoam	no q', mean flow, choked BC	to evaluate boundary damping
tacFoam	linear q', no mean flow, closed BC	to evaluate linear growth rate
tacFoam	non-linear q', mean flow, choked BC	to predict limit cycle amplitude

5.2.3 RANS Simulation for Mean Flow

The Reynolds Averaged Navier Stokes (RANS) equations were solved using the finite volume method in OpenFOAM. The k-ω SST model was used for turbulence closure [51]. The combustion was modelled using a single-step reaction tracked by a reaction progress variable b. Chemical closure was obtained through a turbulent flame speed correlation [52] using a laminar flame speed calculated from a network reactor modelling tool in Cantera [53]. The mass flow and total temperature were specified at the inlet from Table 5.9 with zero gradient pressure. The turbulent intensity and length scale (estimated as one fourth of the hydraulic diameter) were used to specify inlet conditions for the turbulent kinetic energy and dissipation rate. The pressure was specified at the exit with zero gradient for the velocity, temperature, and turbulent quantities.

The walls were assumed to be at the preheat temperature. A rough one-dimensional heat transfer calculation using the lumped capacitance model (valid in this case due to the low Biot number) showed a maximum increase of about 50 K over the duration of the experiment, while a thermocouple on the outside of the chamber walls verified this estimation. The single thermocouple also showed that the walls were not even close to a thermal steady state. The specification of the fixed wall temperature as preheat temperature is the best approximation for RANS boundaries because the temperature of the walls rises slowly but steadily during the extent of the experiment. The grid resolution was controlled so as to keep the first cell in the so-called "log-law" region. Wall functions were used for wall boundary conditions for

the turbulence quantities. The velocity at the wall was set to zero (no-slip) and the pressure was set to zero gradient.

The simulation was advanced to a steady solution using OpenFOAM's bi-conjugate gradient solver. The simulation converged to a steady-state solution when the residuals dropped by three or more orders of magnitude and simulation variables from point probes showed negligible changes.

5.2.4 Grid Resolution Study

The RANS simulation was performed on three grids in order to apply the Richardson extrapolation procedure for estimating numerical discretization uncertainty [56]. The finest grid has been shown in Fig. 5.10. The uncertainty of the RANS simulation was judged in terms of the flame length, exit bulk temperature, and center-line velocity at the dump plane. These three quantities were judged to be the most influential quantities on the acoustic simulation. The flame length describes the location of the heat release that is driving any instabilities as well as the sharp density gradient that accompanies the flame. The maximum dump plane velocity describes the velocity profile seen by the flame for a given flow rate, which influences the acoustic wave propagation speed, flame length, and recirculation length. The exit bulk temperature is the most convenience measure of the amount of heat transfer through the chamber walls. For an ideal gas, the temperature

determines the sound speed. Table 5.12 summarizes the results from the grid resolution study, including the Grid Convergence Index (GCI) [56] for judging numerical uncertainty.

Table 5.12: Results from the grid resolution study for the validation with the Purdue dump combustor experiment.

No. Cells	Flame Length $[m]$	Max Dump Plane Vel. $[m/s]$	Exit Bulk Temp. $[K]$
194,400	0.628	85.1	1409
449,280	0.642	85.5	1426
1,001,640	0.666	85.9	1441
GCI [56]	5.8%	10.3%	8.4%

The uncertainties were relatively high if the study were to focus on the details of the RANS solution. For the present purposes, the RANS simulation serves only the purpose of providing the acoustic simulation with an approximate backdrop on which to study thermoacoustic stability. Other uncertainties, such as turbulence closure and flame speed closure, likely play are large role in reducing the overall accuracy of the RANS approach. In addition, the RANS simulation provides Favre-averaged variables, whereas the derivation in previous chapters showed that the thermoacoustic simulation requires simple mean variables (not density weighted). In view of these technicalities, the RANS simulation should be seen as a "quick-and-dirty" method by which the mean fields are estimated for the thermoacoustic simulation.

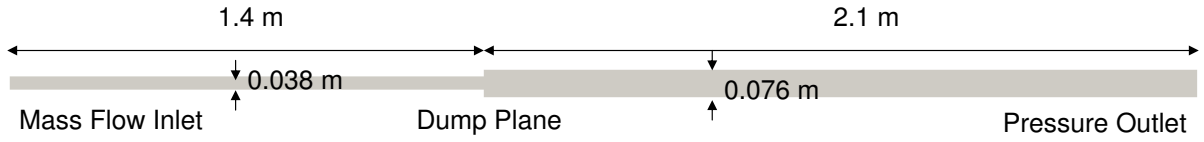

(a)

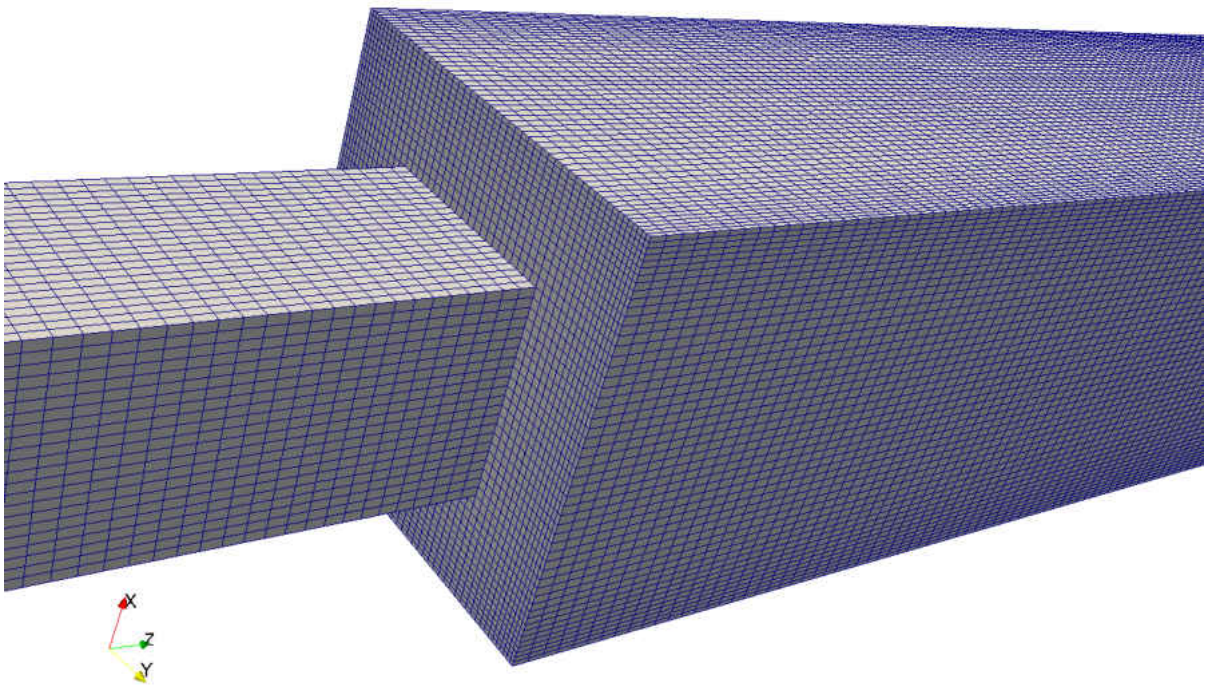

(b)

Figure 5.10: Purdue dump combustor RANS (a) domain and (b) finite volume mesh.

5.2.5 RANS Results

The mean fields, as resolved by the RANS simulation are now briefly shown. Figure 5.11 shows iso-surfaces of reaction progress variable (at b = 0.25, 0.5, and 0.75). Such iso-surfaces mark the location of the flame spatially. The flame is cone-shaped and symmetric with respect to the transverse directions. The heat release occurs in a relatively compact region of the domain, where the gas composition transitions from premixed air and fuel reactants to high temperature burnt combustion products.

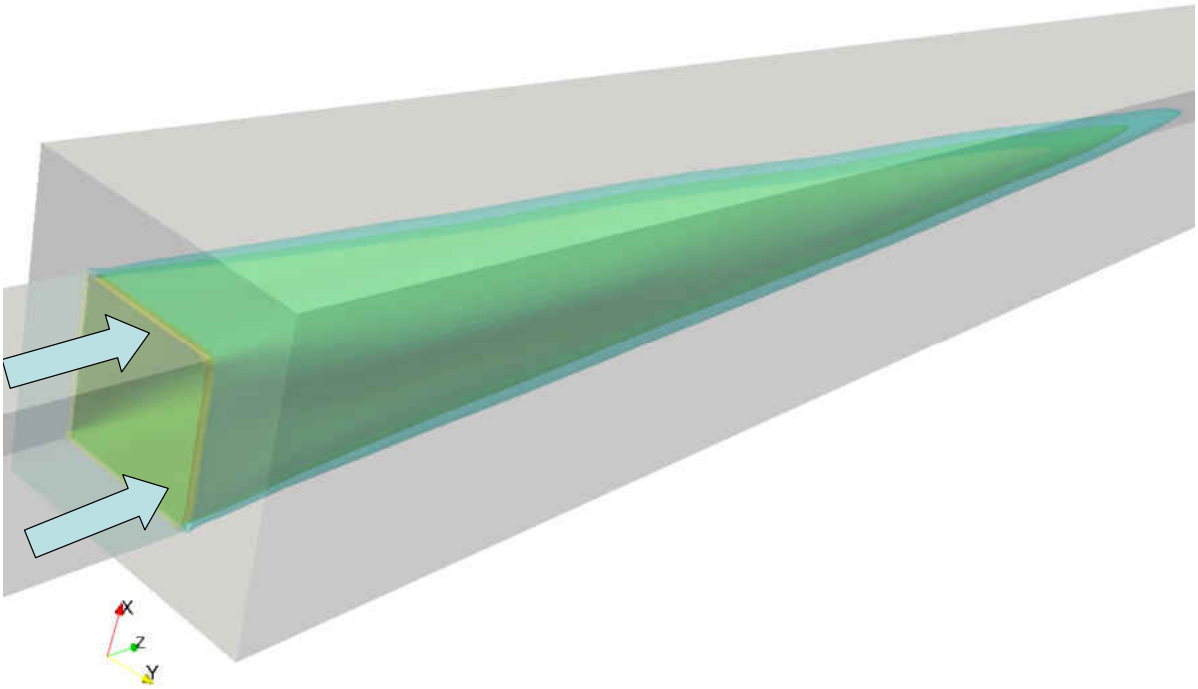

Figure 5.11: Translucent iso-surfaces of reaction progress variable outlining the spatial structure of the flame. Flow from left to right as shown by the arrows.

The variables relevant to the tacFoam simulation (after mapping) are shown in Fig. 5.12 along the center-plane of the duct. The temperature determines the sound speed, while the velocity determines the extent to which the mean flow affects the acoustic behavior of the duct. The temperature increases dramatically across the flame then slowly drops due to heat transfer through the combustion chamber walls. The amount of heat transfer predicted by the RANS is important in determining the sound speed and hence natural frequencies of the test section. The heat release, however, is the most important field to be mapped, because it contains the spatial information about the mean heat release, from which the heat release model will obtain its spatial information.

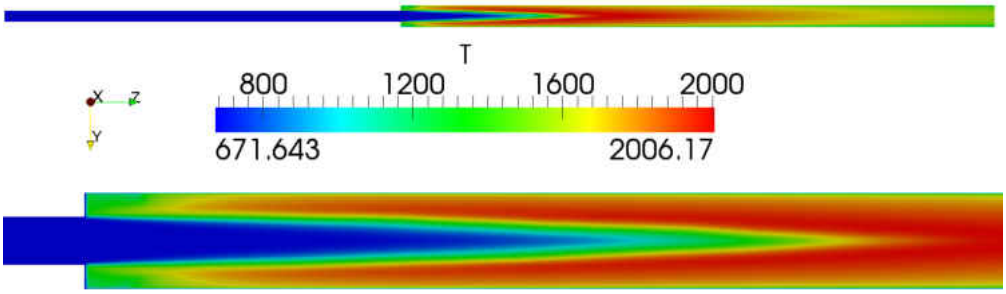

(a)

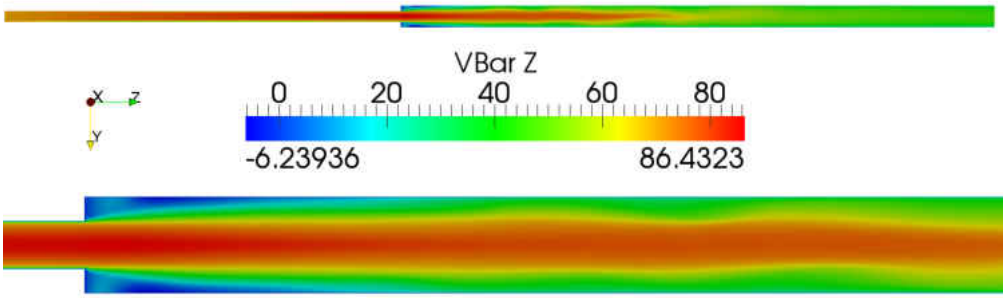

(b)

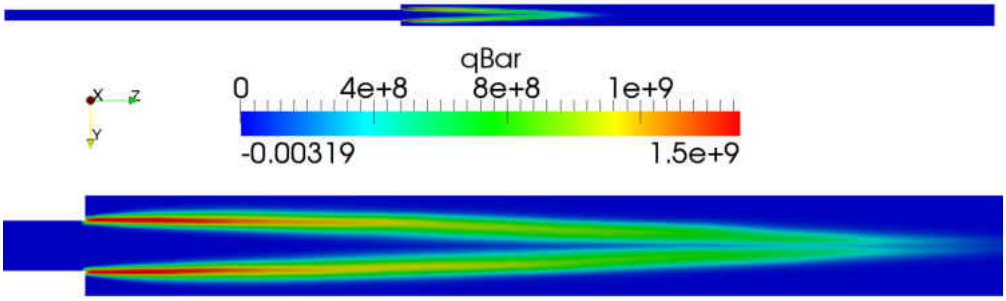

(c)

Figure 5.12: Centerplane of Purdue RANS results for the finest mesh: (a) temperature $[K]$ and (b) axial velocity $[m/s]$ and (c) heat release $[W/m^3]$.

5.2.6 Comparison of Frequencies and Modeshapes

An initial tacFoam simulation was run with perfectly reflecting boundaries and no mean velocity effects. This simulation provides baseline frequencies and modeshapes of the expected acoustic modes while also allowing to test the numerical damping from the finite volume method. The RANS simulation is interpolated to an acoustic grid, which is much coarser than the RANS meshes discussed above. The domain and grid for the tacFoam simulations is shown in Fig. 5.13. The extent of the domain is the same as in the RANS simulations, but the inlet and outlet boundaries are now specified in terms of acoustics. Three different grids were constructed for the tacFoam simulations to explore the effect of grid resolution, especially at the step change in area and in the flame region. The resolution of the step change in area has a large effect on the numerical damping of a given mode, while the resolution of the flame region affects the fidelity with which the mean field (particularly, the heat release) is translated to the thermoacoustic solver. Grid refinement is only preformed in the region containing the dump plane and the flame. The details of the grids are given in Table 5.13.

The resonant frequencies of the domain were found to be relatively insensitive to the resolution of the grid, see Table 5.14. The frequencies for the second and fourth modes were matched with less than 2% error. The main effect of grid refinement was a drop in numerical damping. As shown in Table 5.15, the 2L and 4L modes have much lower damping coefficients than the odd-numbered modes. In other words, the presence of the area change

adds a significant amount of damping to the 1L and 3L modes, but not for the 2L and 4L modes. The even-numbered modes have a velocity node at the dump plane, but the odd-numbered modes have a velocity anti-node. The amplitude of velocity fluctuations at the dump plane likely controls the amount of numerical damping added by the area change for a mode. The reason for this is that the velocity is a vector quantity, requiring an abrupt change in direction at the dump plane. Modes with a high velocity component at the dump plane are then more sensitive to the grid resolution in that region.

Table 5.13: Grid characteristics for thermoacoustic grids of Purdue experiment.

	No. Cells	Min. Cells/Wave (2L)	Cells/Step-Height	Max. Aspect Ratio
coarse	10,560	207	2	1.6
medium	35,760	207	4	1.6
fine	206,896	207	8	1.6

Table 5.14: Resonant frequencies (Hz) for first four modes with perfectly-reflecting boundaries.

	1L	2L	3L	4L
(Exp.)	–	189	–	382
coarse	92	189	275	377
medium	92	189	276	376
fine	92	189	276	376

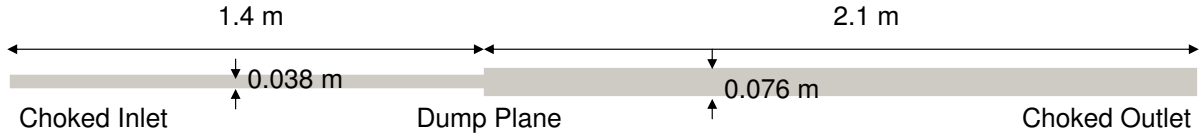

(a)

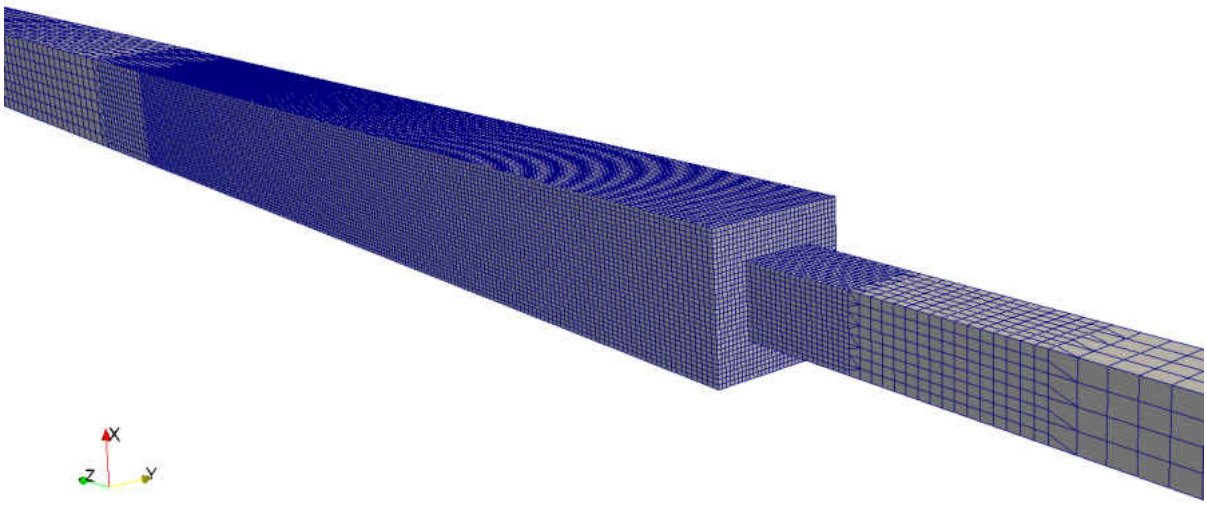

(b)

Figure 5.13: Purdue dump combustor acoustic simulation (a) domain and (b) finite volume mesh.

Table 5.15: Numerical damping coefficient (1/sec) for first four modes.

	1L	2L	3L	4L
coarse	5.9	0.20	10.3	0.52
medium	3.4	0.05	6.3	0.16
fine	1.8	0.03	3.3	0.10

The pressure modeshapes on a cut-plane through the center of the domain are shown in Fig. 5.14. For this figure, no color scale is necessary, since it is customary to discuss acoustic modes in terms of normalized amplitudes. The blue regions of this figure correspond to a normalized amplitude of zero and the red regions correspond to a normalized amplitude of one. It can be seen from this figure that the modes contain little variation in the transverse direction. In view of this fact, the modes are best presented in a one-dimensional manner, as done in Fig. 5.15.

The odd-numbered modes have low normalized amplitudes in the combustion chamber, while the even-numbered modes have approximately equal amplitude in the regions upstream and downstream of the dump plane. Also, the even-numbered modes have pressure anti-nodes at the dump plane which the odd-numbered modes have pressure nodes. In the view that acoustic modes are fed energy via the coupling of heat release and pressure oscillations (Rayleigh's criterion), the above reasons suggest that the even-numbered acoustic modes will be much more likely excited than the odd-numbered modes. This is, in fact, what the experiment observed.

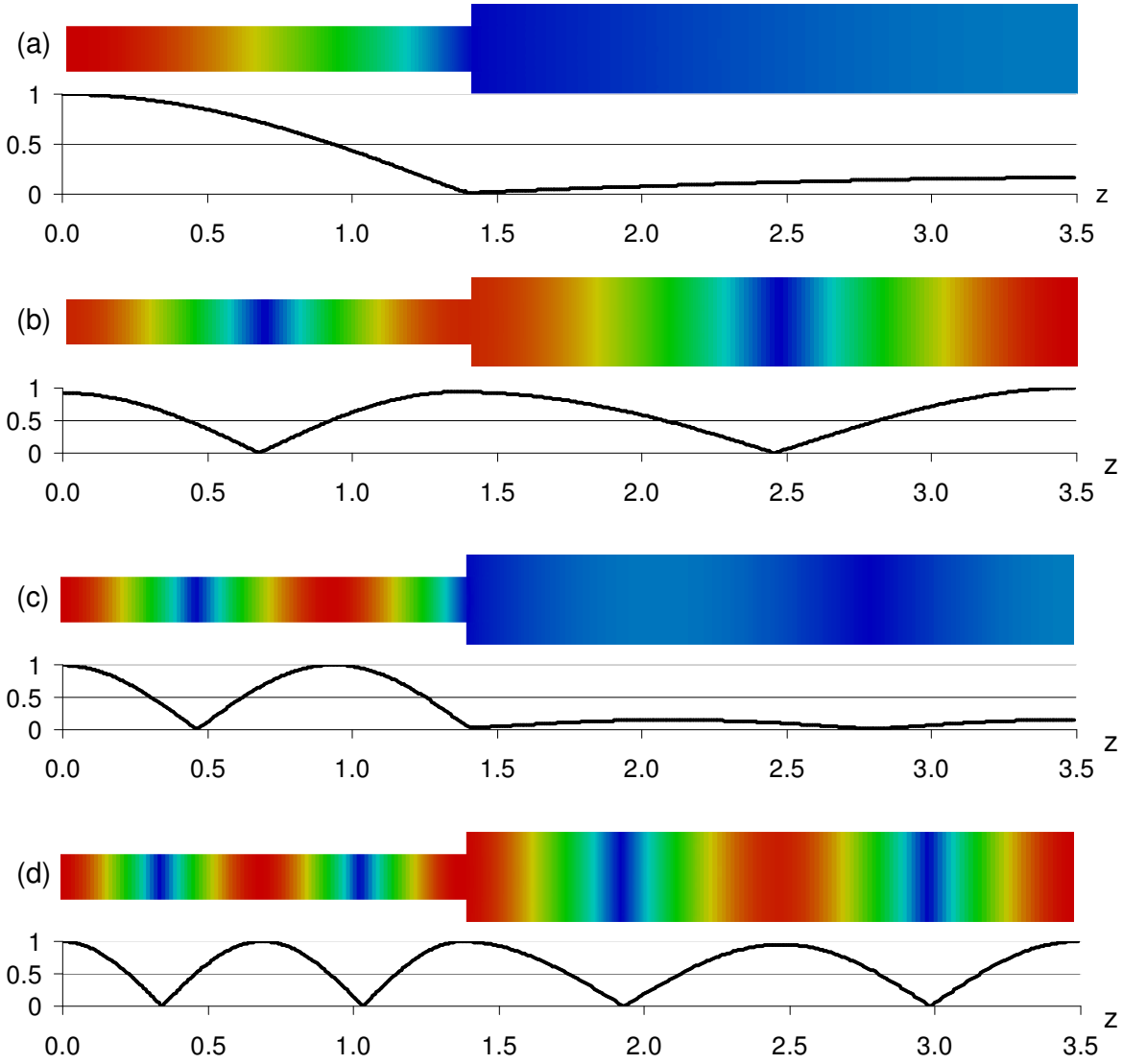

Figure 5.14: Purdue rig normalized acoustic pressure mode amplitudes on a color scale of blue (zero amplitude) to red (max amplitude) : (a) 1L, (b) 2L, (c) 3L, (d) 4L.

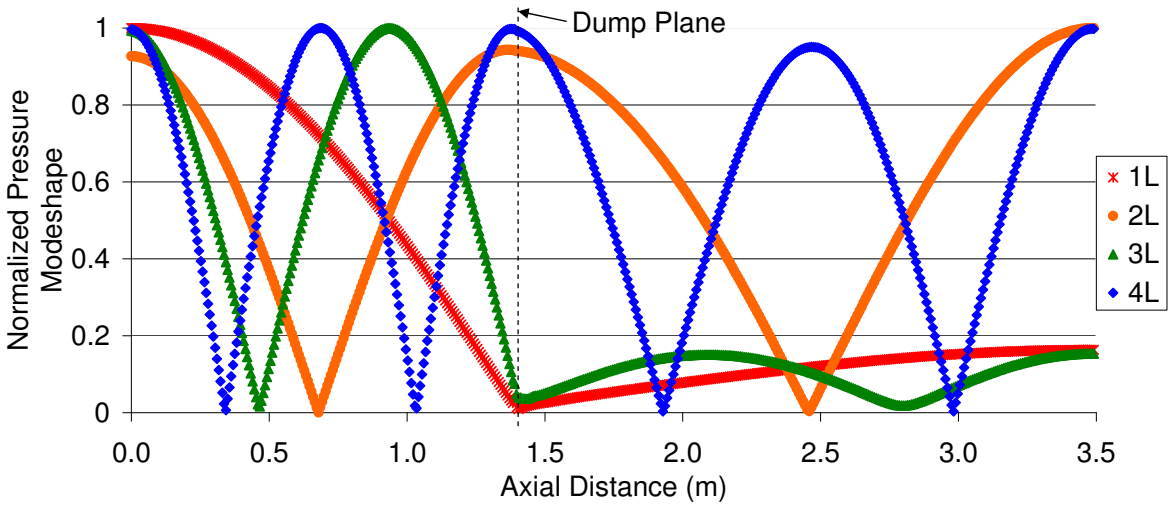

Figure 5.15: Normalized acoustic pressure fluctuation amplitude for the first four modes along the center-line of the domain.

5.2.7 Boundary Damping

Following the initial simulations for determining frequencies and modeshapes for the acoustics of the domain, two additional simulations were executed to ascertain the damping rates from boundary and mean flow effects as well as the linear growth rate from the heat release. The comparison of these rates with the numerical damping is important to show the extent to which numerical damping may affect the results of the solver. Unlike the previous simulations, the mean velocity field from the RANS simulation is retained for this second set of simulations.

First, without adding any heat release to the simulation, the perfectly-reflecting boundary conditions are replaced by a choked inlet [24] and choked outlet boundaries [54]. Without taking into account entropy waves, the reflection coefficients for these boundaries are given by Eqs. (5.1) and (5.12)

$$R_{outlet} = \frac{1 - \gamma\bar{M} + (\gamma - 1)\bar{M}^2}{1 + \gamma\bar{M} + (\gamma - 1)\bar{M}^2} \tag{5.12}$$

These reflection coefficient formulae are used to set the boundary impedance at the inlet and outlet to the domain. For this particular case, the reflection coefficient of the choked inlet is 0.764 and the reflection coefficient of the outlet is 0.985. The purpose of this simulation is to quantify the damping of the acoustic modes due to acoustic energy flux through the boundaries and through interaction with the mean flow. The resulting frequencies and damping coefficients are given in Table 5.16 respectively. Because the odd-numbered modes are dominant in the upstream region, the reflection coefficient at the inlet has a larger effect on these modes. In fact the peaks for the 1L and 3L modes are absent from the results of this simulation. A small shift in the frequencies were observed, but the 2L and 4L modes are still predicted with less than 3% error from the experimental frequencies. The damping coefficient (negative growth rate) is now much higher than in the previous simulation (Table 5.15). Because of this, the influence of numerical damping on the values in Table 5.16 is negligible and these values can be interpreted as the damping rate associated with the loss of acoustic energy through the boundaries and to the mean flow.

Table 5.16: Resonant frequencies (Hz) and damping coefficients (1/sec) for first four modes with choked boundaries.

	2L frequency	2L damping	4L frequency	4L damping
(Exp.)	189	–	382	–
coarse	188	10.1	374	12.4
medium	188	11.3	373	15.3
fine	188	10.6	373	13.2

5.2.8 Linear Heat Release Model

For the third simulation of this geometry, the mean velocity is once again removed and the boundaries are reset to perfectly-reflecting conditions. After eliminating those sources of damping, a linear heat release model is implemented. This simulation, therefore, measures the linear growth rate due to heat release. The comparison of growth rate due to heat release and damping due to acoustic energy losses indicates the linear stability of a mode. The linear stability of a mode could be determined with one simulation rather than two by including both heat release and loss mechanisms in a single simulation. For illustrative purposes, the simulations were performed separately.

For flames anchored by a backward-facing step or sudden area change, a vortex shedding model is common for capturing the physics of the acoustics-heat release feedback loop

[57]. With this in mind the Strouhal numbers of the 2L and 4L modes are 0.053 and 0.107, respectively. Here, Strouhal number is defined as

$$St_H = \frac{fH}{U_0} \tag{5.13}$$

where H is the step height and U_0 is the approaching velocity. The experiments of [58] found a dominant frequency of vortex shedding with $St_H = 0.07$. Large-eddy simulations of the same geometry and flow conditions [59] found $St_H = 0.09$ was the dominant frequency of vortex shedding. Meanwhile, other experiments [60] found that the drag for a backward facing step is minimum with local forcing at $St_H = 0.27$. Appealing to [61], the authors argue that this represents the vortex shedding frequency of the backward-facing step. The spectra from their measurements, however, reveal peaks at $St_H/4$ and $St_H/2$, suggesting that the actual dominant frequency of the step may be lower, with the minimal drag forcing frequency of $St_H = 0.27$ being a higher harmonic of the base frequency. Reynolds number dependence is the other likely explanation for the disagreement.

Apparently, the frequencies of the 2L and 4L modes in the Purdue experiment lay in the approximate region necessary for interaction with vortex shedding from the dump plane. A sophisticated heat release model for vortex shedding combustion instability has been developed, leading to a kicked oscillator equation [16]. For the present purposes (demonstrating a numerical technique), a simpler model is constructed. In this model the shedding pattern of vortices promotes a sinusoidal heat release pattern in time. The release of a vortex occurs at an acoustic pressure minimum at the dump plane and the vortex travels downstream at a half of the mean flow velocity upstream of the dump plane [16]. The heat release maximum

occurs at the center of the vortex. This leads to the mathematical phrasing

$$q'(x,y,z,t) = -n\frac{\bar{q}(x,y,z)}{\bar{p}_0}p'_0(t-\tau(z)) \tag{5.14}$$

where the time lag

$$\tau(z) = \frac{z-z_0}{0.5U_0} \tag{5.15}$$

represents the time it takes for the vortex to travel from the dump plane to the location of the heat release. The subscript $_0$ represents the value at the dump plane. The negative sign represents the fact that this model predicts that the vortex release (maximum heat release) occurs at an acoustic pressure minimum at the dump plane. For the linear heat release model, the gain factor n is assumed independent of the acoustic variables. A value of $n = 25$ is used for the present case, but this value would likely need to be tuned to experimental results to result in accurate reproduction of linear growth rate or limit cycle amplitude (for a non-linear model). For this simulation, the 2L mode grew rapidly, drowning out any growth of the 4L mode. For this reason, Table 5.17 reports values for only the 2L mode. Because the two previous simulations indicated that the numerical damping would not play a large role in determining accuracy of growth rates, the finest mesh was not simulated.

The frequency errors are again less that 3%. However, the linear growth rates for the two mesh resolutions are quite different. The previous discussion ruled out numerical or boundary damping as a reason for such a discrepancy. The numerical damping for the 2L mode was much to small to create the difference shown here, and the boundary damping was very similar for these two meshes. There is significant difference in the grid resolution

as it relates to the flame thickness, however, suggesting that the discretization as it relates to heat release plays an important role in the determination of the linear growth rate. To illustrate this point, Fig. 5.16 shows the heat release distribution on a cut plane for the two tacFoam meshes. Qualitatively, the heat release distributions are very different, since they are both mapping from a one million cell RANS mesh that is much finer in resolution. When coupled with a heat release model that is dependent on distance from the dump plane, it is no surprise that this difference leads to the difference in linear growth rates shown in Table 5.17. Consequently, this also leads to the expectation that there may be a noticeable difference in limit cycle amplitude when a non-linear model of the same type is used.

Table 5.17: Resonant frequencies (Hz) and linear growth rate (1/sec) for the linear heat release model simulation.

	2L frequency	2L amplitude
(Exp.)	189	–
coarse	192	27.8
medium	193	15.7

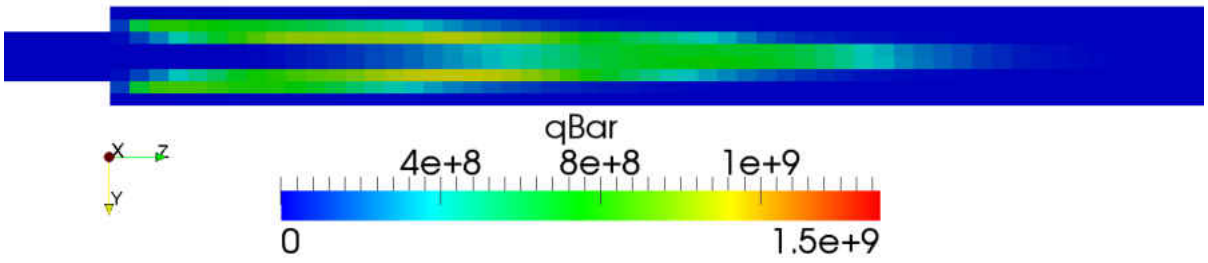

(a)

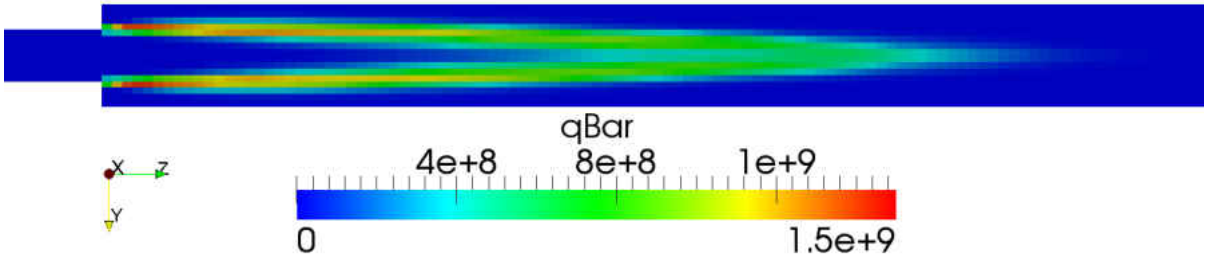

(b)

Figure 5.16: Mean heat release fields on the center-plane after mapping from RANS solution onto tacFoam grid : (a) no refinement, (b) one level of refinement

5.2.9 Non-linear Heat Release Model

For a final simulation set with non-linear heat release model, the time lag calculation is not changed from Eq. (5.14) and Eq (5.15). Only the gain factor n becomes a function of the acoustic pressure amplitude. In particular, the form

$$n = A_n e^{-B_n p'_{RMS}} + C_n \tag{5.16}$$

is used, as was the form for the Hield et al. [47] validation case. Here, the values chosen for the constants A_n, B_n, C_n are not from an experimental correlation. For the present demonstrations, the values taken are

$$A_n = -24 \tag{5.17}$$

$$B_n = 0.0001 \frac{1}{Pa} \tag{5.18}$$

$$C_n = -1 \tag{5.19}$$

The values A_n and C_n add to -25, so that the small signal limit yields the same gain factor ($n = -25$) as the linear model. The negative value reflects that the model assumes that the vortex is released at the pressure minimum and the maximum heat release corresponds to the location of the vortex as it convects downstream. The value for B_n (specifically, its multiplicative inverse) sets the characteristic pressure value at which the non-linearities of the flame become manifest. As previously mentioned, a complete model would require the tuning of these constants to a specific configuration, as done by [47, 48] for a bluff body stabilized flame.

The temporal evolution of acoustic pressure for the non-linear heat release simulations is shown in Fig. 5.17. The mode from the medium grid grows more slowly than that from the coarsest grid. This observation is consistent with the lower linear growth rate observed in Table 5.17 for the medium grid. The limit cycle amplitude reached is also lower for the simulation with the refined grid. This shows the proportionality of linear growth rate and limit cycle amplitude [12] for the two different grids.

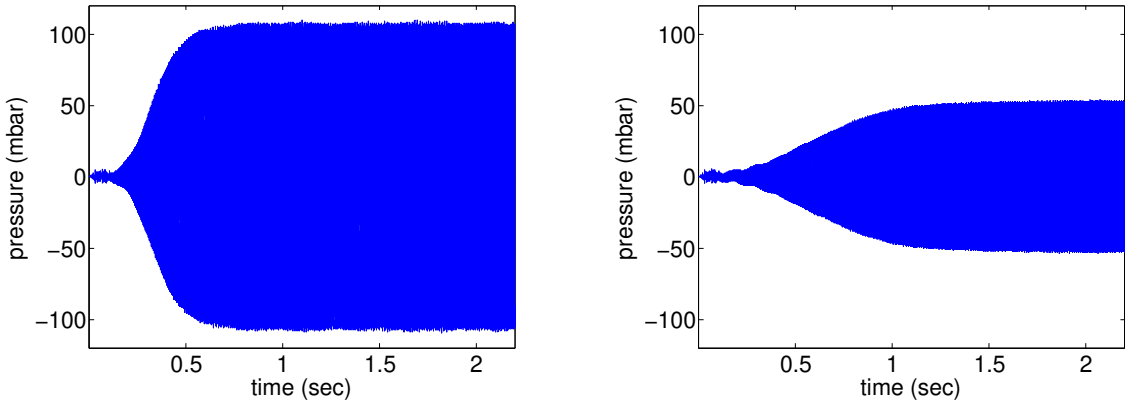

(a) (b)

Figure 5.17: Pressure time histories for a simulation probe near the exit of the domain : (a) no grid refinement, (b) one level of grid refinement

Table 5.18 gives the comparison of limit cycle amplitude for the two simulations with experimental data for these flow conditions. Note that for both the experimental and numerical data, the limit cycle amplitude is an average of amplitudes from five pressure probes placed along the length of the combustor (downstream of the flame). The probe locations for the experiment and simulation were identical. Both simulations under-predict

the limit cycle amplitude of the 2L mode, but are of the right order of magnitude. The 4L mode, while very strong in the experiment is absent from the simulation.

Table 5.18: Limit cycle amplitudes (mbar) for first four modes.

	2L frequency	2L limit cycle	4L frequency	4L limit cycle
(Exp.)	189	54	382	279
coarse	189	123	374	0.2
medium	190	59	375	0.3

The Rayleigh index (RI), defined in Eq. (5.20), is calculated over the course of each equation at each cell. The Rayleigh index calculation is done in the frequency domain, so that the index is available as a function of frequency. The results of such a calculation gives insight into what regions of the domain are driving or damping a given mode. Negative values indicate that the heat release at that point, over the course of the simulation, tends to remove acoustic energy from the domain. On the other hand, positive values indicate the addition of acoustic energy by the unsteady heat release.

$$RI = \int p'q'dt \tag{5.20}$$

The comparison in Figs. 5.18 and 5.19 highlight the effect of grid resolution on the stability of the mode. The Rayleigh index shows an alternating pattern of damping and driving regions. Physically, this represents the vortex, shed from the dump plane at a pressure minimum, convecting downstream. The continuing acoustic oscillations bring the

vortex (positive heat release fluctuation) in an out of phase with the pressure, leading to the pattern seen in Fig. 5.18 for the 2L frequency. A similar pattern is seen in Fig. 5.19 for the 4L frequency, except that the phase of the vortex is altered at a higher frequency than the 2L mode.

While the 2L and 4L modes display the same pattern, the results showed that only the 2L mode was excited to a large amplitude limit cycle. The overall excitation of the mode is related to the Rayleigh criterion, which is determined by the integration of the Rayleigh index over the entire domain. The 2L integrated Rayleigh index shows an increase by three to four orders of magnitude over the 4L, while the odd numbered modes are even much below that. The integrated Rayleigh index for the 2L decreases from the coarse grid to the fine grid, which was manifest in the decrease of the limit cycle amplitude from 36 millibar to 21 millibar. The 4L mode integrated Rayleigh index increases as the mesh is refined, however.

Table 5.19: Volume integrated Rayleigh index ($W \cdot Pa$) for first four modes.

	1L	2L	3L	4L
coarse	–	4.29E+05	–	6.55E+01
medium	6.90E-01	1.57E+05	1.12E-01	2.75E+02

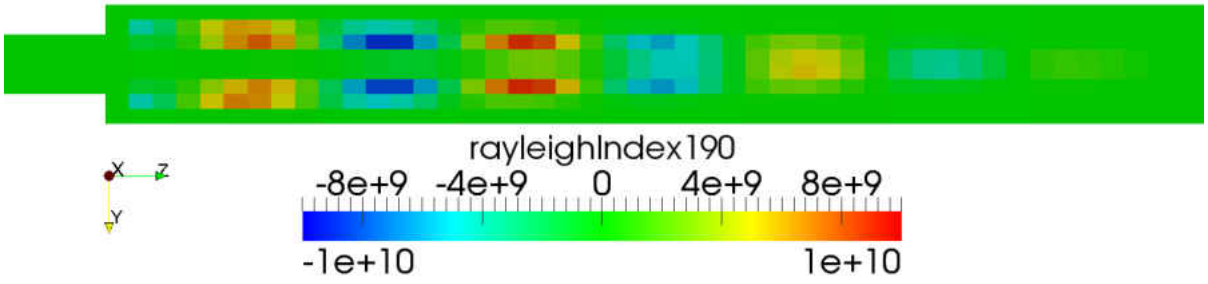

(a)

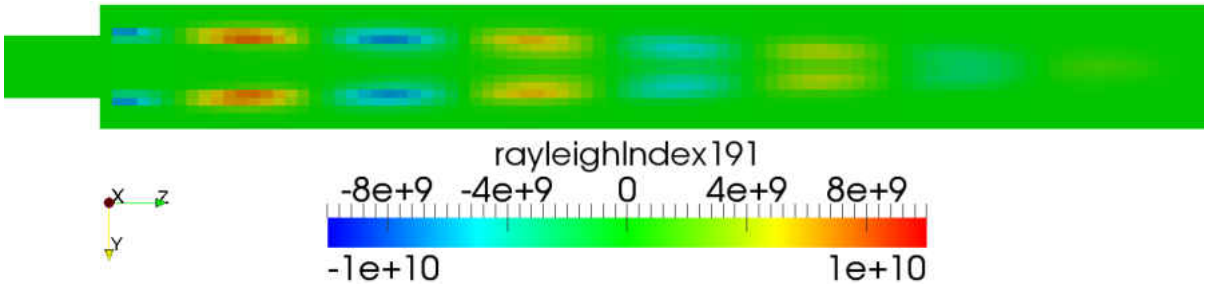

(b)

Figure 5.18: Rayleigh index ($W \cdot Pa/m^3$) field for 2L frequency on two grids: (a) no refinement, (b) one level of refinement

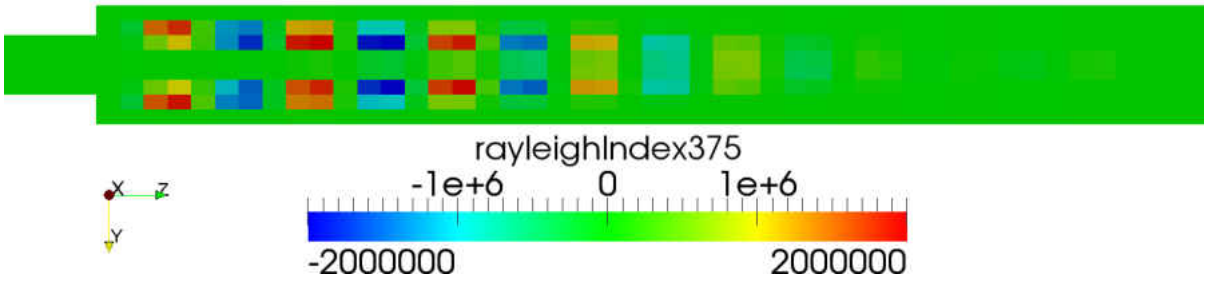

(a)

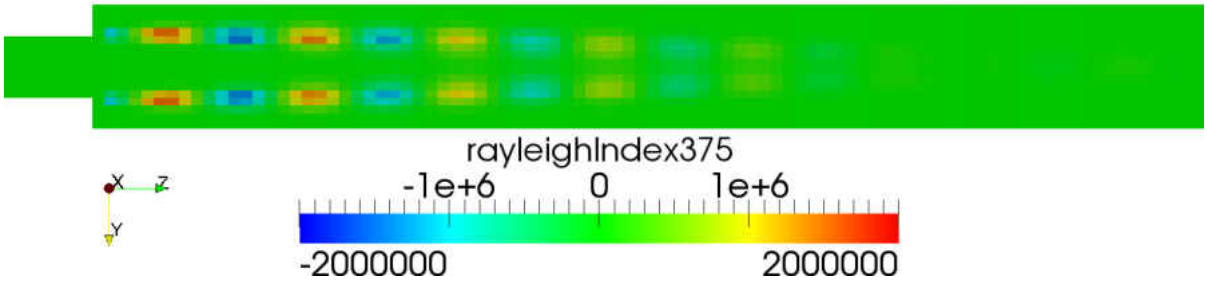

(b)

Figure 5.19: Rayleigh index ($W \cdot Pa/m^3$) field for 4L frequency on two grids: (a) coarse grid, (b) fine grid

5.2.10 Sensitivity to Model Constants

The experimental study of this combustor did not result in an empirical flame model as provided by Hield et al. [47]. Because of this, the constants (A_n, B_n, C_n, and α) used for the heat release model were determined in a somewhat arbitrary way. The least arbitrary of the coefficients is the vortex convection speed coefficient α, which is typically close to the average of the two velocities in a shear layer. In this case, the average between the jet flow and the recirculation region yields and value of $\alpha = 0.5$ if the recirculation region is assumed to be approximately stagnant compared to the velocity of the jet.

A sensitivity analysis of these model parameters provides information about how the choice of parameters affects the limit cycle amplitude prediction. The goal is to show that the model parameters can be tuned (e.g. as a function of equivalence ratio and pre-heat temperature) so as to match experimental limit-cycle amplitudes. The sensitivity analysis was performed simply by varying one parameter at a time from the baseline values that produced the results in Table 5.18. The values used in the sensitivity analysis are shown in Table 5.20.

The results are shown in Fig. 5.20. The three first three parameters have clear trends, while the trend is less clear for the vortex convection speed coefficient. The pre-multiplier value A_n directly controls the low amplitude limit of the heat release model. As A_n increases, the value of the gain coefficient given by Eq. (5.16) increases for a given value of pressure amplitude. As a result, the limit cycle amplitude prediction is increased for an increasing

Table 5.20: Parameter variation for sensitivity analysis.

	low	baseline	high
A_n	-12	-24	-28
$B_n(1/Pa)$	0.00005	0.0001	0.0002
C_n	-0.5	-1	-2
α	0.25	0.5	1.0

A_n. A similar analysis applies to C_n which controls the high amplitude limit of the flame describing function. The limit cycle is not as sensitive to this value, however, indicating that the flame does not approach the high amplitude limit in the simulation. The third coefficient in Eq. (5.16) has the opposite trend. The primary interpretation of B_n is that it is the inverse of a characteristic pressure scale. Thus, its inverse indicates the order of magnitude of pressure amplitude at which non-linear flame saturation effects are relevant. In this way, it has a strong effect on the limit cycle amplitude, but with the opposite trend as A_n and C_n. Unlike A_n, however, adjusting only B_n cannot lead to the complete elimination of the oscillations.

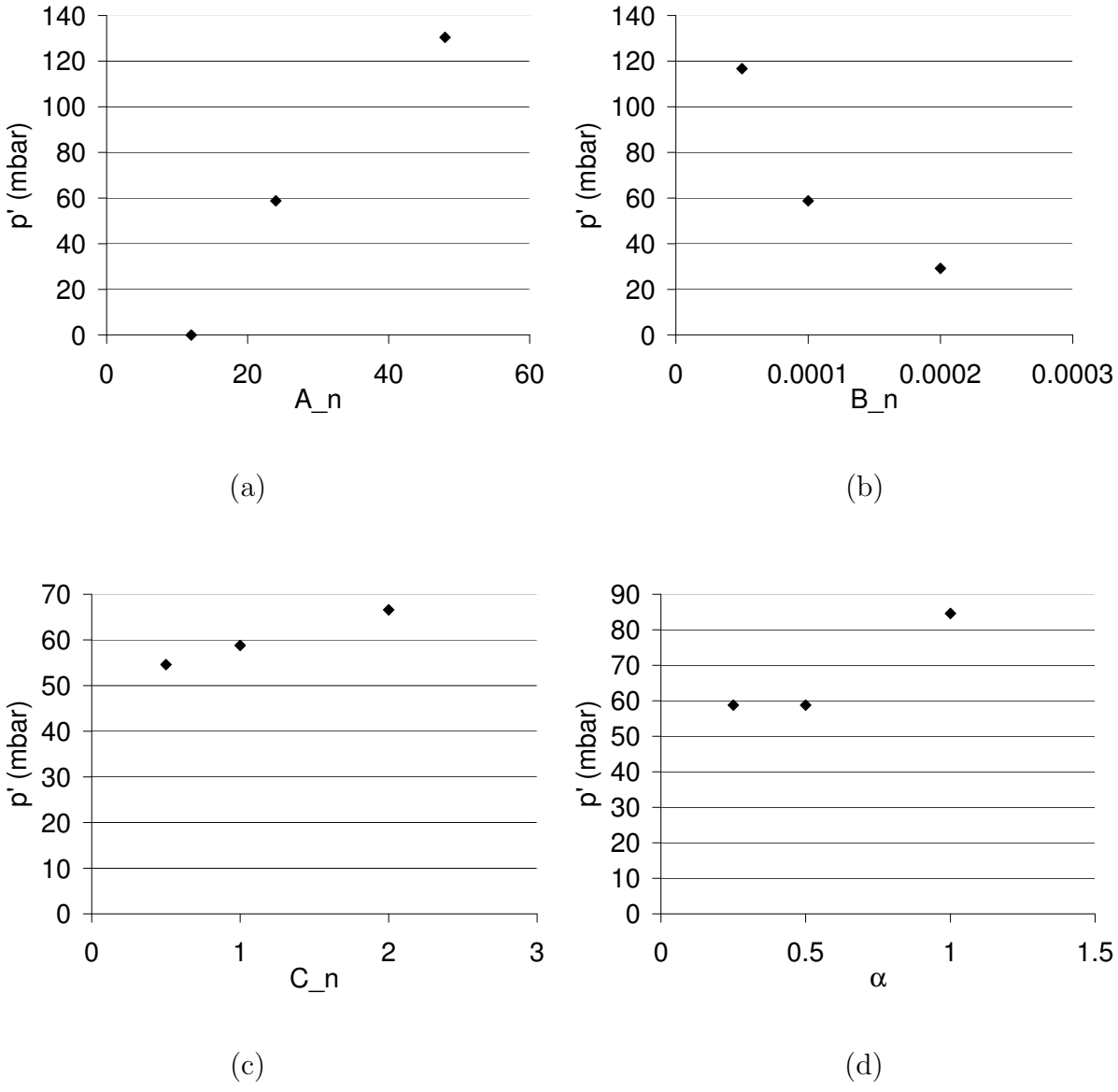

Figure 5.20: Sensitivity analysis for adjustable parameters in non-linear vortex shedding model.

5.2.11 Cost of Simulations

As a final note, it is instructive to compare the computational resources necessary for tacFoam simulations with that of LES simulations. This validation case is optimal for such comparisons due to the availability of LES work on this very same geometry [62]. As discussed above, two different grids were run for the tacFoam case. The first was a baseline coarse mesh with no refinement. The second mesh was refined in the flame region. Similarly, the LES study used two grids, one coarse and one refined. A comparison in computational cost is shown in Table 5.21.

Table 5.21: Comparison of computational resources for tacFoam and LES analysis of Purdue dump combustor.

	tacFoam coarse	tacFoam fine	LES coarse	LES fine
cells	10,560	35,680	840,200	2,986,748
time step (sec)	1e-5	5e-6	5e-7	4e-7
total time (sec)	1.2	1.2	0.5	0.5
processors	4	12	240	240
wall-time (hours)	2.75	15.6	120	336

5.2.12 Conclusion

In conclusion, the Purdue dump combustor experiments were modelled by the present thermoacoustic simulation code. The numerical damping for the 2L and 4L modes was much less than the boundary damping and linear growth rates provided by the choked boundaries and non-linear flame describing function, respectively. A physically motivated vortex shedding model was used for the unsteady heat release based on mean heat release profiles mapped from a RANS solution. A high amplitude limit cycle was observed for the 2L mode, but the 4L mode was not present, most likely due the model or the model's constants. The amplitude of the 2L mode was on the same order of magnitude as the experiment, but the coefficients used in the model would need to be tuned to match the experiment (similar to that done by Hield et al. [47, 48]). The absence of the 4L mode from the simulation was in contrast to the experiment, where the 4L mode was a greater amplitude than the 2L mode. This result suggests that the vortex-based heat release model, while shown plausible for the 2L mode, is not plausible in its current form for the 4L mechanism. Further research and simulation is needed to determine other possible mechanisms for the 4L mode. One possibility is that two different sets of tuned coefficients would be necessary to capture both modes with the vortex model. Another possibility is to vary phase relationships could be employed with respect to the pressure fluctuations at the dump plane. The most important characteristic of the above model is its explicit dependence on dump plane pressure rather than velocity. Velocity dependence, in this case, would most likely lead to strong 1L and

3L coupling, since these modes have pressure nodes and velocity anti-nodes at the dump plane. Pressure dependence, however, gives the desired strength to 2L coupling, which has a pressure anti-node and a velocity node at the dump plane.

The necessity of tuning the constants underscores a major limitation in the present approach to modelling the unsteady heat release of a turbulent flame under the influence of acoustic perturbations. Further work with modelling the Purdue experiments could include tuning the coefficients (or phase relationship between the dump plane pressure and the release of a vortex). The coefficients could also be tuned with variables such as pre-heat temperature and equivalence ratio to model lean blow-off effects. This limitation is a natural consequence of its standing on the cost versus accuracy scale. Just as many RANS models rely on constants tuned for various canonical flows but by no means universal. In the same way, constants could be tuned for a particular flame and used for predicting trends on similar flames, but lack on universality is certainly expected for $n - /tau$ heat release models. For simulations requiring less constants (or less influential constants), large-eddy simulations can be performed, albeit at a significant cost increase. The tuning of constants for appropriate time lag models is out of the scope of this work.

CONCLUSION

Summary

In this thesis, the development of a novel three-dimensional linear thermoacoustic solver was presented. The solver was written using the OpenFOAM C++ libraries for unstructured finite volume meshes. The solution process includes interpolating a known mean field solution onto the finite volume mesh intended for the acoustic solution. The linearized Euler equations with a source term for unsteady heat release are discretized and solved using a fourth-order Runge-Kutta method and second-order total variation diminishing Godunov flux calculation. The Riemann solution for acoustics in inhomogeneous media is utilized at each numerical face in a non-conservative flux scheme, allowing for accurate high-resolution capturing of variations in both acoustic and pre-computed mean field data. For application to gas turbine combustors, it was shown that the accurate representation of the effect of density gradients on acoustic waves is vital to the successful prediction of resonant frequencies and modeshapes. The thin premixed flames appear as sharp density gradients, greatly altering the acoustic behavior of the combustion chamber. The governing equations require an unsteady heat release model based on acoustic velocity or acoustic pressure to close the system and provide a feedback path between the acoustic and heat release oscilla-

tions. The modelling success of the simulation relies heavily on the physical fidelity of the heat release model. Indeed, a major ability of this code is to test such models in a complex three-dimensional geometry with accurate mean fields. In this way, physical insight can be gained through the comparison of various heat release models with known results. In addition, models constants can be tuned to match experiments for exploring operating ranges and parametric effects. A number of verification tests were run to identify to validity of the solver for various simple "academic" problems. The solver successfully reproduced analytical solutions for one-, two-, and three-dimensional acoustics, gradual and sharp density gradients, subsonic mean flow, arbitrary (real, constant) impedance boundary conditions (e.g. choked), and linear growth rates in a Rijke tube with simple n-τ heat release model. These tests were designed to verify the ability of the solver to account for the important physics governing the development of large amplitude acoustic oscillations in gas turbine combustors. Finally, the solver was validated with two different laboratory-scale combustors. First, a bluff body stabilized flame experiment at the University of Melbourne provided an excellent validation case. The experimental study performed in Melbourne used chemiluminescence data over a range of operating conditions to establish a non-linear heat release law in which the gain and time lag were dependent on the amplitude of oscillation. The descrease in gain with increasing acoustic amplitude, along with choked boundaries, allowed for the development of a limit cycle in the linear simulation. The limit cycle amplitude found reproduced the experimental limit cycle accurately. The second validation case involved a recent dump combustor experiment at Purdue University. No empirical heat release was developed by the

experimentalists in this case. Instead, a physically motivated vortex shedding model was used for the simulation. With arbitrary (untuned) coefficients in the model, a limit cycle of the same order of magnitude as the experiments was obtained was obtained for one of the modes but not for the other. The effect of grid resolution for RANS and acoustics were also explored.

Further Work

The following steps are recommended for further development of the numerical simulation procedure described in this thesis.

(1) For this thesis, the solver was limited to analytical and laboratory-scale scenarios. The solver remains to be tested in a full-scale engine geometry with comparison to engine data. This is the end goal of the solver and represents the most obvious extension of the work in this thesis.

(2) The governing equations used for this thesis solved for acoustic velocity and pressure, relying on the isentropic signal assumption to account for acoustic density. In real combustors, an unsteady flame generates entropy waves which convect downstream with the mean flow. These entropy waves can play an important role not only in the effecting acoustic propagation, but also in the exit boundary conditions, where the interaction of entropy waves with the boundary can produce an upstream-travelling acoustic wave. In addition to the four linearized equations solve in this thesis, the inclusion of a fifth equation for the acoustic

density fluctuations would give the solver the ability to account for entropy waves. While causing additional cost to the simulation, this enhancement would add important physical fidelity to the model. The choked outlet case from the University of Melbourne experiments could be used to validate the ability of the code to capture entropy waves, since the observed instabilities in that case were due to the propagation of entropy waves and generation of an acoustic wave at the choked exit.

(3) The solver developed in this thesis is designed to play a role in the design and development process between one-dimensional thermoacoustic tools and large-eddy simulations. Based on the three-dimensional modeshapes that can be found by the finite volume solver, a weighted-residuals approximation method can be developed within the OpenFOAM framework. This extension would allow for quick solution including only evaluation of three-dimensional integrals over the domain and solution to the resulting ODE. Sophisticated ODE solvers, such as Runge-Kutta methods, are already available in the OpenFOAM libraries. Many of the mean flow and boundary effects could be easily accounted for in an accurate three-dimensional manner by integrating over the finite volume domain otherwise used to solve the full system of PDEs. Such a weighted residual method would offer a quick, approximate solution that would have advantages over one-dimensional tools, but have a solution time orders of magnitude less than the full thermoacoustic solution. This would allow for parametric sweeps of important variables or of hypothesized heat release models.

(4) The boundary conditions for the solver developed in this thesis accounted for traditional acoustic boundary conditions (no mean flow, etc...). Improved boundary conditions

using a characteristic approach similar to the LODI approach of compressible DNS/LES would allow for more accurate representation of boundary conditions in a more complex, inhomogeneous field. Additionally, the initial success of the time-domain complex impedance boundary conditions was limited. Additional testing and research into the implementation of this boundary condition is suggested.

APPENDIX A
DERIVATION OF GOVERNING EQUATIONS

APPENDIX A
DERIVATION OF GOVERNING EQUATIONS

Starting with the general governing equations for the continuum model of fluid flow, this section will develop the equations of motion by which thermoacoustic phenomena can be modelled. The physical principles applicable to the continuum model of gas dynamics are the conservation equations of mass, momentum, energy, and entropy, as well as an equation of state to close the system.

A.1 Conservation of Mass

The conservation of mass, or continuity equation, simply states that the rate of change of mass inside a fixed control volume in laboratory coordinates is equal to the difference between the incoming and outgoing mass, adding any mass sources or sinks. For an arbitrary control volume

$$\frac{\partial}{\partial t}\iiint_{\Omega} \rho dV = -\iint_{\partial\Omega} \rho u_j dA_j + \iiint_{\Omega} \mathcal{M} dV \tag{A.1}$$

where the outward pointing normal has been used to define the differential surface area dA_i and $\mathcal{M}$ is the mass source/sink density. In Eq. (A.1), $\mathcal{M}$ represents any source of mass present within a given control volume. For example, the evaporation of liquid droplets into

gas can be modelled simply by this term. Applying the divergence theorem to the first term on the right hand side bringing the time derivative inside the integration on the left hand side

$$\iiint_{\Omega} \frac{\partial \rho}{\partial t} dV = - \iiint_{\Omega} \frac{\partial (\rho u_j)}{\partial x_j} dV + \iiint_{\Omega} \mathcal{M} dV. \tag{A.2}$$

This is the integral form of the mass conservation, provided the differentiability considerations for the divergence theorem are satisfied and the interchangeability of differentiation in time and integration in space is valid. In some fluid flows, such as those containing shock waves, the differentiability considerations are not met and the solution must be sought in terms of the integral form. Such solutions are often referred to as weak solutions [41, 40]. Disregarding these cases, requiring that Eq. (A.2) be satisfied for any and all control volumes results in the criteria that the integrands must be satisfied at all locations

$$\frac{\partial \rho}{\partial t} + \frac{\partial (\rho u_j)}{\partial x_j} = \mathcal{M}. \tag{A.3}$$

This is the conservative form of the partial differential equation describing the conservation of mass. It can also be written in non-conservative form

$$\frac{\partial \rho}{\partial t} + \rho \frac{\partial u_j}{\partial x_j} + u_j \frac{\partial \rho}{\partial x_j} = \mathcal{M} \tag{A.4}$$

which is sometimes useful for analysis and manipulation.

A.2 Conservation of Momentum

The conservation of momentum, also known as Newton's second law of motion, equates the forces acting on a control volume with the change in momentum within the control volume. For the Newtonian formulation of the continuum model for fluid mechanics, the change of momentum within the volume is equal to the net amount of momentum flowing into the volume plus the forces acting on the volume. In three-dimensional space, the conservation of momentum is expressed by three equations, which can be written concisely using summation notation

$$\frac{\partial}{\partial t}\iiint_{\Omega} \rho u_i dV = -\iint_{\partial\Omega} \rho u_i u_j dA_j + \iiint_{\Omega} \mathcal{F}_i dV. \tag{A.5}$$

Assuming differentiability, the divergence theorem is applied to the first term on the right hand side, as in the mass equation. Also, the interchange of time differentiation and volume integration is performed on the left hand side, leading to

$$\iiint_{\Omega} \frac{\partial(\rho u_i)}{\partial t} dV = -\iiint_{\Omega} \frac{\partial(\rho u_j u_i)}{\partial x_j} dV + \iiint_{\Omega} \mathcal{F}_i dV \tag{A.6}$$

and equating the integrands gives

$$\frac{\partial(\rho u_i)}{\partial t} + \frac{\partial(\rho u_j u_i)}{\partial x_j} = \mathcal{F}_i^{surface} + \mathcal{F}_i^{body}. \tag{A.7}$$

In Eqs. (A.5)-(A.7), $\mathcal{F}_i$ represents any forces acting on the fluid. In Eq. (A.7), the forces are split into surface forces $\mathcal{F}_i^{surface}$ and body forces $\mathcal{F}_i^{body}$. The surface forces can be further divided into normal and shear forces. The normal surface forces are due to the local

pressure, while the shear forces are due to the local viscosity

$$\mathcal{F}_i^{surface} = \mathcal{F}_i^{normal} + \mathcal{F}_i^{shear} = -\frac{\partial p}{\partial x_j}\delta_{ij} + \frac{\partial}{\partial x_j}\left(\mu\frac{\partial u_i}{\partial x_j}\right). \tag{A.8}$$

For convenience the viscous terms are combined with the body force terms into a general term $\mathcal{F}_i$, which accounts for all forces except the pressure forces. The momentum conservation equation becomes

$$\frac{\partial(\rho u_i)}{\partial t} + \frac{\partial(\rho u_j u_i)}{\partial x_j} + \frac{\partial p}{\partial x_j}\delta_{ij} = \mathcal{F}_i. \tag{A.9}$$

Momentum conservation can also be written in non-conservative form in order to express the equation in terms of the primitive variable, velocity. Multiplying u_i to Eq. (A.3) and subtracting this from Eq. (A.9) yields

$$\rho\frac{\partial u_i}{\partial t} + \rho u_j\frac{\partial u_i}{\partial x_j} + \frac{\partial p}{\partial x_j}\delta_{ij} = \mathcal{F}_i - u_i\mathcal{M}. \tag{A.10}$$

A.3 Equation of State

The state postulate of thermodynamics ensures that any unknown intensive property of a fluid can be determined from two known independent intensive properties. This is often useful for achieving closure to a set of fluid mechanical equations. In the mass and momentum equations discussed above, two intensive thermodynamic quantities have already been introduced: p and ρ. From knowledge of these two quantities, any other intensive thermodynamic quantity can be deduced, provided a physically accurate model for the thermodynamic

behavior of the fluid. In this thesis, the topic at hand (pre-mixed combustion) deals almost exclusively with gases well-approximated by the ideal gas equation of state

$$p = \rho RT. \tag{A.11}$$

Furthermore, the internal energy e and the enthalpy h of an ideal gas is a function of temperature only

$$e(T_{state}) = e(T_{ref}) + \int_{T_{ref}}^{T_{state}} c_v dT \tag{A.12}$$

and

$$h(T_{state}) = h(T_{ref}) + \int_{T_{ref}}^{T_{state}} c_p dT. \tag{A.13}$$

Note that the definitions of internal energy and enthalpy are therefore arbitrary to an additive constant based on the reference temperature chosen. Choosing a constant specific heat with a convenient reference condition, Eqs. (A.12) and (A.13) can be written simply as

$$e = c_v T \tag{A.14}$$

and

$$h = c_p T. \tag{A.15}$$

Substituting Eq. (A.14) into Eq. (A.11), the equation of state for an ideal gas with constant specific heat can be written as

$$e = \frac{p}{(\gamma - 1)\rho} \tag{A.16}$$

where

$$\gamma = \frac{c_p}{c_v}. \tag{A.17}$$

A.4 Conservation of Energy

The conservation of energy, also known as the first law of thermodynamics, states that the change in energy content of a mass is equal to the heat addition to the mass minus the work done by the mass. For a fluid control volume, the rate of change of the energy within the volume is equal to the net energy flow into the volume plus the net heat addition to the volume minus the net work done by the volume. For an arbitrary control volume in laboratory coordinates

$$\begin{aligned} &\tfrac{\partial}{\partial t}\iiint\limits_{\Omega}\rho(e+\tfrac{1}{2}u_iu_i)dV = \\ &-\iint\limits_{\partial\Omega}\rho(e+\tfrac{1}{2}u_iu_i)u_jdA_j+\iiint\limits_{\Omega}\mathcal{Q}dV-\iiint\limits_{\Omega}\mathcal{W}dV \end{aligned} \tag{A.18}$$

where $\mathcal{Q}$ is the volumetric heat to the system and $\mathcal{W}$ is the volumetric work from the system.

Performing the same manipulations as before

$$\begin{aligned} &\iiint\limits_{\Omega}\tfrac{\partial[\rho(e+\frac{1}{2}u_iu_i)]}{\partial t}dV = \\ &-\iiint\limits_{\Omega}\tfrac{\partial[\rho u_j(e+\frac{1}{2}u_iu_i)]}{\partial x_j}dV+\iiint\limits_{\Omega}\mathcal{Q}dV-\iiint\limits_{\Omega}\mathcal{W}dV \end{aligned} \tag{A.19}$$

the partial differential equation for energy conservation is acquired by requiring Eq. (A.19) to be satisfied for any arbitrary control volume

$$\frac{\partial[\rho(e+\frac{1}{2}u_iu_i)]}{\partial t}+\frac{\partial[\rho u_j(e+\frac{1}{2}u_iu_i)]}{\partial x_j}=\mathcal{Q}-\mathcal{W}. \tag{A.20}$$

This equation describes the total sensible energy of the system, which is the sum of internal energy (e) and kinetic energy ($\frac{1}{2}u_iu_i$).

A.4.1 Kinetic Energy Equation

An equation for the kinetic energy of the flow can be developed by multiplying Eq. (A.10) by u_i and noting that $u_i \partial u_i = \partial(\frac{1}{2} u_i u_i)$ and $u_i \delta_{ij} = u_j$

$$\frac{\partial(\frac{1}{2} u_i u_i)}{\partial t} + \rho u_j \frac{\partial(\frac{1}{2} u_i u_i)}{\partial x_j} + u_j \frac{\partial p}{\partial x_j} = u_i \mathcal{F} - u_i u_i \mathcal{M}. \tag{A.21}$$

This equation can be used to manipulate Eq. (A.20) conservation equation.

A.4.2 Work

The work term $\mathcal{W}$ represents the work done by the gas and is composed of the work done by the pressure gradient on the moving fluid (force times velocity, with force equal to the negative pressure gradient) and the thermodynamic expansion work done by the gas (pressure times change in specific volume)

$$\begin{aligned} \mathcal{W} &= -\mathcal{W}^{\nabla p} + \mathcal{W}^{expansion} - \mathcal{W}^{other} \\ &= u_j \tfrac{\partial p}{\partial x_j} + \rho p \tfrac{D\left(\frac{1}{\rho}\right)}{Dt} - u_j \mathcal{F}_j. \end{aligned} \tag{A.22}$$

The second term can be simplified using the chain rule

$$\rho p \frac{D\left(\frac{1}{\rho}\right)}{Dt} = -\rho p \frac{1}{\rho^2} \frac{D\rho}{Dt} = -\frac{p}{\rho} \frac{D\rho}{Dt}. \tag{A.23}$$

Using the non-conservative form of the mass equation, Eq. (A.4), the material derivative of the density can be substituted, yielding

$$\rho p \frac{D\left(\frac{1}{\rho}\right)}{Dt} = p\frac{\partial u_j}{\partial x_j} - \frac{p}{\rho}\mathcal{M}. \tag{A.24}$$

Substituting this result into Eq. (A.22) gives

$$\begin{aligned} \mathcal{W} &= u_j \tfrac{\partial p}{\partial x_j} + p\tfrac{\partial u_j}{\partial x_j} - \tfrac{p}{\rho}\mathcal{M} - u_j\mathcal{F}_j \\ &= \tfrac{\partial (p u_j)}{\partial x_j} - \tfrac{p}{\rho}\mathcal{M} - u_j\mathcal{F}_j \end{aligned} . \tag{A.25}$$

A.4.3 Heat

The heat term $\mathcal{Q}$ represents both the heat transferred into the control volume via conduction and the heat produced in the control volume via electrical dissipation or chemical reaction. Mathematically, the expression for the heat is

$$\begin{aligned} \mathcal{Q} &= \mathcal{Q}^{conduction} + \mathcal{Q}^{electrical} + \mathcal{Q}^{chemical} \\ &= \tfrac{\partial}{\partial x_j}\left(k\tfrac{\partial T}{\partial x_j}\right) + j^2\rho^{elec} + \dot{\omega}\mathcal{H} \end{aligned} \tag{A.26}$$

where k is the thermal conductivity, ρ^elec is the electrical resistivity, j is the electrical current density, $\dot{\omega}$ is the mass conversion rate of a chemical reaction, and $\mathcal{H}$ is the enthalpy of reaction per unit mass. At this point, the heat term will be left in the equation as is, though later, the chemical source of heat will be crucial. This term models the energy added to the flow by combustion.

A.4.4 Various Forms of the Energy Equation

Substituting the formulation for the work term $\mathcal{W}$ from Eq. (A.25) into Eq. (A.20) and rearranging

$$\frac{\partial[\rho(e+\frac{1}{2}u_iu_i)]}{\partial t}+\frac{\partial[\rho u_j(e+\frac{1}{2}u_iu_i+\frac{p}{\rho})]}{\partial x_j}=\mathcal{Q}+\frac{p}{\rho}\mathcal{M}+u_j\mathcal{F}_j. \tag{A.27}$$

This is the conservation form of the energy equation often employed in computational fluid dynamics. Defining the enthalpy as $h=e+\frac{p}{\rho}$, this equation can be rephrased as

$$\frac{\partial[\rho(e+\frac{1}{2}u_iu_i)]}{\partial t}+\frac{\partial[\rho u_j(h+\frac{1}{2}u_iu_i)]}{\partial x_j}=\mathcal{Q}+\frac{p}{\rho}\mathcal{M}+u_j\mathcal{F}_j. \tag{A.28}$$

Even more concisely, the kinetic energy can be absorbed into the definitions of $e^o=e+\frac{1}{2}u_iu_i$ and $h^o=h+\frac{1}{2}u_iu_i$

$$\frac{\partial(\rho e^o)}{\partial t}+\frac{\partial(\rho u_j h^o)}{\partial x_j}=\mathcal{Q}+\frac{p}{\rho}\mathcal{M}+u_j\mathcal{F}_j. \tag{A.29}$$

From this equation, subtracting e^o multiplied by the conservative form of the mass equation, Eq. (A.3), then also subtracting the kinetic energy equation, Eq. (A.21), a non-conservative energy equation can be written in terms of the evolution of internal energy

$$\rho\frac{\partial e}{\partial t}+\rho u_j\frac{\partial e}{\partial x_j}=-p\frac{\partial u_j}{\partial x_j}+\mathcal{Q}+\left(\frac{p}{\rho}+\frac{1}{2}u_iu_i-e\right)\mathcal{M}. \tag{A.30}$$

Using a constant specific heat model for the fluid, $e=c_vT$, this equation can be phrased in terms of temperature

$$\rho c_v\frac{\partial T}{\partial t}+\rho c_v u_j\frac{\partial T}{\partial x_j}=-p\frac{\partial u_j}{\partial x_j}+\mathcal{Q}+\left(\frac{p}{\rho}+\frac{1}{2}u_iu_i-e\right)\mathcal{M}. \tag{A.31}$$

This is the form used by Culick (2006). Alternatively, from Eq. (A.29), subtracting h^o multiplied by Eq. (A.3) and subtracting the kinetic energy equation, a non-conservative enthalpy equation can be written

$$\rho\frac{\partial h}{\partial t}+\rho u_j\frac{\partial h}{\partial x_j}=\frac{\partial p}{\partial t}+u_j\frac{\partial p}{\partial x_j}+\mathcal{Q}+\left(\frac{1}{2}u_iu_i-e\right)\mathcal{M}. \tag{A.32}$$

Using a constant specific heat model for the fluid, $h=c_pT$, this equation can be phrased in terms of temperature

$$\rho c_p\frac{\partial T}{\partial t}+\rho c_pu_j\frac{\partial T}{\partial x_j}=\frac{\partial p}{\partial t}+u_j\frac{\partial p}{\partial x_j}+\mathcal{Q}+\left(\frac{1}{2}u_iu_i-e\right)\mathcal{M}. \tag{A.33}$$

Using the ideal gas equation of state (A.11), an substituting for T in Eq. (A.33)

$$\begin{aligned}\rho c_p\tfrac{DT}{Dt}&=\tfrac{\rho c_p}{R}\tfrac{D(p/\rho)}{Dt}\\&=\tfrac{c_p}{R}\tfrac{Dp}{Dt}+\tfrac{\rho c_pp}{R}\tfrac{D(1/\rho)}{Dt}\\&=\tfrac{\gamma}{\gamma-1}\tfrac{Dp}{Dt}-\tfrac{c_pp}{\rho R}\tfrac{D\rho}{Dt}\\&=\tfrac{\gamma}{\gamma-1}\tfrac{Dp}{Dt}+\tfrac{\gamma}{\gamma-1}p\tfrac{\partial u_j}{\partial x_j}-\tfrac{\gamma}{\gamma-1}\tfrac{p}{\rho}\mathcal{M}\end{aligned} \tag{A.34}$$

where Eq. (A.4) has been used to simplify the material derivative of density. Substituting Eq. (A.34) into Eq. (A.33) and multiplying by $\gamma-1$ leads to a non-conservative energy equation in terms of pressure

$$\frac{\partial p}{\partial t}+u_j\frac{\partial p}{\partial x_j}+\gamma p\frac{\partial u_j}{\partial x_j}=(\gamma-1)\mathcal{Q}+\left(\frac{1}{2}(\gamma-1)u_iu_i-(\gamma-1)e-\frac{\gamma p}{\rho}\right)\mathcal{M}. \tag{A.35}$$

The pressure form of the energy equation is very useful in the field of thermoacoustics, because it is natural to treat acoustic fields in terms of pressure and velocity. A pressure form

of the energy equation can also be derived by substituting Eq. (A.16) into the conservative formulation of the energy conservation, Eq. (A.27), which results in

$$\frac{\partial[p+\frac{1}{2}(\gamma-1)\rho u_i u_i]}{\partial t}+\frac{\partial[\gamma u_j p+\frac{1}{2}(\gamma-1)\rho u_j u_i u_i]}{\partial x_j}=(\gamma-1)(\mathcal{Q}+\frac{p}{\rho}\mathcal{M}). \tag{A.36}$$

APPENDIX B
RIEMANN SOLVER APPROACH TO FINITE VOLUME METHODS FOR HYPERBOLIC EQUATIONS

APPENDIX B
RIEMANN SOLVER APPROACH TO FINITE VOLUME METHODS FOR HYPERBOLIC EQUATIONS

B.1 Advection Equation

For simplicity's sake, perhaps the best manner in which to begin analysis of hyperbolic equations is the one-dimensional homogeneous advection equation

$$\frac{\partial \phi}{\partial t} + \bar{u}\frac{\partial \phi}{\partial x} = 0. \tag{B.1}$$

While the advection equation can be seen as parabolic in nature (since information travels only in one direction), it is best for the current discussion to view it as a hyperbolic equation with a single eigenvalue ($\lambda^{(1)} = \bar{u}$). This allows for a simple introduction to the analysis of hyperbolic equations.

B.1.1 General Solution

The general form of the solution to Eq. (B.1) is well-known and quite simple to verify:

$$\phi(x,t) = f(x - \bar{u}t) \tag{B.2}$$

where f(x) is any differentiable function. Differentiating Eq. (B.2) in time and space, respectively, yields

$$\begin{aligned} \frac{\partial \phi}{\partial t} &= -\bar{u} f'(x - \bar{u}t) \\ \frac{\partial \phi}{\partial x} &= f'(x - \bar{u}t) \end{aligned} \tag{B.3}$$

Simple substitution the verifies that Eq. (B.1) is satisfied.

B.1.2 Initial Value Problem

For an initial value problem in which no physical boundaries play a significant role, the analysis can be further clarified. Using initial data

$$\phi(x, 0) = \overset{o}{\phi}(x) \tag{B.4}$$

the general function $f(x)$ can be found by setting $t = 0$

$$\phi(x, 0) = f(x) = \overset{o}{\phi}(x) \tag{B.5}$$

which yields the IVP solution to the advection equation

$$\phi(x, t) = \overset{o}{\phi}(x - \bar{u}t). \tag{B.6}$$

Physically, the insight offered by Eq. (B.6) is as follows. The initial data provided to the system simply translates (advects) with the characteristic speed $\bar{u}$.

B.1.3 Riemann Problem

It is in this simple context that the Riemann problem can be first introduced. The Riemann problem is a specific type of initial value problem in which the initial conditions are piecewise constant with a single discontinuity at the origin ($x = 0$). The initial conditions can be stated in terms of the two constant values: to the left of the origin (ϕ_L) and to the right of the origin (ϕ_R)

$$\overset{o}{\phi}(x) = \begin{cases} \phi_L : x < 0 \\ \\ \phi_R : x \geq 0 \end{cases} . \tag{B.7}$$

Applying the general solution to the hyperbolic IVP, Eq. (B.6), the solution to the Riemann problem for the advection equation is simply

$$\phi(x,t) = \begin{cases} \phi_L : x - \bar{u}t < 0 \\ \\ \phi_R : x - \bar{u}t \geq 0 \end{cases} \tag{B.8}$$

or

$$\phi(x,t) = \begin{cases} \phi_L : x < \bar{u}t \\ \\ \phi_R : x \geq \bar{u}t \end{cases} \tag{B.9}$$

or, finally

$$\phi(x,t) = \begin{cases} \phi_L : \bar{u} > \frac{x}{t} \\ \\ \phi_R : \bar{u} \leq \frac{x}{t} \end{cases} \tag{B.10}$$

This final form of the solution is perhaps the most useful moving forward, since it relates the discontinuity location in terms of the eigenvalue ($\bar{u}$) and the similarity variable ($\frac{x}{t}$). As a final note, a value of importance later is the solution to the Riemann problem at the origin

for finite positive time

$$\phi(0,t) = \begin{cases} \phi_L : \bar{u} > 0 \\ \\ \phi_R : \bar{u} \leq 0 \end{cases} \tag{B.11}$$

Noting that the solution at the origin is not a function of time for linear systems, we follow the nomenclature of LeVeque (2002) to denote the solution at the origin

$$\phi^{\downarrow}(\phi_L, \phi_R) = \begin{cases} \phi_L : \bar{u} > 0 \\ \\ \phi_R : \bar{u} \leq 0 \end{cases} \tag{B.12}$$

This has a simple interpretation that the solution at the origin is equal to the upwind initial condition. Later, this will be and important starting place for a class of finite volume numerical methods.

B.2 Hyperbolic Systems of Equations

A natural extension of the above discussion for a single hyperbolic equation is a system of m hyperbolic equations defined by

$$\frac{\partial \underset{\sim}{\phi}}{\partial t} + \frac{\underset{\sim}{f}(\underset{\sim}{\phi})}{\partial x} = 0 \tag{B.13}$$

where subscripts are used to denote partial differentiation, ϕ is the vector of solution variables

$$\underset{\sim}{\phi} = \begin{pmatrix} \phi_1 \\ \\ \phi_2 \\ \\ \vdots \\ \\ \phi_m \end{pmatrix} \tag{B.14}$$

and the f is the flux vector given by

$$\underset{\sim}{f} = \begin{pmatrix} f_1(\phi_1, \phi_2, , \phi_m) \\ f_2(\phi_1, \phi_2, , \phi_m) \\ \vdots \\ f_m(\phi_1, \phi_2, , \phi_m) \end{pmatrix} \tag{B.15}$$

Applying the chain rule to the flux in Eq. (B.13), the system of equations can be rewritten as

$$\frac{\partial \underset{\sim}{\phi}}{\partial t} + \underset{\approx}{A} \frac{\partial \underset{\sim}{\phi}}{\partial x} = 0 \tag{B.16}$$

where $\underset{\approx}{A}$ is the Jacobian matrix given by

$$\underset{\approx}{A} = \partial \underset{\sim}{f} / \partial \underset{\sim}{\phi} = \begin{bmatrix} \partial f_1/\partial\phi_1 & \partial f_1/\partial\phi_2 & \cdots & \partial f_1/\partial\phi_m \\ \partial f_2/\partial\phi_1 & \partial f_2/\partial\phi_2 & \cdots & \partial f_2/\partial\phi_m \\ \vdots & \vdots & \ddots & \vdots \\ \partial f_m/\partial\phi_1 & \partial f_m/\partial\phi_2 & \cdots & \partial f_m/\partial\phi_m \end{bmatrix} \tag{B.17}$$

B.2.1 Transformation to Decoupled Equations

Equation (B.13) is a system of m coupled PDEs. Next, it is useful to decouple these into m independent PDEs. In the event that the entries in the Jacobian matrix $\underset{\approx}{A}$, Eq. (B.17), are constant functions of the variables $\underset{\sim}{\phi}$, it is useful to consider the eigenvalue

problem related to the Jacobian matrix, namely

$$\underset{\approx}{A}\underset{\approx}{R} = \underset{\approx}{R}\underset{\approx}{\Lambda} \tag{B.18}$$

where $\underset{\approx}{R}$ is the right eigenvector matrix associated with the diagonal eigenvalue matrix $\underset{\approx}{\Lambda}$.

$$\underset{\approx}{\Lambda} = \begin{bmatrix} \lambda^1 & 0 & \cdots & 0 \\ 0 & \lambda^2 & \cdots & 0 \\ \vdots & \vdots & \ddots & \vdots \\ 0 & 0 & \cdots & \lambda^m \end{bmatrix} \tag{B.19}$$

$$\underset{\approx}{R} = \begin{bmatrix} \underset{\sim}{r}^1 & \underset{\sim}{r}^2 & \cdots & \underset{\sim}{r}^m \end{bmatrix} \tag{B.20}$$

where $\underset{\sim}{r}^p$ is the p^{th} eigenvector and λ^p is its corresponding p^{th} eigenvalue. In this way, each eigenvalue-eigenvector pair satisfies the relationship

$$\underset{\approx}{A}\underset{\sim}{r}^p = \lambda^p \underset{\sim}{r}^p. \tag{B.21}$$

Rearranging Eq. (B.18), it is evident that the Jacobian can be diagonalized if its eigenvalues are real

$$\underset{\approx}{A} = \underset{\approx}{R}\underset{\approx}{\Lambda}\underset{\approx}{R}^{-1} \tag{B.22}$$

.

Similarly, the left eigenvectors matrix $\underset{\approx}{L}$ is defined as

$$\underset{\approx}{L}\underset{\approx}{A} = \underset{\approx}{\Lambda}\underset{\approx}{L} \tag{B.23}$$

and is populated with the left eigenvectors as row vectors

$$\underset{\approx}{L} = \begin{pmatrix} \underset{\sim}{l}^1 \\ \underset{\sim}{l}^2 \\ \vdots \\ \underset{\sim}{l}^m \end{pmatrix}. \tag{B.24}$$

Rearranging Eq. (B.23), the A matrix can also be written as

$$\underset{\approx}{A} = \underset{\approx}{L}^{-1} \underset{\approx}{\Lambda} \underset{\approx}{L}. \tag{B.25}$$

Equating Eq. (B.22) with Eq. (B.25) shows the following relationship between the left and right eigenvector matrices

$$\underset{\approx}{L} = \underset{\approx}{R}^{-1}. \tag{B.26}$$

The system of partial differential equations is called *hyperbolic* provided that the eigenvalues of the Jacobian are real. The term *strictly hyperbolic* refers to a system in which the real eigenvalues are distinct. Assuming the Jacobian matrix to be constant in space and time, except for its dependence on the variables $\underset{\sim}{\phi}$, Eq. (B.22) can be substituted into Eq. (B.16) giving

$$\begin{aligned} \frac{\partial \underset{\sim}{\phi}}{\partial t} + \underset{\approx}{R} \underset{\approx}{\Lambda} \underset{\approx}{R}^{-1} \frac{\partial \underset{\sim}{\phi}}{\partial x} &= 0 \\ \underset{\approx}{R}^{-1} \frac{\partial \underset{\sim}{\phi}}{\partial t} + \underset{\approx}{\Lambda} \underset{\approx}{R}^{-1} \frac{\partial \underset{\sim}{\phi}}{\partial x} &= 0 \\ \frac{\partial (\underset{\approx}{R}^{-1} \underset{\sim}{\phi})}{\partial t} + \underset{\approx}{\Lambda} \frac{\partial (\underset{\approx}{R}^{-1} \underset{\sim}{\phi})}{\partial x} &= 0 \\ \frac{\partial \underset{\sim}{w}}{\partial t} + \underset{\approx}{\Lambda} \frac{\partial \underset{\sim}{w}}{\partial x} &= 0 \end{aligned} \tag{B.27}$$

where a new set of transformed variables $\underset{\sim}{w}$ is defined by

$$\begin{aligned} \underset{\sim}{w} &= \underset{\approx}{R}^{-1}\underset{\sim}{\phi} = \underset{\approx}{L}\,\underset{\sim}{\phi} \\ w^p &= \underset{\sim}{l}^p \cdot \underset{\sim}{\phi} \end{aligned} \tag{B.28}$$

such that the coupled system of m equations given by Eq. (B.16) is transformed into m independent equations, the p^{th} equation given by

$$\frac{\partial w^p}{\partial t} + \lambda^p \frac{\partial w^p}{\partial x} = 0 \tag{B.29}$$

.

B.2.2 General Solution

Each of the decoupled equations resulting from the above transformation can be solved separately following the procedure shown for the advection equation. Each solution consists of a wave, with the corresponding eigenvalue giving the speed of propagation. The general solution to each independent equation is, by analogy with Eq. (B.2)

$$w^p(x,t) = f(x - \bar{u}t). \tag{B.30}$$

B.2.3 Initial Value Problem

When the initial conditions of a system are given by

$$\underset{\sim}{\phi}(x,0) = \overset{o}{\underset{\sim}{\phi}}(x) \tag{B.31}$$

the initial conditions for the decoupled system can be found using the same transformation as Eq. (B.28)

$$\begin{aligned} \overset{o}{\underset{\sim}{w}}(x) &= \underset{\approx}{R}^{-1} \overset{o}{\underset{\sim}{\phi}}(x) = \underset{\approx}{L} \overset{o}{\underset{\sim}{\phi}}(x) \\ \overset{o}{w}^p(x) &= \underset{\sim}{l}^p \cdot \overset{o}{\underset{\sim}{\phi}}(x) \end{aligned} \tag{B.32}$$

where

$$\overset{o}{w}^p(x) = w^p(x, 0) \tag{B.33}$$

and the solution is found for each advection-like equation for the transformed variables

$$w^p(x, t) = \overset{o}{w}^p(x - \lambda^p t). \tag{B.34}$$

After each independent equation is solved using Eq. (B.34), the desired solution in terms of $\underset{\sim}{\phi}$ can be found by reversing the transformation in Eq. (B.28)

$$\begin{aligned} \underset{\sim}{\phi}(x, t) &= \underset{\approx}{R} \underset{\sim}{w}(x, t) \\ &= \sum_{p=1}^{m} w^p(x, t) \underset{\sim}{r}^p \\ &= \sum_{p=1}^{m} \overset{o}{w}{}^p(x - \lambda^p t) \underset{\sim}{r}^p \\ &= \sum_{p=1}^{m} \left(\underset{\sim}{l}^p \cdot \overset{o}{\underset{\sim}{\phi}}(x - \lambda^p t) \right) \underset{\sim}{r}^p \end{aligned} . \tag{B.35}$$

Hence, the hyperbolic system can be described by m independently propagating waves, with strengths in terms of original variables determined by the eigenvectors of the Jacobian.

B.2.4 Riemann Problem

The Riemann problem is a special case of the initial value problem, when the initial conditions are given by a piecewise-constant function with a single discontinuity at the origin ($x = 0$)

$$\overset{o}{\underset{\sim}{\phi}}(x) = \begin{cases} \underset{\sim}{\phi}_L : x < 0 \\ \\ \underset{\sim}{\phi}_R : x \geq 0 \end{cases} . \tag{B.36}$$

Transforming the initial conditions using Eq. (B.32), the Riemann problem in terms of transformed variables can be written

$$\overset{o}{w}^p(x) = \begin{cases} w_L^p : x < 0 \\ \\ w_R^p : x \geq 0 \end{cases} . \tag{B.37}$$

Following the solution procedure for the advection equation Riemann problem, the solution for each of the decoupled equations is

$$w^p(x,t) = \begin{cases} w_L^p : \lambda^p > \frac{x}{t} \\ \\ w_R^p : \lambda^p \leq \frac{x}{t} \end{cases} \tag{B.38}$$

and the reverse transformation, Eq. (B.35) can then be used to write the solution in terms of the original variables

$$\underset{\sim}{\phi}(x,t) = \sum_{p:\lambda^p > x/t} w_L^p \underset{\sim}{r}^p + \sum_{p:\lambda^p \leq x/t} w_R^p \underset{\sim}{r}^p. \tag{B.39}$$

This solution consists of m waves propagating from the origin at $t = 0$ with speeds given by their respective eigenvalues. The strength of each wave $\underset{\sim}{\mathcal{W}}^p$ is defined as the change

in the original variables across the wave $\Delta(\underset{\sim}{\phi})^p$. From Eq. (B.39), the change in the original variables across a wave is given by

$$\underset{\sim}{\mathcal{W}}^p = \Delta(\underset{\sim}{\phi})^p = (w_R^p - w_L^p)\underset{\sim}{r}^p = \alpha^p \underset{\sim}{r}^p \tag{B.40}$$

where α^p is the strength coefficient for the p^{th} wave. Equation (B.40) can be considered as the mathematical definition of α^p. The values for α^p can be found by considering the change in original variables across all of the waves is the sum of the individual changes shown in Eq. (B.40)

$$\underset{\sim}{\phi}_R - \underset{\sim}{\phi}_L = \sum_{p=1}^{m} \underset{\sim}{r}^p \alpha^p = \underset{\approx}{R}\underset{\sim}{\alpha}. \tag{B.41}$$

Inverting this equation to solve for α

$$\begin{aligned} \underset{\sim}{\alpha} = \underset{\sim}{w}_R - \underset{\sim}{w}_L = \underset{\approx}{R}^{-1}(\underset{\sim}{\phi}_R - \underset{\sim}{\phi}_L) = \underset{\approx}{L}(\underset{\sim}{\phi}_R - \underset{\sim}{\phi}_L) \\ \alpha^p = w_R^p - w_L^p = \underset{\sim}{l}^p \cdot (\underset{\sim}{\phi}_R - \underset{\sim}{\phi}_L) \end{aligned} . \tag{B.42}$$

Given this definition for the wave strength, the solution to the Riemann problem, first given by Eq. (B.39), can also be written as

$$\begin{aligned} \underset{\sim}{\phi}(x,t) &= \underset{\sim}{\phi}_L + \sum_{p:\lambda^p \le x/t} \underset{\sim}{\mathcal{W}}^p \\ &= \underset{\sim}{\phi}_R - \sum_{p:\lambda^p > x/t} \underset{\sim}{\mathcal{W}}^p \\ &= \frac{1}{2}(\underset{\sim}{\phi}_L + \underset{\sim}{\phi}_R) + \frac{1}{2}\left(\sum_{p:\lambda^p \le x/t} \underset{\sim}{\mathcal{W}}^p - \sum_{p:\lambda^p > x/t} \underset{\sim}{\mathcal{W}}^p \right). \end{aligned} \tag{B.43}$$

Finally, the value on the origin, useful in the next section, is easily found

$$\underset{\sim}{\phi}(0,t) = \underset{\sim}{\phi}^{\downarrow}(\underset{\sim}{\phi}_L, \underset{\sim}{\phi}_R) = \frac{1}{2}(\underset{\sim}{\phi}_L + \underset{\sim}{\phi}_R) + \frac{1}{2}\left(\sum_{p:\lambda^p \le 0} \underset{\sim}{\mathcal{W}}^p - \sum_{p:\lambda^p > 0} \underset{\sim}{\mathcal{W}}^p \right). \tag{B.44}$$

B.3 Finite Volume Formulation

The solutions to hyperbolic initial value problems, specifically Riemann problems, are useful in establishing numerical methods for calculating the flux through an internal face between two numerical cells. At a given time step, the values from the two neighboring cells provide the left and right initial conditions for the Riemann problem. The flux through the face can then be calculated using the solution to the Riemann problem on the face (at $x = 0$). The finite volume formulation for using the Riemann solution for flux calculations is presented first in one dimension for a single advection equation and then expanded to a system of hyperbolic equations. At first, focus is put on first order upwind methods, with extension to higher-order methods reserved for later.

B.3.1 One-Dimensional Upwind Formulation

To introduce the use of the Riemann problem for numerical methods, first consider a single advection equations, given by Eq. (B.1). For a one-dimensional finite volume method, consider a face connecting to neighboring cells. At a given time step n, the right and left cells contain a single value for each of the solution variables at the cell center. As a first approximation, assume that such cell-centered values are constant over the entire cell volume. In this way, using the values at time n as initial conditions, the problem resembles the Riemann problem described above in Eq. (B.7). The flux through the face (for a constant

$\bar{u}$) is defined as

$$f(\phi) = \bar{u}\phi. \tag{B.45}$$

Defining a coordinate system to reflect the relationship of the finite volume problem with the Riemann problem, set the origin $x = 0$ at the face where the discontinuity occurs. At the face, the solution variable ϕ transitions from the left cell center's value to the right cell-center's value. The numerical flux, vital for finite volume calculations, is given by

$$f_{face} = \bar{u}\phi(0, t). \tag{B.46}$$

Using the results from the above solution to the one-dimensional advection equation for the Riemann problem, the flux through the face is

$$f_{face} = \bar{u}\phi^{\downarrow}(\phi_L, \phi_R) = \bar{u}^{-}\phi_R + \bar{u}^{+}\phi_L \tag{B.47}$$

where the plus and minus superscripts denote

$$\bar{u}^{+} = \max(\bar{u}, 0) \quad \bar{u}^{-} = \min(\bar{u}, 0). \tag{B.48}$$

Furthermore, it is useful to describe this in terms of the wave strength $\mathcal{W} = \phi_R - \phi_L$. There is only one wave in this case, of course. The flux at the face can also be given by

$$\bar{u}\phi^{\downarrow}(\phi_L, \phi_R) = \bar{u}\phi_L - \bar{u}^{-}\mathcal{W} = \bar{u}\phi_R - \bar{u}^{+}\mathcal{W}. \tag{B.49}$$

This is merely a mathematical way to describe that, for a given direction of the wave propagation velocity (eigenvalue), the value of the solution variable used at the face to calculate the flux comes from the upstream side. For the single variable linear advection

equation, as shown, the results is quite simply the first-order upwind method. This method is stable, but highly diffusive, especially when used for a non-linear term, such as the advection term in the momentum equations of fluid flow. This task of this thesis is solely concerned with linearized equations, so further discussion of non-linearity is not needed.

B.3.2 System of Hyperbolic Equations: Godunov Method

The extension of the upwind flux calculation method introduced above to systems of linear equations makes use of the previously discussed theory. Such an extension is quite straight-forward. Under the assumption of constant coefficients

$$\underset{\sim}{f}(\underset{\sim}{\phi}) = \underset{\approx}{A}\underset{\sim}{\phi}. \tag{B.50}$$

Therefore, proceeding as above, the flux at the face for each of the variables in the $\underset{\sim}{\phi}$ vector can be written as

$$\underset{\sim}{f}_{face} = \underset{\approx}{A}\underset{\sim}{\phi}(0,t) \tag{B.51}$$

where again the face between two adjacent one-dimensional cells is placed at the origin ($x = 0$). As foreshadowed, Eq. (B.43) is now extremely useful for defining the flux through the face. The first expression of Eq. (B.43) at the face becomes

$$\underset{\sim}{f}_{face} = \underset{\approx}{A}\phi_L + \sum_{p:\lambda^p<0} \underset{\approx}{A}\underset{\sim}{\mathcal{W}}^p. \tag{B.52}$$

This essentially states that the variables at the face can be calculated as the values at the left cell center plus the changes across each wave propagating to the left. Noting from

Eq. (B.40) that the wave strength vector $\underset{\sim}{\mathcal{W}}^p$ is a multiple of the p^{th} eigenvector, Eq. (B.52) can be rewritten, using Eq. (B.18), as

$$\underset{\sim}{f}_{face} = \underset{\approx}{A}\phi_L + \sum_{p:\lambda^p<0} \lambda^p \underset{\sim}{\mathcal{W}}^p \tag{B.53}$$

or, using the notation developed in Eq. (B.48), as

$$\underset{\sim}{f}_{face} = \underset{\approx}{A}\phi_L + \sum_{p=1}^{m} (\lambda^p)^- \underset{\sim}{\mathcal{W}}^p. \tag{B.54}$$

Likewise, the flux at the face can be calculated coming from the right using the second expression from Eq. (B.43)

$$\underset{\sim}{f}_{face} = \underset{\approx}{A}\phi_R - \sum_{p:\lambda^p>0} \underset{\approx}{A}\underset{\sim}{\mathcal{W}}^p. \tag{B.55}$$

Here, the face fluxes are calculated using the cell center values from the right cell minus the changes across each of the waves propagating to the right. Using the definition of the eigenvectors here as on the left side

$$\underset{\sim}{f}_{face} = \underset{\approx}{A}\phi_R - \sum_{p=1}^{m} (\lambda^p)^+ \underset{\sim}{\mathcal{W}}^p. \tag{B.56}$$

For constant coefficient linear problems, Eqs. (B.54) and (B.56) give the same value. A convenient way to calculate this value is found by averaging these two equations (that is, multiplying each by 1/2 and adding).

$$\underset{\sim}{f}_{face} = \frac{1}{2}\underset{\approx}{A}(\underset{\sim}{\phi}_L + \underset{\sim}{\phi}_R) - \sum_{p=1}^{m} \left[(\lambda^p)^+ - (\lambda^p)^-\right] \underset{\sim}{\mathcal{W}}^p. \tag{B.57}$$

Noting from Eq. (B.48) the identity

$$\lambda^+ - \lambda^- = |\lambda| \tag{B.58}$$

the so-called Roe's method for calculating face fluxes is given most succinctly by

$$\underset{\sim}{f}_{face} = \frac{1}{2}\underset{\approx}{A}(\underset{\sim}{\phi}_L + \underset{\sim}{\phi}_R) - \sum_{p=1}^{m} |\lambda^p| \underset{\sim}{\mathcal{W}}^p. \tag{B.59}$$

In the context of using this flux calculation to support a finite volume calculation, this first-order upwind method is known as Godunov's method. As mentioned with the simple advection equation, such upwinding is highly diffusive. Therefore, extension to higher orders is necessary for useful in the present context (linear growth rates and limit cycle amplitudes for combustion instabilities). Prediction of thermoacoustic stability is polluted if numerical diffusion adds significant damping to the acoustic modes of interest.

B.3.3 Extension to Higher Order Methods

Second-order methods can be constructed by evaluating the gradient of each solution variable as each cell center and extrapolating the cell center variables to the either side of the face using such gradient. For a given variable

$$\phi_L = \phi_{L,center} + \frac{\partial \phi}{\partial x}_L \frac{\Delta_L x}{2} \tag{B.60}$$

and

$$\phi_R = \phi_{R,center} - \frac{\partial \phi}{\partial x}_R \frac{\Delta_R x}{2}. \tag{B.61}$$

The extrapolated values on either side then serve as the initial condition for the Riemann problem and the fluxes can be calculated using Eq. (B.54), (B.56), or (B.59). This

often leads in the best case to spurious oscillations in the solution and in the worst case to numerical instability. To mitigate such factors that arise when the solution varies rapidly, the theory of total variation diminishing (TVD) gradient limiters has been heavily developed within the CFD community [41]. Applying a TVD limiter to the gradients calculated for each cell center, Eqs. (B.60) and (B.61) can be used to develop a second-order Godunov type approach to the finite volume method. Of course, in the neighborhood of sharp changes in solution variables, the method reduces to first order. This is unavoidable, however, in this context, if a stable, total variation diminishing solution is desired. This TVD-based approach with piecewise linear reconstruction of the solution in space gives a so-called "high-resolution" method for solving the hyperbolic system of equations. Such high-resolution methods are known to give much less numerical diffusion than more traditional CFD flux calculations involving simple interpolation between two cell centers. This comes at a price, however, as the solution to the Riemann problem creates additional operations at each cell for each iteration. Nevertheless, the extra computing time is often worth it in simulations sensitive to numerical diffusion.

APPENDIX C
ANALYTICAL SOLUTIONS TO VERIFICATION CASES

APPENDIX C
ANALYTICAL SOLUTIONS TO VERIFICATION CASES

The purpose of this appendix is to show the derivation of the analytical solutions used for verification cases for the tacFoam solver. For a general background in acoustic analysis, the author recommends [43].

C.1 One-Dimensional Acoustics in a Duct

The simplest verification for an acoustics solver is the one-dimensional duct with no mean flow and no mean property gradients. In this case, the linearized momentum and energy conservation laws for classical acoustics in one spatial dimension (z) can be applied

$$\begin{aligned} \frac{\partial u'}{\partial t} + \frac{1}{\bar{\rho}}\frac{\partial p'}{\partial z} &= 0 \\ \frac{\partial p'}{\partial t} + \gamma \bar{p}\frac{\partial u'}{\partial z} &= 0 \end{aligned} \tag{C.1}$$

For the constant area, constant property, zero flow duct, the eigenfrequencies are those of classical acoustics. The conservation laws of Eq. (C.1) can be combined to form the classical wave equation for the acoustic pressure with wave speed $\bar{a} = \sqrt{\frac{\gamma \bar{p}}{\bar{\rho}}}$, which is the isentropic speed of sound in an ideal gas

$$\frac{\partial^2 p'}{\partial t^2} - \bar{a}^2 \frac{\partial^2 p'}{\partial z^2} = 0 \tag{C.2}$$

The separation of variables technique suggests

$$p' = \psi(z)h(t) \tag{C.3}$$

Substitution of Eq. (C.3) into Eq. (C.2) gives

$$\frac{d^2h/dt^2}{\bar{a}h} = \frac{d^2\psi/dz^2}{\psi} = -k^2 \tag{C.4}$$

Because the first statement in Eq. (C.4) is a function of time only and the second is a function of space only, the only scenario in which their equality can be upheld is their mutual equality with a constant, here labelled $-k^2$. The temporal evolution equation gives the harmonic oscillator equation

$$\frac{d^2h}{dt^2} + \omega^2 h = 0 \tag{C.5}$$

where

$$\omega^2 = k^2\bar{a}^2 \tag{C.6}$$

The solution to Eq. (C.5) is a linear superposition of sine and cosine functions defined by the initial conditions. For this case, the exact form of the temporal behavior is not important, since this analysis is ambivalent to the initial conditions. Separation of variables, in this case, is equivalent to the assumption that $p' \approx exp(i\omega t)$. The spatial ODE from the separation of variables in Eq. (C.4) is also a harmonic oscillator form

$$\frac{d^2\psi}{dz^2} + k^2\psi = 0 \tag{C.7}$$

The solution to this equation for the modeshape ψ is

$$\psi(z) = C_1\cos(kz) + C_2\sin(kz) \tag{C.8}$$

Hence, there are two arbitrary constants to be determined by the boundary conditions. Two basic boundary conditions are used here. First, the open boundary condition, also referred to as a pressure release boundary, is defined by the absence of pressure fluctuations: $p' = 0$. Assuming harmonic temporal behavior, $p'(x,t) = \psi(z)\exp(i\omega t)$, the open boundary is described by the homogeneous Dirichlet condition $\psi = 0$. The second boundary condition is the closed boundary condition, in which the velocity normal to the boundary vanishes: $u' = 0$. The momentum equation can be used to state the closed boundary condition in terms of pressure

$$\frac{\partial u'}{\partial t} = -\frac{1}{\bar{\rho}}\frac{\partial p'}{\partial z} \tag{C.9}$$

Substituting the harmonic behavior in time, $u'(z,t) = U'(z)\exp(i\omega t), p'(z,t) = \psi(z)\exp(i\omega t)$ into Eq. (C.9) yields

$$i\omega U'(z) = -\frac{1}{\bar{\rho}}\frac{d\psi}{dz} \tag{C.10}$$

Requiring that the velocity modeshape vanish at a closed boundary thus gives the homogeneous second kind boundary condition: $\frac{d\psi}{dz} = 0$.

C.1.1 Closed-Closed Boundary Conditions

For closed boundaries in a one-dimensional domain $0 \leq z \leq L$, the boundary conditions are

$$\begin{aligned} \tfrac{d\psi}{dz}(0) &= 0 \\ \tfrac{d\psi}{dz}(L) &= 0 \end{aligned} \tag{C.11}$$

Substitution of the first condition into Eq. (C.8) gives $C_2 = 0$ and

$$\psi(z) = C_1 \cos(kz) \tag{C.12}$$

Substitution of the second boundary condition yields the eigenfrequencies

$$f_n = \frac{n\bar{a}}{2L} \tag{C.13}$$

where the frequency in Hertz is $f_n = \omega_n/2\pi$ and $n = 1, 2, , \infty$ denotes the mode number. The corresponding acoustic pressure modeshapes are given by Eq. (C.12), where C_1 is an arbitrary scaling factor and

$$k_n = n\pi/L \tag{C.14}$$

C.1.2 Closed-Open Boundary Conditions

For a closed boundary at $z = 0$ and an open boundary at $z = L$, the boundary conditions are

$$\begin{aligned} \tfrac{d\psi}{dz}(0) &= 0 \\ \psi(L) &= 0 \end{aligned} \tag{C.15}$$

Substitution of the first condition into Eq. (C.8) gives $C_2 = 0$ and

$$\psi(z) = C_1 \cos(kz) \tag{C.16}$$

Substitution of the second boundary condition yields the eigenfrequencies

$$f_n = \frac{(n - \frac{1}{2})\bar{a}}{2L} \tag{C.17}$$

where the frequency in Hertz is $f_n = \omega_n/2\pi$ and $n = 1, 2, , \infty$ denotes the mode number. The corresponding acoustic pressure modeshapes are given by Eq. (C.16), where C_1 is an arbitrary scaling factor and

$$k_n = \frac{(n - \frac{1}{2})\pi}{L} \tag{C.18}$$

C.2 One-Dimensional Acoustics with a Linear Temperature Distribution

Another scenario with an accessible exact solution involving mean temperature and density gradients is the case of a linear temperature distribution over the entire domain. The following solution was first posed by [63]. The wave equation constructed from the linearized momentum and energy equations, accounting for the existence of mean density gradients is

$$\frac{\partial^2 p'}{\partial t^2} + \frac{\bar{a}^2}{\bar{\rho}}\frac{\partial \bar{\rho}}{\partial z}\frac{\partial p'}{\partial z} - \bar{a}^2\frac{\partial^2 p'}{\partial z^2} = 0 \tag{C.19}$$

or

$$\frac{\partial^2 p'}{\partial z^2} - \frac{1}{\bar{\rho}}\frac{\partial \bar{\rho}}{\partial z}\frac{\partial p'}{\partial z} - \frac{1}{\bar{a}^2}\frac{\partial^2 p'}{\partial t^2} = 0 \tag{C.20}$$

The separation of variables technique suggests

$$p' = \psi(z)h(t) \tag{C.21}$$

Substitution of Eq. (C.3) into Eq. (C.20) gives

$$\frac{d^2h/dt^2}{h} = \bar{a}^2\frac{d^2\psi/dz^2 - (1/\bar{\rho})(d\bar{\rho}/dz)(d\psi/dz)}{\psi} = -\omega^2 \tag{C.22}$$

Because the first statement in Eq. (C.4) is a function of time only and the second is a function of space only, the only scenario in which their equality can be upheld is their

mutual equality with a constant, here labelled $-\omega^2$ to denote that this constant represents the eigenfrequencies. The temporal evolution equation gives the harmonic oscillator equation

$$\frac{d^2h}{dt^2} + \omega^2 h = 0 \tag{C.23}$$

The solution to Eq. (C.5) is a linear superposition of sine and cosine functions defined by the initial conditions. For this case, the exact form of the temporal behavior is not important, since this analysis is ambivalent to the initial conditions. Separation of variables, in this case, is equivalent to the assumption that $p' \approx exp(i\omega t)$. The spatial ODE from the separation of variables in Eq. (C.4) is also a harmonic oscillator form

$$\frac{d^2\psi}{dz^2} - \frac{1}{\bar{\rho}}\frac{d\bar{\rho}}{dz}\frac{d\psi}{dz} + \frac{\omega^2}{\gamma R\bar{T}}\psi = 0 \tag{C.24}$$

From the equation of state for an ideal gas, $\bar{p} = \bar{\rho}R\bar{T}$, the density and temperature gradients can be related under constant mean pressure by

$$\frac{1}{\bar{\rho}}\frac{d\bar{\rho}}{dz} = -\frac{1}{\bar{T}}\frac{d\bar{T}}{dz} \tag{C.25}$$

Substitution of Eq. (C.25) into Eq. (C.24) yields

$$\frac{d^2\psi}{dz^2} + \frac{1}{\bar{T}}\frac{d\bar{T}}{dz}\frac{d\psi}{dz} + \frac{\omega^2}{\gamma R\bar{T}}\psi = 0 \tag{C.26}$$

This spatial ODE is not directly solvable in the present form due to the variable coefficients arising from the temperature gradient. The situation is improved, however, by transformation of dependent variable from x to $\bar{T}$.

$$\frac{d\psi}{dz} = \frac{d\psi}{d\bar{T}}\frac{d\bar{T}}{dz} \tag{C.27}$$

$$\frac{d^2\psi}{dz} = \frac{d^2\psi}{d\bar{T}^2}\left(\frac{d\bar{T}}{dz}\right)^2 + \frac{d\psi}{d\bar{T}}\frac{d^2\bar{T}}{dz^2} \tag{C.28}$$

Under this transformation, the modeshape ODE becomes

$$\frac{\bar{T}}{dz}^2\frac{d^2\psi}{d\bar{T}^2} + \frac{1}{\bar{T}}\frac{d}{dz}\left(\bar{T}\frac{d\bar{T}}{dz}\right)\frac{d\psi}{d\bar{T}} + \frac{\omega^2}{\gamma R\bar{T}}\psi = 0 \tag{C.29}$$

The temperature in the domain $0 \leq z \leq L$ is given by

$$\bar{T}(z) = \bar{T}_0 + mz \tag{C.30}$$

such that the temperature gradient is constant given by $d\bar{T}/dz = m$. Substitution of this temperature profile into Eq. (C.29) gives

$$m^2\frac{d^2\psi}{d\bar{T}^2} + \frac{1}{\bar{T}}m^2\frac{d\psi}{d\bar{T}} + \frac{\omega^2}{\gamma R\bar{T}}\psi = 0 \tag{C.31}$$

or

$$\frac{d^2\psi}{d\bar{T}^2} + \frac{1}{\bar{T}}\frac{d\psi}{d\bar{T}} + \frac{\omega^2/m^2}{\gamma R\bar{T}}\psi = 0 \tag{C.32}$$

The solution to the equation remains elusive at this step, but becomes visible with one more transformation of the dependent variable.

$$\bar{\tau} = 2\sqrt{\frac{\omega^2}{m^2\gamma R}\bar{T}} \tag{C.33}$$

$$\frac{d\psi}{d\bar{T}} = \frac{d\psi}{d\bar{\tau}}\frac{d\bar{\tau}}{d\bar{T}} = \sqrt{\frac{\omega^2}{m^2\gamma R\bar{T}}}\frac{d\psi}{d\bar{\tau}} = \frac{1}{2}\frac{\bar{\tau}}{\bar{T}}\frac{d\psi}{d\bar{\tau}} \tag{C.34}$$

$$\frac{d^2\psi}{d\bar{T}^2} = \frac{d}{d\bar{T}}\left(\frac{d\psi}{d\bar{\tau}}\frac{d\bar{\tau}}{d\bar{T}}\right) = \frac{d^2\psi}{d\bar{\tau}^2}\left(\frac{d\bar{\tau}}{d\bar{T}}\right)^2 + \frac{d\psi}{d\bar{\tau}}\frac{d^2\bar{\tau}}{d\bar{T}^2} = \frac{1}{4}\frac{\bar{\tau}^2}{\bar{T}^2}\frac{d^2\psi}{d\bar{\tau}^2} - \frac{1}{4}\frac{\bar{\tau}}{\bar{T}^2}\frac{d\psi}{d\bar{\tau}} \tag{C.35}$$

Substitution of these transformation relations into the governing ODE, Eq. (C.32) leads to

$$\frac{1}{4}\frac{\bar{\tau}^2}{\bar{T}^2}\frac{d^2\psi}{d\bar{\tau}^2} + \frac{1}{4}\frac{\bar{\tau}}{\bar{T}^2}\frac{d\psi}{d\bar{\tau}} + \frac{1}{4}\frac{\bar{\tau}^2}{\bar{T}^2}\psi = 0 \tag{C.36}$$

or

$$\bar{\tau}^2 \frac{d^2\psi}{d\bar{\tau}^2} + \bar{\tau}\frac{d\psi}{d\bar{\tau}} + \bar{\tau}^2\psi = 0 \tag{C.37}$$

While Eq. (C.37) has variable coefficients, it is now recognizable as Bessel's equation with order zero. The solution is a linear combination of the first and second kind Bessel functions of order zero.

$$\psi(\bar{\tau}) = C_1 J_0(\bar{\tau}) + C_2 Y_0(\bar{\tau}) \tag{C.38}$$

or, reversing the two transformations

$$\psi(z) = C_1 J_0\left(\frac{2\omega}{|m|\sqrt{\gamma R}}\sqrt{\bar{T}_0 + mz}\right) + C_2 Y_0\left(\frac{2\omega}{|m|\sqrt{\gamma R}}\sqrt{\bar{T}_0 + mz}\right) \tag{C.39}$$

The derivative of the modeshape, useful for applying boundary conditions, is given by

$$\begin{aligned}\psi(z) = &-C_1 \frac{m\omega}{|m|\sqrt{\gamma R(\bar{T}_0+mz)}} J_1\left(\frac{2\omega}{|m|\sqrt{\gamma R}}\sqrt{\bar{T}_0 + mz}\right) \\ &-C_2 \frac{m\omega}{|m|\sqrt{\gamma R(\bar{T}_0+mz)}} Y_1\left(\frac{2\omega}{|m|\sqrt{\gamma R}}\sqrt{\bar{T}_0 + mz}\right)\end{aligned} \tag{C.40}$$

For this example, only the solution for closed-open boundary conditions is shown, though the process is similar for other boundary conditions. The closed-open boundary conditions are, as before

$$\begin{aligned}\tfrac{d\psi}{dz}(0) &= 0 \\ \psi(L) &= 0\end{aligned} \tag{C.41}$$

Application of the first boundary conditions gives

$$C_1 J_1\left(\frac{2\omega\sqrt{\bar{T}_0}}{|m|\sqrt{\gamma R}}\right) + C_2 Y_1\left(\frac{2\omega\sqrt{\bar{T}_0}}{|m|\sqrt{\gamma R}}\right) = 0 \tag{C.42}$$

The second boundary condition gives

$$C_1 J_0\left(\frac{2\omega\sqrt{\bar{T}_L}}{|m|\sqrt{\gamma R}}\right) + C_2 Y_0\left(\frac{2\omega\sqrt{\bar{T}_L}}{|m|\sqrt{\gamma R}}\right) = 0 \tag{C.43}$$

where $\bar{T}_L = \bar{T}(L) = \bar{T}_0 + mL$. Simultaneous solution of these two equations yields the following characteristic equation

$$Y_1\left(\frac{2\omega\sqrt{\bar{T}_0}}{|m|\sqrt{\gamma R}}\right) J_0\left(\frac{2\omega\sqrt{\bar{T}_L}}{|m|\sqrt{\gamma R}}\right) - J_1\left(\frac{2\omega\sqrt{\bar{T}_0}}{|m|\sqrt{\gamma R}}\right) Y_0\left(\frac{2\omega\sqrt{\bar{T}_L}}{|m|\sqrt{\gamma R}}\right) = 0 \tag{C.44}$$

with modeshapes given by

$$\begin{aligned}\psi(z) = -Y_1\left(\tfrac{2\omega\sqrt{\bar{T}_0}}{|m|\sqrt{\gamma R}}\right) J_0\left(\tfrac{2\omega\sqrt{\bar{T}_0+mz}}{|m|\sqrt{\gamma R}}\right) \\ +J_1\left(\tfrac{2\omega\sqrt{\bar{T}_0}}{|m|\sqrt{\gamma R}}\right) Y_0\left(\tfrac{2\omega\sqrt{\bar{T}_0+mz}}{|m|\sqrt{\gamma R}}\right)\end{aligned} \tag{C.45}$$

C.3 One-Dimensional Acoustics with an Acoustically Compact Temperature Rise

When an acoustically compact temperature jump is present in a one-dimensional duct at $x = b$, there are two different sound speeds on either side of the jump. This example is a simple model for an acoustically compact deflagration wave, where the pressure is (approximately) constant across the flame and the density and temperature change rapidly. The acoustic behavior can be constructed piecewise from classical acoustics. On either side of the rapid temperature (density) change, the acoustic motions are describe as in classical acoustics if no entropy waves are generated by the flame. This is assured by requiring that the unsteady heat input be zero. On either side of the flame, the analysis from the previous

problem holds and the pressure modeshape is given by

$$\psi(z) = \begin{cases} A_1 \cos(k_1 z) + B_1 \sin(k_1 z) : z < b \\ \\ A_2 \cos[k_2(z-L)] + B_2 \sin[k_2(z-L)] : z > b \end{cases} \tag{C.46}$$

Note that the basis functions for the $z > b$ domain have been shifted to simplify the use of the boundary conditions. The interface conditions require the continuity of acoustic pressure (momentum conservation) and acoustic velocity (from the energy equation)

$$\begin{aligned} p'(b_-) &= p'(b_+) \\ u'(b_-) &= u'(b_+) \end{aligned} \tag{C.47}$$

Assuming a time harmonic solution is assumed at the eigenfrequencies, $p'(x,t) = \psi(x)e^{i\omega t}, u'(x,t) = U'(x)e^{i\omega t}$, and using the acoustic momentum equation from Eq. (C.1) to relate the acoustic velocity to the acoustic pressure given by Eq. (C.50), the interface conditions from Eq. (C.47) become

$$\begin{aligned} \psi(b_-) &= \psi(b_+) \\ \tfrac{1}{\bar{\rho}_1}\tfrac{d\psi}{dz}(b_-) &= \tfrac{1}{\bar{\rho}_2}\tfrac{d\psi}{dz}(b_+) \end{aligned} \tag{C.48}$$

C.3.1 Closed-Closed Boundary Conditions

For closed conditions at $z = 0$ and $z = L$, the boundary conditions can be stated as before

$$\begin{aligned} \tfrac{d\psi}{dz}(0) &= 0 \\ \tfrac{d\psi}{dz}(L) &= 0 \end{aligned} \tag{C.49}$$

Applying the first boundary condition to Eq. (C.46) gives $B_1 = 0$ and applying the second boundary conditions gives $B_2 = 0$. The modeshape for these boundary conditions is given by

$$\psi(z) = \begin{cases} A_1 \cos(k_1 z) : x < b \\ \\ A_2 \cos[k_2(z - L)] : x > b \end{cases} \tag{C.50}$$

where k_i and A_i are the wavenumber and relative magnitude of the i^{th} segment, respectively. The wavenumbers in Eq. (C.50) are related to the eigenfrequencies by

$$\begin{aligned} k_i &= \tfrac{\omega}{\bar{a}_i} \\ \bar{a}_i &= \sqrt{\gamma R \bar{T}_i} \end{aligned} \tag{C.51}$$

Substituting the modeshape from Eq. (C.50) into the two relationships from Eq. (C.48) the following characteristic equation can be found

$$\tan\left(\frac{\omega}{\sqrt{\gamma R \bar{T}_2}}(L - b)\right) + \sqrt{\frac{\bar{T}_1}{\bar{T}_2}} \tan\left(\frac{\omega}{\sqrt{\gamma R \bar{T}_1}} b\right) = 0 \tag{C.52}$$

Equation (C.52) has an infinite set of roots, each representing an eigenfrequency of the duct. The roots can be found by a suitable numerical method and substituted back into Eq. (C.50) for the modeshape, using Eq. (C.51) for the wavenumbers. The ratio of wave amplitudes can also be derived from the two relationships in Eq. (C.48)

$$\frac{A_1}{A_2} = \frac{\cos[k_2(L - b)]}{\cos(k_1 b)} \tag{C.53}$$

C.3.2 Closed-Open Boundary Conditions

For closed condition at $z = 0$ and open boundary at $z = L$, the boundary conditions can be stated as before

$$\begin{aligned} \tfrac{d\psi}{dz}(0) &= 0 \\ \psi(L) &= 0 \end{aligned} \tag{C.54}$$

Applying the first boundary condition to Eq. (C.46) gives $B_1 = 0$ and applying the second boundary conditions gives $A_2 = 0$. The modeshape for these boundary conditions is given by

$$\psi(z) = \begin{cases} A_1 \cos(k_1 z) : z < b \\ \\ B_2 \sin[k_2(z - L)] : z > b \end{cases} \tag{C.55}$$

where k_i and A_i are the wavenumber and relative magnitude of the i^{th} segment, respectively. Substituting the modeshape from Eq. (C.55) into the two relationships from Eq. (C.48) the following characteristic equation can be found

$$\tan\left(\frac{\omega}{\sqrt{\gamma R \bar{T}_2}}(L - b)\right) \tan\left(\frac{\omega}{\sqrt{\gamma R \bar{T}_1}} b\right) - \sqrt{\frac{\bar{T}_2}{\bar{T}_1}} = 0 \tag{C.56}$$

Equation (C.56) has an infinite set of roots, each representing an eigenfrequency of the duct. The roots can be found by a suitable numerical method and substituted back into Eq. (C.55) for the modeshape, using Eq. (C.51) for the wavenumbers. The ratio of wave amplitudes can also be derived from the two relationships in Eq. (C.48)

$$\frac{A_1}{B_2} = \frac{-\sin[k_2(L - b)]}{\cos(k_1 b)} \tag{C.57}$$

C.4 One-Dimensional Acoustics with an Exponential Cross-sectional Area Distribution

Another example problem in which a simple analytical solution exists for one-dimensional acoustics with cross-sectional area changes is the exponential horn. In contrast to a sudden expansion or contraction, this problem has smooth area variation. The cross-sectional area, as a function of axial location z, is given by

$$S(z) = S_0 e^{mz} \tag{C.58}$$

The equations for one-dimensional acoustics with variation in cross-sectional area are

$$\frac{1}{S(z)}\frac{\partial}{\partial z}\left(S(z)\frac{\partial p'}{\partial z}\right) - \frac{1}{\bar{a}^2}\frac{\partial^2 p'}{\partial t^2} = 0 \tag{C.59}$$

which can be rewritten

$$\frac{\partial^2 p'}{\partial z^2} + \frac{1}{S(z)}\frac{\partial S}{\partial z}\frac{\partial p'}{\partial z} - \frac{1}{\bar{a}^2}\frac{\partial^2 p'}{\partial t^2} = 0 \tag{C.60}$$

or

$$\frac{\partial^2 p'}{\partial z^2} + \frac{\partial \ln(S)}{\partial z}\frac{\partial p'}{\partial z} - \frac{1}{\bar{a}^2}\frac{\partial^2 p'}{\partial t^2} = 0 \tag{C.61}$$

Substituting Eq. (C.58) into Eq. (C.61), the governing equation becomes

$$\frac{\partial^2 p'}{\partial z^2} + m\frac{\partial p'}{\partial z} - \frac{1}{\bar{a}^2}\frac{\partial^2 p'}{\partial t^2} = 0 \tag{C.62}$$

where m is a constant. Using the technique of separation of variables, the solution can be written as

$$p'(z,t) = \psi(z)h(t) \tag{C.63}$$

Substitution of Eq. (C.63) into Eq. (C.62) and rearrangement leads to

$$\frac{d^2\psi/dz^2 + m(d\psi/dz)}{\psi/\bar{a}^2} = \frac{d^2h/dt^2}{h} = -\omega^2 \tag{C.64}$$

The first term is a function of x only, while the second term is a function of time only. Therefore, the eigenvalue ω^2 is a constant. This fact splits the PDE into two ODEs. The temporal evolution of a mode is given by

$$\frac{\partial^2 h}{\partial t^2} + \omega^2 h = 0 \tag{C.65}$$

which is simply the harmonic oscillator equation. Because initial conditions are not relevant to the current goals, the solution to Eq. (C.65) can be written as

$$h(t) = e^{i\omega t} \tag{C.66}$$

The spatial ODE from Eq. (C.64) is

$$\frac{\partial^2 \psi}{\partial z^2} + m\frac{\partial \psi}{\partial z} + \frac{\omega^2}{\bar{a}^2}\psi = 0 \tag{C.67}$$

This is a constant coefficient second-order homogeneous ODE which can be solved by assuming solutions of the form

$$\psi(z) = e^{nx} \tag{C.68}$$

Substitution of this form into Eq. (C.67) leads to values of n satisfying

$$n^2 + mn + \frac{\omega^2}{\bar{a}^2} = 0 \tag{C.69}$$

Using the quadratic formula

$$n = -\frac{m}{2} \pm i\sqrt{\left(\frac{\omega}{\bar{a}}\right)^2 - \left(\frac{m}{2}\right)^2} \tag{C.70}$$

and

$$\psi(z) = e^{-(m/2)z}(A^{+}e^{-ikz} + A^{-}e^{ikz}) \tag{C.71}$$

with

$$k = \sqrt{\left(\frac{\omega}{\bar{a}}\right)^{2} - \left(\frac{m}{2}\right)^{2}} \tag{C.72}$$

This problem is solved here only for open-open boundaries, which are given by

$$\begin{aligned} p'(0,t) &= 0 \\ p'(L,t) &= 0 \end{aligned} \tag{C.73}$$

or

$$\begin{aligned} \psi(0) &= 0 \\ \psi(L) &= 0 \end{aligned} \tag{C.74}$$

Using the first boundary condition, $\psi(0) = 0$, with Eq. (C.71), the following is found

$$A^{+} = -A^{-} = A \tag{C.75}$$

Then, using the second boundary condition, $\psi(L) = 0$, the following characteristic equation is found

$$e^{-ikL} = e^{ikL} \tag{C.76}$$

By noting that $e^{-}i(2\pi n) = 1$ for integer n, Eq. (C.76) can be rewritten

$$e^{-ikL} = e^{ikL - 2\pi n} \tag{C.77}$$

or

$$-kL = kL - 2\pi n \tag{C.78}$$

using Eq. (C.72)

$$k = \sqrt{\left(\frac{\omega}{\bar{a}}\right)^2 - \left(\frac{m}{2}\right)^2} = \frac{\pi n}{L} \tag{C.79}$$

which gives frequencies of

$$\omega = \sqrt{\left(\frac{n\pi\bar{a}}{L}\right)^2 + \left(\frac{m\bar{a}}{2}\right)^2} \tag{C.80}$$

The equations for the modeshapes, Eq. (C.71), with Eq. (C.75), simplifies to

$$\psi(x) = e^{-(m/2)z}\sin(kz) \tag{C.81}$$

C.5 One-Dimensional Acoustics with an Acoustically Compact Area Change

The duct with an area discontinuity at $x = b$ in the absence of property variation and mean flow can be solved in the same piecewise manner as above. On either side of the rapid cross-sectional area change, the acoustic motions are describe as in classical acoustics with no duct area changes. On either side of the discontinuity, the analysis from classical acoustics in a constant area duct holds and the pressure modeshape is given by

$$\psi(z) = \begin{cases} A_1\cos(kz) + B_1\sin(kz) : z < b \\ \\ A_2\cos[k(z-L)] + B_2\sin[k(z-L)] : z > b \end{cases} \tag{C.82}$$

Note that the sound speed is not changed by the area discontinuity, therefore the wavenumbers of the two sections are equal. Also, note that the basis functions for the $z > b$ domain have again been shifted to simplify the use of the boundary conditions. The interface conditions require the continuity of acoustic pressure (momentum conservation) and acoustic

volume flux (from the energy equation)

$$\begin{aligned} p'(b_-) &= p'(b_+) \\ S_1 u'(b_-) &= S_2 u'(b_+) \end{aligned} \tag{C.83}$$

where S_i is the cross-sectional area of the i^{th} section. Assuming a time harmonic solution is assumed at the eigenfrequencies, $p'(x,t) = \psi(x)e^{i\omega t}, u'(x,t) = U'(x)e^{i\omega t}$, and using the acoustic momentum equation from Eq. (C.1) to relate the acoustic velocity to the acoustic pressure given by Eq. (C.82), the interface conditions from Eq. (C.47) become

$$\begin{aligned} \psi(b_-) &= \psi(b_+) \\ S_1 \tfrac{d\psi}{dx}(b_-) &= S_2 \tfrac{d\psi}{dx}(b_+) \end{aligned} \tag{C.84}$$

C.5.1 Closed-Closed Boundary Conditions

For closed condition at $z = 0$ and $z = L$, the boundary conditions can be stated as before

$$\begin{aligned} \tfrac{d\psi}{dz}(0) &= 0 \\ \tfrac{d\psi}{dz}(L) &= 0 \end{aligned} \tag{C.85}$$

Applying the first boundary condition to Eq. (C.82) gives $B_1 = 0$ and applying the second boundary conditions gives $B_2 = 0$. The modeshape for these boundary conditions is given by

$$\psi(z) = \begin{cases} A_1 \cos(kz) : x < b \\ A_2 \cos[k(z-L)] : x > b \end{cases} \tag{C.86}$$

Substituting Eq. (C.86) into these the two interface conditions of Eq. (C.84), the following characteristic equation is found

$$\tan\left(\frac{\omega}{\bar{a}}(L-b)\right)+\frac{S_1}{S_2}\tan\left(\frac{\omega}{\bar{a}}b\right)=0 \tag{C.87}$$

As with Eq. (C.56), the infinite zeros of Eq. (C.87), representing the eigenfrequencies of the duct, can be found using a suitable root solver. The modeshapes are then given by substituting the eigenfrequencies back into Eq. (C.86) using the relation $k=\omega/\bar{a}$. Also derived from Eq. (C.84) is the ratio of wave amplitudes

$$\frac{A_1}{A_2}=\frac{\cos[k(L-b)]}{\cos(kb)} \tag{C.88}$$

C.5.2 Closed-Open Boundary Conditions

For closed condition at $z=0$ and open boundary at $z=L$, the boundary conditions can be stated as before

$$\begin{aligned}\tfrac{d\psi}{dz}(0)&=0\\ \psi(L)&=0\end{aligned} \tag{C.89}$$

Applying the first boundary condition to Eq. (C.82) gives $B_1=0$ and applying the second boundary conditions gives $A_2=0$. The modeshape for these boundary conditions is given by

$$\psi(z)=\begin{cases}A_1\cos(kz):x<b\\ B_2\sin[k(z-L)]:x>b\end{cases} \tag{C.90}$$

Substituting Eq. (C.90) into these the two interface conditions of Eq. (C.84), the following characteristic equation is found

$$\tan\left(\frac{\omega}{\bar{a}}(L-b)\right)\tan\left(\frac{\omega}{\bar{a}}b\right)-\frac{S_2}{S_1}=0 \tag{C.91}$$

As with Eq. (C.56), the infinite zeros of Eq. (C.91), representing the eigenfrequencies of the duct, can be found using a suitable root solver. The modeshapes are then given by substituting the eigenfrequencies back into Eq. (C.90) using the relation $k=\omega/\bar{a}$. Also derived from Eq. (C.84) is the ratio of wave amplitudes

$$\frac{A_1}{B_2}=\frac{-\sin[k(L-b)]}{\cos(kb)} \tag{C.92}$$

C.6 One-Dimensional Acoustics with a Uniform Mean Flow

For the constant area, constant property duct with a subsonic mean flow ($M<1$), the linearized conservation laws for momentum and energy become

$$\begin{aligned}\tfrac{\partial u'}{\partial t}+\bar{u}\tfrac{\partial u'}{\partial z}+\tfrac{1}{\bar{\rho}}\tfrac{\partial p'}{\partial z}&=0\\ \tfrac{\partial p'}{\partial t}+\bar{u}\tfrac{\partial p'}{\partial z}+\gamma\bar{p}\tfrac{\partial u'}{\partial z}&=0\end{aligned} \tag{C.93}$$

The solution to this system of hyperbolic equations is given by a superposition of forward and backward travelling waves with propagation speeds

$$\lambda^{\pm}=\bar{u}\pm\bar{a} \tag{C.94}$$

and wavenumbers

$$k^{\pm}=\frac{\omega}{\lambda^{\pm}} \tag{C.95}$$

The general acoustic pressure modeshape before the application of boundary conditions ca be written as

$$p'(x,t) = A^+ e^{i(\omega t - k^+ x)} + A^- e^{i(\omega t - k^- x)} \tag{C.96}$$

Substituting Eq. (C.96) into the energy conservation Eq. (C.93) and simplifying yields the general acoustic velocity modeshape

$$u'(x,t) = \frac{A^+}{Z_0} e^{i(\omega t - k^+ x)} - \frac{A^-}{Z_0} e^{i(\omega t - k^- x)} \tag{C.97}$$

where $Z_0 = \bar{\rho}\bar{a}$ is the characteristic impedance of the gaseous medium.

C.6.1 Closed-Closed Boundary Conditions

Applying the closed inlet boundary condition $u'(0,t) = 0$, Eq. (C.97) reduces to

$$A^+ = A^- = A \tag{C.98}$$

Substituting Eq. (C.98) into the pressure modeshape, Eq. (C.96), and applying the open exit boundary condition $u'(L,t) = 0$, leads to the characteristic equation

$$e^{-ik^+ L} - e^{-ik^- L} = 0 \tag{C.99}$$

Noting that $e^{i(2n)\pi} = 1$ and equating the exponents

$$k^+ L - k^- L = (2n)\pi \tag{C.100}$$

Using Eq. (C.94) and Eq. (C.95) the characteristic equation can be solved analytically

$$f_n = \frac{n\bar{a}}{2L}(1 - \bar{M}^2) \tag{C.101}$$

where $\bar{M} = \frac{\bar{u}}{\bar{a}}$. Note that this reduces to the classical acoustic frequencies in the absence of mean flow ($\bar{M} = 0$).

C.6.2 Closed-Open Boundary Conditions

Applying the closed inlet boundary condition $u'(0,t) = 0$, Eq. (C.97) reduces to

$$A^+ = -A^- = A \tag{C.102}$$

Substituting Eq. (C.102) into the pressure modeshape, Eq. (C.96), and applying the open exit boundary condition $p'(L,t) = 0$, leads to the characteristic equation

$$e^{-ik^+L} + e^{-ik^-L} = 0 \tag{C.103}$$

Noting that $e^{i(2n-1)\pi} = -1$ and equating the exponents

$$k^+L - k^-L = (2n-1)\pi \tag{C.104}$$

Using Eq. (C.94) and Eq. (C.95) the characteristic equation can be solved analytically

$$f_n = \frac{(n-\frac{1}{2})\bar{a}}{2L}(1-\bar{M}^2) \tag{C.105}$$

where $\bar{M} = \frac{\bar{u}}{\bar{a}}$. Note that this reduces to the classical acoustic frequencies in the absence of mean flow ($\bar{M} = 0$).

C.7 Three-dimensional Acoustics in a Circular Cylinder

For simple geometries, three-dimensional modeshapes can be constructed by separation of variables, allowing for the calculation of frequencies for transverse, radial, and combined modes in addition to the longitudinal modes found above. The equation for three-dimensional acoustics in the absence of mean flow, mean property gradients, and non-linear effects is given by

$$\frac{\partial^2 p'}{\partial x_i^2} - \frac{1}{\bar{a}^2}\frac{\partial^2 p'}{\partial t^2} = 0 \tag{C.106}$$

For cylindrical coordinates, the Laplacian term in Eq. (C.106) is written as

$$\frac{\partial^2 p'}{\partial x_i^2} = \frac{1}{r}\frac{\partial}{\partial r}\left(r\frac{\partial p'}{\partial r}\right) + \frac{1}{r^2}\frac{\partial^2 p'}{\partial \theta^2} + \frac{\partial^2 p'}{\partial z^2} = \frac{\partial^2 p'}{\partial r^2} + \frac{1}{r}\frac{\partial p'}{\partial r} + \frac{1}{r^2}\frac{\partial^2 p'}{\partial \theta^2} + \frac{\partial^2 p'}{\partial z^2} \tag{C.107}$$

Performing separation of variables for all four independent variables

$$p'(r,\theta,z,t) = \phi(r)\chi(\theta)\psi(z)h(t) \tag{C.108}$$

Substituting Eq. (C.108) into Eq. (C.106) and rearranging

$$\frac{d^2\phi/dr^2}{\phi} + \frac{1}{r}\frac{d\phi/dr}{\phi} + \frac{1}{r^2}\frac{d\chi/d\theta}{\chi} + \frac{d^2\psi/dz^2}{\psi} = \frac{1}{\bar{a}^2}\frac{d^2h/dt^2}{h} = -k^2 \tag{C.109}$$

Using the same arguments used in one dimension, with constant speed of sound, the temporal ODE is as before

$$\frac{d^2h}{dt^2} + k^2\bar{a}^2 h = \frac{d^2h}{dt^2} + \omega^2 h = 0 \tag{C.110}$$

In the present derivation, the initial conditions are not important and only the frequencies and modeshapes are sought. Hence the solution to Eq. (C.110) is simply written as

$$h(t) = e^{i\omega t} \tag{C.111}$$

F Next, the spatial components in Eq. (C.109) can be separated one at a time.

C.7.1 Longitudinal Modes

First, rearranging Eq. (C.109)

$$\frac{d^2\phi/dr^2}{\phi} + \frac{1}{r}\frac{d\phi/dr}{\phi} + \frac{1}{r^2}\frac{d\chi/d\theta}{\chi} + k^2 = -\frac{d^2\psi/dz^2}{\psi} = k_z^2 \tag{C.112}$$

The left hand side is a function of r and θ only, while the middle is a function of z only, making them both equal to a constant, here labelled k_z^2, since it will be related to the axial component of the wave number. The axial ODE is then

$$\frac{d^2\psi}{dz^2} + k_z\psi = 0 \tag{C.113}$$

which is the same as the modes from the simple 1D acoustic duct with constant temperature and cross-section without mean flow. The general solution to Eq. (C.113) is a linear combination of sine and cosine waves

$$\psi(z) = A_1\cos(k_z z) + A_2\sin(k_z z) \tag{C.114}$$

The coefficients A_1 and A_2 can be found by using boundary conditions at $z = 0$ and $z = L$. The following is a summary of modeshapes and axial wavenumbers for different boundary

conditions, along with frequencies for pure longitudinal modes. Details of the derivation of these are in previous sections.

C.7.1.1 Closed-Closed Boundary Conditions

Modeshape:

$$\psi_j(z) = \cos\left(\frac{j\pi z}{L}\right) \tag{C.115}$$

Wave-number:

$$(k_z)_j = \frac{j\pi}{L} \tag{C.116}$$

Pure longitudinal frequency:

$$\omega_j = \frac{j\pi\bar{a}}{L} \tag{C.117}$$

C.7.1.2 Open-Open Boundary Conditions

Modeshape:

$$\psi_j(z) = \sin\left(\frac{j\pi z}{L}\right) \tag{C.118}$$

Wave-number:

$$(k_z)_j = \frac{j\pi}{L} \tag{C.119}$$

Pure longitudinal frequency:

$$\omega_j = \frac{j\pi\bar{a}}{L} \tag{C.120}$$

C.7.1.3 Closed-Open Boundary Conditions

Modeshape:

$$\psi_j(z) = \cos\left(\frac{(j-1/2)\pi z}{L}\right) \tag{C.121}$$

Wave-number:

$$(k_z)_j = \frac{(j-1/2)\pi}{L} \tag{C.122}$$

Pure longitudinal frequency:

$$\omega_j = \frac{(j-1/2)\pi \bar{a}}{L} \tag{C.123}$$

C.7.1.4 Open-Closed Boundary Conditions

Modeshape:

$$\psi_j(z) = \sin\left(\frac{(j-1/2)\pi z}{L}\right) \tag{C.124}$$

Wave-number:

$$(k_z)_j = \frac{(j-1/2)\pi}{L} \tag{C.125}$$

Pure longitudinal frequency:

$$\omega_j = \frac{(j-1/2)\pi \bar{a}}{L} \tag{C.126}$$

C.7.2 Tangential and Radial Modes

Re-arranging Eq. (C.112)

$$r^2\frac{d^2\phi/dr^2}{\phi} + r\frac{d\phi/dr}{\phi} + r^2(k^2 - k_z^2) = -\frac{d\chi/d\theta}{\chi} = m^2 \tag{C.127}$$

Again, because the left side is a function of r only and the middle is a function of θ only, the right hand side is a constant, here denoted as m^2 given the fact that it does not represent a physical wave number. The boundary conditions in the circumferential direction are periodic, thus there cannot be pure circumferential modes due to the singularity at $r = 0$. Instead, m must be an dimensionless integer. Therefore, the circumferential modeshape must be combined with a radial modeshape for the creation of a tangential mode. The circumferential ODE is

$$\frac{d^2\chi}{d\theta^2} + m^2\chi = 0 \tag{C.128}$$

whose solution is

$$\chi(\theta) = B_1\cos(m\theta) + B_2\sin(m\theta) \tag{C.129}$$

The coefficients B_1 and B_2 can be set arbitrarily by the alignment of the mode due to radial symmetry. Setting

$$k^2 = k_r^2 + k_z^2 \tag{C.130}$$

and applying this to Eq. (C.127)

$$r^2\frac{d^2\phi/dr^2}{\phi} + r\frac{d\phi/dr}{\phi} + (r^2k_r^2 - m^2) = 0 \tag{C.131}$$

which can be recognized as an m^{th} order Bessel equation. The solution to Eq. (C.131) is given by a linear superposition of first and second kind Bessel functions

$$\phi(r) = C_1 J_m(k_r r) + C_2 Y_m(k_r r) \tag{C.132}$$

For circular cylinders, the second kind Bessel function $Y_m(k_r r)$ has a singularity at $r = 0$ and hence cannot contribute to the solution of Eq. (C.131). Eliminating this term from Eq. (C.133)

$$\phi(r) = J_m(k_r r) \tag{C.133}$$

C.7.2.1 Radial Modes

Pure radial modes are constructed from the above when $m = 0$ and the circumferential modeshape χ is a constant. Similarly, $k_z = 0$ and the longitudinal modeshape is a constant, which means that the frequency is, using Eq. (C.130) given by

$$\omega = k\bar{a} = k_r\bar{a} \tag{C.134}$$

and the modeshape from Eq. (C.133) with $m = 0$

$$\phi(r) = J_0(k_r r) \tag{C.135}$$

For cylindrical combustion systems, the relevant radial boundary condition is closed, $u' = 0$ and $dp/dr = 0$, thus $d\phi/dr = 0$ at $r = R$. Differentiation of the modeshape gives

$$\frac{d\phi}{dr} = -k_r J_1(k_r r) \tag{C.136}$$

and substitution of the homogeneous boundary condition yields the characteristic equation for the frequencies

$$J_1(k_r R) = 0 \tag{C.137}$$

Denoting $\zeta_n^{(m)}$ as the n^{th} root of the m^{th} order first-kind Bessel function, the solution to Eq. (C.137) is

$$(k_r)_n = \frac{\zeta_n^{(1)}}{R} \tag{C.138}$$

$$\omega_n = \frac{\zeta_n^{(1)} \bar{a}}{R} \tag{C.139}$$

where for any integer n

$$J_m(\zeta_n^{(m)}) = 0 \tag{C.140}$$

and the modeshapes are given by

$$\phi_{0n}(r) = J_0 \left(\zeta_n^{(1)} \frac{r}{R} \right) \tag{C.141}$$

The first five roots, $\zeta_n^{(1)}$ are tabulated in Table C.1.

Table C.1: Roots of the first order Bessel function or the first kind, $J_1(\zeta_n^{(1)}) = 0$

n	1	2	3	4	5
$\zeta_n^{(1)}$	3.832	7.016	10.173	13.324	16.471

C.7.2.2 Tangential Modes

For tangential modes, the approach is similar, except the absence of circumferential variation ($m = 0$) is no longer required. For arbitrary integer m

$$\chi(\theta) = \cos(m\theta + \Phi) \tag{C.142}$$

where Φ is an arbitrary phase which controls a particular circumferential alignment. The value of Φ is irrelevant to the frequencies, therefore, the angle θ can be defined with reference such that the circumferential component of the tangential mode is

$$\chi(\theta) = \cos(m\theta) \tag{C.143}$$

Requiring a closed boundary, $d\phi/dr = 0$ at $r = R$

$$\frac{dJ_m(k_r r)}{dr}|_{r=R} = 0 \tag{C.144}$$

Letting $\xi_n^{(m)}$ denote the n^{th} root of the derivative of the first-kind Bessel function of order m, the solution to Eq. (C.144) is

$$(k_r)_{mn} = \frac{\xi_n^{(m)}}{R} \tag{C.145}$$

$$\omega_{mn} = \frac{\xi_n^{(m)} \bar{a}}{R} \tag{C.146}$$

radial component of the tangential mode is given by

$$\phi_{mn}(r) = J_m \left(\xi_n^{(m)} \frac{r}{R} \right) \tag{C.147}$$

The overall modeshape is given by

$$\chi_m(\theta)\phi_{mn}(r) = \cos(m\theta)J_m\left(\xi_n^{(m)}\frac{r}{R}\right) \tag{C.148}$$

Pure tangential modes are constructed with $n = 1$, the roots of which are tabulated in Table C.2

$$\chi_m(\theta)\phi_{m1}(r) = \cos(m\theta)J_m\left(\xi_1^{(m)}\frac{r}{R}\right) \tag{C.149}$$

Table C.2: Roots of the first order Bessel function or the first kind, $\frac{dJ_1}{dr}(\xi_1^{(m)}) = 0$

m	1	2	3	4
$\xi_1^{(m)}$	1.841	3.054	4.201	5.318

C.7.3 Combined Modes

Combined modes are constructed by combining the above longitudinal and radial/tangential modes. Equation (C.130) gives the frequency for combined modes. The modeshapes are given by

$$\phi_{mn}(r)\chi_m(\theta)\psi_j(z) \tag{C.150}$$

and frequencies given by

$$\omega_{jmn} = \bar{a}\sqrt{(k_r)_{mn}^2 + (k_z)_j^2} \tag{C.151}$$

Note that $m = 0$ and $n = 0$ with $j = 1, 2, 3$, gives pure longitudinal modes; $m = 0$ and $j = 0$ with $n = 1, 2, 3$, gives pure radial modes; $n = 1$ and $j = 0$ with $m = 1, 2, 3$ gives pure tangential modes. Also note that

$$\zeta_n^{(1)} = \xi_n^{(0)} \tag{C.152}$$

C.8 Three Dimensional Acoustics in an Annular Cylinder

Similar to the previous discussion of the circular cylinder, acoustics in an annular cylinder can be described using separation of variables. Many of the mathematical details are the same as those above. Starting with the acoustic pressure wave equation

$$\frac{\partial^2 p'}{\partial x_i^2} - \frac{1}{\bar{a}^2}\frac{\partial^2 p'}{\partial t^2} = 0 \tag{C.153}$$

With the above equation written in cylindrical coordinates, performing separation of variables for all four independent variables

$$p'(r, \theta, z, t) = \phi(r)\chi(\theta)\psi(z)h(t) \tag{C.154}$$

Substituting Eq. (C.154) into Eq. (C.153) and rearranging

$$\frac{d^2\phi/dr^2}{\phi} + \frac{1}{r}\frac{d\phi/dr}{\phi} + \frac{1}{r^2}\frac{d\chi/d\theta}{\chi} + \frac{d^2\psi/dz^2}{\psi} = \frac{1}{\bar{a}^2}\frac{d^2h/dt^2}{h} = -k^2 \tag{C.155}$$

Skipping intermediate steps shown above, the temporal evolution is described by the harmonic oscillator equation, with solution

$$h(t) = e^{i\omega t} \tag{C.156}$$

As with the circular cylinder, each coordinate direction can now be separated into its own ODE.

C.8.1 Longitudinal Modes

First, rearranging Eq. (C.155)

$$\frac{d^2\phi/dr^2}{\phi} + \frac{1}{r}\frac{d\phi/dr}{\phi} + \frac{1}{r^2}\frac{d\chi/d\theta}{\chi} + k^2 = -\frac{d^2\psi/dz^2}{\psi} = k_z^2 \tag{C.157}$$

which, by intermediate steps shown in more detail for the circular cylinder, leads to the harmonic oscillator ODE in the axial direction, with solution

$$\psi(z) = A_1 \cos(k_z z) + A_2 \sin(k_z z) \tag{C.158}$$

As before, the coefficients A_1 and A_2 are dependent on the boundary conditions at $z = 0$ and $z = L$. The results are identical to the circular cylinder, since no fundamental change has occurred in the axial direction. The modeshapes and frequencies for longitudinal modes are the same as the circular cylinder, and there is no need to repeat them here.

C.8.2 Tangential and Radial Modes

Re-arranging Eq. (C.112)

$$r^2\frac{d^2\phi/dr^2}{\phi} + r\frac{d\phi/dr}{\phi} + r^2(k^2 - k_z^2) = -\frac{d\chi/d\theta}{\chi} = m^2 \tag{C.159}$$

This further separation of variables leads the harmonic oscillator ODE in the circumferential direction, whose solution is

$$\chi(\theta) = B_1 \cos(m\theta) + B_2 \sin(m\theta) \tag{C.160}$$

This solution must satisfy periodic boundary conditions. The coefficients B_1 and B_2 can be set arbitrarily by the alignment of the mode due to radial symmetry. Setting

$$k^2 = k_r^2 + k_z^2 \tag{C.161}$$

and applying this to Eq. (C.159)

$$r^2 \frac{d^2\phi/dr^2}{\phi} + r\frac{d\phi/dr}{\phi} + (r^2 k_r^2 - m^2) = 0 \tag{C.162}$$

which can be recognized as an m^{th} order Bessel equation. The solution to Eq. (C.162) is given by a linear superposition of first and second kind Bessel functions

$$\phi(r) = C_1 J_m(k_r r) + C_2 Y_m(k_r r) \tag{C.163}$$

The second-kind Bessel function cannot be eliminated, as with the circular cylinder, because the location $r = 0$ is not in the annular domain. Instead, the coefficients C_1 and C_2 are found for a particular annulus by setting boundary conditions at $r = R_{inner}$ and $r = R_{outer}$, the inner and outer radii.

C.8.2.1 Radial Modes

Pure radial modes are constructed from the above when $m = 0$ and the circumferential modeshape χ is a constant. Similarly, $k_z = 0$ and the longitudinal modeshape is a constant,

which means that the frequency is, using Eq. (C.130) given by

$$\omega = k\bar{a} = k_r\bar{a} \tag{C.164}$$

and the modeshape from Eq. (C.163) with $m = 0$

$$\phi(r) = C_1 J_0(k_r r) + C_2 Y_0(k_r r) \tag{C.165}$$

the derivative of which is

$$\frac{d\phi}{dr} = -C_1 k_r J_1(k_r r) - C_2 k_r Y_1(k_r r) \tag{C.166}$$

Requiring a closed boundary (wall) at both inner and outer radii, $d\phi/dr = 0$ at $r = R_{inner}$ and $r = R_{outer}$, leads to the characteristic equation

$$J_1(k_r R_{outer})Y_1(k_r R_{inner}) - J_1(k_r R_{inner})Y_1(k_r R_{outer}) = 0 \tag{C.167}$$

This equation has an infinite number of solutions, $(k_r)_{0n}$ $(n = 1, 2, 3,)$, and can be solved numerically for the frequencies using a root finder. The frequencies and modeshapes are then given by

$$\omega_{0n} = (k_r)_{0n}\ \bar{a} \tag{C.168}$$

$$\phi_{0n}(r) = Y_1((k_r)_{0n}R_{inner})J_0((k_r)_{0n}r) - J_1((k_r)_{0n}R_{inner})Y_0((k_r)_{0n}r) \tag{C.169}$$

C.8.2.2 Tangential Modes

For $m \neq 0$ and $n = 1$, pure tangential modes can be constructed. As discussed for the circular cylinder, the circumferential contribution to the modeshape is

$$\chi_m(\theta) = \cos(m\theta) \tag{C.170}$$

Requiring closed boundaries, $d\phi/dr = 0$ at $r = R_{inner}$ and $r = R_{outer}$, the characteristic equation becomes

$$J'_m(k_r R_{outer})Y'_m(k_r R_{inner}) - J'_m(k_r R_{inner})Y'_m(k_r R_{outer}) = 0 \tag{C.171}$$

where the prime denotes differentiation of the Bessel function. The zeros of this function can be found using a suitable numerical root finder and labelled here as $(k_r)_m n$ for the n^{th} root with m^{th} order Bessel functions. In general frequencies and modeshapes are given by

$$\omega_{mn} = (k_r)_{mn}\ \bar{a} \tag{C.172}$$

$$\phi_{mn}(r) = Y'_m((k_r)_{mn}R_{inner})J'_m((k_r)_{mn}r) - J'_m((k_r)_{mn}R_{inner})Y'_m((k_r)_{mn}r) \tag{C.173}$$

For pure tangential modes, $n = 1$, the first solution to the characteristic equation is taken

$$\omega_{m1} = (k_r)_{m1}\ \bar{a} \tag{C.174}$$

$$\phi_{m1}(r) = Y'_m((k_r)_{m1}R_{inner})J'_m((k_r)_{m1}r) - J'_m((k_r)_{m1}R_{inner})Y'_m((k_r)_{m1}r) \tag{C.175}$$

C.8.3 Combined Modes

Combined modes, as with the circular cylinder, are constructed by combining the above longitudinal and radial/tangential modes. Equation (C.161) gives the frequency for combined modes. The modeshapes are given by

$$\phi_{mn}(r)\chi_m(\theta)\psi_j(z) \tag{C.176}$$

and frequencies given by

$$\omega_{jmn} = \bar{a}\sqrt{(k_r)_{mn}^2 + (k_z)_j^2} \tag{C.177}$$

Note that $m = 0$ and $n = 0$ with $j = 1, 2, 3$, gives pure longitudinal modes; $m = 0$ and $j = 0$ with $n = 1, 2, 3$, gives pure radial modes; $n = 1$ and $j = 0$ with $m = 1, 2, 3$ gives pure tangential modes.

C.9 General Rijke Tube Formulation

A Rijke tube presents an idealized thermoacoustic flow with all of the basic physics of combustion instability problems. All motions are assumed one-dimensional from $z = 0$ to $z = L$, with constant mean flow and mean variables on either side of an infinitesimally thin flame sheet at $z = L$. The heat release is thus modelled as

$$\bar{q}(z) = \bar{Q}\delta(z - b) \tag{C.178}$$

$$q'(z, t) = Q'(t)\delta(z - b) \tag{C.179}$$

The region $0 < z < b$ is given the subscript $_1$ and the region $b < z < L$ is given the subscript $_2$. The deflagration flame is modelled to have no effect on the mean pressure. The mean fields are thus described by

$$\bar{p}(z) = \bar{p}_1 = \bar{p}_2 = \bar{p} \tag{C.180}$$

$$\bar{T}(z) = \bar{T}_1 + \mathcal{H}(z-b)(\bar{T}_2 - \bar{T}_1) \tag{C.181}$$

$$\bar{\rho}(z) = \bar{\rho}_1 + \mathcal{H}(z-b)(\bar{\rho}_2 - \bar{\rho}_1) \tag{C.182}$$

$$\bar{u}(z) = \bar{u}_1 + \mathcal{H}(z-b)(\bar{u}_2 - \bar{u}_1) \tag{C.183}$$

The mean continuity equation relates the mean densities and velocities as follows

$$\bar{\rho}_1 \bar{u}_1 = \bar{\rho}_2 \bar{u}_2 \tag{C.184}$$

C.9.1 Governing Equations

On either side of the discontinuity at $x = b$, the mean gradients are zero and there is no heat release. In this case, the governing equations are Mass:

$$\frac{\partial \rho'}{\partial t} + \bar{\rho}\frac{\partial u'}{\partial z} + \bar{u}\frac{\partial \rho'}{\partial z} = 0 \tag{C.185}$$

Momentum:

$$\frac{\partial u'}{\partial t} + \bar{u}\frac{\partial u'}{\partial z} + \frac{1}{\bar{\rho}}\frac{\partial p'}{\partial z} = 0 \tag{C.186}$$

Energy (Pressure):

$$\frac{\partial p'}{\partial t} + \bar{u}\frac{\partial p'}{\partial z} + \gamma\bar{p}\frac{\partial u'}{\partial z} = 0 \tag{C.187}$$

These can be written in vector form as

$$\frac{\partial \underset{\sim}{q}}{\partial t} + \underset{\approx}{A}\frac{\partial \underset{\sim}{q}}{\partial z} = 0 \tag{C.188}$$

with

$$\underset{\sim}{q} = (\rho' \quad u' \quad p')^T \tag{C.189}$$

and

$$\underset{\approx}{A} = \begin{bmatrix} \bar{u} & \bar{\rho} & 0 \\ 0 & \bar{u} & \frac{1}{\bar{\rho}} \\ 0 & \gamma\bar{p} & \bar{u} \end{bmatrix} \tag{C.190}$$

C.9.2 General Solution

The eigenvalues of the flux matrix $\underset{\approx}{A}$ are

$$\lambda^- = \bar{u} - \bar{a} \tag{C.191}$$

$$\lambda^s = \bar{u} \tag{C.192}$$

$$\lambda^+ = \bar{u} + \bar{a} \tag{C.193}$$

where $\bar{a}$ is the sound speed on either side of the flame given by

$$\bar{a} = \sqrt{\frac{\gamma\bar{p}}{\bar{\rho}}} \tag{C.194}$$

The left eigenvectors are

$$\underset{\sim}{l}^- = (0 \quad -\bar{\rho}\bar{a} \quad 1) \tag{C.195}$$

$$\underset{\sim}{l}^s = (-\bar{a}^2 \quad 0 \quad 1) \tag{C.196}$$

$$\underset{\sim}{l}^+ = (0 \quad \bar{\rho}\bar{a} \quad 1) \tag{C.197}$$

Hence, the waves for a harmonic signal with complex frequency ($\Omega = \omega - i\alpha$) propagate as

$$\hat{p}^- \sim \exp\left[\Omega\left(t - \frac{z}{\bar{u} - \bar{a}}\right)\right] \tag{C.198}$$

$$\hat{p}^s \sim \exp\left[\Omega\left(t - \frac{z}{\bar{u}}\right)\right] \tag{C.199}$$

$$\hat{p}^+ \sim \exp\left[\Omega\left(t - \frac{z}{\bar{u} + \bar{a}}\right)\right] \tag{C.200}$$

with strengths given by

$$\hat{p}^- = \hat{p} - \bar{\rho}\bar{a}\hat{u} \tag{C.201}$$

$$\hat{p}^s = \hat{p} - \bar{a}^2\hat{\rho} \tag{C.202}$$

$$\hat{p}^+ = \hat{p} + \bar{\rho}\bar{a}\hat{u} \tag{C.203}$$

Rearranging these relations, the fluctuation of primitive variables can be written as

$$\hat{p} = \frac{1}{2}\left(\hat{p}^+ + \hat{p}^-\right) \tag{C.204}$$

$$\hat{u} = \frac{1}{2\bar{\rho}\bar{a}}\left(\hat{p}^+ - \hat{p}^-\right) \tag{C.205}$$

$$\hat{\rho} = \frac{1}{2\bar{a}^2}\left(\hat{p}^+ + \hat{p}^-\right) - \frac{1}{\bar{a}^2}\hat{p}^s \tag{C.206}$$

In terms of wave amplitudes (A^-, A^s, and A^+), write

$$\hat{p}^- = 2A^- \exp\left[\Omega\left(t - \frac{z}{\bar{u} - \bar{a}}\right)\right] \tag{C.207}$$

$$\hat{p}^s = A^s \exp\left[\Omega\left(t - \frac{z}{\bar{u}}\right)\right] \tag{C.208}$$

$$\hat{p}^+ = 2A^+ \exp\left[\Omega\left(t - \frac{z}{\bar{u}+\bar{a}}\right)\right] \tag{C.209}$$

Combination of the previous six equations gives

$$p'(z,t) = A^+ \exp\left[\Omega\left(t - \frac{z}{\bar{u}+\bar{a}}\right)\right] + A^- \exp\left[\Omega\left(t - \frac{z}{\bar{u}-\bar{a}}\right)\right] \tag{C.210}$$

$$\bar{\rho}\bar{a}u'(z,t) = A^+ \exp\left[\Omega\left(t - \frac{z}{\bar{u}+\bar{a}}\right)\right] - A^- \exp\left[\Omega\left(t - \frac{z}{\bar{u}-\bar{a}}\right)\right] \tag{C.211}$$

$$\bar{a}^2\rho'(z,t) = A^+ \exp\left[\Omega\left(t - \frac{z}{\bar{u}+\bar{a}}\right)\right] + A^- \exp\left[\Omega\left(t - \frac{z}{\bar{u}-\bar{a}}\right)\right] - A^s \exp\left[\Omega\left(t - \frac{z}{\bar{u}}\right)\right] \tag{C.212}$$

Note that if the entropy wave is zero ($A^s = 0$), then the density is related to the pressure via the isentropic relation

$$\rho' = \frac{p'}{\bar{a}^2} \tag{C.213}$$

Writing Eqns. (C.210) - (C.212) for either side of the flame

$$p'_1(z,t) = A_1^+ \exp\left[\Omega\left(t - \frac{z}{\bar{u}_1+\bar{a}_1}\right)\right] + A_1^- \exp\left[\Omega\left(t - \frac{z}{\bar{u}_1-\bar{a}_1}\right)\right] \tag{C.214}$$

$$\bar{\rho}\bar{a}u'_1(z,t) = A_1^+ \exp\left[\Omega\left(t - \frac{z}{\bar{u}_1+\bar{a}_1}\right)\right] - A_1^- \exp\left[\Omega\left(t - \frac{z}{\bar{u}_1-\bar{a}_1}\right)\right] \tag{C.215}$$

$$\bar{a}^2\rho'_1(z,t) = A_1^+ \exp\left[\Omega\left(t - \frac{z}{\bar{u}_1+\bar{a}_1}\right)\right] + A_1^- \exp\left[\Omega\left(t - \frac{z}{\bar{u}_1-\bar{a}_1}\right)\right] - A_1^s \exp\left[\Omega\left(t - \frac{z}{\bar{u}_1}\right)\right] \tag{C.216}$$

and

$$p'_2(z,t) = A_2^+ \exp\left[\Omega\left(t - \frac{z-L}{\bar{u}_2+\bar{a}_2}\right)\right] + A_2^- \exp\left[\Omega\left(t - \frac{z-L}{\bar{u}_2-\bar{a}_2}\right)\right] \tag{C.217}$$

$$\bar{\rho}\bar{a}u'_2(z,t) = A_2^+ \exp\left[\Omega\left(t - \frac{z-L}{\bar{u}_2+\bar{a}_2}\right)\right] - A_2^- \exp\left[\Omega\left(t - \frac{z-L}{\bar{u}_2-\bar{a}_2}\right)\right] \tag{C.218}$$

$$\bar{a}^2\rho_2'(z,t) = A_2^+ \exp\left[\Omega\left(t - \frac{z-L}{\bar{u}_2+\bar{a}_2}\right)\right] + A_2^- \exp\left[\Omega\left(t - \frac{z-L}{\bar{u}_2-\bar{a}_2}\right)\right] - A_2^s \exp\left[\Omega\left(t - \frac{z-L}{\bar{u}_2}\right)\right] \tag{C.219}$$

Note that the wave structure on the downstream side of the flame is written in terms of a shifted variable $z - L$, which conveniently goes to zero at the outlet boundary. Finally, we also assume harmonic dependence on time for the unsteady heat release

$$\frac{1}{\bar{a}}Q'(t) = A^Q \exp(i\Omega t) \tag{C.220}$$

In this way, the original problem in terms of the seven primitive variables (ρ_1', u_1', p_1', ρ_2', u_2', p_2', q') has been rephrased in terms of seven wave strengths (A_1^-, A_1^s, A_1^+, A_2^-, A_2^s, A_2^+, A_Q). The advantage we have gained in doing this, by assuming the space-time behavior of the solution, is that boundary conditions and interface matching conditions can now provide algebraic relations for the new unknowns and matrix methods can be employed to reach the solution.

C.9.3 Boundary Conditions

The three most common acoustic boundary conditions are

Closed:

$$u' = 0 \tag{C.221}$$

Open:

$$p' = 0 \tag{C.222}$$

Choked:

$$\rho' \bar{u} + \bar{\rho} u' = 0 \tag{C.223}$$

In addition to an acoustic boundary provided at the inlet and outlet, a boundary condition for the incoming entropy wave must be provided to the inlet. The most common and easiest to implement is the isentropic assumption, hence

$$p' - \bar{a}^2 \rho' = 0 \tag{C.224}$$

Substituting Eqns. (C.214) - (C.212) into the boundary conditions at the inlet Closed inlet:

$$u_1'(0,t) = A_1^+ \exp(i\Omega t) - A_1^- \exp(i\Omega t) = 0 \tag{C.225}$$

$$A_1^- - A_1^+ = 0 \tag{C.226}$$

Open inlet:

$$p_1'(0,t) = A_1^+ \exp(i\Omega t) + A_1^- \exp(i\Omega t) = 0 \tag{C.227}$$

$$A_1^- + A_1^+ = 0 \tag{C.228}$$

Isentropic inlet:

$$p_1'(0,t) - \bar{a}^2 \rho_1'(0,t) = A_1^s \exp(i\Omega t) = 0 \tag{C.229}$$

$$A_1^s = 0 \tag{C.230}$$

Isentropic choked inlet:

$$\rho_1'(0,t)\bar{u}_1 + \bar{\rho}_1 u_1'(0,t) = (1+\bar{M})A_1^+ \exp(i\Omega t) - (1-\bar{M})A_1^- \exp(i\Omega t) = 0 \tag{C.231}$$

$$(1+\bar{M}_1)A_1^+ - (1-\bar{M}_1)A_1^- = 0 \tag{C.232}$$

Similarly, the substitution of Eqns. (C.217) - (C.219) into the exit boundary conditions

Closed outlet:

$$u_2'(0,t) = A_2^+ \exp(i\Omega t) - A_2^- \exp(i\Omega t) = 0 \tag{C.233}$$

$$A_2^- - A_2^+ = 0 \tag{C.234}$$

Open outlet:

$$p_2'(0,t) = A_2^+ \exp(i\Omega t) + A_2^- \exp(i\Omega t) = 0 \tag{C.235}$$

$$A_2^- + A_2^+ = 0 \tag{C.236}$$

Choked outlet:

$$\rho_2'(0,t)\bar{u}_2 + \bar{\rho}_2 u_2'(0,t) = (1+\bar{M})A_2^+ \exp(i\Omega t) - (1-\bar{M})A_2^- \exp(i\Omega t) - \bar{M}A_2^s \exp(i\Omega t) = 0 \tag{C.237}$$

$$(1+\bar{M})A_2^+ - (1-\bar{M})A_2^- - \bar{M}A_2^s = 0 \tag{C.238}$$

Note that the choked outlet allows the entropy wave to interact with the acoustic waves at the outlet boundary, which could provide another means of feedback to the combustion oscillations.

C.9.4 Interface Conditions

Across the discontinuity at the flame, the conservative form of the governing equations are used to construct interface matching conditions for the acoustic waves and entropy wave.

The conservative form of the equations are

Mass:

$$\frac{\partial \rho}{\partial t} + \frac{\partial (\rho u)}{\partial z} = 0 \tag{C.239}$$

Momentum:

$$\frac{\partial (\rho u)}{\partial t} + \frac{\partial (\rho u^2 + p\delta_{ij})}{\partial z} = 0 \tag{C.240}$$

Energy:

$$\frac{\partial [\rho(e + \frac{1}{2}u^2)]}{\partial t} + \frac{\partial [\rho u(e + \frac{1}{2}u^2 + \frac{p}{\rho})]}{\partial z} = q \tag{C.241}$$

Rewriting the energy in terms of pressure (using the perfect gas equations of state):

$$\frac{\partial [p + \frac{1}{2}(\gamma - 1)\rho u^2]}{\partial t} + \frac{\partial [\gamma u p + \frac{1}{2}(\gamma - 1)\rho u^3]}{\partial z} = (\gamma - 1)q \tag{C.242}$$

Satisfying the integral form of these equations amounts to considering an infinitessimal volume straddling the discontinuity and integrating the above equations. The following interface relations are found

Mass:

$$\rho_2 u_2 - \rho_1 u_1 = 0 \tag{C.243}$$

Momentum:

$$(p_2 + \rho_2 u_2^2) - (p_1 + \rho_1 u_1^2) = 0 \tag{C.244}$$

Pressure:

$$\left(\gamma u_2 p_2 + \frac{1}{2}(\gamma - 1)\rho_2 u_2^3\right) - \left(\gamma u_1 p_1 + \frac{1}{2}(\gamma - 1)\rho_1 u_1^3\right) = \int_{b_-}^{b_+} (\gamma - 1) q(z) dz \tag{C.245}$$

With Eq. (C.178), the pressure equations becomes

$$\left(\gamma u_2 p_2 + \frac{1}{2}(\gamma-1)\rho_2 u_2^3\right) - \left(\gamma u_1 p_1 + \frac{1}{2}(\gamma-1)\rho_1 u_1^3\right) = (\gamma-1)Q \tag{C.246}$$

Equations (C.243), (C.244), and (C.246) give the relations for the behavior of instantaneous values across the flame. In the absence of fluctuations, these govern the fluid dynamical behavior of a laminar flame, hence aid in the calculation of laminar flame speeds and detonation speeds. For the present purposes, the these equations are perturbed and linearized to find the interface conditions for the acoustic fluctuations.

Mass:

$$(\rho_2'\bar{u}_2 + \bar{\rho}_2 u_2') - (\rho_1'\bar{u}_1 + \bar{\rho}_1 u_1') = 0 \tag{C.247}$$

Momentum:

$$(p_2' + \rho_2'\bar{u}_2^2 + 2\bar{\rho}_2\bar{u}_2 u_2') - (p_1' + \rho_1'\bar{u}_1^2 + 2\bar{\rho}_1\bar{u}_1 u_1') = 0 \tag{C.248}$$

Pressure:

$$\begin{aligned}&\left(\gamma u_2'\bar{p}_2 + \gamma\bar{u}_2 p_2' + \frac{1}{2}(\gamma-1)\rho_2'\bar{u}_2^3 + \frac{3}{2}(\gamma-1)\bar{\rho}_2\bar{u}_2^2 u_2'\right)\\ -&\left(\gamma u_1'\bar{p}_1 + \gamma\bar{u}_1 p_1' + \frac{1}{2}(\gamma-1)\rho_1'\bar{u}_1^3 + \frac{3}{2}(\gamma-1)\bar{\rho}_1\bar{u}_1^2 u_1'\right) = (\gamma-1)Q'\end{aligned} \tag{C.249}$$

Substitution of Eqns. (C.214) - (C.220) into these three interface conditions yields

Mass:

$$\begin{aligned}&\left((1+\bar{M}_1)e_1^+ A_1^+ - (1-\bar{M}_1)e_1^- A_1^-\right)\\ -&\frac{\bar{a}_1}{\bar{a}_2}\left((1+\bar{M}_2)e_2^+ A_2^+ - (1-\bar{M}_2)e_2^- A_2^- - \bar{M}_2 e_2^s A_2^s\right) = 0\end{aligned} \tag{C.250}$$

Momentum:

$$\left((1+\bar{M}_1)^2 e_1^+ A_1^+ + (1-\bar{M}_1)^2 e_1^- A_1^-\right)$$

$$- \left((1+\bar{M}_2)^2 e_2^+ A_2^+ + (1-\bar{M}_2)^2 e_2^- A_2^- - \bar{M}_2^2 e_2^s A_2^s \right) = 0 \tag{C.251}$$

Pressure:

$$\begin{aligned}
&\left(1 + \gamma\bar{M}_1 + \frac{3}{2}(\gamma-1)\bar{M}_1^2 + \frac{1}{2}(\gamma-1)\bar{M}_1^3\right) e_1^+ A_1^+ \\
&- \left(1 - \gamma\bar{M}_1 + \frac{3}{2}(\gamma-1)\bar{M}_1^2 - \frac{1}{2}(\gamma-1)\bar{M}_1^3\right) e_1^- A_1^- \\
&-\frac{\bar{a}_2}{\bar{a}_1}\left(1 + \gamma\bar{M}_2 + \frac{3}{2}(\gamma-1)\bar{M}_2^2 + \frac{1}{2}(\gamma-1)\bar{M}_2^3\right) e_2^+ A_2^+ \\
&+\frac{\bar{a}_2}{\bar{a}_1}\left(1 - \gamma\bar{M}_2 + \frac{3}{2}(\gamma-1)\bar{M}_2^2 - \frac{1}{2}(\gamma-1)\bar{M}_2^3\right) e_2^- A_2^- \\
&+ \frac{\bar{a}_2}{\bar{a}_1}\frac{1}{2}\gamma\bar{M}_2^3 e_2^s A_2^s + (\gamma-1)A^Q = 0
\end{aligned} \tag{C.252}$$

In the above three equations, the following shorthand has been used for the exponential terms

$$e_1^- = \exp\left(\Omega\frac{b}{\bar{u}_1 - \bar{a}_1}\right) \tag{C.253}$$

$$e_1^+ = \exp\left(\Omega\frac{b}{\bar{u}_1 + \bar{a}_1}\right) \tag{C.254}$$

$$e_2^- = \exp\left(\Omega\frac{b-L}{\bar{u}_2 - \bar{a}_2}\right) \tag{C.255}$$

$$e_2^s = \exp\left(\Omega\frac{b-L}{\bar{u}_2}\right) \tag{C.256}$$

$$e_2^+ = \exp\left(\Omega\frac{b-L}{\bar{u}_2 + \bar{a}_2}\right) \tag{C.257}$$

Thus, Eqns (C.250) - (C.252) give the three interface conditions for the system.

C.9.5 Heat Release Model

The general solution contains seven unknown wave strengths. Three boundary conditions and three interface conditions give six independent equations. Hence, one more equation is needed for closure. This equation is provided by the heat release model. The heat release model relates the unsteady heat release to the acoustic density, velocity and pressure fields.

C.9.5.1 Pressure Mechanism

In some cases, the heat release behavior may be modeled by

$$\frac{Q'(t)}{\bar{Q}} = n\frac{p_1'(t-\tau)}{\bar{p}_1} \tag{C.258}$$

When the mean heat release is written as

$$\bar{Q} = \bar{\rho}_1 \bar{u}_1 c_p (\bar{T}_2 - \bar{T}_1) \tag{C.259}$$

this pressure-coupled mechanism model becomes

$$Q'(t) = n\frac{\gamma}{\gamma-1}\bar{M}_1(TR-1)\bar{a}_1 p_1'(t-\tau) \tag{C.260}$$

where $TR = \bar{T}_2/\bar{T}_1$ is the temperature ratio across the flame. Substitution of Eqs. (C.214) and (C.220) gives

$$n\gamma\bar{M}_1(TR-1)(e_1^+A_1^+ + e_1^-A_1^-) - (\gamma-1)\exp(i\Omega\tau)A^Q = 0 \tag{C.261}$$

which closes the set of equations for this model.

C.9.5.2 Weak Velocity Model

While the first model predicts that the heat release oscillations are coupled to acoustic pressure oscillations, an alternate model couples the heat release fluctuations to acoustic velocity fluctuations

$$\frac{Q'(t)}{\bar{Q}} = n\frac{u_1'(t-\tau)}{\bar{a}_1} \tag{C.262}$$

With the mean heat release from Eq (C.259), this velocity-coupled model becomes

$$Q'(t) = n\frac{1}{\gamma-1}\bar{M}_1(TR-1)\bar{p}_1 u_1'(t-\tau) \tag{C.263}$$

Substitution of Eqs. (C.215) and (C.220) gives

$$n\bar{M}_1(TR-1)(e_1^+A_1^+ - e_1^-A_1^-) - (\gamma-1)\exp(i\Omega\tau)A^Q = 0 \tag{C.264}$$

C.9.5.3 Strong Velocity Mechanism

Note that the denominator in Eq. (C.262) is chosen as the sound speed (the relevant velocity scale for the acoustic fluctuations). The flame could also respond to velocity fluctuations related to the order of the mean flow

$$\frac{Q'(t)}{\bar{Q}} = n\frac{u_1'(t-\tau)}{\bar{u}_1} \tag{C.265}$$

This heat release model is stronger than the previous by the factor $\bar{M}_1^{-1}$. For most gas turbine combustors, this is a rather large factor. In this case the heat release fluctuations can be written as

$$Q'(t) = n\frac{1}{\gamma - 1}(TR - 1)\bar{p}_1 u_1'(t - \tau) \tag{C.266}$$

which, in terms of wave strengths, gives the equation

$$n(TR - 1)(e_1^+ A_1^+ - e_1^- A_1^-) - (\gamma - 1)\exp(i\Omega\tau)A^Q = 0 \tag{C.267}$$

Note that, with this model, the strength of the heat release A^Q is on the same order as the acoustic wave strengths A_1^-, A_1^+. This is in contrast to the first two models, where the heat release is $O(\bar{M})$ compared to the acoustic wave strengths. Hence, this mechanism is referred to as a 'strong' model.

C.9.5.4 Mass Flow Rate Mechanism

The heat release could also be modelled as responsive to fluctuations in the mass flow rate

$$\frac{Q'(t)}{\bar{Q}} = n\frac{\dot{m}'(t - \tau)}{\bar{\dot{m}}} \tag{C.268}$$

or

$$\frac{Q'(t)}{\bar{Q}} = n\left(\frac{\rho_1'(t - \tau)}{\bar{\rho}_1} + \frac{u_1'(t - \tau)}{\bar{u}_1}\right) \tag{C.269}$$

With the mean heat release from Eq (C.259), this velocity-coupled model becomes

$$Q'(t) = n\frac{1}{\gamma - 1}(TR - 1)\left(\bar{u}_1\rho_1'(t - \tau) + \bar{\rho}_1 u_1'(t - \tau)\right) \tag{C.270}$$

Substitution of Eqs. (C.215), (C.216) and (C.220) gives

$$n(TR-1)\left((1+\bar{M}_1)e_1^+A_1^+-(1-\bar{M}_1)e_1^-A_1^-)\right)-(\gamma-1)\exp(i\Omega\tau)A^Q=0 \qquad \text{(C.271)}$$

Because there is no entropy wave entering the domain at the inlet, the density and pressure on the upstream side of the flame are related via the isentropic relation. The mass flow rate mechanism is thus a combination of the pressure mechanism $O(\bar{M}_1)$ and the strong velocity mechanism $O(1)$. For small Mach numbers, this is approximately equivalent to the strong velocity mechanism.

C.9.5.5 No Entropy Wave Mechanism

A final simple model worth mentioning is one that produces no entropy wave (for $n=1$)

$$\frac{Q'(t)}{\bar{Q}}=n\left(\frac{p_1'(t-\tau)}{\bar{p}_1}+\frac{u_1'(t-\tau)}{\bar{u}_1}\right) \qquad \text{(C.272)}$$

With the mean heat release from Eq (C.259), this velocity-coupled model becomes

$$Q'(t)=n\frac{1}{\gamma-1}(TR-1)\left(\frac{\bar{\rho}_1\bar{u}_1}{\bar{p}_1}p_1'(t-\tau)+\bar{\rho}_1u_1'(t-\tau)\right) \qquad \text{(C.273)}$$

Substitution of Eqs. (C.214), (C.215) and (C.220) gives

$$n(TR-1)\left((1+\gamma\bar{M}_1)e_1^+A_1^+-(1-\gamma\bar{M}_1)e_1^-A_1^-)\right)-(\gamma-1)\exp(i\Omega\tau)A^Q=0 \qquad \text{(C.274)}$$

C.9.6 Example

To show how this procedure can be used to solve a Rijke tube problem for the frequency and growth rate, we consider a Rijke tube with a choked isentropic inlet, Eq. (C.232), open outlet, Eq. (C.236), the three fixed interface conditions, Eqs. (C.250), (C.9.4), (C.252), and a mean flow rate mechanism, Eq. (C.268). This problem was explored by [24]. Since the incoming entropy wave is zero, we have 6 unknowns with 2 boundary conditions, 3 interface conditions, and a heat release model. Stacking these six algebraic equations into a 6x6 matrix

$$\underset{\approx}{M}\underset{\sim}{A} = \underset{\sim}{0} \tag{C.275}$$

where the vector of wave strengths is

$$\underset{\sim}{A} = (A_1^+ \quad A_1^- \quad A_2^+ \quad A_2^- \quad A_2^s \quad A^Q) \tag{C.276}$$

and the coefficient matrix is

$$\underset{\approx}{M} = \begin{bmatrix} (1+\bar{M}_1) & -(1-\bar{M}_1) & 0 & 0 & 0 & 0 \\ (1+\bar{M}_1)e_1^+ & -(1-\bar{M}_1)e_1^- & -\frac{\bar{a}_1}{\bar{a}_2}(1+\bar{M}_2)e_2^+ & \frac{\bar{a}_1}{\bar{a}_2}(1-\bar{M}_2)e_2^- & \frac{\bar{a}_1}{\bar{a}_2}\bar{M}_2 e_2^s & 0 \\ (1+\bar{M}_1)^2 e_1^+ & (1-\bar{M}_1)^2 e_1^- & -(1+\bar{M}_2)^2 e_2^+ & -(1-\bar{M}_2)^2 e_2^- & \bar{M}_2^2 e_2^s & 0 \\ p_1^+ e_1^+ & -p_1^- e_1^- & -\frac{\bar{a}_2}{\bar{a}_1}p_2^+ e_2^+ & \frac{\bar{a}_2}{\bar{a}_1}p_2^- e_2^- & \frac{1}{2}\frac{\bar{a}_2}{\bar{a}_1}\gamma\bar{M}_2^3 e_2^s & (\gamma-1) \\ 0 & 0 & 1 & 1 & 0 & 0 \\ q_1^+ e_1^+ & -q_1^- e_1^- & 0 & 0 & 0 & -1 \end{bmatrix} \tag{C.277}$$

where the abbreviated polynomials are

$$p_1^+ = 1 + \gamma\bar{M}_1 + \frac{3}{2}(\gamma-1)\bar{M}_1^2 + \frac{1}{2}(\gamma-1)\bar{M}_1^3 \tag{C.278}$$

$$p_1^- = 1 - \gamma\bar{M}_1 + \frac{3}{2}(\gamma-1)\bar{M}_1^2 - \frac{1}{2}(\gamma-1)\bar{M}_1^3) \tag{C.279}$$

$$p_2^+ = 1 + \gamma\bar{M}_2 + \frac{3}{2}(\gamma-1)\bar{M}_2^2 + \frac{1}{2}(\gamma-1)\bar{M}_2^3) \tag{C.280}$$

$$p_2^- = 1 - \gamma\bar{M}_2 + \frac{3}{2}(\gamma-1)\bar{M}_2^2 - \frac{1}{2}(\gamma-1)\bar{M}_2^3) \tag{C.281}$$

$$q_1^+ = \frac{n(TR-1)}{\gamma-1}(1+\bar{M}_1)\exp(-i\Omega\tau) \tag{C.282}$$

$$q_1^- = \frac{n(TR-1)}{\gamma-1}(1-\bar{M}_1)\exp(-i\Omega\tau) \tag{C.283}$$

and the abbreviated exponentials are given in the interface conditions section. As suggested by Eq. (C.275), a non-trivial solution for the wave amplitudes can only be achieved when the determinant of $\underset{\approx}{M}$ vanishes. A standard numerical root solver coupled with a determinant calculation can be used to quickly solve for the frequencies. In general, no analytical solution exists, but this matrix can be simplified to the temperature jump, mean flow, and simple duct acoustics problems shown in previous sections of this appendix. Under such simplifications, the solutions derived in previous sections can be recovered from this more general method.

APPENDIX D
ANALYTICAL SPATIAL AVERAGING OF RIJKE TUBE CASES

APPENDIX D
ANALYTICAL SPATIAL AVERAGING OF RIJKE TUBE CASES

Application of the method of spatial averaging for approximate treatment of combustion instabilities was introduced by Culick in his doctoral thesis [23]. The method was recently summarized by [8]. Recently, Dowling [24] used the method for a simple one-dimensional Rijke tube geometry for which there exists an analytical solution. The result of this paper's comparison showed a large discrepancy between the predicted frequency shift from the spatial averaged approximation and the analytical solution. Dowling concluded that this is an inherent limitation of the method. Recently, however, Culick [64] has argued that the large disagreement between theory and approximation for the simplified problem introduced by Dowling was due to her neglect of the mean density gradient term in the governing equations. In fact, a more thorough derivation of the spatial averaging process for the proposed geometry, boundary conditions, and heat release model was given by Palm [65]. Palm's solution showed better agreement with the analytical solution, ascribing the success of his reworked model to the inclusion of the mean density gradient term previously neglected by Dowling.

It turns out that neither Dowling nor Palm do proper justice to the problem at hand. It is shown here that the error committed by Dowling was unrelated to any of the density

gradient terms in the governing equations. In fact, Dowling's procedure is equivalent to Palm's with respect to the mean density gradient effects. Though not shown explicitly by Dowling, the spatial averaging equations she used properly account for the effect of the density gradient. It is also shown that in Palm's solution, while extra care is taken not to leave out any important mean density gradient terms, the terms stemming from the density gradient terms cancel in the final frequency shift formula. Palm's failure to recognize this fact led Culick to incorrectly identify the source of Dowling's error. In fact, the difference between the solution of Dowling and Palm arises from differing approximations of the acoustic velocity fluctuations (u') in terms of the acoustic pressure fluctuations (p').

This paper derives a more robust method of spatial averaging using the acoustic pressure wave equation, incorporating the density gradient within the Sturm-Liouville operator. In this method, it is shown that the harmonic oscillation equations are obtained in the same form and Culick [8], but without any source terms relating to the mean density gradient. The equivalence of the results of this derivation with Dowling's spatial averaging equations is then demonstrated. The solution to this method is shown using two different relations for the acoustic velocity in terms of acoustic pressure. The first method uses the linearized acoustic momentum equation and results in the estimations of Dowling. The second method uses the linearized energy equation and results in the frequency shift shown by Palm. After deriving each of the two results, the key error of Dowling is highlighted, as well as the error in Culick's diagnosis of Dowling's poor estimation.

D.1 Modified Spatial Averaging Procedure for the Acoustic Wave Equation

In the following, a spatial averaging procedure very similar to that of Dowling [24], Culick [8] and Palm [65] is derived from the linearized Euler equations by combining them into the acoustic pressure wave equation. Where applicable, the relationship with this derivation and others is explained. The key difference in this derivation is the natural inclusion of mean density gradients within the Sturm-Liouville eigenvalue problem. This leads to clear understanding where other previous methods (see [65]) have led to confusion.

D.1.1 Derivation of the Governing Wave Equation

The linearized equations for acoustic momentum and energy are, respectively

$$\bar{\rho}\frac{\partial u_i'}{\partial t} + \bar{\rho}\bar{u}_j\frac{\partial u_i'}{\partial x_j} + \bar{\rho}u_j'\frac{\partial \bar{u}_i}{\partial x_j} + \rho'\bar{u}_j\frac{\partial \bar{u}_i}{\partial x_j} + \frac{\partial p'}{\partial x_i} = 0 \tag{D.1}$$

$$\frac{\partial p'}{\partial t} + \bar{u}_j\frac{\partial p'}{\partial x_j} + u_j'\frac{\partial \bar{p}}{\partial x_j} + \gamma\bar{p}\frac{\partial u_j'}{\partial x_j} + \gamma p'\frac{\partial \bar{u}_j}{\partial x_j} = (\gamma-1)q' \tag{D.2}$$

Rewriting these equations to put mean flow and mean pressure gradient effects, which are viewed as perturbations to the equations of classical acoustics, on the right hand side

$$\frac{\partial u_i'}{\partial t} + \frac{1}{\bar{\rho}}\frac{\partial p'}{\partial x_i} = -\bar{u}_j\frac{\partial u_i'}{\partial x_j} - u_j'\frac{\partial \bar{u}_i}{\partial x_j} - \frac{\rho'}{\bar{\rho}}\bar{u}_j\frac{\partial \bar{u}_i}{\partial x_j} \tag{D.3}$$

$$\frac{\partial p'}{\partial t} + \gamma\bar{p}\frac{\partial u_j'}{\partial x_j} = (\gamma-1)q' - \bar{u}_j\frac{\partial p'}{\partial x_j} - u_j'\frac{\partial \bar{p}}{\partial x_j} - \gamma p'\frac{\partial \bar{u}_j}{\partial x_j} \tag{D.4}$$

Differentiating Eq. (D.4) in time and subtracting γp times the divergence of Eq. (D.3) results in

$$\frac{\partial^2 p'}{\partial t^2} - \gamma\bar{p}\frac{\partial}{\partial x_j}\left(\frac{1}{\bar{\rho}}\frac{\partial p'}{\partial x_j}\right) = h \tag{D.5}$$

where the source term h is given by

$$h = (\gamma-1)\frac{\partial q'}{\partial t} - \frac{\partial u_j'}{\partial t}\frac{\partial \bar{p}}{\partial x_j} - \bar{u}_j\frac{\partial^2 p'}{\partial t \partial x_j} - \gamma\frac{\partial p'}{\partial t}\frac{\partial \bar{u}_j}{\partial x_j} + \gamma\bar{p}\frac{\partial}{\partial x_i}\left(\bar{u}_j\frac{\partial u_i'}{\partial x_j} + u_j'\frac{\partial \bar{u}_i}{\partial x_j} + \frac{\rho'}{\bar{\rho}}\bar{u}_j\frac{\partial \bar{u}_i}{\partial x_j}\right) \tag{D.6}$$

As an aside, it is at this point that Culick [8] further simplifies the spatial derivatives on the left hand side of Eq. (D.5) using

$$\gamma\bar{p}\frac{\partial}{\partial x_j}\left(\frac{1}{\bar{\rho}}\frac{\partial p'}{\partial x_j}\right) = \frac{\gamma\bar{p}}{\bar{\rho}}\frac{\partial^2 p'}{\partial x_j^2} + \gamma\bar{p}\frac{\partial(1/\bar{\rho})}{\partial x_j}\frac{\partial p'}{\partial x_j} = \bar{a}^2\frac{\partial^2 p'}{\partial x_j^2} - \frac{\bar{a}^2}{\bar{\rho}}\frac{\partial \bar{\rho}}{\partial x_j}\frac{\partial p'}{\partial x_j} \tag{D.7}$$

Substituting Eq. (D.7) into Eq. (D.5) and moving the $\frac{\partial \bar{\rho}}{\partial x_j}$ term to the right hand side, Culick [8] arrives at his form of the wave equation for acoustic pressure

$$\frac{\partial^2 p'}{\partial t^2} - \frac{\gamma\bar{p}}{\bar{\rho}}\frac{\partial^2 p'}{\partial x_j \partial x_j} = h_{Culick} \tag{D.8}$$

where his source term h_{Culick} is given by

$$\begin{aligned} h_{Culick} = (\gamma-1)\frac{\partial q'}{\partial t} - \frac{\bar{a}^2}{\bar{\rho}}\frac{\partial \bar{\rho}}{\partial x_j}\frac{\partial p'}{\partial x_j} - \frac{\partial u_j'}{\partial t}\frac{\partial \bar{p}}{\partial x_j} - \bar{u}_j\frac{\partial^2 p'}{\partial t \partial x_j} - \gamma\frac{\partial p'}{\partial t}\frac{\partial \bar{u}_j}{\partial x_j} \\ + \gamma\bar{p}\frac{\partial}{\partial x_i}\left(\bar{u}_j\frac{\partial u_i'}{\partial x_j} + u_j'\frac{\partial \bar{u}_i}{\partial x_j} + \frac{\rho'}{\bar{\rho}}\bar{u}_j\frac{\partial \bar{u}_i}{\partial x_j}\right) \end{aligned} \tag{D.9}$$

Therefore, the difference between the current derivation in Eq. (D.5) and Culick's in Eq. (D.9) is the position of the mean density gradient effects. Culick views these on the right hand side as a perturbation to the wave equation, while the current derivation includes them in the spatial operator in the wave equation.

D.1.2 General Solution to the Homogeneous Problem

Returning to the derivation at hand, the weighting and expansion functions are found via solution to the unperturbed problem

$$\frac{\partial^2 p'}{\partial t^2} - \gamma\bar{p}\frac{\partial}{\partial x_j}\left(\frac{1}{\bar{\rho}}\frac{\partial p'}{\partial x_j}\right) = 0 \tag{D.10}$$

which can be solved via separation of variables. Substitution of

$$p' = \psi_n(x_j)\eta_n(t) \tag{D.11}$$

leads to the following to ordinary differential equations

$$\ddot{\eta}_n + \omega_n^2\eta_n = 0 \tag{D.12}$$

$$\gamma\bar{p}\frac{\partial}{\partial x_j}\left(\frac{1}{\bar{\rho}}\frac{\partial \psi_n}{\partial x_j}\right) + \omega_n^2\psi_n = 0 \tag{D.13}$$

where ω_n^2 is the eigenvalue. Performing the same operations which led from Eq. (D.5) to Eq. (D.8) can reformulate this spatial ODE in the form similar to Palm's [65] solution

$$\frac{\partial^2\psi_n}{\partial x_j \partial x_j} + k_n^2\psi_n = \frac{1}{\bar{\rho}}\frac{\partial\bar{\rho}}{\partial x_j}\frac{\partial\psi_n}{\partial x_j} \tag{D.14}$$

Here, the density gradient is again moved to the right hand side and viewed as a perturbation to the homogeneous Helmholtz equation with eigenvalue $k_n^2 = \frac{\omega_n^2}{\bar{a}^2}$. The drawback is that viewing the mean density gradient as a perturbation to wave equation rather than as part of the spatial operator causes one to miss some nice results from the three-dimensional extension of Sturm-Liouville theory. Note that Eq. (D.13), can be rephrased as

$$\frac{\partial}{\partial x_j}\left(\frac{(\gamma\bar{p})_{ref}}{\bar{\rho}}\frac{\partial\psi_n}{\partial x_j}\right) + \omega_n^2\frac{(\gamma\bar{p})_{ref}}{\gamma\bar{p}}\psi_n = 0 \tag{D.15}$$

where $(\gamma\bar{p})_{ref}$ represents reference values of specific heat and pressure that are not a function of space. It is recognized that, though deflagration waves in premixed combustion cause changes mostly in mean density, that small changes in mean pressure and specific heat are also incurred. With the use of reference values, Eq. (D.15) is of Sturm-Liouville form in its three-dimensional extension

$$\mathcal{L}[\psi_n(x_j)] + \lambda_n \sigma(x_j)\psi_n(x_j) = 0 \tag{D.16}$$

where the linear differential operator is

$$\mathcal{L}[\psi_n] = \frac{\partial}{\partial x_j}\left(\frac{(\gamma\bar{p})_{ref}}{\bar{\rho}}\frac{\partial \psi_n}{\partial x_j}\right) \tag{D.17}$$

the eigenvalue is

$$\lambda_n = \omega_n^2 \tag{D.18}$$

and the weighting function for orthogonality is

$$\sigma(x_j) = \frac{(\gamma\bar{p})_{ref}}{\gamma(x_j)\bar{p}(x_j)} \tag{D.19}$$

In the context of extending Sturm-Liouville, it is useful to discuss Green's formula. Note that the inclusion of the surface discontinuities, which are important for applications with acoustically compact flames, is calculated from the use of the divergence theorem in the derivation of Green's formula. For a vector field F_j in the domain Ω with boundaries $\partial\Omega$ and K surface discontinuities marked by $g_k(x_j) = 0$ with $k = 1, 2, , K$ the divergence theorem becomes

$$\iiint_{\Omega} \frac{\partial F_j}{\partial x_j} dV = \iint_{\partial\Omega} F_j n_j dS - \sum_{k=1}^{K}\left(\iint_{g_k=0} \Delta(F_j) n_j dS\right) \tag{D.20}$$

where $\Delta(F_j)$ represents the instantaneous change in the vector across the surface in the direction of the normal vector n_j. Green's formula for the linear operator is then

$$\iiint_{\Omega} \left(\psi_n \mathcal{L}[\psi_m] - \psi_m \mathcal{L}[\psi_n] \right) dV =$$

$$(\gamma\bar{p})_{ref} \iint_{\partial\Omega} \left[\frac{1}{\bar{\rho}} \left(\psi_n \frac{\partial \psi_m}{\partial x_j} - \psi_m \frac{\partial \psi_n}{\partial x_j} \right) \right] n_j dS - \sum_{k=1}^{K} \left\{ \iint_{g_k=0} \Delta \left[\frac{1}{\bar{\rho}} \left(\psi_n \frac{\partial \psi_m}{\partial x_j} - \psi_m \frac{\partial \psi_n}{\partial x_j} \right) \right] n_j dS \right\} \tag{D.21}$$

In order to evaluate the right hand side integrals for surface discontinuities, interface conditions for flame interfaces are necessary. For a flame interface, from the acoustic momentum equation, Eq. (D.3), neglecting mean flow and mean pressure gradients

$$\frac{\partial u_i'}{\partial t} + \frac{1}{\bar{\rho}} \frac{\partial p'}{\partial x_i} = 0 \tag{D.22}$$

Integrating across an infinitesimally thin control volume surrounding the surface discontinuity described by $g(x_j) = 0$ leads to

$$p'(g_+) - p'(g_-) = 0 \tag{D.23}$$

or

$$\Delta(p') = 0 \tag{D.24}$$

The second interface condition is provided by the non-homogeneous wave equation, Eq. (D.5), only accounting for the heat release and neglecting the contributions of mean flow and mean pressure gradient

$$\frac{\partial^2 p'}{\partial t^2} - \gamma\bar{p} \frac{\partial}{\partial x_j} \left(\frac{1}{\bar{\rho}} \frac{\partial p'}{\partial x_j} \right) = (\gamma - 1) \frac{\partial q'}{\partial t} \tag{D.25}$$

where the heat release function for a flame discontinuity on the surface $g(x_j) = 0$ is given by

$$q'(x_j, t) = Q'(t)\delta(g(x_j)) \tag{D.26}$$

where δ is the Dirac delta function. When Eq. (D.25) is integrated over an infinitesimal control volume around the surface discontinuity $g(x_j) = 0$, yields

$$\left(\frac{1}{\bar{\rho}} \frac{\partial p'}{\partial x_j} \right) n_j \Big|_{g_+} - \left(\frac{1}{\bar{\rho}} \frac{\partial p'}{\partial x_j} \right) n_j \Big|_{g_-} = -\frac{\gamma - 1}{\gamma \bar{p}} \frac{dQ'}{dt} \tag{D.27}$$

or

$$\Delta \left(\frac{1}{\bar{\rho}} \frac{\partial p'}{\partial x_j} \right) n_j = -\frac{\gamma - 1}{\gamma \bar{p}} \frac{dQ'}{dt} \tag{D.28}$$

Interface conditions for the acoustic modeshapes ψ_n can be derived from the homogeneous form of Eq. (D.3) and the spatial ODE Eq. (D.15). Substituting the separation of variables in Eq. (D.11) into Eq. (D.22)

$$\frac{\partial u_i'}{\partial t} + \frac{1}{\bar{\rho}} \frac{\partial \psi_n}{\partial x_i} \eta_n = 0 \tag{D.29}$$

and integrating across the flame at $g(x_j) = 0$, gives

$$\psi_n(g_+) - \psi_n(g_-) = 0 \tag{D.30}$$

or

$$\Delta(\psi_n) = 0 \tag{D.31}$$

Similarly, integrating Eq. (D.15) across a discontinuity at $g = 0$

$$\left(\frac{1}{\bar{\rho}} \frac{\partial \psi_n}{\partial x_j} \right) n_j \Big|_{g_+} - \left(\frac{1}{\bar{\rho}} \frac{\partial \psi_n}{\partial x_j} \right) n_j \Big|_{g_-} = 0 \tag{D.32}$$

or

$$\Delta \left(\frac{1}{\bar{\rho}} \frac{\partial \psi_n}{\partial x_j} \right) n_j = 0 \tag{D.33}$$

Based on the interface relations from Eq. (D.31) and (D.33), the latter integral on the right hand side of Eq. (D.21) vanishes. If homogeneous first, second, or third kind boundary conditions are used, the boundary integration also vanishes. With these conditions, the right hand side of Eq. (D.21) vanishes and the linear operator is self-adjoint

$$\iiint_{\Omega} \left(\psi_n \mathcal{L}[\psi_m] - \psi_m \mathcal{L}[\psi_n] \right) dV = 0 \tag{D.34}$$

Note that the linear differential operator is not self-adjoint when considering the acoustic pressure field, as pointed out by [66]. The interface condition given by Eq. (D.28) is non-homogeneous, the heat release term preventing the operator from being self-adjoint. Substituting Eq. (D.16) into Eq. (D.34) and simplifying yields

$$(\omega_n^2 - \omega_m^2) \iiint_{\Omega} \left(\frac{(\gamma \bar{p})_{ref}}{\gamma \bar{p}} \psi_n \psi_m \right) dV = 0 \tag{D.35}$$

This shows the orthogonality of the modeshapes found from solving Eq. (D.15).

$$\iiint_{\Omega} \frac{(\gamma \bar{p})_{ref}}{\gamma \bar{p}} \psi_m \psi_n dV = \begin{cases} E_n^2 & m = n \\ 0 & m \neq n \end{cases} \tag{D.36}$$

where E_n^2 are the normalization constant for the modeshapes.

D.1.3 Application of Spatial Averaging

The method of spatial averaging is now applied to Eq. (D.5) using the eigenfunctions from Eq. (D.15) as weighting functions. Multiplying Eq. (D.5) by $\frac{1}{\gamma\bar{p}}\psi_n$ and integrating over an arbitrary volume Ω with boundaries $\partial\Omega$ and surface discontinuities $g_k = 0$, the following is obtained

$$\underbrace{\iiint_{\Omega} \psi_n \frac{1}{\gamma\bar{p}} \frac{\partial^2 p'}{\partial t^2} dV}_{[a]} - \underbrace{\iiint_{\Omega} \psi_n \frac{\partial}{\partial x_j} \left(\frac{1}{\bar{\rho}} \frac{\partial p'}{\partial x_j} \right) dV}_{[b]} = \underbrace{\iiint_{\Omega} \psi_n \frac{1}{\gamma\bar{p}} h dV}_{[c]} \tag{D.37}$$

Using Green's formula, Eq. (D.21), term $[b]$ in Eq. (D.37) can be manipulated

$$[b] = \iiint_{\Omega} \psi_n \frac{\partial}{\partial x_j} \left(\frac{1}{\bar{\rho}} \frac{\partial p'}{\partial x_j} \right) dV = \underbrace{\iiint_{\Omega} p' \frac{\partial}{\partial x_j} \left(\frac{1}{\bar{\rho}} \frac{\partial \psi_n}{\partial x_j} \right) dV}_{[b1]}$$

$$+ \underbrace{\iint_{\partial\Omega} \frac{1}{\bar{\rho}} \left(\psi_n \frac{\partial p'}{\partial x_j} - p' \frac{\partial \psi_n}{\partial x_j} \right) n_j dS}_{[b2]} - \underbrace{\sum_{k=1}^{K} \left\{ \iint_{g_k=0} \Delta \left[\frac{1}{\bar{\rho}} \left(\psi_n \frac{\partial p'}{\partial x_j} - p' \frac{\partial \psi_n}{\partial x_j} \right) \right] n_j dS \right\}}_{[b3]} \tag{D.38}$$

Furthermore, substitution of Eq. (D.15) for term $[b1]$ gives

$$[b1] = \iiint_{\Omega} p' \frac{\partial}{\partial x_j} \left(\frac{1}{\bar{\rho}} \frac{\partial \psi_n}{\partial x_j} \right) dV = - \iiint_{\Omega} p' \omega_n^2 \frac{1}{\gamma\bar{p}} \psi_n dV \tag{D.39}$$

Substitution of Eq. (D.38) and Eq. (D.39) into Eq. (D.37) leads to

$$\underbrace{\iiint_{\Omega} \psi_n \frac{1}{\gamma\bar{p}} \frac{\partial^2 p'}{\partial t^2} dV}_{[a]} + \underbrace{\iiint_{\Omega} p' \omega_n^2 \frac{1}{\gamma\bar{p}} \psi_n dV}_{[b1]} = \underbrace{\iiint_{\Omega} \psi_n \frac{1}{\gamma\bar{p}} h dV}_{[c]}$$

$$+ \underbrace{\iint_{\partial\Omega} \frac{1}{\bar{\rho}} \left(\psi_n \frac{\partial p'}{\partial x_j} - p' \frac{\partial \psi_n}{\partial x_j} \right) n_j dS}_{[b2]} - \underbrace{\sum_{k=1}^{K} \left\{ \iint_{g_k=0} \Delta \left[\frac{1}{\bar{\rho}} \left(\psi_n \frac{\partial p'}{\partial x_j} - p' \frac{\partial \psi_n}{\partial x_j} \right) \right] n_j dS \right\}}_{[b3]} \tag{D.40}$$

Then replacing the acoustic pressure p' by a series expansion on the basis functions ψ_m

$$p' = \bar{p}_{ref} \sum_{m=0}^{\infty} \left(\psi_m(x_j) \eta_m(t) \right) \tag{D.41}$$

such that

$$\frac{\partial^2 p'}{\partial t^2} = \bar{p}_{ref} \sum_{m=0}^{\infty} \left(\psi_m(x_j) \ddot{\eta}_m(t) \right) \tag{D.42}$$

then Eq. (D.40) becomes

$$\begin{aligned} &\underbrace{\iiint_{\Omega} \psi_n \frac{1}{\gamma \bar{p}} \bar{p}_{ref} \sum_{m=0}^{\infty} \left(\psi_m \ddot{\eta}_m \right) dV}_{[a]} + \underbrace{\iiint_{\Omega} \bar{p}_{ref} \sum_{m=0}^{\infty} \left(\psi_m \eta_m \right) \omega_n^2 \frac{1}{\gamma \bar{p}} \psi_n dV}_{[b1]} = \\ &\underbrace{\iiint_{\Omega} \psi_n \frac{1}{\gamma \bar{p}} h dV}_{[c]} + \underbrace{\iint_{\partial\Omega} \frac{1}{\bar{\rho}} \left(\psi_n \frac{\partial p'}{\partial x_j} - p' \frac{\partial \psi_n}{\partial x_j} \right) n_j dS}_{[b2]} \\ &\underbrace{- \sum_{k=1}^{K} \left\{ \iint_{g_k=0} \Delta \left[\frac{1}{\bar{\rho}} \left(\psi_n \frac{\partial p'}{\partial x_j} - p' \frac{\partial \psi_n}{\partial x_j} \right) \right] n_j dS \right\}}_{[b3]} \end{aligned} \tag{D.43}$$

interchanging integration and summation

$$\begin{aligned} &\underbrace{\sum_{m=0}^{\infty} \left(\ddot{\eta}_m \iiint_{\Omega} \frac{\bar{p}_{ref}}{\gamma \bar{p}} \psi_m \psi_n dV \right)}_{[a]} + \underbrace{\omega_n^2 \sum_{m=0}^{\infty} \left(\eta_m \iiint_{\Omega} \frac{\bar{p}_{ref}}{\gamma \bar{p}} \psi_m \psi_n dV \right)}_{[b1]} = \\ &\underbrace{\iiint_{\Omega} \psi_n \frac{1}{\gamma \bar{p}} h dV}_{[c]} + \underbrace{\iint_{\partial\Omega} \frac{1}{\bar{\rho}} \left(\psi_n \frac{\partial p'}{\partial x_j} - p' \frac{\partial \psi_n}{\partial x_j} \right) n_j dS}_{[b2]} \\ &\underbrace{- \sum_{k=1}^{K} \left\{ \iint_{g_k=0} \Delta \left[\frac{1}{\bar{\rho}} \left(\psi_n \frac{\partial p'}{\partial x_j} - p' \frac{\partial \psi_n}{\partial x_j} \right) \right] n_j dS \right\}}_{[b3]} \end{aligned} \tag{D.44}$$

Using the orthogonality property, Eq. (D.36), then

$$\iiint_{\Omega} \frac{\bar{p}_{ref}}{\gamma\bar{p}}\psi_m\psi_n dV = \frac{1}{\gamma_{ref}}\iiint_{\Omega} \frac{(\gamma\bar{p})_{ref}}{\gamma\bar{p}}\psi_m\psi_n dV = \begin{cases} E_n^2/\gamma_{ref} & m = n \\ 0 & m \neq n \end{cases} \tag{D.45}$$

which simplifies Eq. (D.44) to

$$\underbrace{\frac{E_n^2}{\gamma_{ref}}\ddot{\eta}_n}_{[a]} + \underbrace{\frac{E_n^2}{\gamma_{ref}}\omega_n^2\eta_n}_{[b1]} = \underbrace{\iiint_{\Omega} \psi_n \frac{1}{\gamma\bar{p}} h dV}_{[c]}$$

$$+ \underbrace{\iint_{\partial\Omega} \frac{1}{\bar{\rho}}\left(\psi_n\frac{\partial p'}{\partial x_j} - p'\frac{\partial\psi_n}{\partial x_j}\right) n_j dS}_{[b2]} - \underbrace{\sum_{k=1}^{K}\left\{ \iint_{g_k=0} \Delta\left[\frac{1}{\bar{\rho}}\left(\psi_n\frac{\partial p'}{\partial x_j} - p'\frac{\partial\psi_n}{\partial x_j}\right)\right] n_j dS\right\}}_{[b3]} \tag{D.46}$$

where E_n^2 is the normalization constant for the orthogonality statement. Rearranging, this leads to the non-homogeneous harmonic oscillator equations

$$\underbrace{\ddot{\eta}_n}_{[a]} + \underbrace{\omega_n^2\eta_n}_{[b1]} = \underbrace{\frac{1}{\bar{p}_{ref}E_n^2}\iiint_{\Omega} h\frac{(\gamma\bar{p})_{ref}}{\gamma\bar{p}}\psi_n dV}_{[c]} + \underbrace{\frac{1}{\bar{p}_{ref}E_n^2}\iint_{\partial\Omega} \frac{(\gamma\bar{p})_{ref}}{\bar{\rho}}\left(\psi_n\frac{\partial p'}{\partial x_j} - p'\frac{\partial\psi_n}{\partial x_j}\right) n_j dS}_{[b2]}$$

$$- \underbrace{\frac{1}{\bar{p}_{ref}E_n^2}\sum_{k=1}^{K}\left\{ \iint_{g_k=0} \Delta\left[\frac{(\gamma\bar{p})_{ref}}{\bar{\rho}}\left(\psi_n\frac{\partial p'}{\partial x_j} - p'\frac{\partial\psi_n}{\partial x_j}\right)\right] n_j dS\right\}}_{[b3]} \tag{D.47}$$

Up to this point, the substitution of Eq. (D.41) has not been used for the boundary and interface surface integrals on the right hand side of the integrated equations. In fact, if the substitution is made and ψ_n is constructed with homogeneous boundary conditions, the two integrals will vanish. This is not desirable for the sake of the approximation method, because there is no other way to account for the effect of non-homogeneous boundary conditions appearing as a perturbation to the homogeneous problem. The interface discontinuity

integrals, arising from the heat release zones, should be left out, however. The effect of the heat release perturbation to the homogeneous problem is included in the source term h, and therefore need not be included in the surface integrals at discontinuities. With this logic, the substitution of Eq. (D.41) into term $[b3]$ of Eq .(D.47) is made, thus causing this term to vanish for heat release driven discontinuities. The final form of the forced harmonic oscillator equation is then

$$\underbrace{\ddot{\eta}_n}_{[a]} + \underbrace{\omega_n^2 \eta_n}_{[b1]} = \underbrace{\frac{1}{\bar{p}_{ref} E_n^2} \iiint_\Omega h \frac{(\gamma \bar{p})_{ref}}{\gamma \bar{p}} \psi_n dV}_{[c]} + \underbrace{\frac{1}{\bar{p}_{ref} E_n^2} \iint_{\partial\Omega} \frac{(\gamma \bar{p})_{ref}}{\bar{\rho}} \left(\psi_n \frac{\partial p'}{\partial x_j} - p' \frac{\partial \psi_n}{\partial x_j} \right) n_j dS}_{[b2]} \tag{D.48}$$

As shown in Appendix D, the accuracy of this method depends on the relation used to put u' in terms of η. When the momentum equation is used, the results resemble those of [24], which are highly inaccurate. If the homogeneous energy equation is used, as suggested by [8], then the method gives remarkably accurate results. In general, the sensitivity of the results is due to the fact that the unsteady heat release for the model used is of the same order of magnitude as the acoustics itself, see Appendix C for discussion of weak and strong velocity mechanism. Suppose a time lag was used such that the heat release was not in phase with the velocity. This would make the Rayleigh criterion for a velocity based method non-zero (it is zero if the time lag is zero). Then, for the strong velocity model, the approximation $\alpha << \omega$ would not hold and the underpinning of the weighted residual method (treating the heat release as a small perturbation on the homogeneous acoustic solution) would not be a reasonable assumption.

D.2 Application to Rijke Tube Problem

The example problem originally introduced by [24] is now considered with the above derivation of the spatial averaged equations. The geometry is one-dimensional from $x = 0$ to $x = L$ with a flame discontinuity at $x = b$. The heat release is given by a Dirac delta function.

$$q'(x,t) = Q'(t)\delta(x-b) \tag{D.49}$$

On either side of the discontinuity, the flow properties are constant and there is no mean flow. For the model problem, the specific heats and mean pressure are constant across the heat input, hence only the mean density and mean temperature change. The subscript $_1$ is used to denote properties in the region $0 \leq x < b$ and the subscript $_2$ is used to denote properties in the region $b < x \leq L$.

$$\bar{u}(x,t) = 0 \tag{D.50}$$

$$\bar{p}(x,t) = p_{ref} \tag{D.51}$$

$$\bar{\gamma}(x,t) = \gamma_{ref} \tag{D.52}$$

$$\bar{T} = \bar{T}_1 + (\bar{T}_2 - \bar{T}_1)\mathcal{H}(x-b) \tag{D.53}$$

$$\bar{\rho} = \bar{\rho}_1 + (\bar{\rho}_2 - \bar{\rho}_1)\mathcal{H}(x-b) \tag{D.54}$$

where $\mathcal{H}$ represents the Heavyside step function. From the ideal gas equation

$$\frac{\bar{\rho}_1}{\bar{\rho}_2} = \frac{\bar{T}_2}{\bar{T}_1} = TR \tag{D.55}$$

and sound speeds given by

$$\bar{a}_1 = \sqrt{\gamma R T_1}$$

$$\bar{a}_2 = \sqrt{\gamma R T_2} \tag{D.56}$$

and wave numbers given by

$$k_{n1} = \frac{\omega_n}{\bar{a}_1}$$

$$k_{n2} = \frac{\omega_n}{\bar{a}_2} \tag{D.57}$$

The boundary conditions are closed-open

$$\left.\frac{\partial p'}{\partial x}\right|_{x=0} = 0 \tag{D.58}$$

$$p'(L) = 0 \tag{D.59}$$

The heat release is given by the model

$$Q'(t) = \bar{\rho}_1 c_p (\bar{T}_2 - \bar{T}_1) u'(b_-, t) \tag{D.60}$$

D.2.1 Analytical Solution

The analytical solution is derived by both [24] and [65]. This can also be derived from the matrix method presented in the last section of Appendix C. The frequencies for the homogeneous problem, Eq. (D.10), satisfy the following characteristic equation

$$\tan(k_{n1} b) \tan(k_{n2}(L - b)) = \sqrt{TR} \tag{D.61}$$

with modeshapes given by

$$\psi_n = \begin{cases} \cos(k_{n1}x) & 0 \le x < b \\ \frac{\cos(k_{n1}b)}{\sin(k_{n2}(L-b))}\sin(k_{n2}(L-x)) & b < x \le L \end{cases} \tag{D.62}$$

The frequencies to the problem with unsteady heat release given by Eq. (D.60) satisfy the following characteristic equation

$$\tan(k_{n1}b)\tan(k_{n2}(L-b)) = \sqrt{TR^{-1}} \tag{D.63}$$

D.2.2 Estimation by Spatial Averaging

To simplify Eq. (D.48) for the given problem, it is recognized that the homogeneous boundary conditions given by Eq. (D.58) and (D.59) cause the boundary integration term $[b2]$ to vanish.

$$[b2] = \frac{1}{\bar{p}_{ref}E_n^2}\iint_{\partial\Omega}\frac{(\gamma\bar{p})_{ref}}{\bar{\rho}}\left(\psi_n\frac{\partial p'}{\partial x_j} - p'\frac{\partial\psi_n}{\partial x_j}\right)n_j dS = 0 \tag{D.64}$$

Because the problem is one-dimensional by definition, the following simplifications hold

$$\iiint_{\Omega}\left(\ \right)\,dV \rightarrow \int_0^L \left(\ \right)\,dx \tag{D.65}$$

$$\iint_{\partial\Omega}\left(\ \right)\,dS \rightarrow \left(\ \right)\Big|_0^L \tag{D.66}$$

Finally, with no mean pressure gradients or mean flow, the source term h becomes

$$h = (\gamma - 1)\frac{\partial q'}{\partial t} \tag{D.67}$$

With these simplifications, the spatial averaged equations become

$$\ddot{\eta}_n + \omega_n^2 \eta_n = \frac{\gamma - 1}{\bar{p} E_n^2} \int_0^L \frac{\partial q'}{\partial t} \psi_n dx \tag{D.68}$$

which is the starting point for Dowling's solution process. Note that the mean density gradient terms are not explicitly present, but rather have been accounted for in the definition of the weighting function ψ_n. Palm [65] includes the mean density gradient term at this point in his analysis and concludes along with Culick [64], that the absence of the mean density gradient term in Eq. (D.68) is the cause for Dowling's error. The following analysis shows that no such error has been committed in the derivation of Eq. (D.68).

The ω_n in Eq. (D.68) comes from the solution to the unperturbed problem given by Eq. (D.61). Using Eqs. (D.49) and (D.60), the unsteady heat release is written as

$$q'(x,t) = \bar{\rho}_1 c_p (\bar{T}_2 - \bar{T}_1) u'(b_-, t) \delta(x - b) \tag{D.69}$$

Substitution of Eq. (D.69) into Eq. (D.68) gives

$$\ddot{\eta}_n + \omega_n^2 \eta_n = \frac{(\gamma - 1) c_p \bar{\rho}_1 (\bar{T}_2 - \bar{T}_1)}{\bar{p} E_n^2} \frac{\partial u'}{\partial t}(b_-) \psi_n(b) \tag{D.70}$$

With some rearranging

$$\ddot{\eta}_n + \omega_n^2 \eta_n = \frac{\bar{a}_1^2 (TR - 1) \bar{\rho}_1}{\bar{p} E_n^2} \frac{\partial u'}{\partial t}(b_-) \psi_n(b) \tag{D.71}$$

The next step is the approximation of u' in terms of the weighting functions. First, the homogeneous momentum or energy equations are used to write u' in terms of p'. Then, Eq. (D.41) converts this to an expressing in ψ_n. The choice of whether to use the momentum or energy equation is crucial. As will be shown, one choice will lead to a poor approximation, while the other leads to an excellent one.

D.2.2.1 Using Momentum Equation to Write u' as a Function of p'

First, the homogeneous momentum equation is used

$$\frac{\partial u_i'}{\partial t} + \frac{1}{\bar{\rho}}\frac{\partial p'}{\partial x_i} = 0 \tag{D.72}$$

The calculation $\frac{\partial u'}{\partial t}$ is straightforward

$$\frac{\partial u_1'}{\partial t} = -\frac{1}{\bar{\rho}}\frac{\partial p_1'}{\partial x} = -\frac{\bar{p}}{\bar{\rho_1}}\frac{\partial \psi_{n1}}{\partial x}\eta_n \tag{D.73}$$

Substitution of Eq. (D.73) into Eq. (D.71) gives

$$\ddot{\eta}_n + \omega_n^2\eta_n = \frac{\bar{a}_1^2(TR-1)}{E_n^2}\frac{\partial \psi_n}{\partial x}(b_-)\psi_n(b) \tag{D.74}$$

Using the unperturbed modeshape given by Eq. (D.62)

$$\psi_n(b) = \cos(k_{1n}b) \tag{D.75}$$

$$\frac{\partial \psi_n}{\partial x}(b_-) = -k_{1n}\sin(k_{1n}b) \tag{D.76}$$

Substitution of these two evaluations into Eq. (D.74) and simplification leads to

$$\ddot{\eta}_n + \omega_n^2\eta_n = \frac{\omega_n^2(TR-1)}{2k_{n1}E_n^2}\sin(2k_{n1}b)\eta_n \tag{D.77}$$

or

$$\ddot{\eta}_n + \left(1 - \frac{TR-1}{2k_{n1}E_n^2}\sin(2k_{n1}b)\right)\omega_n^2\eta_n = 0 \tag{D.78}$$

hence the frequency of the system with unsteady heat release is

$$\omega = \omega_n\sqrt{1 - \frac{TR-1}{2k_{n1}E_n^2}\sin(2k_{n1}b)} \tag{D.79}$$

This is the shifted frequency equivalent to that of Dowling's solution. It generates an estimation of frequency shift that is very poor, dropping to zero before a temperature ratio of four.

D.2.2.2 Using Unperturbed Energy Equation to Write u' as a Function of p'

Alternatively, the unperturbed energy equation can be used to write $\frac{\partial u'}{\partial t}$ in terms of ψ_n. In one dimension

$$\frac{\partial p'}{\partial t} + \gamma \bar{p} \frac{\partial u'}{\partial x} = 0 \tag{D.80}$$

Rearranging

$$\frac{\partial u'}{\partial x} = -\frac{1}{\gamma \bar{p}} \frac{\partial p'}{\partial t} \tag{D.81}$$

Integrating this expression in x

$$u' = -\frac{1}{\gamma \bar{p}} \int \frac{\partial p'}{\partial t} dx \tag{D.82}$$

Differentiating in time

$$\frac{\partial u'}{\partial t} = -\frac{1}{\gamma \bar{p}} \int \frac{\partial^2 p'}{\partial t^2} dx \tag{D.83}$$

Substituting the expansion Eq. (D.41)

$$\frac{\partial u'}{\partial t} = -\frac{1}{\gamma} \left(\int \psi_n dx \right) \ddot{\eta}_n \tag{D.84}$$

This is inconvenient because it contains the integration of the modeshape, hence use Eq. (D.15) to substitute for ψ_n

$$\frac{\partial u'}{\partial t} = \frac{1}{\gamma \omega_n^2} \left[\int \frac{\partial}{\partial x} \left(\frac{\gamma \bar{p}}{\bar{\rho}} \frac{\partial \psi_n}{\partial x} \right) dx \right] \ddot{\eta}_n \tag{D.85}$$

Simplifying this

$$\frac{\partial u'}{\partial t} = \frac{1}{\gamma k_n^2} \frac{\partial \psi_n}{\partial x} \ddot{\eta}_n \tag{D.86}$$

This is of the form used by Palm [65] in his analysis and suggested in general by Culick [8]. Note that the heat release in now proportional to the second derivative in time, hence suggesting interpretation of adding inertia to the system. Substituting Eq. (D.86) into Eq. (D.71) leads to

$$\ddot{\eta}_n + \omega_n^2 \eta_n = \frac{(TR-1)}{k_{n1}^2 E_n^2} \frac{\partial \psi_n}{\partial x}(b_-)\psi_n(b)\ddot{\eta}_n \tag{D.87}$$

Using Eq. (D.75) and (D.76) to substitute

$$\ddot{\eta}_n + \omega_n^2 \eta_n = -\frac{(TR-1)}{2k_{n1} E_n^2} \sin(2k_{n1}b)\ddot{\eta}_n \tag{D.88}$$

or

$$\left(1 + \frac{(TR-1)}{2k_{1n} E_n^2} \sin(2k_{n1}b)\right) \ddot{\eta}_n + \omega_n^2 \eta_n = 0 \tag{D.89}$$

finally

$$\ddot{\eta}_n + \frac{\omega_n^2}{1 + \frac{(TR-1)}{2k_{n1}E_n^2} \sin(2k_{n1}b)} \eta_n = 0 \tag{D.90}$$

This indicates a shifted frequency given by

$$\omega = \omega_n \sqrt{\frac{1}{1 + \frac{(TR-1)}{2k_{n1}E_n^2} \sin(2k_{n1}b)}} \tag{D.91}$$

This frequency gives identical results to Palm's solution, and in fact it will be shown later that Palm's solution can be reduced to this form.

D.2.3 Clarification of Dowling's Results

Now that the solution has been carried out for the method derived here, in what the author believes to be a very clear and concise manner, it is worthwhile to consider the cause of the poor estimation in Dowling's case. The previous section showed that Dowling's error was not caused by neglecting mean density gradients. In fact, her solution is equivalent to that obtained by use of the linearized momentum equation to relate u' to the expansion functions. This is not the actual error committed by Dowling, however. Dowling, indeed uses Eq. (D.86) to estimate $\frac{\partial u'}{\partial t}$, but then quickly follows this with the substitution

$$\ddot{\eta}_n = -\omega_n^2 \eta_n \tag{D.92}$$

which is directly inconsistent with the starting equation, Eq. (D.68). In fact, the above derivation shows that this substitution is entirely unneceesary. With this substitution, the results are the same as if the momentum equation had been used to relate u' to ψ.

D.2.4 Clarification of Culick's Diagnosis

It is also worthwhile to discuss Palm's solution, which caused Culick to conclude that the exclusion of the density gradient term from the right hand side of the wave equation was Dowling's crucial mistake. As shown above, no mean density gradient term is needed to derive a frequency shift in agreement with Palm's solution. One may note that the

mathematical form of Palm's frequency (for $\kappa = 1$) is

$$\omega = \omega_n \sqrt{\frac{1 - \frac{1}{k_{n1}E_n^2}\frac{\beta_1 - \beta_3}{2}\ln(TR)}{1 + \frac{1}{k_{n1}E_n^2}\left(\beta_1(TR-1) - \frac{\beta_1-\beta_3}{2}\ln(TR)\right)}} \tag{D.93}$$

which indeed contains terms related to the density gradient. The portions of Eq. (D.93) stemming from the inclusion of the mean density gradient term can be recognized as those proportional to $(\beta_1 - \beta_3)$. These two terms are given by

$$\beta_1 = \cos(k_{n1}b)\sin(k_{1n}b) \tag{D.94}$$

$$\beta_3 = \sqrt{TR}\frac{\cos^2(k_{n1}b)}{\tan(\sqrt{(TR^{-}1)}k_{n1}(L-b))} \tag{D.95}$$

Evaluating their difference

$$\beta_1 - \beta_3 = \cos(k_{n1}b)\sin(k_{n1}b) - \sqrt{TR}\frac{\cos^2(k_{n1}b)}{\tan(\sqrt{(TR^{-1})}k_{n1}(L-b))} \tag{D.96}$$

Noting that

$$\sqrt{TR^{-1}}k_{n1} = k_{n2} \tag{D.97}$$

then

$$\beta_1 - \beta_3 = \frac{\cos^2(k_{n1}b)}{\tan(k_{n2}(L-b))}\left(\tan(k_{n1}b)\tan(k_{n2}(L-b)) - \sqrt{TR}\right) = 0 \tag{D.98}$$

which is identically zero using Eq. (D.61) for the definition of the unperturbed frequency and wave numbers. Therefore, the terms in Palm's solution which he gains by including the density gradient term on the right hand side actually cancel in the final equation. The frequency from Palm's solution with $\kappa = 1$ can then be reduced to

$$\omega = \omega_n \sqrt{\frac{1}{1 + \frac{1}{k_{n1}E_n^2}\beta_1(TR-1)}} \tag{D.99}$$

or, with the substitution of Eq.(D.94) for β_1

$$\omega = \omega_n \sqrt{\frac{1}{1 + \frac{(TR-1)}{2k_{n1}E_n^2}\sin(2k_{n1}b)}} \tag{D.100}$$

which is in complete agreement with Eq. (D.91), resulting from the derivation using the unperturbed energy equation to write u' in terms of ψ_n.

D.2.5 Conclusions

In addition to the above derivations, the geometry was solved using a numerical integration in the Generalized Instability Model (GIM) [25]. Note that in this code, the discontinuity in mean density is smoothed using a Gaussian cumulative distribution function and the differentiation of the modeshapes is accomplished via a five point scheme. In this way, the precise mathematics of integrating over a Dirac delta function is lost. The comparison of the frequency shift from all these methods is shown in Fig. D.1.

It is interesting to note that the plot shown by Palm gives a different curve for his results. The present paper shows that Palm's solution is in much better agreement than Palm recognized. Notice that, as discussed above, the present derivation using unperturbed energy equation for relating u' to ψ_n agrees exactly with Palm's results. This is, as discussed above, Palm's solution can be reduced to agree mathematically with the present derivation. Such reduction of the frequency shift statement shows that the terms gained by including the right hand side density gradient term in fact cancel in the final form. Also, the present

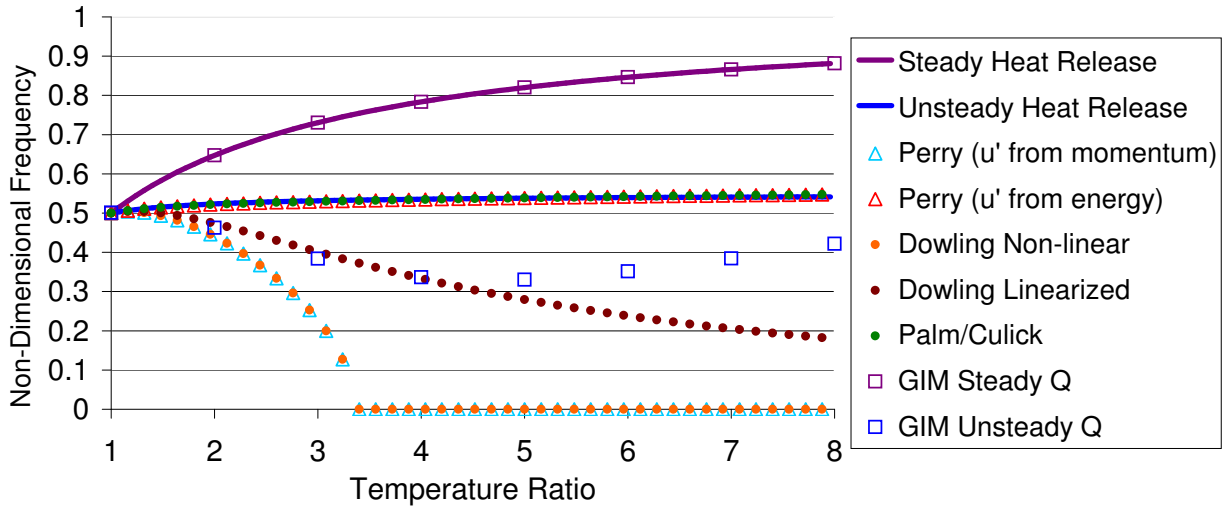

Figure D.1: Comparison of frequency shift when unsteady heat release is added with the given u' mechanism.

solution derived using the momentum equation for relating u' to ψ_n is in agreement with Dowling's solution, which used the estimation $\ddot{\eta}_n = -\omega_n \eta_n$ on top of the unperturbed energy equation. These two estimations can be seen to be mathematically similar.

In conclusion, the unperturbed energy equation should be used to estimate u' in terms of the expansion functions when carrying out the spatial averaging technique. Any deviation from this, whether it be the use of the momentum equation or unperturbed harmonic oscillator equation, leads to the dramatic errors seen by Dowling. Dowling's errors are completely explained by this step and are completely unrelated to the inclusion (or lack thereof) of mean density gradient terms.

APPENDIX E
BOUNDARY CONDITIONS

APPENDIX E
BOUNDARY CONDITIONS

E.1 Simple Boundary Conditions

There are three simple boundary conditions commonly used for acoustics, particularly aeroacoustics and thermoacoustics: closed, open, and choked. Before a discussion of more complicated boundary conditions is

E.1.1 Closed BC

The closed boundary condition in acoustics refers to

$$u_n'(t) = 0 \tag{E.1}$$

Physically, this represents a rigid wall (the normal component of velocity vanishes). Because the no-slip condition is often ignored in first-order acoustics, this boundary condition for the acoustic velocity is best represented by the "slip" boundary condition in OpenFOAM, in which the tangential velocity components have zero-gradient conditions at the boundary. The boundary condition for the pressure at a closed boundary is obtained substituting Eq.

(E.1) into the normal component of Eq. (2.26) and rearranging to form a third-kind BC

$$\frac{\partial p'}{\partial x_n} + \frac{\bar{u}_j}{\bar{a}} \frac{\partial \bar{u}_n}{\partial x_j} p' = -\bar{\rho}\bar{u}_j \frac{\partial u'_n}{\partial x_j} - \bar{\rho} u'_j \frac{\partial \bar{u}_n}{\partial x_j} \tag{E.2}$$

In the absence of mean flow gradients ($\frac{\partial \bar{u}_i}{\partial x_j} = 0$), the assumptions leading to the current equations of tacFoam hold. The pressure boundary condition for a closed boundary becomes

$$\frac{\partial p'}{\partial x_n} = -\bar{\rho}\bar{u}_j \frac{\partial u'_n}{\partial x_j} \tag{E.3}$$

Note that this form is consistent with the current equations of tacFoam, but Eq. (E.2) is consistent with the physics of linear acoustics. Finally, if the mean flow is negligible all together, the closed boundary condition for pressure takes on its classical form

$$\frac{\partial p'}{\partial x_n} = 0 \tag{E.4}$$

E.1.2 Open BC

The open boundary condition in acoustics refers to

$$p'(t) = 0 \tag{E.5}$$

Physically, this represents a pressure release boundary, such as the ideal behavior of an exit from a confined duct into a large ambient space. The open boundary condition for velocity is found by substituting Eq. (E.5) into Eq. (2.27) and rearranging (assuming there is no heat release at the boundary; indeed, placing an open boundary condition near a heat release

location is numerically ill-advised)

$$\frac{\partial u_j'}{\partial x_j} + \frac{1}{\gamma \bar{p}} \frac{\partial \bar{p}}{\partial x_j} u_j' = -\frac{\bar{u}_j}{\gamma \bar{p}} \frac{\partial p'}{\partial x_j} - \frac{p'}{\bar{p}} \frac{\partial \bar{u}_j}{\partial x_j} \tag{E.6}$$

This form is consistent with the physics of linear acoustics. To be consistent with the current version of tacFoam, the mean velocity and mean pressure gradients must be ignored

$$\frac{\partial u_j'}{\partial x_j} = -\frac{\bar{u}_j}{\gamma \bar{p}} \frac{\partial p'}{\partial x_j} \tag{E.7}$$

For classical acoustics with no mean flow, the pressure release (or open) boundary condition for velocity is given by

$$\frac{\partial u_j'}{\partial x_j} = 0 \tag{E.8}$$

Note that in these equations, the divergence contains transverse derivatives of velocity components transverse to the boundary normal. These terms should be move to the RHS of the equation, which gives the normal derivative of the normal velocity at the boundary. The transverse derivatives, for lack of other easy way to specify BC, can be given zero gradient boundary conditions.

E.1.3 Choked BC

The choked boundary condition refers to an acoustic boundary condition applied at the choke point (Mach = 1) of a flow. Because of the nature of choked flows, this dictates that the mass flow remains constant at the throat, hence, for a given area

$$\rho(t) u_n(t) = constant \tag{E.9}$$

for linearized acoustics

$$\rho' \bar{u}_n + \bar{\rho} u'_n = 0 \tag{E.10}$$

which can be rearranged, using the isentropic signal assumption, to

$$\frac{p'}{\gamma \bar{p}} + \frac{u'_n}{\bar{u}_n} = 0 \tag{E.11}$$

or

$$p' + \frac{\gamma \bar{p}}{\bar{u}_n} u'_n = 0 \tag{E.12}$$

Equation (E.6) or (E.2) along with zero gradient BC for the components tangential to the surface can then be used to close the system for the four variables on the boundary.

E.2 Arbitrary Impedance Boundary Conditions

For arbitrary impedance (Z), the boundary condition is given by

$$p' - Z \bar{\rho} \bar{a} u'_n = 0 \tag{E.13}$$

The closed boundary condition is the limit $Z \to \infty$ and the open boundary condition is the limit when $Z \to 0$. In the limit of small Mach number, the choked boundary impedance also tends to infinity, hence behaves similarly to a closed boundary. Anything in between can be considered arbitrary impedance. That is, any boundary to an acoustic domain not behaving like an open or closed boundary is in this group. A number of practical scenarios in gas turbines give rise to the necessity of arbitrary impedance boundary conditions [67]. Most

obviously, the inlet and outlet of the combustion chamber, namely the compressor exit and the turbine inlet, respectively. Also, common acoustic mitigation techniques such as wall liners and absorbing Helmholtz resonators are also of this type. These boundaries do not fall conveniently as open, closed, or choked boundaries. Also, they typically exhibit reactance behavior as well as resistance. Thus, in mathematical terms, their impedance is complex, having both real and imaginary components. To make matters worse, the impedance of combustor boundaries have impedances that are a function of frequency. For this reason, the discussion must begin in the complex frequency plane.

$$\hat{p}(\omega) = Z(\omega)\bar{\rho}\bar{a}\hat{u}_n(\omega) \tag{E.14}$$

where the hat symbol designates the Fourier transform of a variable as a function of time.

$$\hat{p}(\omega) = \frac{1}{2\pi}\int_{-\infty}^{\infty} p'(t)\exp(-i\omega t)dt \tag{E.15}$$

$$\hat{u}_n(\omega) = \frac{1}{2\pi}\int_{-\infty}^{\infty} u'_n(t)\exp(-i\omega t)dt \tag{E.16}$$

The relationship between the acoustic pressure and acoustic velocity in time can be written by performing an inverse Fourier transform on Eq. (E.14).

$$p'(t) = \int_{-\infty}^{\infty} \hat{p}(\omega)\exp(i\omega t)d\omega \tag{E.17}$$

$$p'(t) = \int_{-\infty}^{\infty} Z(\omega)\bar{\rho}\bar{a}\hat{u}_n(\omega)\exp(i\omega t)d\omega \tag{E.18}$$

Using the convolution theorem

$$p'(t) = \int_{-\infty}^{\infty} \bar{Z}(\tau)\bar{\rho}\bar{a}u'_n(t-\tau)d\tau \tag{E.19}$$

where

$$\bar{Z}(t) = \int_{-\infty}^{\infty} Z(\omega) \exp(i\omega t) d\omega \tag{E.20}$$

and

$$u_n'(t) = \int_{-\infty}^{\infty} \hat{u}_n(\omega) \exp(i\omega t) d\omega \tag{E.21}$$

In order to prevent violation of the causality principle, based on Eq. (E.19), the function $\bar{Z}(t)$ should be exactly zero for all negative values of t. This effectively requires that the poles of the function $Z(\omega)$ lie in the upper half of the complex frequency plane. From input complex impedance data, the basis functions for a curve fit can be chosen such that causality is upheld and the inverse Fourier transform of the impedance, Eq. (E.20), can be performed analytically prior to the simulation. The pressure-velocity relationship at the boundary can be calculated within the simulation by numerically approximating

$$p'(t) = \int_{0}^{t} \bar{Z}(\tau) \bar{\rho} \bar{a} u_n'(t - \tau) d\tau \tag{E.22}$$

Note that the negative τ region of the integral is eliminated by the causality principle, namely, that the present value of acoustic pressure cannot depend on future values of the acoustic velocity. Secondly, for the sake of a finite simulation in time, the integration can only be performed up to $\tau = t$, since no values of acoustic velocity are available from before the start of the simulation. As with the choked boundary condition, either Eq. (E.2) or (E.6) can be used with zero gradient conditions on the transverse acoustic velocities to provide a closed system of equations for the boundary.

The approach for implementing this time-domain complex impedance boundary condition for a broadband impedance model requires a curve fitting technique for translating $Z(\omega)$ data into a function with form such that it can be transformed analytically and causality can be upheld. The approach used here is that described by [68] and implemented for aeroacoustic applications in [69]. The curve fit uses bases functions in the form

$$Z(\omega) = \frac{A}{i\omega + \lambda} \tag{E.23}$$

where the residue (A) and the pole location ($\omega = i\lambda$) are constants to be determined by the curve fitting algorithm. These constants are either real or complex conjugates. In the case they are complex conjugates

$$Z(\omega) = \frac{A + iB}{i\omega + (\alpha + i\beta)} + \frac{A - iB}{i\omega + (\alpha - i\beta)} \tag{E.24}$$

It is more convenient to write

$$Z(\omega) = \frac{i\omega C + D}{(i\omega + \alpha)^2 + \beta^2} \tag{E.25}$$

where the residue is $A \pm iB$ and the pole location is $\omega = i\lambda = i(\alpha \pm i\beta)$. The relationships are

$$\begin{aligned} C &= 2A \\ D &= 2A\alpha + 2B\beta \end{aligned} \tag{E.26}$$

As discussed by [70], in order for the convolution integral, Eq. (E.19), to depend only on past values of acoustic velocity (i.e. not on future values of acoustic velocity, to satisfy causality), the transformed function $\bar{Z}(t)$ must be zero for all negative values of t. Thus, the

lower bound on the integral in Eq. (E.19) can be set to 0. Note, for finite time simulations, the upper bound on the convolution integral is simply the time duration of the simulation. Thus, Eq. (E.22) is recovered for implementation into tacFoam. For $\bar{Z}(t) = 0 \forall t < 0$, the poles of the function $Z(\omega)$ must all lie in the upper half of the ω-plane. Any poles in the lower-half plane will contribute non-zero values to the negative t part of the impedance, which violates causality. Poles in the upper-half plane contribute to the positive t part of $\bar{Z}(t)$, which satisfies causality. Therefore, for basis functions defined by Eqs. (E.23) and (E.25) to satisfy causality, the imaginary part of their pole location (specifically, λ or α) must be positive. Performing the transform, Eq. (E.20), for Eqs. (E.23) and (E.25), the time domain impedance functions are respectively given by

$$\bar{Z}(t) = A \exp(-\lambda t)\mathcal{H}(t) \tag{E.27}$$

$$\bar{Z}(t) = \exp(-\alpha t)\left(C\cos(\beta t) + \frac{D - \alpha C}{\beta}\sin(\beta t)\right)\mathcal{H}(t) \tag{E.28}$$

where $\mathcal{H}$ is the Heaviside step function, which explicitly shows that these impedance functions satisfy causality. For a curve fit to arbitrary data in the frequency domain, a summation of these basis functions can be used and the constants can be chosen so as to optimized the accuracy of the fit.

$$Z(\omega) = \sum_{j=1}^{J} \frac{A_j}{i\omega + \lambda_j} + \sum_{k=1}^{K} \frac{i\omega C_k + D_k}{(i\omega + \alpha_k)^2 + \beta_k^2} \tag{E.29}$$

where the λ_j and α_k values are positive to enforce causality. The transformed impedance in the time domain is then given by

$$\bar{Z}(t) = \left[\sum_{j=1}^{J} A_j \exp(-\lambda_j t) + \sum_{k=1}^{K} \exp(-\alpha_k t) \left(C_k \cos(\beta_k t) + \frac{D_k - \alpha_k C_k}{\beta_k} \sin(\beta_k t) \right) \right] \mathcal{H}(t) \tag{E.30}$$

Substitution of Eq. (E.30) into Eq. (E.22) provides the boundary condition for the time domain solver. Alternatively, the admittance $Y(\omega)$ could be used to write the acoustic velocity in terms of the acoustic pressure. The only remaining numerical issue is the calculation of the integral. For this task, the recursive convolution method of [71] with piecewise linear reconstruction of the time history is used. Further details of the methods are available in [68]. As recommended by [69], the vector fitting method from [72], [73], and [74] is used as provided online [75].

Note that the code provides a curve fit of the form

$$Z(\omega) = \sum_{j=1}^{J} \frac{A_j}{i\omega - \lambda_j} \tag{E.31}$$

with complex conjugates sometimes resulting for A_j and λ_j. Notice the subtraction in the denominator instead of addition as in Eq. (E.29).

E.2.1 Real Pole

First, an impedance curve fit with a single real pole is shown. The input frequency domain impedance data is given in Table E.1. The impedance is specified at three values and a curve fit of order three is found. The results from the code are given in Table E.2.

Table E.1: Complex frequency-domain impedance data for example curve fit

$f = \omega/2\pi$ (Hz)	250
$Z(\omega)$ Magnitude	3.0
$Z(\omega)$ Phase	-45^o

Table E.2: Results from curve fitting code

j	1
Poles	$-6.664e03$
Residues	$1.571e03$

In terms of Eq. (E.29), the parameters of this curve fit are

$$\begin{aligned} A_1 &= 1.571e03 \\ \lambda_1 &= 6.664e03 \end{aligned} \tag{E.32}$$

The resulting curve fit is shown in Fig. E.1.

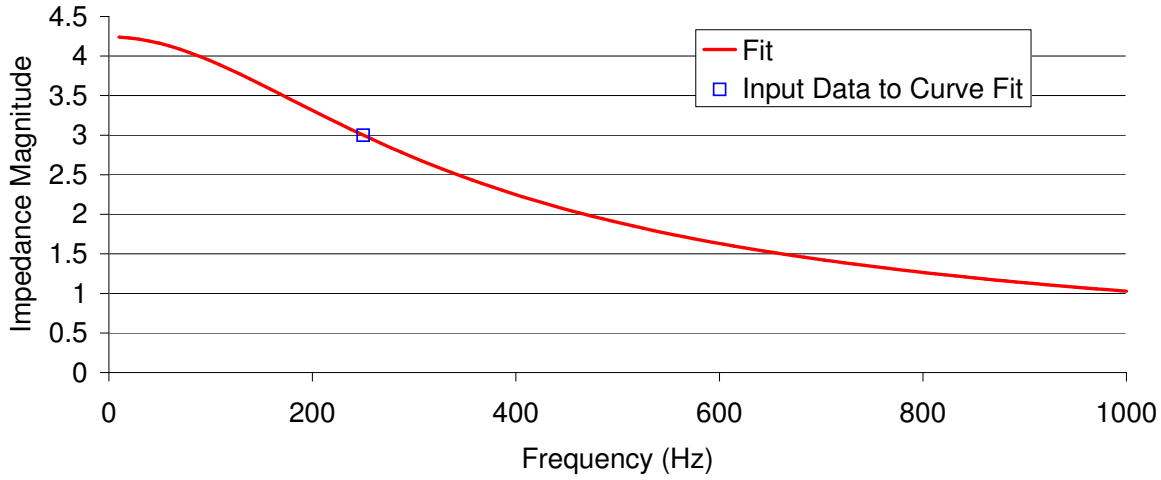

(a)

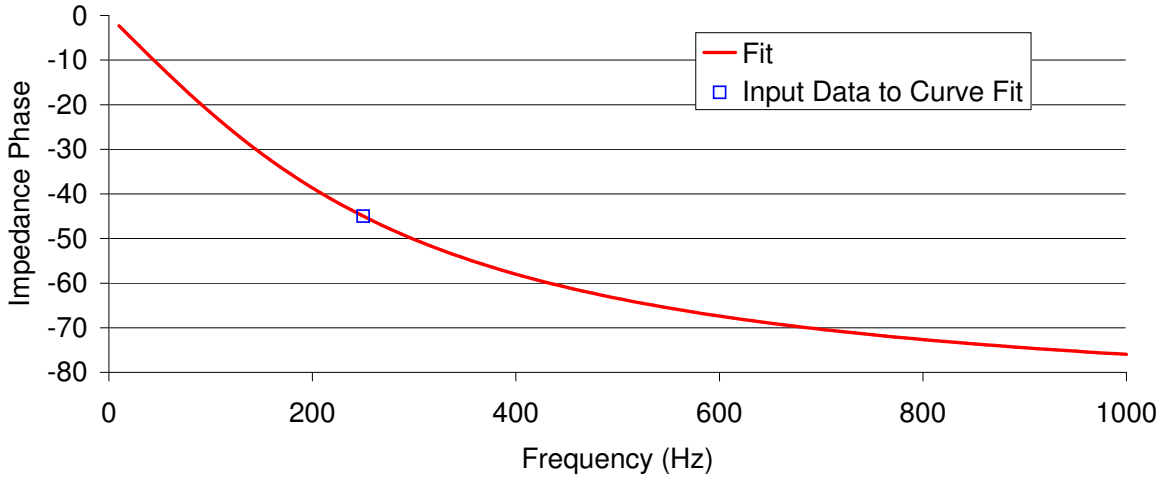

(b)

Figure E.1: Curve fits for complex impedance example.

E.2.2 Complex Conjugate Pair of Poles

Next, an impedance curve fit with a single pair of complex conjugate poles is shown. The input frequency domain impedance data is given in Table E.3. The impedance is specified at three values and a curve fit of order three is found.

Table E.3: Complex frequency-domain impedance data for example curve fit

$f = \omega/2\pi$ (Hz)	200	400
$Z(\omega)$ Magnitude	3.0	2.0
$Z(\omega)$ Phase	-45^o	-100^o

The results from the code in terms of Eq. (E.29), the parameters of this curve fit are

$$\begin{aligned} C_1 &= 8.498e02 \\ D_1 &= 1.144e07 \\ \alpha_1 &= 1.084e03 \\ \beta_1 &= 1.760e03 \end{aligned} \tag{E.33}$$

The resulting curve fit is shown in Fig. E.2.

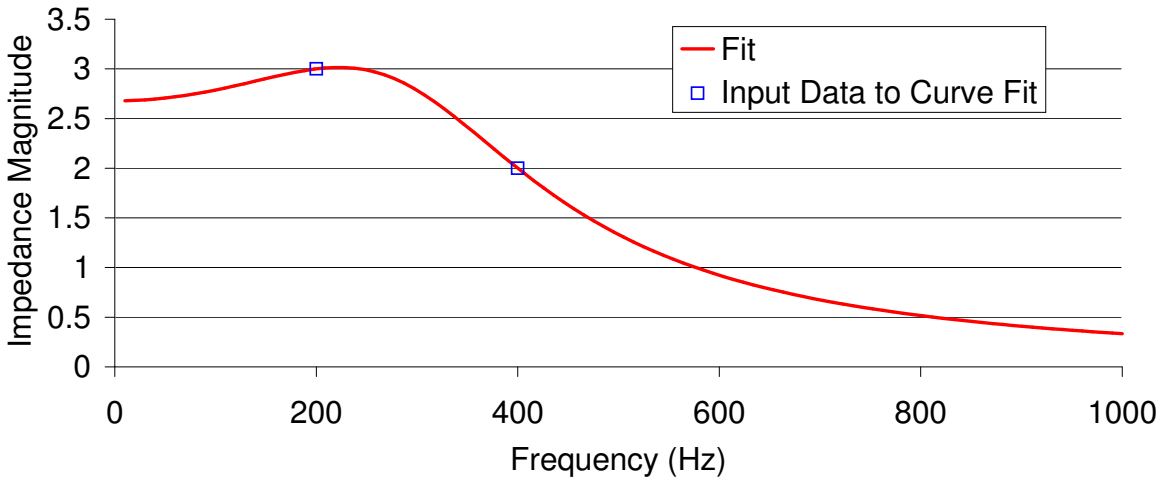

(a)

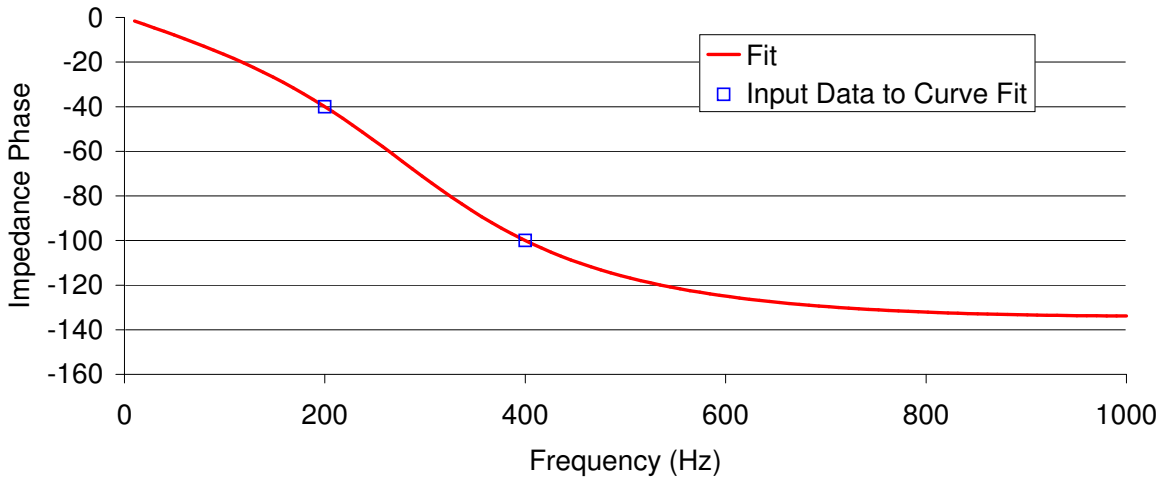

(b)

Figure E.2: Curve fits for complex impedance example.

E.2.3 Real Pole and Complex Conjugate Pair of Poles

Finally, an example curve fit is shown for a complex impedance containing a real pole and a complex conjugate pair of poles. The input frequency domain impedance data is given in Table E.4. The impedance is specified at three values and a curve fit of order three is found. The results from the code are given in Table E.5.

Table E.4: Complex frequency-domain impedance data for example curve fit

$f = \omega/2\pi$ (Hz)	100	300	500
$Z(\omega)$ Magnitude	0.9	0.5	0.4
$Z(\omega)$ Phase	-50^o	-120^o	-140^o

Table E.5: Results from curve fitting code

j	1	2	3
Poles	$-1.290e05$	$-5.224e02 + i5.410e02$	$-5.224e02 - i5.410e02$
Residues	$-4.315e04$	$3.868e02 - i1.900e02$	$3.868e02 + i1.900e02$

In terms of Eq. (E.29), the parameters of this curve fit are

$$
\begin{aligned}
A_1 &= -4.315e04 \\
\lambda_1 &= 1.290e05 \\
C_2 &= 7.736e02 \\
D_2 &= 6.097e05 \\
\alpha_2 &= 5.224e02 \\
\beta_2 &= 5.410e02
\end{aligned}
\tag{E.34}
$$

The resulting curve fit is shown in Fig. E.3.

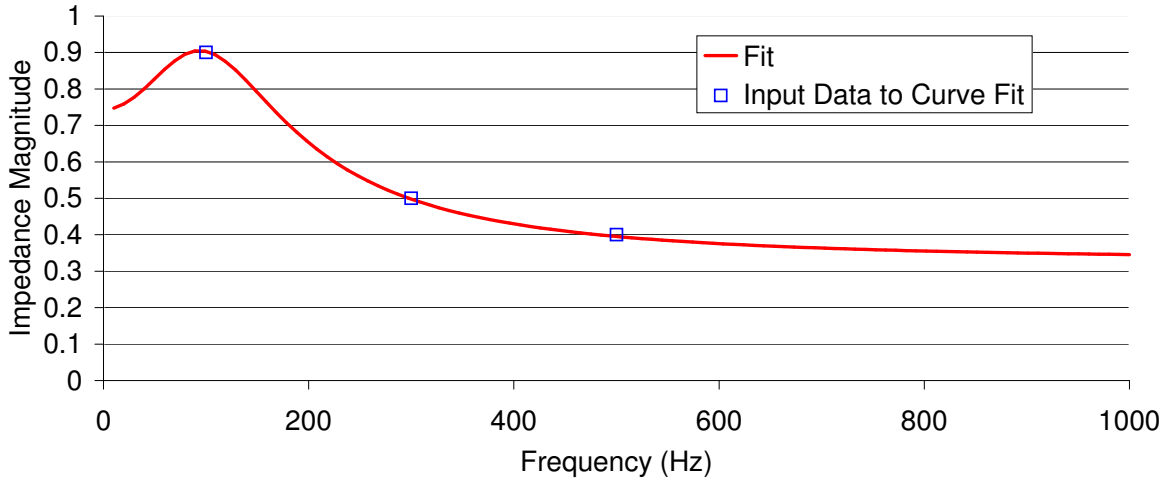

(a)

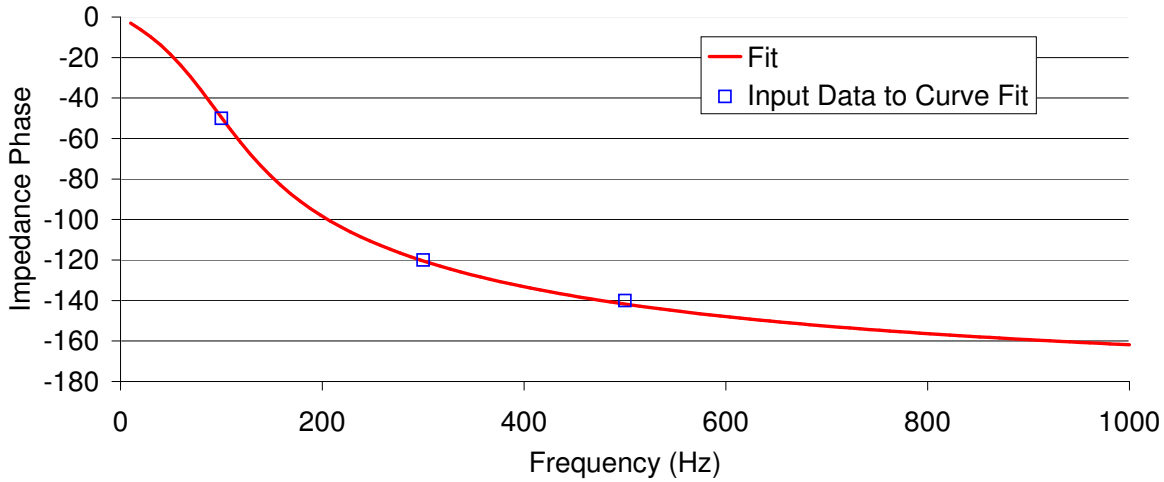

(b)

Figure E.3: Curve fits for complex impedance example.

E.3 Characteristic Boundary Conditions

As with direct numerical simulations (DNS) and highly-resolved large-eddy simulations (LES), the numerical boundary conditions of acoustic solvers must also be given with care. The Navier-Stokes Characteristic Boundary Condition (NSCBC) approach given by Poinsot and Lele [76] uses the Local One-Dimensional Inviscid approximation. A similar approach can be taken to develop characteristic boundary conditions for the acoustic equations used in tacFoam. In the above formulation of the boundary conditions, as in Eq. (E.2) or Eq. (E.6), the second boundary condition ("soft" BC) is derived from the physical BC using one of the governing equations. The above formulation then gives boundary conditions for one acoustic variable in terms of the normal derivative of the other acoustic variables. These then must be approximated from the solution internal to the numerical domain. In reality, these partially depend on waves entering the domain from the outside, however. Thus, estimation of such derivatives for the above BC is inaccurate. An alternate, more involved formulation of boundary conditions follows the procedure outlined in the definition of NSCBC for DNS and LES calculations. First, assume that there is no heat release at the boundary and no gradients of mean velocity or mean pressure. (This is good modelling practice, anyhow). The governing equations become

$$\frac{\partial p}{\partial t} + \bar{u}\frac{\partial p}{\partial x} + \bar{v}\frac{\partial p}{\partial y} + \bar{w}\frac{\partial p}{\partial z} + \gamma\bar{p}\left(\frac{\partial u}{\partial x} + \frac{\partial v}{\partial y} + \frac{\partial w}{\partial z}\right) = 0 \tag{E.35}$$

$$\frac{\partial u}{\partial t} + \bar{u}\frac{\partial u}{\partial x} + \bar{v}\frac{\partial u}{\partial y} + \bar{w}\frac{\partial u}{\partial z} + \frac{1}{\bar{\rho}}\frac{\partial p}{\partial x} = 0 \tag{E.36}$$

$$\frac{\partial v}{\partial t} + \bar{u}\frac{\partial v}{\partial x} + \bar{v}\frac{\partial v}{\partial y} + \bar{w}\frac{\partial v}{\partial z} + \frac{1}{\bar{\rho}}\frac{\partial p}{\partial y} = 0 \tag{E.37}$$

$$\frac{\partial w}{\partial t} + \bar{u}\frac{\partial w}{\partial x} + \bar{v}\frac{\partial w}{\partial y} + \bar{w}\frac{\partial w}{\partial z} + \frac{1}{\bar{\rho}}\frac{\partial p}{\partial z} = 0 \tag{E.38}$$

With the x-direction normal to the boundary, the related Local One-Dimensional Inviscid (LODI) equations are

$$\frac{\partial p}{\partial t} + \bar{u}\frac{\partial p}{\partial x} + \gamma\bar{p}\frac{\partial u}{\partial x} = 0 \tag{E.39}$$

$$\frac{\partial u}{\partial t} + \bar{u}\frac{\partial u}{\partial x} + \frac{1}{\bar{\rho}}\frac{\partial p}{\partial x} = 0 \tag{E.40}$$

$$\frac{\partial v}{\partial t} + \bar{u}\frac{\partial v}{\partial x} = 0 \tag{E.41}$$

$$\frac{\partial w}{\partial t} + \bar{u}\frac{\partial w}{\partial x} = 0 \tag{E.42}$$

The LODI system has eigenvalues

$$\lambda_1 = \bar{u} - \bar{a}, \lambda_2 = \lambda_3 = \bar{u}, \lambda_4 = \bar{u} + \bar{a} \tag{E.43}$$

left eigenvectors

$$l_1 = (1 \quad -\bar{\rho}\bar{a} \quad 0 \quad 0) \tag{E.44}$$

$$l_2 = (0 \quad 0 \quad 1 \quad 0) \tag{E.45}$$

$$l_3 = (0 \quad 0 \quad 0 \quad 1) \tag{E.46}$$

$$l_4 = (1 \quad \bar{\rho}\bar{a} \quad 0 \quad 0) \tag{E.47}$$

which leads to wave strengths of

$$\mathcal{L}_1 = (\bar{u} - \bar{a}) \left(\frac{\partial p}{\partial x} - \bar{\rho}\bar{a}\frac{\partial u}{\partial x} \right) \tag{E.48}$$

$$\mathcal{L}_2 = \bar{u}\frac{\partial v}{\partial x} \tag{E.49}$$

$$\mathcal{L}_3 = \bar{u}\frac{\partial w}{\partial x} \tag{E.50}$$

$$\mathcal{L}_4 = (\bar{u} + \bar{a})\left(\frac{\partial p}{\partial x} + \bar{\rho}\bar{a}\frac{\partial u}{\partial x}\right) \tag{E.51}$$

The governing equations can be rewritten as

$$\frac{\partial p}{\partial t} + d_1 + \bar{v}\frac{\partial p}{\partial y} + \bar{w}\frac{\partial p}{\partial z} + \gamma\bar{p}\left(\frac{\partial v}{\partial y} + \frac{\partial w}{\partial z}\right) = 0 \tag{E.52}$$

$$\frac{\partial u}{\partial t} + d_2 + \bar{v}\frac{\partial u}{\partial y} + \bar{w}\frac{\partial u}{\partial z} = 0 \tag{E.53}$$

$$\frac{\partial v}{\partial t} + d_3 + \bar{v}\frac{\partial v}{\partial y} + \bar{w}\frac{\partial v}{\partial z} + \frac{1}{\bar{\rho}}\frac{\partial p}{\partial y} = 0 \tag{E.54}$$

$$\frac{\partial w}{\partial t} + d_4 + \bar{v}\frac{\partial w}{\partial y} + \bar{w}\frac{\partial w}{\partial z} + \frac{1}{\bar{\rho}}\frac{\partial p}{\partial z} = 0 \tag{E.55}$$

where

$$d_1 = \frac{1}{2}(\mathcal{L}_4 + \mathcal{L}_1) \tag{E.56}$$

$$d_2 = \frac{1}{2\bar{\rho}\bar{a}}(\mathcal{L}_4 - \mathcal{L}_1) \tag{E.57}$$

$$d_3 = \mathcal{L}_2 \tag{E.58}$$

$$d_4 = \mathcal{L}_3 \tag{E.59}$$

and the LODI equations can be rewritten as

$$\frac{\partial p}{\partial t} + d_1 = 0 \tag{E.60}$$

$$\frac{\partial u}{\partial t} + d_2 = 0 \tag{E.61}$$

$$\frac{\partial v}{\partial t} + d_3 = 0 \tag{E.62}$$

$$\frac{\partial w}{\partial t} + d_4 = 0 \tag{E.63}$$

With these in hand, the following characteristic boundary conditions can be derived.

E.3.1 Closed Inlet

The physical boundary condition is

$$u(y, z, t) = 0 \tag{E.64}$$

The soft boundary conditions must determine $p(y, z, t)$. The $\mathcal{L}_1$ wave is outgoing and hence can be approximated from the interior solution. The other three waves ($\mathcal{L}_2, \mathcal{L}_3, \mathcal{L}_4$) are incoming and must be specified. For closed conditions, it is best to specify that there are no incoming convective waves, i.e. $\mathcal{L}_2 = \mathcal{L}_3 = 0$. This effectively enforces zero gradient boundary conditions on the transverse acoustic velocity components.

$$\frac{\partial v}{\partial x} = \frac{\partial w}{\partial x} = 0 \tag{E.65}$$

Thus, only the pressure boundary condition remains unknown.

E.3.1.1 Step 1

Eliminate the velocity equations from the governing equations. Retain only the pressure equation.

E.3.1.2 Step 2

With fixed u, use the LODI equation

$$\frac{\partial u}{\partial t} + d_2 = 0 \tag{E.66}$$

which gives $d_2 = 0$ or $\mathcal{L}_4 = \mathcal{L}_1$, hence $d_1 = \mathcal{L}_1$.

E.3.1.3 Step 3

The remaining equation to be solved on the boundary is

$$\frac{\partial p}{\partial t} + d_1 + \bar{v}\frac{\partial p}{\partial y} + \bar{w}\frac{\partial p}{\partial z} + \gamma\bar{p}\left(\frac{\partial v}{\partial y} + \frac{\partial w}{\partial z}\right) = 0 \tag{E.67}$$

where $d_1 = \mathcal{L}_1$, which given by Eq. (E.48) and can be approximated from the interior solution.

E.3.2 Closed Outlet

The physical boundary condition is

$$u(y, z, t) = 0 \tag{E.68}$$

The soft boundary conditions must determine $p(y, z, t)$, $v(y, z, t)$, $w(y, z, t)$. The $\mathcal{L}_1$ wave is incoming and hence unknown to the interior solution. The other three waves $(\mathcal{L}_2, \mathcal{L}_3, \mathcal{L}_4)$ are outgoing and can be properly estimated from the interior solution.

E.3.2.1 Step 1

Eliminate only the normal velocity equation from the governing equations. Retain the other three equations.

E.3.2.2 Step 2

With fixed u, use the LODI equation

$$\frac{\partial u}{\partial t} + d_2 = 0 \tag{E.69}$$

which gives $d_2 = 0$ or $\mathcal{L}_1 = \mathcal{L}_4$, hence $d_1 = \mathcal{L}_4$.

E.3.2.3 Step 3

The remaining equations to be solved on the boundary are

$$\frac{\partial p}{\partial t} + d_1 + \bar{v}\frac{\partial p}{\partial y} + \bar{w}\frac{\partial p}{\partial z} + \gamma\bar{p}\left(\frac{\partial v}{\partial y} + \frac{\partial w}{\partial z}\right) = 0 \tag{E.70}$$

$$\frac{\partial v}{\partial t} + d_3 + \bar{v}\frac{\partial v}{\partial y} + \bar{w}\frac{\partial v}{\partial z} + \frac{1}{\bar{\rho}}\frac{\partial p}{\partial y} = 0 \tag{E.71}$$

$$\frac{\partial w}{\partial t} + d_4 + \bar{v}\frac{\partial w}{\partial y} + \bar{w}\frac{\partial w}{\partial z} + \frac{1}{\bar{\rho}}\frac{\partial p}{\partial z} = 0 \tag{E.72}$$

where $d_1 = \mathcal{L}_4, d_3 = \mathcal{L}_2, d_4 = \mathcal{L}_3$, which are given respectively by Eqs. (E.51), (E.49), (E.50), and can be approximated from the interior solution.

E.3.3 Open Inlet

The physical boundary condition is

$$p(y, z, t) = 0 \tag{E.73}$$

The soft boundary conditions must determine $u(y, z, t)$. The $\mathcal{L}_1$ wave is outgoing and hence can be approximated from the interior solution. The other three waves ($\mathcal{L}_2, \mathcal{L}_3, \mathcal{L}_4$) are incoming and must be specified. As with closed conditions, it is best to specify that there are no incoming convective waves, i.e. $\mathcal{L}_2 = \mathcal{L}_3 = 0$. This effectively enforces zero gradient boundary conditions on the transverse acoustic velocity components.

$$\frac{\partial v}{\partial x} = \frac{\partial w}{\partial x} = 0 \tag{E.74}$$

Thus, only the normal velocity boundary condition remains unknown.

E.3.3.1 Step 1

Eliminate the pressure and tangential velocity equations from the governing equations. Retain only the normal velocity equation.

E.3.3.2 Step 2

With fixed p, use the LODI equation

$$\frac{\partial p}{\partial t} + d_1 = 0 \tag{E.75}$$

which gives $d_1 = 0$ or $\mathcal{L}_4 = -\mathcal{L}_1$, hence $d_2 = -\mathcal{L}_1/(\bar{\rho}\bar{a})$.

E.3.3.3 Step 3

The remaining equation to be solved on the boundary is

$$\frac{\partial u}{\partial t} + d_2 + \bar{v}\frac{\partial u}{\partial y} + \bar{w}\frac{\partial u}{\partial z} = 0 \tag{E.76}$$

where $d_2 = -\mathcal{L}_1/(\bar{\rho}\bar{a})$, which can be approximated from the interior solution using Eq. (E.48).

E.3.4 Open Outlet

The physical boundary condition is

$$p(y, z, t) = 0 \tag{E.77}$$

The soft boundary conditions must determine $u(y, z, t)$, $v(y, z, t)$, $w(y, z, t)$. The $\mathcal{L}_1$ wave is incoming and hence unknown to the interior solution. The other three waves $(\mathcal{L}_2, \mathcal{L}_3, \mathcal{L}_4)$ are outgoing and can be properly estimated from the interior solution.

E.3.4.1 Step 1

Eliminate only the pressure equation from the governing equations. Retain the three velocity equations.

E.3.4.2 Step 2

With fixed p, use the LODI equation

$$\frac{\partial p}{\partial t} + d_1 = 0 \tag{E.78}$$

which gives $d_1 = 0$ or $\mathcal{L}_1 = -\mathcal{L}_4$, hence $d_2 = \mathcal{L}_4/(\bar{\rho}\bar{a})$.

E.3.4.3 Step 3

The remaining equations to be solved on the boundary are

$$\frac{\partial u}{\partial t} + d_2 + \bar{v}\frac{\partial u}{\partial y} + \bar{w}\frac{\partial u}{\partial z} = 0 \tag{E.79}$$

$$\frac{\partial v}{\partial t} + d_3 + \bar{v}\frac{\partial v}{\partial y} + \bar{w}\frac{\partial v}{\partial z} = 0 \tag{E.80}$$

$$\frac{\partial w}{\partial t} + d_4 + \bar{v}\frac{\partial w}{\partial y} + \bar{w}\frac{\partial w}{\partial z} = 0 \tag{E.81}$$

where $d_2 = \mathcal{L}_4/(\bar{\rho}\bar{a}), d_3 = \mathcal{L}_2, d_4 = \mathcal{L}_3$, which are given respectively by Eqs. (E.51), (E.49), (E.50), and can be approximated from the interior solution.

E.3.5 Slip Wall

Note: here, the slip wall is oriented as an outlet, such that the outward pointing normal of the boundary is in the positive x direction. The physical boundary condition is

$$u(y, z, t) = 0 \tag{E.82}$$

The soft boundary conditions must determine $p(y, z, t)$, $v(y, z, t)$, $w(y, z, t)$. The $\mathcal{L}_1$ wave is incoming and hence unknown to the interior solution. The $\mathcal{L}_4$ wave is outgoing and can be properly estimated from the interior solution. The two convective waves, based on the impermeability condition ($\bar{u} = 0$), have zero strength, i.e. $\mathcal{L}_2 = \mathcal{L}_3 = 0$.

E.3.5.1 Step 1

Eliminate only the normal velocity equation from the governing equations. Retain the other three equations.

E.3.5.2 Step 2

With fixed u, use the LODI equation

$$\frac{\partial u}{\partial t} + d_2 = 0 \tag{E.83}$$

which gives $d_2 = 0$ or $\mathcal{L}_1 = \mathcal{L}_4$, hence $d_1 = \mathcal{L}_4$.

E.3.5.3 Step 3

The remaining equations to be solved on the boundary are

$$\frac{\partial p}{\partial t} + d_1 + \bar{v}\frac{\partial p}{\partial y} + \bar{w}\frac{\partial p}{\partial z} + \gamma\bar{p}\left(\frac{\partial v}{\partial y} + \frac{\partial w}{\partial z}\right) = 0 \tag{E.84}$$

$$\frac{\partial v}{\partial t} + \bar{v}\frac{\partial v}{\partial y} + \bar{w}\frac{\partial v}{\partial z} + \frac{1}{\bar{\rho}}\frac{\partial p}{\partial y} = 0 \tag{E.85}$$

$$\frac{\partial w}{\partial t} + \bar{v}\frac{\partial w}{\partial y} + \bar{w}\frac{\partial w}{\partial z} + \frac{1}{\bar{\rho}}\frac{\partial p}{\partial z} = 0 \tag{E.86}$$

where $d_1 = \mathcal{L}_4$, which is given by Eq. (E.51) and can be approximated from the interior solution.

E.3.6 Arbitrary Real Constant Impedance Inlet

The physical boundary condition is

$$p(y, z, t) = Zu(y, z, t) \tag{E.87}$$

where Z is a real constant. For example, a choked inlet could be enforced by setting $Z = -\gamma\bar{p}/\bar{u}$. The soft boundary conditions must determine $u(y, z, t)$. The $\mathcal{L}_1$ wave is outgoing and hence can be approximated from the interior solution. The other three waves ($\mathcal{L}_2, \mathcal{L}_3, \mathcal{L}_4$) are incoming and must be specified. As previously for inlets, it is best to specify that there are no incoming convective waves, i.e. $\mathcal{L}_2 = \mathcal{L}_3 = 0$. This effectively enforces zero gradient boundary conditions on the transverse acoustic velocity components.

$$\frac{\partial v}{\partial x} = \frac{\partial w}{\partial x} = 0 \tag{E.88}$$

Thus, only the normal velocity boundary condition remains unknown.

E.3.6.1 Step 1

Eliminate the pressure and tangential velocity equations from the governing equations. Retain only the normal velocity equation.

E.3.6.2 Step 2

With fixed p, use the LODI equation

$$\frac{\partial p}{\partial t} + d_1 = 0 \tag{E.89}$$

which gives $d_1 = -Z\partial u/\partial t$ or $\mathcal{L}_4 = -\mathcal{L}_1 - 2Z\partial u/\partial t$, hence $d_2 = -(\mathcal{L}_1 + Z\partial u/\partial t)/(\bar{\rho}\bar{a})$.

E.3.6.3 Step 3

The remaining equation to be solved on the boundary is

$$\frac{\partial u}{\partial t} + d_2 + \bar{v}\frac{\partial u}{\partial y} + \bar{w}\frac{\partial u}{\partial z} = 0 \tag{E.90}$$

where $d_2 = -(\mathcal{L}_1 + Z\partial u/\partial t)/(\bar{\rho}\bar{a})$, which can be approximated from the interior solution using Eq. (E.48).

E.3.7 Arbitrary Real Constant Impedance Outlet

The physical boundary condition is

$$p(y,z,t) = Zu(y,z,t) \tag{E.91}$$

The soft boundary conditions must determine $u(y,z,t)$, $v(y,z,t)$, $w(y,z,t)$. The $\mathcal{L}_1$ wave is incoming and hence unknown to the interior solution. The other three waves $(\mathcal{L}_2, \mathcal{L}_3, \mathcal{L}_4)$ are outgoing and can be properly estimated from the interior solution.

E.3.7.1 Step 1

Eliminate only the pressure equation from the governing equations. Retain the three velocity equations.

E.3.7.2 Step 2

With fixed p, use the LODI equation

$$\frac{\partial p}{\partial t} + d_1 = 0 \tag{E.92}$$

which gives $d_1 = -Z\partial u/\partial t$ or $\mathcal{L}_1 = -\mathcal{L}_4 - 2Z\partial u/\partial t$, hence $d_2 = (\mathcal{L}_4 + Z\partial u/\partial t)/(\bar{\rho}\bar{a})$.

E.3.7.3 Step 3

The remaining equations to be solved on the boundary are

$$\frac{\partial u}{\partial t} + d_2 + \bar{v}\frac{\partial u}{\partial y} + \bar{w}\frac{\partial u}{\partial z} = 0 \tag{E.93}$$

$$\frac{\partial v}{\partial t} + d_3 + \bar{v}\frac{\partial v}{\partial y} + \bar{w}\frac{\partial v}{\partial z} = 0 \tag{E.94}$$

$$\frac{\partial w}{\partial t} + d_4 + \bar{v}\frac{\partial w}{\partial y} + \bar{w}\frac{\partial w}{\partial z} = 0 \tag{E.95}$$

where $d_2 = \mathcal{L}_4/(\bar{\rho}\bar{a}), d_3 = \mathcal{L}_2, d_4 = \mathcal{L}_3$, which are given respectively by Eqs. (E.51), (E.49), (E.50), and can be approximated from the interior solution.

LIST OF REFERENCES

[1] H. Krediet, *Prediction of Limit Cycle Pressure Oscillations in Gas Turbine Combustion Systems Using the Flame Describing Function*. PhD thesis, University of Twente, 2012.

[2] Y. A. Cengel and M. A. Boles, *Thermodynamics: An Engineering Approach*. New York, NY: McGraw-Hill, 6 ed., 2008.

[3] Y. Huang and V. Yang, "Dynamics and stability of lean-premixed swirl-stabilized combustion," *Progress in Energy and Combustion Science*, vol. 35, pp. 293–364, 2009.

[4] I. Glassman and R. Yetter, *Combustion*. Academic Press, 4 ed., 2007.

[5] P. Leighton, *Photochemistry of air pollution*, vol. 9. Academic Press, 1961.

[6] J. Zeldovich, "The oxidation of nitrogen in combustion and explosions," *Acta Physicochimica*, vol. 21, no. 4, pp. 577–628, 1946.

[7] T. Lieuwen, V. Yang, and F. Lu, *Combustion instabilities in gas turbine engines: operational experience, fundamental mechanisms and modeling*. American Institute of Aeronautics and Astronautics, 2005.

[8] F. E. C. Culick, "Unsteady Motions in Combustion Chambers for Propulsion Systems," tech. rep., NATO RTO, 2006. AGARDograph RTO-AG-AVT-039.

[9] J. W. S. Rayleigh, "The explanation of certain acoustical phenomena," vol. 18, pp. 319–321, 1878.

[10] T. Lieuwen, "Modeling premixed combustion – acoustic wave interactions: a review," *AIAA Journal of Propulsion and Power*, vol. 19, no. 5, pp. 765–781, 2003.

[11] A. Fichera, C. Losenno, and A. Pagano, "Clustering of chaotic dynamics of a lean gas-turbine combustor," *Applied Energy*, vol. 69, no. 2, pp. 101–117, 2001.

[12] W. Krebs, H. Krediet, S. Hermeth, T. Poinsot, and E. Portillo, "Comparison of nonlinear to linear thermoacoustic stability analysis of a gas turbine combustion system," ASME Turbo Expo, 2012. GT2012-69477.

[13] L. Crocco and S. Cheng, *Theory of Combustion Instability in Liquid Propellant Rocket Motors*. London: Butterworths Science Publication, 1956. AGARDograph 8.

[14] A. Gelb and W. E. VanderVelde, *Multiple-Input Describing Functions and Nonlinear System Design*. New York, NY: McGraw-Hill Book Co., 1968.

[15] J. OConnor and T. Lieuwen, "Disturbance field characteristics of a transversely excited burner," *Combustion Science and Technology*, pp. 427–443, 2011.

[16] K. I. Matveev and F. E. C. Culick, "A model for combustion instability involving vortex shedding," *Combustion Science and Technology*, vol. 175, no. 6, pp. 1059–1083, 2003.

[17] T. Lieuwen, *Investigation of combustion instability mechanisms in premixed gas turbines*. PhD thesis, Georgia Institute of Technology, 1999.

[18] A. P. Dowling and A. S. Morgans, "Feedback control of combustion oscillations," *Annual Review of Fluid Mechanics*, vol. 57, pp. 151–182, 2005.

[19] D. L. Gysling, G. S. Copeland, D. C. McCormick, and W. M. Proscia, "Combustion system damping augmentation with helmholtz resonators," *Journal of engineering for gas turbines and power*, vol. 122, no. 2, pp. 269–274, 2000.

[20] V. Bellucci, P. Flohr, C. O. Paschereit, and F. Magni, "On the use of helmholtz resonators for damping acoustic pulsations in industrial gas turbines," *Journal of engineering for gas turbines and power*, vol. 126, no. 2, pp. 271–275, 2004.

[21] D. Zhao and A. S. Morgans, "Tuned passive control of combustion instabilities using multiple helmholtz resonators," *Journal of Sound and Vibrations*, vol. 320, no. 4.

[22] T. Sattelmayer and W. Polifke, "Assessment of methods for the computation of the linear stability of combustors," *Combustion Science and Technology*, vol. 175, no. 3, pp. 453–476, 2003.

[23] F. E. C. Culick, *High Frequency Pressure Oscillations in Liquid Rockets*. ScD Thesis, Massachusetts Institute of Technology, 1961. Department of Aeronautics and Astronautics.

[24] A. P. Dowling, "The calculation of thermoacoustic oscillations," *Journal of Sound and Vibration*, vol. 180, no. 4, pp. 557–581, 1995.

[25] J. E. Portillo, J. C. Sisco, M. J. Corless, W. E. Anderson, and V. Sankaran, "Generalized combustion instability model," AIAA/ASME/SAE/ASEE Joint Propulsion Conference, 2006. AIAA-2006-4889.

[26] J. Pent, B. F. Kock, W. Krebs, and J. E. Portillo, "Application of a generalized instability model to industrial annular combustion chambers," AIAA Aerospace Sciences Meeting, 2012. AIAA 2012-0010.

[27] J. Smagorinsky, "General circulation experiments with the primitive equations, i: The basic experiment," *Monthly Weather Review*, vol. 91, no. 3, pp. 99–164, 1963.

[28] T. Poinsot and D. Veynante, *Theoretical and Numerical Combustion*. R. T. Edwards, Inc., 2005.

[29] A. Giauque, L. Selle, T. Poinsot, H. Buechner, P. Kaufmann, and W. Krebs, "System identification of a large-scale swirled partially premixed combustor using les and measurements," *Journal of Turbulence*, vol. 6, no. 21, 2005.

[30] J. F. van Kampen, *Acoustic Pressure Oscillations Induced by Confined Turbulent Premixed Natural Gas Flames*. PhD thesis, University of Twente, 2006.

[31] A. Roux, L. Y. M. Gicquel, S. Reichstadt, N. Bertier, G. Staffelback, F. Vuillot, and T. J. Poinsot, "Analysis of unsteady reacting flows and impact of chemistry description in large eddy simulations of side-dump ramjet combustors," *Combustion and Flame*, vol. 157, no. 1, pp. 176–191, 2010.

[32] C. Stone and S. Menon, "Open-loop control of combustion instabilities in a model gas turbine combustor," *Journal of Turbulence*, vol. 4, no. 1, 2003.

[33] P. Chatterjee, U. Vandsburger, W. R. Saunders, V. K. Khanna, and W. T. Baumann, "On the spectral characteristics of a self-excited rijke tube combustor - numerical simulation and experimental measurements," *Journal of Sound and Vibration*, vol. 283, pp. 573–588, 2005.

[34] U. G. Hedge, D. Reuter, B. T. Zinn, and B. R. Daniel, "Fluid mechanically coupled combustion instabilities in ramjet combustors," AIAA Aerospace Sciences Meeting, 1987. AIAA-87-0216.

[35] Z. M. Ibrahim, F. A. Williams, S. G. Buckley, and C. Z. Twardochleb, "An acoustic-energy method for estimating the onset of acoustic instabilities in premixed gas-turbine combustors," *ASME Journal of Engineering for Gas Turbines and Power*, vol. 130, no. 5, 2008.

[36] "Lms engineering innovation." http://www.lmsintl.com/simulation/virtuallab, May 2011.

[37] A. Jemcov and B. Jojic, "Numerical modelling of combustion instability in rijke tubes," (Kingston, Canada), 14th Annual Conferfence of CFD Society of Canada, July 2006. CFD2006.

[38] R. J. LeVeque, "Wave propagation algorithm for multidimensional hyperbolic systems," *Journal of Computational Physics*, vol. 131, pp. 327–353, 1997.

[39] *OpenFOAM, The Open Source CFD Toolbox: User Guide*. OpenFOAM Foundation, 2011. Available online: www.openfoam.org.

[40] R. J. LeVeque, *Finite Volume Methods for Hyperbolic Problems*. Cambridge, UK: Cambridge University Press, 2002.

[41] E. F. Toro, *Riemann Solvers and Numerical Methods for Fluid Dynamics*. New York, NY: Springer-Verlag, 1999.

[42] T. Barth and D. Jespersen, "The design and application of upwind schemes on unstructured meshes," 1989. AIAA-89-0366.

[43] D. G. Blackstock, *Fundamentals of Physical Acoustics*. New York, NY: John Wiley and Sons, Inc., 2000.

[44] J. Lepers, R. Roper, and T. Sockheim, "Combustion stability code manual." Internal Report, June 2003. Siemens Energy Inc.

[45] "Acoustics – determination of sound absorption coefficient and impedance in impedance tubes – part 2: Transfer-function method." ISO 10534-2:1998(E).

[46] M. Summerfield, "A theory of unstable propulsion in liquid propellant rocket systems," *ARS J.*, vol. 21, no. 5, pp. 108–114, 1951.

[47] P. A. Hield, M. J. Braer, and S. H. Jin, "Thermoacoustic limit cycles in a premixed laboratory combustor with open and choked exits," *Combustion and Flame*, vol. 156, pp. 1683–1691, 2009.

[48] P. A. Hield, *An Experimental and Theoretical Investigation of Thermoacoustic Instability in a Turbulent Premixed Laboratory Combustor*. PhD thesis, University of Melbourne, 2007.

[49] A. P. Dowling, "Nonlinear self-excited oscillations of a ducted flame," *Journal of Fluid Mechanics*, vol. 346, pp. 271–290, 1997.

[50] H. Krediet, W. Krebs, E. Portillo, and J. Kok, "Prediction of thermoacoustic limit cycles during premixed combustion using the modified galerkin approach," AIAA/ASME/SAE/ASEE Joint Propulsion Conference, 2010. AIAA 2010-7150.

[51] F. Menter and T. Esch, "Elements of industrial heat transfer prediction," 2001. 16th Brazilian Congress of Mechanical Engineering (COBEM).

[52] D. Bradley, "How fast can we burn?," *Proceedings of the Combustion Institute*, vol. 24, pp. 247–262, 1992.

[53] D. Goodwin, "Cantera: An object-oriented software toolkit for chemical kinetics, thermodynamics, and transport processes." Caltech, Pasadena, 2009. [Online]. Available: http://code.google.com/p/cantera.

[54] S. R. Stow, A. P. Dowling, and T. P. Hynes, "Reflection of circumferential modes in a choked nozzle," *Journal of Fluid Mechanics*, vol. 467, 2002.

[55] C. Fugger, Y. Yu, Y. Matsutomi, W. Anderson, J. Pent, W. Krebs, and E. Portillo, "Investigation of a premixed reacting jet in an unstable transverse flow field," AIAA/ASME/SAE/ASEE Joint Propulsion Conference, 2011. AIAA-2011-5703.

[56] I. B. Celik, U. Ghia, P. J. Roache, C. J. Freitas, H. Coleman, and P. E. Raad, "Procedure for estimation and reporting of uncertainty due to distretization in cfd applications," *ASME Journal of Fluids Engineering*, vol. 130, 2008. 078001-1.

[57] K. Schadow and E. Gutmark, "Combustion instability related to vortex shedding in dump combustors and their passive control," *Progress in Energy and Combustion Science*, vol. 18, pp. 117–132, 1992.

[58] J. K. Eaton and J. P. Johnston, "Turbulent flow re-attachment: An experimental study of the flow and structure behind a backward-facing step," *Stanford University Report*, 1980.

[59] A. S. Neto, D. Grand, L. Metais, and M. Lesieur, "A numerical investigation of the coherent vortices in turbulence behind a backward-facing step," *Journal of Fluid Mechanics*, vol. 256, pp. 1–25, 1993.

[60] K. B. Chun and H. J. Sung, "Control of turbulent separated flow over a backward-facing step by local forcing," *Experiments in Fluids*, vol. 21, pp. 417–426, 1996.

[61] L. W. Sigurdson, "The structure and control of a turbulent reattaching flow," *Journal of Fluid Mechanics*, vol. 298, pp. 139–165, 1995.

[62] J. Pent, "Lessons learned for numerical modeling using self-excited large eddy simulations in openfoam." Internal Report, 2013. Siemens Energy Inc.

[63] R. I. Sujith, G. A. Waldherr, and B. T. Zinn, "An exact solution for one-dimensional acoustic fields in ducts with an axial temperature gradient," *Journal of Sound and Vibration*, vol. 183, no. 3, pp. 389–402, 1995.

[64] F. E. C. Culick, "Spatial averaging combined with perturbation/iteration procedure," *International Journal of Spray and Combustion Dynamics*, vol. 4, no. 3, pp. 185–216, 2012.

[65] S. Palm, *PLIF for Thermoacoustics*. PhD Thesis, California Institute of Technology, 2013. Department of Aerospace Engineering (not yet published).

[66] K. Balasubramanian and R. I. Sujith, "Non-normality and nonlinearity in combustion-acoustic interaction in diffusion flames," *Journal of Fluid Mechanics*, vol. 594, pp. 29–57, 2008.

[67] N. Lamarque and T. Poinsot, "Boundary conditions for acoustic eigenmode computations in gas turbine combustion chambers," *AIAA J.*, vol. 46, no. 9, pp. 2282–2292, 2008.

[68] Y. Reymen, M. Baelmans, and W. Desmet, "Time-domain impedance formulation based on recursive convolution," 12th AIAA/CEAS Aeroacoustics Conference, May 2006. AIAA 2006-2685.

[69] Y. Reymen, M. Baelmans, and W. Desmet, "Time-domain impedance formulation suited for broadband simulations," 13th AIAA/CEAS Aeroacoustics Conference, May 2007. AIAA 2007-3519.

[70] K. Y. Fung and H. Ju, "Time-domain impedance boundary conditions for computational acoustics and aeroacoustics," *International Journal of Computational Fluid Dynamics*, vol. 18, no. 6, pp. 503–511, 2004.

[71] D. F. Kelley and R. J. Luebbers, "Piecewise linear recursive convolution for dispersive media using fdtd," *International Journal of Computational Fluid Dynamics*, vol. 18, no. 6, pp. 503–511, 2004.

[72] B. Gustavsen and A. Semlyen, "Rational approximation of frequency domain responses by vector fitting," *IEEE Trans. Power Delivery*, vol. 14, no. 3, pp. 1052–1061, 1999.

[73] B. Gustavsen, "Improving the pole relocating properties of vector fitting," *IEEE Trans. Power Delivery*, vol. 21, no. 3, pp. 1587–1592, 2006.

[74] T. D. D. Deschrijver, M. Mrozowski and D. D. Zutter, "Macromodeling of multiport systems using a fast implementation of the vector fitting method," *IEEE Microwave and Wireless Components Letters*, vol. 18, no. 6, pp. 383–385, 2008.

[75] "The vector fitting website." http://www.energy.sintef.no/Produkt/VECTFIT/index.asp.

[76] T. J. Poinsot and S. K. Lele, "Boundary conditions for direct simulations of compressible viscous flows," *Journal of Computational Physics*, vol. 101, no. 1, pp. 104–129, 1992.